Dissertation zur Erlangung des Doktorgrades
der Fakultät für Chemie und Pharmazie
der Ludwig-Maximilians-Universität München

Sorafenib Resistance of Hepatocellular Carcinoma

–

Antibiotics Second-line to Sorafenib Therapy Inhibit Mitochondrial Biogenesis and Prevent Tumor Growth Resumption

Martina Meßner

aus

Starnberg, Deutschland

2020

I. ERKLÄRUNG

Diese Dissertation wurde im Sinne von § 7 der Promotionsordnung vom 28. November 2011 von Frau Prof. Dr. Johanna Pachmayr betreut.

II. EIDESSTATTLICHE VERSICHERUNG

Diese Dissertation wurde eigenständig und ohne unerlaubte Hilfe erarbeitet.

München, den 05.08.2020

_____

(Martina Meßner)

Dissertation eingereicht am 29.06.2020

1. Gutachterin: Prof. Dr. Johanna Pachmayr

2. Gutachterin: Prof. Dr. Angelika M. Vollmar

Mündliche Prüfung am 20.07.2020

III. TABLE OF CONTENTS

ABSTRACT

1 ABSTRACT

Sorafenib represents the current standard of care for patients with advanced-stage hepatocellular carcinoma (HCC). Nonetheless, its use is hampered by the frequent occurrence of drug resistance and up to 80% of patients treated with sorafenib suffer from side effects necessitating dose reduction, "drug holidays" or treatment termination. This study aimed to extend the current knowledge on the mechanism of sorafenib resistance with focus on a potential relapse of tumor growth after sorafenib withdrawal. Tumor growth resumption essentially contributes to a poor therapy outcome of sorafenib, but to date there is no therapeutic strategy to address this problem.

Herein, a robust sorafenib resistance HCC cell model was established and characterized by mass spectrometry (MS)-based proteomics and lipidomics, in order to reveal targets for a potential second-line therapy after sorafenib failure. The impact of continuous sorafenib exposure and drug withdrawal on cellular metabolism and mitochondrial functionality was then specified by glycolytic stress tests, high resolution respirometry and transmission electron microscopy (TEM).

We found that acquired chemoresistance of HCC is accompanied by severe mitochondrial damage and impairment of the electron transport chain (ETC). These sorafenib-resistant cells, fail to maintain their cellular redox homeostasis and obtain broad chemotherapeutic cross-resistance. In fact, sorafenib withdrawal leads to a rapid resumption of tumor cell proliferation, while cells resensitize towards chemotherapeutic treatment. Upon this tumor "rebound" growth, regeneration of the mitochondrial integrity and a boost of oxidative phosphorylation were observed. Inhibition of mitochondrial biogenesis by bacterial translation-inhibiting antibiotics, such as tigecycline (TGC), decreases the renewal of critical ETC subunits and limits the regeneration of reducing equivalents. Thereby, TGC efficiently blocks the oxidative glutamine metabolism of the tricarboxylic acid (TCA) cycle, which fuels rapid tumor regrowth. Importantly, TGC prevents the therapy-limiting tumor relapse after sorafenib withdrawal *in vitro* and in ectopic murine HCC xenografts *in vivo*.

Approved bacterial translation inhibiting antibiotics are generally characterized by favorable safety profiles with low incidence of adverse side-effects and good experience on dosing schedules, therefore holding tremendous promise for clinical translation. With regard to the clinical potential of the approved antibiotic TGC, we present a novel promising second-line therapeutic approach for HCC patients with progressive disease during sorafenib therapy, but also for patients who need a treatment interruption due to severe adverse events. Our study encourages a clinical evaluation of TGC for a new designation in advanced-stage HCC, to prevent the tumor growth resumption after therapy termination and prolong the patient's life expectancy after sorafenib failure.

INTRODUCTION

2 INTRODUCTION

2.1 Hepatocellular carcinoma (HCC)

HCC ranks as the third leading cause of cancer-related mortality in the human population and the most common primary cancer of the liver (Njei et al., 2015; WHO, 2012). In addition, HCC is nowadays reported to be one of the fastest growing causes of death with increasing incidence in the western population and poses, especially in the United States (US), an underestimated economic burden on the healthcare system (Ghouri et al., 2017). The tumorigenesis of HCC comprises angiogenesis, chronic inflammation, as well as alterations in the tumor macro- and micro-environment. Thereby, both the intrinsic genetic background and extrinsic risk factors, such as viral infections and the western lifestyle, have a decisive impact on the development of HCC.

2.1.1 Epidemiology and etiology

Since the 1970s, the epidemic of HCC has spread beyond Eastern Asia with a growing number of cases reported in the US, Canada and Western Europe (Ghouri et al., 2017). Thereby, the incidence has more than quadrupled from 1973 (1.51 cases/ 100.000 population) to 2011 (6.20 cases/ 100.000 population). Thus, HCC emerged to be the fifth most abundant malignancy worldwide with 745.000 reported deaths in 2012 (Njei et al., 2015). In high-risk countries, liver cancer can arise before the age of 20 years, whereas in countries at low risk, liver cancer is rare before the age of 50 years, classifying liver cancer as one of the seven most common age-adjusted malignancies in the human population (WHO, 2012). In its worldwide distribution, rates of liver cancer in men (523,000 cases/year, 7.9% of all cancers) are typically two to three times higher than in women (226,000 cases/year, 6.5% of all cancers) (Parkin et al., 2005). Further, regional differences have been noted with more than 80% of HCC cases occurring in sub-Saharan Africa and in Eastern Asia (>20 cases/100.000 population). Mid-incidence levels are reported in Southern European countries (10-20 cases/100.000 population) and comparable few cases (<5 cases/ 100.000 population) are known in the United States, Canada, and in Scandinavia (Bosch et al., 2004; El-Serag, 2012). The pathogenesis of HCC varies based on the underlying etiological background with cirrhosis being the most common risk factor, as found in 80%-90% of patients. Cirrhosis is essentially promoted by infections with the hepatitis B (HBV) (contributes to 44% of all HCC cases) and hepatitis C virus (HCV) (contributes to 21% of all HCC cases), resulting in a 5-year cumulative risk of HCC development between 5% and 30%, depending on the incidence of further risk factors, region, ethnicity and the stage of cirrhosis (Baecker et al., 2018; El-Serag, 2012). Besides, the intoxication by alcohol and aflatoxins, metabolic disorders, the non-alcoholic fatty liver disease and immune-related disorders contribute to the rising numbers of cirrhosis and HCC development (Baecker et al., 2018; Bugianesi, 2007; Parikh and Hyman, 2007).

2.1.2 Current treatment strategies

The development of new treatment strategies for HCC is a highly dynamic and research-intensive field since the approval of sorafenib in 2007. As a consequence of earlier diagnosis and a more frequent use of curative treatment modalities, the outcome for patients improved significantly. Remarkably, between 1975 and 2005 the 5-year survival trend in the US increased by more than 60% (Altekruse et al., 2009). In general, therapy allocation depends on variables known to impact prognosis including tumor burden, liver function, and the performance status (PS) of the patient.

2.1.2.1 The Barcelona Clinic Liver Cancer (BCLC) staging system

Staging is of high importance in the management of HCC, in order to apply the best individual treatment strategy. For this purpose, the Barcelona Clinic Liver Cancer (BCLC) system is the most commonly used staging approach and has been widely accepted in clinical practice. The BCLC system determines the cancer stage and the patient's prognosis alongside an established criteria catalog *(Figure 1)* (Bruix et al., 2016; Bruix, 2011; Llovet et al., 1999). Thereby, patients are classified into very early, early, intermediate, advanced, and terminal stage HCC, depending on the size and number of nodules (N), macrovascular invasion or extrahepatic spread by metastasis (M) and the outcome of the patient's performance status test (PST) (Forner et al., 2010).

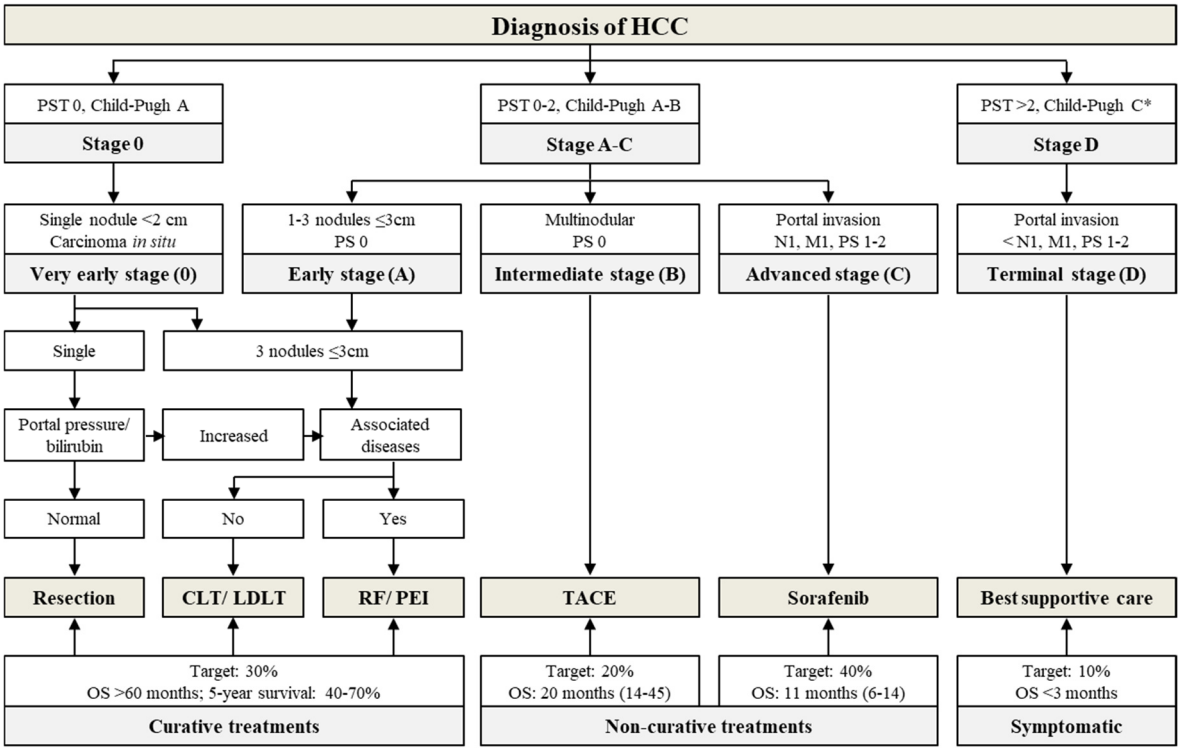

Figure 1. **The BCLC staging system for HCC**. CLT, cadaveric liver transplantation; LDLT, living donor liver transplantation; M, metastasis classification; N, node classification; OS, overall survival; PEI, percutaneous ethanol injection; PST, performance status test; RF(A), radiofrequency (ablation); TACE, transarterial chemoembolization; *, Stage C with PST 1-2 and/ or vascular invasion/ extrahepatic spread.

Very early and early-stage patients (BCLC 0 or BCLC A) exhibit a solitary lesion or up to 3 nodules ≤3 cm with preserved liver function. These patients can benefit from potentially curative therapies such as resection, transplantation and ablation (Bruix et al., 2016). Hepatic resection is often performed in non-cirrhotic patients, resulting in an overall low morbidity. However, strict screening for the presence of cirrhosis is required as cirrhosis potentiates the risk of post-operative complications and hepatic failure (Bismuth and Majno, 2000). Liver transplantation (CLT/ LDLT) eliminates HCC together with potential preexisting illnesses, providing the best outcome for patients, but is highly limited by the availability of organs (Schlachterman et al., 2015). For early stage patients, a comparable shorter recovery period can be achieved by minimally invasive percutaneous radiofrequency ablation (RFA) and percutaneous ethanol injection (PEI) (Schlachterman et al., 2015). Patients with intermediate stage HCC (BCLC B) are free of symptoms, but have large, multifocal tumors, rendering them poor candidates for curative therapies. Among those, patients with preserved liver function can benefit from transarterial chemoembolization (TACE), a treatment modality that combines obstruction of the hepatic artery with embolizing particles and intraarterial injection of cytotoxic agents, such as doxorubicin or cisplatin (Bruix, 2011; Marelli et al., 2007; Schlachterman et al., 2015). However, most patients are still diagnosed with advanced-stage HCC (BCLC C) with tumors that have spread beyond the liver, vascular invasion and cancer-related symptoms (Bruix et al., 2016). They cannot benefit from curative therapies and are standardly treated with the multikinase inhibitor sorafenib. Patients with end stage HCC (BCLC D) have an impaired liver function and marked cancer-related symptoms (PST >2). Those patients have a poor prognosis and require palliative care (Forner et al., 2010).

2.1.2.2 A glance on recent clinical trials

Within the past decade, a large variety of therapeutic agents has been developed and tested in clinical trials aiming to increase efficiency or safety to the standard of care sorafenib *(Table 1)*.

2.1.2.2.1 Phase III trials on first-line alternatives to sorafenib

Despite increasing mechanistic insights, phase III trials for advanced-stage HCC conducted with the alternative first-line agents sunitinib (Cheng et al., 2013), brivanib (Johnson et al., 2013) and linifanib (Cainap et al., 2015) were reported as negative and also combination therapies of sorafenib with erlotinib (Zhu et al., 2015b) and doxorubicin (Abou-Alfa et al., 2010) failed. Further, first-line minimal invasive approaches including hepatic arterial infusion chemotherapy (HAIC) (Kudo et al., 2018b) as well as selective internal radiation therapy (SIRT) with yttrium-90 (^{90}Y) resin microsphere radio-embolization were shown to be non-superior to sorafenib in the treatment of advanced-stage HCC (Chow et al., 2018; Vilgrain et al., 2017). The amount of negative first-line trials indicates a clear difficulty of newly developed agents to meet the predefined clinical study endpoints in terms of superiority to sorafenib in the overall survival (OS) of patients. Only a recent phase III first-line

trial of the multi-targeted tyrosine kinase inhibitor lenvatinib (REFLECT) was announced positive, showing non-inferiority to sorafenib in the OS of advanced-stage HCC patients (Kudo et al., 2018a). Differences, however, occurred in the safety profile, as lenvatinib accompanied with a high incidence of hypertension, anorexia, and fatigue, whereas sorafenib predominantly caused hand-foot skin reaction (HFSR) *(chapter 6.3.4.1)*. Further, immunotherapy evoked as a promising first-line alternative with ongoing phase III trials of tislelizumab, atezolizumab with bevacicumab (IMbrave150) and durvalumab with tremelimumab as mono- or combination-therapies (Raoul et al., 2018). In 2019, preliminary study endpoints of the IMbrave150 trial indicated a promising outcome in terms of OS and accelerated approval of this drug combination was sought in 2020 *(chapter 6.3.4.1)*. To date, despite the numerous advents of new agents, sorafenib maintains its role as gold standard and remains favorable in the systemic first-line therapy of advanced-stage HCC with regard to the overall OS benefit and the good experience on the safety profile and dosing schedules.

2.1.2.2.2 Phase III trials on second-line therapies after sorafenib failure

Similar to the phase III trials on first-line alternatives to sorafenib, a number of trials have failed in the second-line setting. Among those, brivanib (Llovet et al., 2013), everolimus (Zhu et al., 2014), ramucimurab (Zhu et al., 2015a), a regional trial with S-1 (tegafur/gimeracil/oteracil) (Hsieh et al., 2015), tivantinib (Rimassa et al., 2018) and the arginine depleting enzyme conjugate ADI-PEG 20 (Abou-Alfa et al., 2018b) were non-beneficial to placebo. Importantly, in 2017 the agents regorafenib (Bruix et al., 2017) and nivolumab (Finkelmeier et al., 2018) have been approved for patients who progressed under sorafenib treatment. Regorafenib demonstrated a significantly improved OS from 10.6 months compared to 7.8 months of the placebo group and an increase of the progression-free survival (PFS) and time to progression (TTP). However, due to its high structural similarity to sorafenib, a comparable toxicity profile was obtained with regorafenib. Therefore, unlike other studies, the RESOURCE trial investigated regorafenib solely in patients refractory but tolerant to sorafenib. The PD-1 targeting antibodies nivolumab and pembrolizumab received accelerated FDA approval as second-line therapies because of promising tumor response rates of phase I/II trials (El-Khoueiry et al., 2017; Finkelmeier et al., 2018). However, phase III trials of both nivolumab and pembrolizumab failed to meet their predefined endpoints (Finn et al., 2020; Liu et al., 2019). More recently, also the small molecule cabozantinib (CELESTRIAL) reported improved OS, but the majority of patients of the cabozantinib-treated arm experienced severe adverse events necessitating treatment termination (Abou-Alfa et al., 2018a). Further, the therapeutic benefit of ramucirumab (anti-VEGFR-2) second-line to sorafenib is limited to patients with high alpha-fetoprotein (AFP) levels (≥ 400 ng/ml) as revealed by the REACH-2 phase III trial (Zhu et al., 2018b). Thus, despite the successful approval of regorafenib, cabozantinib, ramucirumab and the fast developing treatment landscape with new immunotherapeutic, an effective second-line therapy with reliable safety profile for sorafenib-intolerant patients remains an urgent need *(see also: chapter 6.3.4.2)*.

Table 1. *Phase III clinical trials of HCC targeting agent.*

BCLC staging	Clinical trial	Status
Early-stage (adjuvant)	peretinoin vs. placebo (NIK-333)	Negative
	sorafenib vs. placebo (STORM)	Negative
Intermediate-stage (Combination with TACE)	sorafenib (Post TACE/ TACE2)	Negative
	brivanib (BRISK-TA)	Terminated
	orantinib (TSU-68) (ORIENTAL)	Terminated
Advanced-stage (first-line)	sunitinib vs. sorafenib (SUN1170)	Negative
	brivanib vs. sorafenib (BRISK-FL)	Negative
	linifanib vs. sorafenib (LiGHT)	Negative
	sorafenib + erlotinib vs. sorafenib (SEARCH)	Negative
	sorafenib + doxorubicin vs. sorafenib (CALGB808028)	Negative
	sorafenib ± HAIC (SILIUS)	Negative
	lenvatinib vs. sorafenib (REFLECT)	Positive
	SIRT vs. sorafenib (SARAH/ SIRveNIB/SORAMIC)	Negative
	nivolumab vs. sorafenib (CheckMate-459)	Negative
	tislelizumab vs. sorafenib (BGB-A317)	Ongoing
	atezolizumab + bevacicumab vs. sorafenib (IMbrave150)	Ongoing
	durvalumab + tremelimumab vs. sorafenib (HIMALAYA)	Ongoing
Advanced-stage (second-line)	brivanib vs. placebo (BRISK-PS)	Negative
	everolimus vs. placebo (EVOLVE-1)	Negative
	ramucirumab vs. placebo (REACH/ REACH-2)	Neg./ Pos.
	S-1 vs. placebo (S-CUBE)	Negative
	tivantinib vs. placebo (METIV-HCC, JET-HCC)	Negative
	regorafenib vs. placebo (RESOUCE)	Positive
	cabozantinib vs. placebo (CELESTRIAL)	Positive
	ADI-PEG 20 vs. placebo (ADI-PEG 20)	Negative
	DT vs. placebo (ReLive)	Negative
	pembrolizumab vs. placebo (KEYNOTE-240)	Negative

*DT: doxorubicin loaded nanoparticels; HAIC, hepatic arterial infusion chemotherapy; Neg., negative; Pos., positive; SIRT, selective internal radiation therapy (table updated: 05/2020).

2.2 The multikinase inhibitor sorafenib

To date, in highly developed countries 30% of HCC patients are diagnosed at initial stages when curative treatments can be optimally applied. But still, with 40% of all reported cases, most patients remain to be diagnosed with advanced-stage HCC (Bruix and Llovet, 2002). For those patients, curative treatment modalities have a poor outcome and medical interventions, such as resection, chemotherapy, RFA and TACE, show tumor recurrence with rapid progression, vascular invasion and multiple intrahepatic metastases. Thus, the 5-year relative survival of advanced-stage HCC patients amounts to only 7% (Bosch et al., 2004). As a consequence of the poor OS, big effort has been ongoing for many years to find new targeted therapies for advanced-stage HCC, finally leading to the development of the multikinase inhibitor sorafenib in 1990 (Daher et al., 2018).

Table 2. *Key efficacy results of the SHARP and AP phase III trials.*

Study	**SHARP trial**		**AP trial**	
Treatment	**sorafenib**	**placebo**	**sorafenib**	**placebo**
Group size	n = 299	n = 303	n = 150	n = 76
Median OS (95% CI)*	10.7 (9.4–13.3)	7.9 (6.8–9.1)	6.5 (5.6–7. 6)	4.2 (3.8–5.6)
P-value OS	<0.001%		0.014%	
Median TTP (95% CI)*	5.5 (4.1–6.9)	2.8 (2.7–3.9)	2.8 (2.6–3.6)	1.4 (1.4–1.6)
P-value TTP	<0.001%		0.0005%	

*AP, Asia-Pacific; CI, confidence interval; SHARP, Sorafenib Hepatocellular Carcinoma Assessment Randomized Protocol; TTP, time to progression; median OS and TTP are shown in months (Raoul et al., 2018).

In 2007, sorafenib (Nexavar, Bayer HealthCare Pharmaceuticals–Onyx Pharmaceuticals) became the first worldwide approved systemic therapy and until today the standard of care first-line treatment for patients with unresectable HCC. Its approval was based on the phase III randomized placebo-controlled SHARP (Sorafenib Hepatocellular Carcinoma Assessment Randomized Protocol) trial (Llovet et al., 2008) and a study conducted in the Asia-Pacific (AP) region (Cheng et al., 2009). Thereby, sorafenib achieved a significantly prolonged OS in both the SHARP and the AP phase III trial *(Table 2)*. These results were confirmed later by the GIDEON (Global Investigation of therapeutic decisions in HCC and of its treatment with sorafenib) (Raoul et al., 2018), a prospective, open-label, cohort study, that evaluated sorafenib safety and HCC treatment practices in 3202 patients across 39 countries (Lencioni et al., 2014; Marrero et al., 2016).

2.2.1 Mechanism of action

Sorafenib is an orally administered multikinase inhibitor that exerts antiproliferative, antiangiogenic and proapoptotic effects. It inhibits the serine-threonine kinases Raf-1 and B-Raf, the receptor tyrosine kinase activity of the vascular endothelial growth factor receptors (VEGFRs) 1, 2, 3, the platelet-derived growth factor receptor-β (PDGFR-β), the FMS-like tyrosine kinase-3 (Flt-3), Ret and c-Kit (Chang et al., 2007; Wilhelm et al., 2004). The Raf proteins are integral components of the Ras/Raf/mitogen-activated protein kinase (MAPK)/extracellular signaling-regulated kinase (ERK) (RAF/MEK/ERK) signaling cascade. The MAPK/ERK pathway consists of three sequentially activated protein kinases, which promote cell proliferation and survival. In contrast, the sorafenib-targeted tyrosine kinase receptors VEGFR and PDGFR are predominantly involved in angiogenesis, whereas Flt-3, Ret and c-Kit enhance tumorigenesis and therefore contribute to the broad-spectrum activity of sorafenib in several cancers (Cervello et al., 2012; Wilhelm et al., 2006). It has been demonstrated that sorafenib dose-dependently decreases the activation of the hypoxia-inducible factor-1α (HIF-1α) protein, playing a potential role in mediating its antiangiogenetic effect (Liu et al., 2012). In addition, sorafenib treatment associates with a reduced expression of the antiapoptotic myeloid cell leukemia 1 (Mcl-1) protein, which may increase the proapoptotic therapeutic efficacy in combination therapies with alternative chemotherapeutic compounds and signal transduction inhibitors (Wilhelm et al., 2004) *(Figure 2)*.

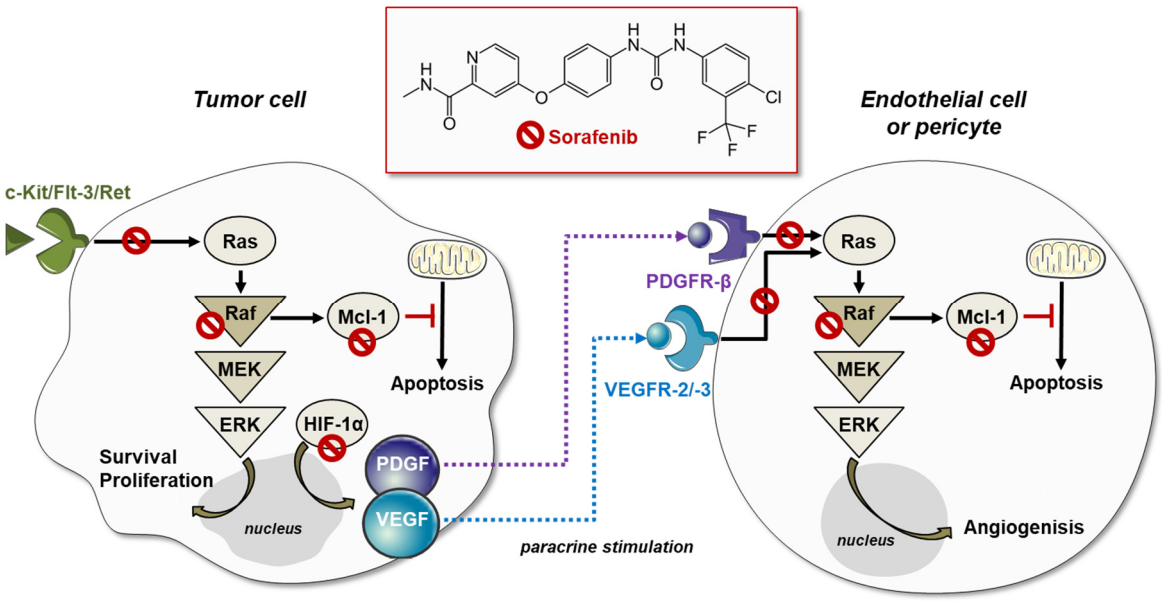

Figure 2. **Mechanism of action and chemical structure of the multikinase inhibitor sorafenib.** ERK, extracellular signaling-regulated kinase; Flt-3, FMS-like tyrosine kinase-3; ERK, extracellular signaling-regulated kinase; HIF-1α, hypoxia-inducible factor-1α; MAPK, Ras/Raf/mitogen-activated protein kinase; Mcl-1, myeloid cell leukemia 1; MEK, MAPK-ERK kinase; PDGFR-β, platelet-derived growth factor receptor-β; VEGFR, vascular endothelial growth factor receptor.

2.2.2 Clinical limitations of sorafenib

The use of sorafenib is hampered by the frequent occurrence of drug-related serious adverse events, as reported in around 80% of patients (Llovet et al., 2008). In addition, only 2% of patients obtain partial responses and many show tumor progression later on. Thus, sorafenib resistance essentially limits the OS and time to symptomatic progression of those patients (Zhai and Sun, 2013).

2.2.2.1 Adverse events and dosing recommendations

Sorafenib therapy is associated with severe side-effects, such as hand-foot skin reaction (HFSR), diarrhea, abdominal pain and weight loss, necessitating dose-reduction (26%), therapy interruptions (44%) or complete sorafenib retraction (38%) (Llovet et al., 2008). Notably, sorafenib-related adverse events have been identified as clinical biomarkers for sorafenib efficacy, rendering a persistent side-effect management inevitable (Raoul et al., 2018). In general, the treatment regimen of sorafenib is limited by its dose-dependent toxicity, with higher tolerance in longer treatment intervals, allowing dosing up to 600 mg twice daily in a 7 days on/7 days off study (Strumberg et al., 2007). Nowadays, patients are standardly treated with the maximal tolerated dose of 400 mg sorafenib, twice daily on a continuous dosing-schedule (Al-Rajabi et al., 2015). However, drug levels were found to be insufficiently low in some patients, indicating the presence of intrinsic pharmacokinetic resistance, which results in approximately 50% interindividual variability in sorafenib exposure (Boudou-Rouquette et al., 2012; Strumberg et al., 2007). Inadequate target inhibition by underdosing, acquired sorafenib resistance and tumor growth resumption might be the consequence (Kuczynski et al., 2015). In addition, sorafenib plasma levels have been shown to significantly decline over time. These drug level changes might involve the induction of cytochrome P450 3A4 (CYP3A4) metabolism and can only be managed by long-term dosage adjustments, which limit the survival due to excessive body weight loss (Kuczynski et al., 2015).

2.2.2.2 Acquired therapy resistance

The genetic heterogeneity of HCC results in initial sorafenib resistance of some patients and has led to the identification of predictive biomarkers for therapy responsiveness, such as basal phospho-ERK -, JNK- and VEGF-A- levels (Zhu et al., 2017). To date, a variety of mechanisms accounting for the development of chemotherapeutic drug resistance have been described. They comprise compensatory pathway activation, epithelial-to-mesenchymal transition (EMT), disabling of pro-apoptotic signaling and the establishment of an hypoxic environment (Zhai and Sun, 2013). However, the exact mechanism of acquired sorafenib resistance has not yet been fully elucidated.

2.2.2.2.1 Epithelial-to-mesenchymal transition (EMT)

EMT is a highly conserved developmental process that governs morphogenesis and cell migration in multicellular organisms. However, in tumorigenesis, EMT contributes to dedifferentiation and gives rise to the dissemination of single carcinoma cells from the sites of the primary tumors (Thiery, 2002). Several ligands and pathways have been implicated to trigger EMT in physiological and pathological conditions, such as transforming growth factor beta (TGF-β), fibroblast growth factor (FGF), PDGF, Wnt-signaling and activation of the mammalian target of rapamycin (mTOR) (Thiery, 2002). Upon EMT the activation of these pathways leads to the stabilization of the Snail protein, which mediates silencing of the cell adhesion molecule E-cadherin (Batlle et al., 2000). In addition, the protein expression of mesenchymal cell markers, such as vimentin and N-cadherin is elevated, resulting in the remodeling of the cellular actin cytoskeleton with loss of polarity, cell-to-cell contacts and increased tumor cell migration (Zhu et al., 2017). In patients, EMT is associated with poor survival, the development of invasive tumor growth and metastasis (Marcucci and Rumio, 2018). Increasing evidence is given that long-term sorafenib exposure triggers EMT with loss of E-cadherin expression, conveying a high invasive potential (van Malenstein et al., 2013).

2.2.2.2.2 Evasive PI3K/AKT pathway activation

A crucial signaling node that contributes to the induction of EMT is the phosphatidylinositol 3-kinase (PI3K)/AKT-signaling pathway, which works in parallel to the sorafenib-targeted MAPK/ERK axis and is involved in cell apoptosis as well as chemotherapeutic drug resistance (Zhai and Sun, 2013). The serine/threonine kinase mTOR, which acts downstream of PI3K and AKT, is modulated by extracellular stimulants and interacts with several proteins to form the active unit mTOR complex (mTORC) 1 and 2 (Marcucci and Rumio, 2018). Besides promoting EMT, mTORC1 inhibits the cytoprotective formation of autophagosomes (He and Klionsky, 2009). Sorafenib-resistant HCC has been shown to increase the abundance of phosphorylated AKT protein (p-Akt) in response to therapy and inhibition of AKT expression or activation sensitizes tumor cells to sorafenib-induced apoptosis (Chen et al., 2011). Thus, evasive PI3K/AKT-signaling might contribute to acquired sorafenib resistance of advanced-stage HCC in the course of therapy.

2.2.2.2.3 Controversial role of stress-induced autophagy

Tumor cells have evolved two distinct mechanisms in order to respond to stress from the tumor microenvironment: EMT *(chapter 2.2.2.2.1)* and macroautophagy (Marcucci and Rumio, 2018). Autophagy is referred to as a self-digestion process by which cytoplasmic contents are sequestered in autophagosomes and delivered to lysosomes for degradation (Pickles et al., 2018). However, the role of autophagy in tumorigenesis and chemotherapeutic resistance is discussed controversially. In addition to the well-established pro-survival functions during nutrient-deprivation, it is suggested that cytotoxicity follows excessive autophagy through digestion of essential cellular components.

Hence, autophagy-mediated cytotoxicity is classified as programmed cell death type II (Abdel-Aziz et al., 2017; Maiuri et al., 2007). In line with this controversy, autophagy modulation contributes to both resistance and cytotoxicity of several chemotherapeutics with a suspected impact on sorafenib responsiveness. It was shown that sorafenib treatment led to an accumulation of autophagosomes and activation of the autophagic flux, indicated by increased LC3 lipidation and a reduction of the autophagy substrate sequestosome 1 (SQSTM1, p62) in HCC cells (Shimizu et al., 2012).

2.2.2.3 Tumor growth resumption in antiangiogenic treatment breaks

Angiogenesis has long been associated with aggressive tumor growth and inhibition of the VEGF axis is the basis of most antiangiogenic drugs (Bagri et al., 2010). Besides preventing the formation of new tumor vessels, VEGF inhibitors eliminate many existing tumor vessels and normalize the phenotype of those that survive treatment (Jain, 2001). This approach was substantiated in 2004 with the approval of the anti-VEGF monoclonal antibody bevacizumab as combination therapy for the treatment of metastatic colorectal cancer. In addition, tyrosine kinase inhibitors (TKIs) with antiangiogenic activity such as sunitinib, sorafenib, and pazopanib have been approved as stand-alone chemotherapy (Bagri et al., 2010; Hurwitz et al., 2004). VEGF pathway inhibitors have achieved objective clinical success over the past decade, however, uncertainty remains about whether vascular and tumor regrowth occurs when therapy is stopped.

Previously, preclinical models have shown that halting antiangiogenic therapy can lead to rapid revascularization (Mancuso et al., 2006) and evidence is accumulating that tumors can quickly resume after therapy withdrawal (Levashova et al., 2010; Nagengast et al., 2011). Further, administering antiangiogenic agents, such as sunitinib, on a discontinuous treatment schedule might involve a certain risk of tumor regrowth in drug-free break periods (Ebos and Pili, 2012). Still, tumor vascular rebound or tumor growth resumption following treatment discontinuation has not been confirmed in all cases (di Tomaso et al., 2011). In case of selective VEGF pathway inhibition by bevacizumab, quantification of tumor growth during and after treatment with anti-VEGF found no evidence of altered tumor proliferation (Bagri et al., 2010). While the underlying mechanisms for this growth resumption remain elusive, microenvironmental changes and hypoxia-induced autophagy are speculated to condition cancer cells for tumor extravasation upon sustained antiangiogenic treatment (Abdel-Aziz et al., 2017). Further, recent work shed light on hypoxic and glycolytic adaptions of the cancer cell metabolism upon antiangiogenic therapy with sunitinib or sorafenib. However, treatment withdrawal led to tumor regrowth, restored angiogenesis, a metabolic shift to enhanced lipid synthesis and a drastic increase in metastatic dissemination (Sounni et al., 2014). To date, sparse research has been done to investigate metabolic adaptions in tumor growth resumption, the impact on the OS and to extrapolate a targeted therapeutic response.

2.3 Targeting mitochondria for anticancer therapy

Mitochondria are the cells' powerhouse mediating metabolic reprogramming, which is described as a central feature of cancer cells. In general, mitochondria exert both vital and lethal functions, making them the Achilles' heel for anticancer therapy. On the one hand, they are indispensable for energy production upon fast proliferation, precursor metabolite biosynthesis and signaling, but on the other hand they are also crucial regulators of the intrinsic apoptosis program (Warburg, 1956; Weinberg and Chandel, 2015). Most chemotherapeutic agents interfere with signaling pathways upstream of mitochondria in order to trigger intrinsic apoptosis, whereas drugs that directly target the mitochondrial metabolism are discussed as tools to bypass drug resistance (Fulda et al., 2010).

2.3.1 Mitochondria-targeting chemotherapeutics

Mitochondria contribute to multiple steps of oncogenesis, such as malignant transformation, tumor progression and the modulation of treatment responsiveness, thus constituting a promising target for the development of novel anticancer agents (Vyas et al., 2016). Importantly, acquired drug resistance is frequently related to alterations in the intrinsic apoptosis pathway and preventing these mitochondrial adaptions appears to be essential for therapeutic resensitization (Fulda et al., 2010; Hanahan and Weinberg, 2011). This new understanding of mitochondria and their role in conferring chemoresistance led to the clinical approval of the B-cell lymphoma 2 (Bcl-2) inhibitor venetoclax, which prevents apoptosis evasion and is nowadays in clinical use for the treatment of chronic lymphocytic leukemia (Ashkenazi et al., 2017). Besides regulating intrinsic apoptosis, mitochondria attracted attention from a metabolic perspective, as evidence was increasing that distinct mitochondrial metabolites are capable of driving oncogenesis (Dang et al., 2009). In addition, cancer cells adapt biosynthetic circuits to obtain metabolic flexibility, which confers chemoresistance and provides intermediates for aggressive tumor growth (Fendt et al., 2013). Thus, various preclinical studies are ongoing, assessing the anticancer potential of hexokinase inhibitors, thiol redox inhibitors, voltage-dependent anion-selective channel/adenine nucleotide translocase (VDAC/ANT) inhibitors, lipophilic cations targeting the mitochondrial membrane as well as agents affecting the tricarboxylic acid (TCA) cycle, the mitochondrial DNA (mtDNA) or the electron transport chain (ETC) (Porporato et al., 2017; Sborov et al., 2015). However, most clinical studies are pending or still in early stages and therapies maintain yet unavailable for clinical application.

2.3.2 The metabolic contribution of mitochondria to tumor growth

Pioneering work in the quantitative investigation of cancer cell metabolism was done in the 1920s by Otto Warburg, showing that under aerobic conditions tumor tissue fermentates approximately tenfold more glucose to lactate compared to normal tissues, a phenomenon known as the Warburg effect (Warburg, 1956). The increased glucose turnover of cancer cells was initially misinterpreted

as an evidence of mitochondrial dysfunctionality. In contrast, current evidence suggests that glycolysis in cancer cells is promoted by altered growth factor signaling that exerts a direct stimulatory effect on glucose uptake and metabolism, rather than by a low energy status (Ward and Thompson, 2012). Further, the role of proto-oncogenes and tumor suppressors has been extended from the ability to regulate the cell cycle by sustaining respectively evading proliferative signaling, to a key function in reprogramming cancer cell metabolism (Hanahan and Weinberg, 2011). Whereas the tumor suppressor p53 promotes the pentose phosphate pathway (PPP) and oxidative phosphorylation, the proto-oncogene MYC is known to enhance the glucose and glutamine turnover in order to fuel cell proliferation (Koppenol et al., 2011). According to the current understanding, cancer cells do not replace the mitochondrial metabolism, but exhibit the Warburg effect while retaining oxidative phosphorylation (OXPHOS) (Koppenol et al., 2011). However, in proliferating cells the production of adenosine triphosphate (ATP) by respiration was shown to appear secondary to the synthesis of anabolic precursor metabolites (Ward and Thompson, 2012).

2.3.2.1 Mitochondrial biosynthesis of amino acids, lipids and nucleotides

The mitochondrial TCA cycle, which is mostly fueled by the abundant nutrients glucose and glutamine, generates intermediates and building blocks used to provide proliferating cells with macromolecules for the synthesis of amino acids, lipids and nucleotides (Ahn and Metallo, 2015).

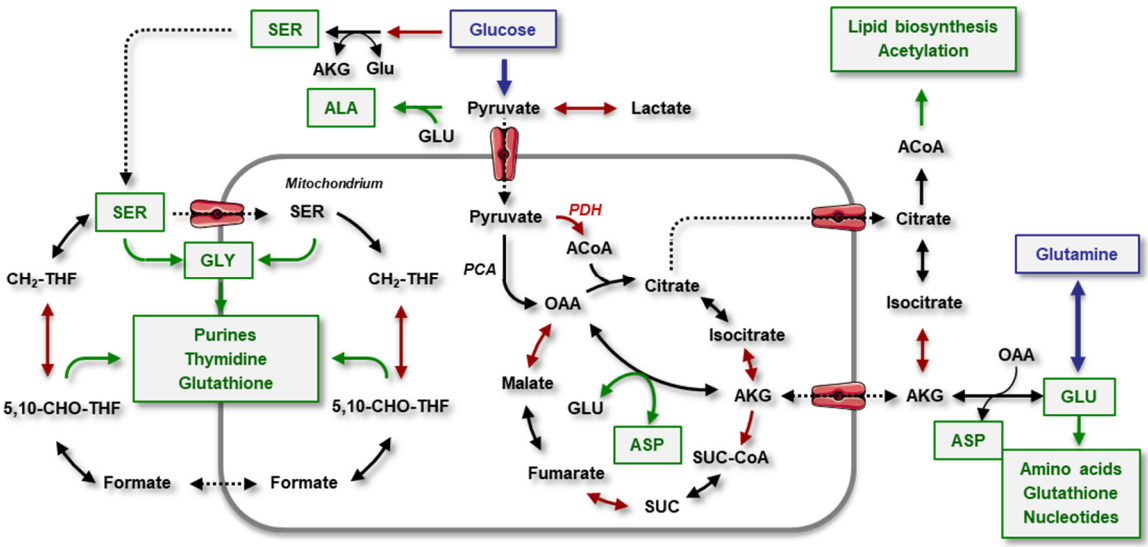

***Figure 3*. Biosynthetic nodes within mitochondria.** Illustration of the metabolic pathways within mitochondria that contribute to the biosynthesis of building blocks in proliferating cells. The TCA cycle and folate one-carbon metabolism (FOCM) enable cells to convert glucose, glutamine and amino acids to lipids, non-essential amino acids, nucleotides, glutathione, purines, pyrimidines and other cellular components. Enzymatic reactions that are dependent on redox-sensitive cofactors are depicted in red. ALA, alanine; AKG, α-ketoglutarate; ASP, aspartate; GLU, glutamine; GLY, glycine; OAA, oxaloacetate; PCA, pyruvate carboxylase; PDH, pyruvate dehydrogenase; SER, Serine; SUC, succinate; THF, tetrahydrofolate.

As previously mentioned, cancer cells are known to consume increased amounts of glucose, which are metabolized to pyruvate and either excreted as lactate or transported into the mitochondria (Warburg, 1956). Thus, upon conditions of limited glutamine availability or turnover, cancer cells tend to increasingly rely on glucose carbon flux through pyruvate carboxylase (PCA) to maintain oxaloacetate (OAA) production and the biosynthesis of downstream TCA cycle intermediates (Ahn and Metallo, 2015). Beyond flux through the PCA, mitochondrial pyruvate is oxidized by the pyruvate dehydrogenase (PDH) complex to form acetyl-coenzyme A (ACoA) (Ahn and Metallo, 2015). ACoA is subsequently converted to citrate via condensation with OAA, which is then either further oxidized to isocitrate in the TCA cycle or transported out of the mitochondria to yield cytosolic ACoA. Extramitochondrial ACoA is the main substrate for *de novo* lipogenesis and acetylation reactions (Wellen et al., 2009) *(Figure 3)*. Recently it was shown that during hypoxia or when mitochondrial respiration is impaired, reductively metabolized glutamine can also serve as a carbon source for fatty acid synthesis (Fendt et al., 2013; Mullen et al., 2011).

For entering into the TCA cycle, glutamine is sequentially converted to glutamate (GLU) by glutaminases and into α-ketoglutarate (AKG) by glutamate dehydrogenases or aminotransferases (Weinberg and Chandel, 2015). Glutamine essentially provides the cell with nitrogen through transamination reactions, contributing to *de novo* purine synthesis and the formation of non-essential amino acids, such as alanine (ALA) and aspartate (ASP). In turn, ASP acts as a nitrogen donor and is a precursor for the amino acid asparagine (Altman et al., 2016). In general, backbone synthesis of purine nucleotides requires nitrogen from ASP, GLU, glycine (GLY) and formate, all precursors primarily derived from the mitochondrial metabolism. In detail, serine (SER), which is derived from glycolysis intermediates by glutamate-dependent transamination, is substrate to the serine hydroxymethyltransferase of the folate one-carbon metabolism (FOCM). The FOCM generates GLY and 5,10-methyl (CHO)-tetrahyfrofolate (THF), thereby providing the educts for purine, thymidine and glutathione (GSH) synthesis (Ahn and Metallo, 2015; Altman et al., 2016) *(Figure 3)*. Further, pyrimidine ring synthesis requires glutamine, ASP, as well as the activity of the dihydroorotate dehydrogenase, a mitochondrial enzyme that converts dihydroorotate to orotate coupled with the reduction of ubiquinone (Coenzyme CoQ, CoQ) to ubiquinol in the ETC. Importantly, oxidation of ubiquinol is necessary to maintain an adequate supply of CoQ and is therefore impaired in cells that lack a functional ETC (Ahn and Metallo, 2015; Mullen et al., 2014).

2.3.2.2 Control of the mitochondrial reduction-oxidation (redox) balance

It is suggested that fast proliferating cells possess an equally important need for the maintenance of redox balance as for the biogenesis of macromolecular building blocks (Cairns et al., 2011; Sullivan et al., 2015). Thus, beyond its role in providing anabolic precursors, glutamine oxidation is essential for the TCA cycle-mediated reduction of the redox-active cofactors nicotinamide adenine dinucleotide (NAD^+) and flavin adenine dinucleotide (FAD). In their reduced state NADH and

$FADH_2$ are metabolized by the ETC, which couples nutrient oxidation to ATP production (Weinberg and Chandel, 2015). Another glutamine-dependent redox-mediator is reduced nicotinamide adenine dinucleotide phosphate (NADPH), which provides reducing power in a variety of biosynthetic enzymatic reactions and essentially contributes to lipid synthesis. NADPH is mostly generated by electron transfer to $NADP^+$ in the course of extramitochondrial conversation of malate to pyruvate (Weinberg and Chandel, 2015). Malate is thereby directly exported from mitochondria to the cytosol or obtained by reduction of OAA, which is exported into the cytoplasm by the malate-aspartate shuttle (DeBerardinis et al., 2007). Besides, mitochondrial $NADP^+$ is reduced by the isocitrate dehydrogenase 2 (IDH2), whereas cytosolic $NADP^+$ is recycled to NADPH by isocitrate dehydrogenase 1 (IDH1) or the oxidative PPP. The PPP was thereby shown to be uniquely required for the maintenance of a normal $NADP^+$/NADPH ratio, the enzymatic hydrogenation of folic acid to THF and nucleotide biosynthesis by the FOCM (Chen et al., 2019). Importantly, NADPH keeps the antioxidant GSH, a tripeptide consisting of the amino acids GLU, GLY and cysteine (CYS), in its reduced state for the defence against reactive oxygen species (ROS) (Panieri and Santoro, 2016). Mitochondria are the most prominent source of intracellular ROS, which are byproducts of the ETC and, at physiologic levels, mediate important signaling events necessary for cell proliferation (Cairns et al., 2011). However, at high abundance due to impaired electron transport or disturbed cellular redox balance, ROS may damage cellular components, promote genetic instability and lead to cell death (Wellen and Thompson, 2010).

2.3.3 Shaping the mitochondrial bioenergetic function

Mitochondria are involved in multiple anabolic processes by supplying cells with both ATP and reduction equivalents. Thus, modulators of the mitochondrial metabolism and, especially, of the ETC activity are frequently applied for experimental analysis of the mitochondrial functionality and respiratory capacity as they shape the oxygen consumption, which is measurable in intact cells.

2.3.3.1 The electron transport system (ETS)

The mitochondrial ETS consists of the F_1F_0-ATPase (complex V, ATP synthase) and the electron-transporting complexes (I-IV), which are embedded in the inner mitochondrial membrane (IMM) and electrically connected by the electron carriers CoQ and cytochrome C (CytC) *(Figure 5)*. Among those, the complexes I, III and IV are transmembrane proton pumps, required to establish an electrochemical gradient (ΔH^+) for ATP production (Mitchell, 1961). Thereby, the respective enzymatic subunits catalyze the electron (e^-) transfer of the reducing equivalents NADH and $FADH_2$ to oxygen (O_2) (Chen, 1988). The energy released from this series of redox-reactions is coupled to the proton (H^+) flux through the F_1F_0-ATPase across the IMM, which harasses this protonmotive force to drive ATP synthesis, membrane transport and thermogenesis (LeBleu et al., 2014; Mitchell, 1961). The adenine nucleotide translocator (ANT), which is localized in the contact sites between

inner and outer mitochondrial membrane, can export ATP in exchange for adenosine diphosphate (ADP) and relies therefore not only on the activity of the ETS, but also on the abundance of cytoplasmic ATP generated by glycolysis (Kalbacova et al., 2003).

2.3.3.2 Mitochondrial superoxide production

Superoxides (O_2^-) are ROS of mitochondrial origin, which are generated through the interaction of one-electron donors with local O_2 in the mitochondria as a consequence of electron leakage from redox centres of the ETC (Turrens, 2003). Thereby, both the complexes I and III, but also electron-transferring dehydrogenase complexes are known sites of O_2^- production (Drose and Brandt, 2012) *(Figure 5)*. In general, the complex I-mediated O_2^- production is increased in cells that have a high protonmotive force respectively a reduced CoQ-pool due to an insufficient ATP-production or a low NAD^+/NADH ratio (Murphy, 2009). Excessive ROS production or insufficient antioxidant defence can lead to oxidative damage of mitochondrial proteins, membranes and DNA. Further, as a consequence of oxidative damage, mitochondrial ATP production and a wide range of metabolic functions such as the TCA cycle, fatty acid oxidation and amino acid synthesis may be disturbed (Murphy, 2009). Importantly, increased ROS abundance has been shown to promote tumor growth and malignant progression, whereas chemotherapeutic sensitization has been reported upon impairment of the antioxidant defense by NADPH or GSH (Panieri and Santoro, 2016).

2.3.3.3 The NADH-ubiquinone oxidoreductase (NDUF)

The mitochondrial multisubunit enzyme complexes I-V act successively in transferring electrons from the electron donating cofactors NADH and $FADH_2$ to oxygen, which is reduced to water. The first enzyme in the ETC, the NDUF (complex I), removes electrons from NADH and passes them via a series of enzyme-bound flavin mononucleotide (FMN) and iron–sulphur (Fe-S) redox centres to CoQ (Larosa and Remacle, 2018) *(Figure 4)*. The NDUF consists of 36 subunits whereby 7 of those represent the enzymatic core, which resembles the bacterial complex I and is, thus, conserved in all eukaryotes (Scarpulla, 2006; Taanman, 1999). Given that the NDUF is involved in the majority of electron uptake and O_2^- production, it represents a sensitive target of the ETS and is inhibited by rotenoids, metformin and a variety of antibiotics (Degli Esposti, 1998; Wheaton et al., 2014).

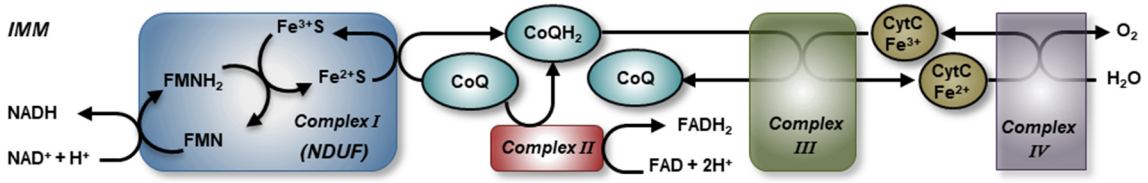

Figure 4. Electron flux through the respiratory complexes I-V. CoQ, Coenzyme Q; CytC, cytochrome C; FAD, flavin adenine dinucleotide; Fe-S, iron–sulphur redox center; FMN, flavin mononucleotide; IMM, inner mitochondrial membrane; NAD, nicotinamide adenine dinucleotide.

2.3.3.4 Experimental modulators of the mitochondrial metabolism

Inhibition of the electron transport across the ETC results in a reduced electrochemical gradient, which is required for ATP production by the complex V. Thereby, inhibition of the complex I, which is targeted by rotenone, appears to be the most sensitive target of the ETS (Sullivan et al., 2015; Wheaton et al., 2014). In addition, inhibition of the complex III by antimycin A or disruption of the protonmotive force by uncouplers, such as carbonyl cyanide 3-chlorophenylhydrazone (CCCP), decrease the oxygen consumption of the complex IV (Kalbacova et al., 2003). CCCP is a lipid-soluble ionophore, which enters in protonated form as a weak acid into intact mitochondria. It discharges the electrochemical gradient and uncouples the proton flow back into the mitochondria from the ATP production by the F_1F_0-ATPase. In order to maintain the mitochondrial membrane potential, CCCP stimulates mitochondria to increasingly translocate electron across the complexes I, III and IV, thus elevating the measured oxygen consumption (Benz and McLaughlin, 1983). In contrast, inhibition of the mitochondrial F_0F_1-ATPase by oligomycin prevents the proton flux out of the mitochondria and increases the mitochondrial membrane potential. Nowadays, oligomycins are extensively used to examine the activity of ETC subunits and to assess the dependency of tumor cells on mitochondrial respiration (Kalbacova et al., 2003; Nagle and Zhou, 2010). In contrast, the antimetabolite 2-deoxy-D-glucose (2-DG) competitively inhibits the generation of glucose-6-phosphate and reveals glycolytic dependency (Barban and Schulze, 1961), whereas the amino-thiol N-acetyl cysteine (NAC) scavenges free cellular radicals (Sun, 2010) *(Figure 5)*.

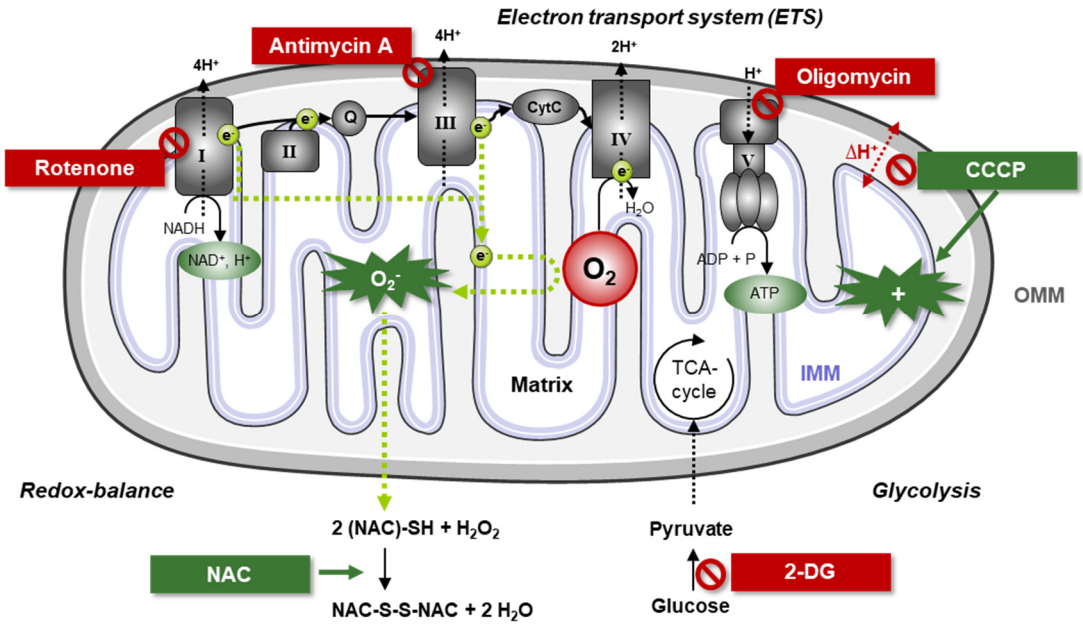

Figure 5. **Modulators of the mitochondrial metabolism used for experimental analysis.** 2-DG, 2-deoxy-D-glucose; CCCP, carbonyl cyanide 3-chlorophenylhydrazone; CytC, cytochrome C; IMM/OMM, inner/ outer mitochondrial membrane; NAC, N-acetyl cysteine; O_2^-, superoxides; Q, Coenzyme Q (CoQ).

2.4 Aim of the study

Acquired sorafenib resistance occurs frequently during therapy for advanced-stage HCC and contributes to a poor outcome for these patients. In addition, the therapeutic benefit of sorafenib is limited by a rapid resumption of tumor growth upon sorafenib withdrawal, which might be necessary due to the occurrence of drug-related serious adverse events. However, a multitude of phase III trials have failed to prolong the OS of patients in the systemic first-line and second-line setting of advanced-stage HCC and, until today, sorafenib remains the standard of care therapy.
Thus, it is an urgent issue to understand how the majority of patients develop resistance to sorafenib and what happens after sorafenib retraction. In order address this question and to extrapolate possibilities for therapeutic interventions, we developed a robust sorafenib resistance HCC model. We aimed to extend the current knowledge of acquired sorafenib resistance with a focus on the mechanistic background of a potential tumor relapse after sorafenib treatment termination, as both resistance and tumor relapse contribute to a poor therapy outcome. Importantly, rapid tumor regrowth has been previously reported upon withdrawal of TKIs in patients, however, the underlying mechanisms remain elusive and, to date, there are no therapeutic strategies to address this problem.

In summary, this study aims at:

1. Characterizing the sorafenib resistance phenotype in a HCC cell model and identifying the underlying mechanisms that contribute to sorafenib resistance *(chapter 4.1)*.

2. Elucidating the metabolic and mechanistic background of growth resumption observed after sorafenib withdrawal to assess which therapeutic implications ensue *(chapter 4.2-4.4)*.

3. Analyzing emerging therapeutic options, to extrapolate an alternative treatment strategy with focus on second-line drug candidates after sorafenib retraction *(chapter 4.5-4.6)*.

4. Presenting an innovative alternative therapeutic approach that can be verified with good effectiveness *in vivo* and that possesses a high potential for clinical translation *(chapter 4.7)*.

MATERIALS AND METHODS

3 MATERIALS AND METHODS

3.1 Materials

3.1.1 Cells

Table 3. *Cell lines.*

Cell line	Supplier or academic partner
HUH7-R/ RIL175-R	Generated from HUH7-WT/ RIL175-WT cells (Meßner, et al., unpublished)
HUH7-R-LUC	Stable lentiviral modification of HUH7-R cells (Meßner, et al., unpublished)
HUH7-WT (JCRB0403)	Japanese Collection of Research Bioresources (JCRB)
RIL175 (RIL-175)	A gift from Prof. S. Rothenfußer, University Hospital, LMU Munich, Germany
VCR-R CEM	M. Kavallaris, University of New South Wales, Sydney, Australia

The generation of sorafenib-resistant HUH7 (HUH7-R) and RIL175 (RIL175-R) cells *(chapter 3.2.1.2)* as well as the genetic modification to luciferase expressing HUH7-R cells (HUH7-R-LUC) *(chapter 3.2.2.1)* will be subsequently described. The establishment and profiling of RIL175 (Kapanadze et al., 2013) and of vincristine-resistant CEM cells (VCR-R CEM) (Haber et al., 1989) was previously done and VCR-R CEM cells were kindly provided by the group of M. Kavallaris.

3.1.2 Compounds and Reagents

Table 4. *Clinical approved chemotherapeutic and antibiotic compounds.*

Compound	CAS Number	Producer
ABT888	912445-05-7	Enzo Life Sciences, Lörrach, Germany
Chloramphenicol	56-75-7	Sigma-Aldrich, Taufkirchen, Germany
Cisplatin	15663-27-1	Sigma-Aldrich, Taufkirchen, Germany
Doxorubicin	25316-40-9	Sigma-Aldrich, Taufkirchen, Germany
Everolimus	159351-69-6	Selleckchem, Munich, Germany
Gefitinib	184475-35-2	Selleckchem, Munich, Germany
Linezolid	165800-03-3	Sigma-Aldrich, Taufkirchen, Germany
SN38	86639-52-3	Tocris Bioscience, Abingdon, UK
Sorafenib	284461-73-0	Enzo Life Sciences, Lörrach, Germany
Tigecycline	1229002-07-6	Sigma-Aldrich, Taufkirchen, Germany
Tivantinib	905854-02-6	Selleckchem, Munich, Germany
Vincristine	2068-78-2	Sigma-Aldrich, Taufkirchen, Germany

Table 5. *Chemicals and Reagents.*

Reagent	Producer
2,2,2-Trichlorethanol (TCE)	Sigma-Aldrich, Taufkirchen, Germany
2,4,6-Tris-(dimethylaminomethyl)phenol	SE, Heidelberg, Germany
Ammonium persulfate (APS)	Sigma-Aldrich, Taufkirchen, Germany
Bovine serum albumin (BSA)	Sigma-Aldrich, Taufkirchen, Germany
Bradford reagent Roti® Quant	Bio-Rad, Munich, Germany
Complete®	Roche Diagnostics, Penzberg, Germany
Coumaric acid	Fluka, Buchs, Switzerland
Crystal violet	Carl Roth, Karlsruhe, Germany
DharmaFECT Transfection Reagent 1	Thermo Scientific, Waltham, MA, USA
Dimethylsulfoxide (DMSO)	Sigma-Aldrich, Taufkirchen, Germany
D-luciferin sodium salt	Biomol GmbH, Hamburg, Germany
Dodecenylsuccinic anhydride	SE, Heidelberg, Germany
ECL Plus WB Detection reagent	GE Healthcare, München, Germany
FluorSave® reagent mounting medium	Merck, Darmstadt, Germany
Glutaraldehyde (2.5%) in sodium cacodylate buffer	EMS, Hatfield, PA, USA
Glycerol	Applichem¸ Darmstadt, Germany
Glycidether 100	SE, Heidelberg, Germany
Glycine	Carl Roth, Karlsruhe, Germany
HEPES	Carl Roth, Karlsruhe, Germany
Hoechst 33342	Sigma-Aldrich, Taufkirchen, Germany
Isoflurane	CP-Pharma®, Burgdorf, Germany
Lead citrate, 3%	Leica, Wetzlar, Germany
Methylnadicanhydride	SE, Heidelberg, Germany
N,N,N',N'-Tetramethylethylendiamin (TEMED)	VWR, Radnor, PA, USA
Osmium tetroxide, 4%	EMS, Hatfield, PA, USA
Page Ruler™ Prestained Protein Ladder	Fermentas, St. Leon-Rot, Germany
Paraformaldehyde solution, 4%	Polysciences, Warrington, PA, USA
Penicillin – Streptomycin (Pen/Strep)	PAN Biotech, Aidenbach, Germany
Polyacrylamide	Carl Roth, Karlsruhe, Germany
Porcine trypsin	Promega, Madison, WI, USA

PowerUp™ SYBR® Green Master Mix	Applied Biosystems, Waltham, USA
Propidium iodide	Sigma-Aldrich, Taufkirchen, Germany
Propylene oxide	SE, Heidelberg, Germany
Pyronin Y	Sigma-Aldrich, Taufkirchen, Germany
Sodium cacodylate buffer, pH 7.4, 0.1 M	EMS, Hatfield, PA, USA
Sodium chloride	Carl Roth, Karlsruhe, Germany
Sodiumdodecylsulfate (SDS)	Carl Roth, Karlsruhe, Germany
TransIT-X2® Transfection Reagent	Mirus Bio LLC, Madison, WI, USA
Tricine	Sigma-Aldrich, Taufkirchen, Germany
Tris base	Sigma-Aldrich, Taufkirchen, Germany
Trisodium citrate	Sigma-Aldrich, Taufkirchen, Germany
Triton X-100	Merck, Darmstadt, Germany
Tween 20	Sigma-Aldrich, Taufkirchen, Germany
UranyLess EM Stain	EMS, Hatfield, PA, USA

*EMS: Electron Microscopy Sciences, SE: Serva Electrophoresis GmbH.

Table 6. *Assay Kits.*

Assay Name	**Producer**
CellTiterBlue® reagent	Promega, Mannheim, Germany
CellTiterGlo® reagent	Promega, Mannheim, Germany
CyQUANT® Cell Proliferation Assay Kit	Life Technologies, Eugene, USA
High-Capacity cDNA Reverse Transcription Kit	Applied Biosystems, Waltham, USA
L-Lactate Assay Kit	Cayman Chemical, Michigan, USA
Multi-Drug Resistance Assay Kit (Calcein AM)	Cayman Chemical, Michigan, USA
NAD/NADH Glo™	Promega, Mannheim, Germany
NADP/NADPH Glo™	Promega, Mannheim, Germany
RNeasy® Mini Kit (250)	QIAGEN, Hilden, Germany
ROS Detection Cell-Based Assay Kit (DCFDA)	Cayman Chemical, Michigan, USA
Seahorse XF Glycolysis Stress Test Kit	Agilent Technologies, Santa Clara, USA

Table 7. *Inhibitors, metabolites and antimetabolites.*

Inhibitor	**Producer**
1,4-Dithioerythritol (DTE)	Sigma-Aldrich, Taufkirchen, Germany
2-deoxy-D-glucose (2-DG)	Sigma-Aldrich, Taufkirchen, Germany
3-methyladenine (3-MA)	Sigma-Aldrich, Taufkirchen, Germany
Acetyl-Coenzyme A (ACH)	Sigma-Aldrich, Taufkirchen, Germany
Antimycin-A	Sigma-Aldrich, Taufkirchen, Germany
Aspartate (ASP)	Sigma-Aldrich, Taufkirchen, Germany
Carbonyl cyanide 3-chlorophenylhydrazone (CCCP)	Sigma-Aldrich, Taufkirchen, Germany
Citrate (CIT)	Sigma-Aldrich, Taufkirchen, Germany
Complete® mini EDTA free	Roche diagnostics, Penzberg, Germany
Concanamycin A	Sigma-Aldrich, Taufkirchen, Germany
Cyclosporine A	Enzo Life Sciences, Lörrach, Germany
Cysteine (CYS)	Sigma-Aldrich, Taufkirchen, Germany
Dithiothreitol (DTT)	Sigma-Aldrich, Taufkirchen, Germany
L-Glutamine	Sigma-Aldrich, Taufkirchen, Germany
Malate (MAL)	Sigma-Aldrich, Taufkirchen, Germany
MitoBlock-6 (MB6)	Focus Biomolecules, Plymouth, USA
N-acetyl cysteine (NAC)	Cayman Chemical, Michigan, USA
Oligomyclin	Sigma-Aldrich, Taufkirchen, Germany
Oxaloacetate (OAA)	Sigma-Aldrich, Taufkirchen, Germany
Phenymethylsulfonyl fluoride (PMSF)	Sigma-Aldrich, Taufkirchen, Germany
Pyruvate (PYR)	Sigma-Aldrich, Taufkirchen, Germany
Rotenone	Sigma-Aldrich, Taufkirchen, Germany
Sodium fluoride (NaF)	Merck, Darmstadt, Germany
Sodium orthovanadate (Na_3VO_4)	ICN, Biomedicals, Aurora, OH, USA
Verapamil	Enzo Life Sciences, Lörrach, Germany
α-ketobutyrate (AKB)	Sigma-Aldrich, Taufkirchen, Germany
α-ketoglutarate (AKG)	Sigma-Aldrich, Taufkirchen, Germany

3.1.3 Antibodies and Dyes

3.1.3.1 Antibodies for Western blot

Table 8. *Primary antibodies for immunoblotting.*

Antigen	Source	Dilution	Cat. No.	Producer
Akt	rabbit	1:1,000	#9272	CST
AMPK	mouse	1:1,000	# 2793	CST
Bak	rabbit	1:1,000	#ab32371	Abcam
Bax	rabbit	1:500	#sc-493	Santa Cruz
Bcl-2	rabbit	1:1,000	#2872	CST
Drp-1	rabbit	1:1,000	#8570	CST
E-Cadherin	rabbit	1:1,000	#3195	CST
Erk	rabbit	1:1,000	#9102	CST
GADD153/CHOP	rabbit	1:500	#sc-793	Santa Cruz
IDH2	rabbit	1:500	#22166SS	Novus Biologicals
LC3	rabbit	1:1,000	#4108	CST
Mfn-1	rabbit	1:1,000	#14739	CST
MMP-2	rabbit	1:1,000	#4022	CST
MMP-9	rabbit	1:1,000	#3852	CST
NFKBp65	goat	1:500	sc-372-G	Santa Cruz
OGDH	rabbit	1:1,000	#19622	Novus Biologicals
OxPhos WB Antibody Cocktail	mouse	1:250	#45-8099	Thermo Scientific
p38MAPK	rabbit	1:1,000	#9212	CST
PGC-1α	rabbit	1:1,000	#ab54481	Abcam
phospho-Akt (Ser473)	rabbit	1:500	#9271	CST
phospho-AMPK (Thr172)	rabbit	1:1,000	#2535	CST
phospho-Erk (Thr202/Tyr204)	rabbit	1:1,000	#9106	CST
phospho-NFKBp65 (Ser536)	rabbit	1:1,000	#3031	CST
phospho-p38MAPK (Thr180/182)	rabbit	1:1,000	#9211	CST
TFE3	rabbit	1:1,000	#PA5-35210	Thermo Scientific
TFEB	rabbit	1:1,000	#4240	CST
Vimentin	rabbit	1:1,000	#5741	CST

Table 9. *Secondary antibodies for immunoblotting.*

Antibody	Dilution	Cat. No.	Producer
Goat-anti-rabbit IgG(H+L)-HRP conjugate	1:1,000	#172-1019	Bio-Rad
Goat-anti-mouse IgG1-HRP conjugate	1:1,000	#ab97240	Abcam
Donkey-anti-goat IgG-HRP conjugate	1:10,000	#ab97120	Abcam

For Western blot analysis all antibodies were diluted in 5% BSA in PBS before use.

3.1.3.2 Antibodies for Immunostaining

Table 10. *Primary antibodies for immunostaining.*

Antigen	Source	Dilution	Cat. No.	Producer
E-Cadherin (HECD1)	mouse	1:1,000	#131700	Invitrogen
N-Cadherin	rabbit	1:200	#4061	CST
PGC-1α	rabbit	1:300	#ab54481	Abcam

*CST: Cell Signaling Technologies.

Table 11. *Secondary antibodies and dyes for immunostaining.*

Antibody/Dye	Dilution	Cat. No.	Producer
Alexa Fluor 488 goat anti-rabbit	1:400	#A-11008	Invitrogen
Alexa Fluor 488 goat-anti-mouse	1:400	#A-11001	Invitrogen
Alexa Fluor 546 donkey-anti-rabbit	1:400	#A-10040	Invitrogen
Hoechst (bisBenzimide H 33342)	1:100	#23491-52-3	Sigma Aldrich

For immunostaining all antibodies were diluted in 0.2% BSA in PBS before use.

3.1.3.3 Fluorescent Dyes

Table 12. *Staining dyes for live cell imaging and flow cytometry.*

Fluorescent Dye	Ex/Em [nm]	Dilution	Cat. No.	Producer
2-NBDG	488/530	100 µM	N13195	Invitrogen
Cal-520 AM	488/530	10 µM	21131	AAT Bioquest
LysoTracker™ Red DND-99	577/590	1:3,000	L7528	Invitrogen
MitoSOX™ Red	488/575	5 µM	M36008	Invitrogen
MitoTracker™ Green FM	490/516	1:9,000	M7514	CST

*2-NBDG, 2-(N-(7-Nitrobenz-2-oxa-1,3-diazol-4-yl)Amino)-2-Deoxyglucose.

3.1.4 Primers

Table 13. *Primer sequences for quantitative real-time PCR.*

Target	Type	Sequence	Producer
E-Cadherin	forward	5′-CAG CAC GTA CAC AGC CCT AA-3′	Metabion
	reverse	5′-AAG ATA CCG GGG GAC ACT CA-3′	Metabion
PGC-1α	TaqMan	PPARGC1A (Hs00173304_m1)	Thermo Scientific

3.1.5 Small interfering RNAs

For transient transfections siRNAs were used in an initial concentration of 50 nM with 0.08% transfection reagent DharmaFECT 1 (T-2001-02, Dharmacon) per well. After stimulation the final concentration per well was reduced to 25 nM siRNA and 0.04% DharmaFECT 1 to avoid toxicity.

Table 14. *siRNAs used for transient gene silencing.*

Target	Cat. No.	Transfection reagent	Producer
LUC (nt)	D 001206-14-05	Dharmafect 1	Dharmacon
IDH2	M 004013-00-0005	Dharmafect 1	Dharmacon
OGDH	M 009679-02-0005	Dharmafect 1	Dharmacon

3.1.6 Technical equipment

Table 15. *Instruments.*

Name	Producer
Acquity Ultraperformance LC system	Waters, Eschborn, Germany
Cell Homogenizer Potter S	Sartorius AG, Göttingen, Germany
ChemiDoc™ Touch Imaging System	Bio-Rad, Munich, Germany
Climate chamber for live cell microscopy	Ibidi GmbH, Martinsried, Germany
Digital Caliper	Emil Lux, Wermelskirchen, Germany
DMi1 microscope	Leica, Wetzlar, Germany
EASY-nLC 1000 chromatography system	Thermo Scientific, Waltham, MA, USA
FACSCalibur	Becton Dickinson, Heidelberg, Germany
FACSCantoII	Becton Dickinson, Heidelberg, Germany
IVIS®spectrum	CLS, Rüsselsheim, Germany
JEOL-1200 EXII transmission electron microscope	JEOL GmbH, Freising, Germany

Leica EM AC20 contrasting system	Reichert und Jung, Germany
Leica SP8 confocal laser scanning microscope	Leica Microsystems, Wetzlar, Germany
MC120 HD camera	Leica, Wetzlar, Germany
Mikro 22R centrifuge	Hettich, Tuttlingen, Germany
Nanodrop® Spectrophotometer	PEQLAB Biotechnologie GmbH
Orbitrap XL instrument	Thermo Scientific, Waltham, MA, USA
Orion II microplate luminometer	BDS, Pforzheim, Germany
OROBOROS Oxygraph-2k	Oroboros Instruments, Innsbruck, Austria
QTRAP 5500 mass spectrometer	Sciex, Darmstadt, Germany
QuantStudio™ 3 Real-Time PCR System	Applied Biosystems, Foster City, CA
Seahorse XFe96 Analyzer	Agilent Technologies
Sonoplus GM3200 with BR30 cup booster	Bandelin, Berlin, Germany
Spark® multimode microplate reader	Tecan, Crailsheim, Germany
SpectraFluor®PLUS	Tecan, Männedorf, Switzerland
Sunrise®	Tecan, Männedorf, Switzerland
Ultramicrotome Ultracut E	Reichert und Jung, Germany
Vi-Cell® CR	Beckmann Coulter, Fullerton, CA, USA
xCELLigence® instrument	Roche Diagnostics, Penzberg, Germany

*CLS, Caliper Life Sciences GmbH, BDS, Berthold Detection Systems.

Table 16. *Assay Materials.*

Name	**Producer**
1 ml syringes	Hartenstein GmbH, Würzburg, Germany
27 G needles	Hartenstein GmbH, Würzburg, Germany
BEEM capsules, 0.95 ml	Plano GmbH, Wetzlar, Germany
Column Acquity UPLC BEH C18 1.7 µM, 2.1×50 mm	Waters, Milford, MA, USA
Column Acquity UPLC BEH C8 1.7 µm, 1×100 mm	Waters, Milford, MA, USA
Column PepMap RSLC C18, 75 µm x 50 cm, 2 µm	Thermo Scientific, Waltham, MA, USA
Column PepMap100 C18, 75 µm x 2 cm, 3 µm	Thermo Scientific, Waltham, MA, USA
Culture flasks, plates and dishes	TPP, Trasadingen, Switzerland
E-Plate®	Roche Diagnostics, Penzberg, Germany

FACS tubes	Thermo Scientific, Waltham, MA, USA
Ibidi® µ-slide	Ibidi GmbH, Martinsried, Germany
Immun-Blot® PVDF membrane (0.2 µM)	Bio-Rad, Munich, Germany
Kolliphor EL (Solutol)	Sigma-Aldrich, Taufkirchen, Germany
MicroAmp® Fast Optical 96-Well Plate, 0.1 ml	Applied Biosystems, Waltham, USA
MicroAmp® Optical Adhesive Film	Applied Biosystems, Waltham, USA
Microplate 96-well transparent/ black/ white	Greiner Bio-One, Kremsmünster, Austria
Nitrocellulose membrane (0.2 µM), Hybond-ECLTM	AmershamBioscience, Freiburg, Germany
QIA-Shredder columns	Qiagen, Hilden, Germany
Seahorse XFe96 FluxPaks (inc. mini)	Agilent Technologies, Santa Clara, USA
XFe96 microplate	Agilent Technologies, Santa Clara, USA

3.1.7 Software

Table 17. *Software tools for data analysis.*

Software name and version	**Supplier**
Analyst 1.6	Sciex, Darmstadt, Germany
FlowJo 7.6	Tree Star, Ashland, OR, USA
Glycolysis Stress Test Report Generator	Agilent Technologies, Santa Clara, USA
GraphPad Prism 7	GraphPad Software, San Diego, CA, USA
GSEA 3.0	The Broad Institute, Massachusetts, USA
Image Lab 5.2	Bio-Rad, Hercules, CA, USA
Leica LAS X	Leica, Wetzlar, Germany
Living Image 4.4	CLS, Rüsselsheim, Germany
MaxQuant	Max Planck Institute of Biochemistry, Munich
Microsoft Office 2010	Microsoft, Redmont, WA, USA
Perseus 1.5.4.1.	Max Planck Institute of Biochemistry, Munich
RTCA	Roche Diagnostics, Penzberg, Germany
Wave 2.3.0	Agilent Technologies, Santa Clara, CA

3.2 Methods

3.2.1 Cell culture

3.2.1.1 Cell culture buffers and solutions

For the cultivation of HUH7 and RIL175 cells, DMEM medium (PAN Biotech GmbH, Aidenbach, Germany) was used. CEM/VCR-R cells were cultured in RPMI 1640 medium with 2 mM glutamine (PAN Biotech GmbH, Aidenbach, Germany). Both media were supplemented with 10% FCS (PAA Laboratories GmbH, Pasching, Austria) and a combination of 100 U/ml penicillin and 100 µg/ml streptomycin (Pen/Strep). All cells were cultured at 37 °C with 5% CO_2 in constant humidity. Before seeding of adherent HUH7 and RIL175 cells, culture flasks, multiwell-plates and dishes were coated with collagen G (0.001% in PBS, Biochrom AG, Berlin, Germany). The buffers and solutions that were used for the cultivation of HUH7, RIL175 and CEM/VCR-R cells are listed below (*Table 18*).

Table 18. *Buffers and solutions used for cell culture.*

	PBS	**PBS + Ca^{2+}/Mg^{2+}**
NaCl	132.2 mM	137 mM
Na_2HPO_4	10.4 mM	8.10 mM
KH_2PO_4	3.2 mM	1.47 mM
KCl	-	2.68 mM
$MgCl_2$	-	0.25 mM
H_2O	add	add
pH	7.4	7.4

	Growth medium	**Freezing medium**
DMEM/ RPMI	500 ml	70%
FCS	50 ml	20%
DMSO	-	10%
Trypsin/EDTA (T/E)		
Trypsin		0.05%
EDTA		0.02%
PBS		add

3.2.1.2 Generation of the sorafenib-resistant cell lines HUH7-R and RIL175-R

The sorafenib-resistant cell line HUH7-R was generated from HuH7 (JCRB0403) cells (indicated as HUH7-WT), which were purchased from the Japanese Collection of Research Bioresources (JCRB). Sorafenib-resistant RIL175-R cells were generated from RIL-175 cells (Kapanadze et al., 2013) (indicated as RIL175-WT) and used to confirm the key-findings obtained by the sorafenib-resistant HUH7-R cell model. Sorafenib resistance was obtained through continuous exposure of HUH7-WT respectively RIL175-WT cells to sorafenib (BAY 43-9006, Enzo Life Sciences GmbH, Lörrach, Germany) just below their IC_{50}-value. Over several weeks, the sorafenib dose was slowly increased with 0.5 µM per time up to a tolerated sorafenib concentration of 10 µM in the growth medium. After establishment, the HUH7-R and RIL175-R cell lines were alternating cultured in growth medium

with and without supplementation of 10 µM sorafenib, as described below, and used for the sorafenib-resistant rebound growth model *(chapter 3.2.1.3)*. The IC_{50}-values of HUH7-R and RIL175-R cells in comparison to their parental cell lines HUH7-WT and RIL175-WT were determined by the CellTiter-Blue® (CTB) viability assay as subsequently described *(chapter 3.2.9.1)*. Cells were cultured in constant humidity at 37 °C and 5% CO_2 in an incubator.

3.2.1.3 The sorafenib-resistant rebound growth model

HUH7-R and RIL175-R cells that were cultured in the presence of 10 µM sorafenib for at least 7 days are indicated as HUH7-R(+) and RIL-175-R(+) cells. For the generation of the rebound growth cell types HUH7-R(-) and RIL175-R(-), sorafenib was withdrawn from R(+) cells for 72 h before seeding. In general, HUH7-R and RIL175-R cells were seeded in growth medium in the respective multiwall-plates and dishes 24 h before performing experiments. Consequently, R(-) cells were cultured without sorafenib for a total of 96 h if not otherwise mentioned. In order to maintain a constant sorafenib resistance phenotype with standardized treatment conditions, R(-) cells were reseeded in the presence of 10 µM sorafenib for another 7 days and used as R(+) cells in the following week. For experiments including a rebound growth time series, R(+) cells were seeded as described above and sorafenib was withdrawn for the specified time (in hours), as indicated in brackets.

3.2.1.4 Passaging

Adherent HUH7 and RIL175 cells were passaged every 3-5 days, when grown to 80-90% of confluence. For passaging, the medium was removed and cells were washed with pre-warmed PBS (*Table 18*). Subsequently, cells were detached with trypsin/ethylene-diamine-tetraacetic acid (EDTA) (*Table 18*) and the enzymatic reaction was stopped by adding growth medium (*Table 18*). Cells were then either re-cultured in a 75cm^2 flask or seeded for experimental analysis. The growth and plating medium of HUH7-R(+) and RIL175-R(+) cells was supplemented with 10 µM sorafenib. Growth medium was changed twice per week for HUH7-WT and RIL175-WT cells and three times per week for R(+) cells, due to strong lactate production. The suspension cell line VCR-R CEM was maintained at a cell density of 0.1-1.0 x 10^6 cells/ml by passaging twice per week. Before seeding, the cell density of all cell lines was determined using the cell viability analyzer ViCell XR.

3.2.1.5 Freezing and thawing

For freezing, confluent HUH7 and RIL175 cells were trypsinized as described above, counted, centrifuged (1,000 rpm, 5 min, 20 °C) and resuspended in 1.5 ml ice-cold freezing medium (*Table 18*). For all cell lines 1-3 x 10^6 cells were snap frozen at -80 °C and the cryovials were transferred to nitrogen tanks (-196 °C) for long-term storage. For thawing, cells were immediately resuspended in culture medium and excessive DMSO was separated by centrifugation. The cell pellet was resuspended in culture medium and cells were grown in a 25 cm^2 flask until passaging.

3.2.2 Stable and transient transfection

3.2.2.1 Stable lentiviral transfection

The stably luciferase-expressing HUH7-R cells (HUH7-R-LUC) were generated by lentiviral transduction. Therefore, virus supernatant from HEK 293T cells that had been transfected with the plasmids pCDH-eFFLuc-T2A-eGFP (Rabinovich et al., 2008) (a gift from Prof. Jeremias, Helmholtz Zentrum München, Germany), pCMV-VSV-G and pCMV-dR8.2 were used.

3.2.2.1.1 Production of lentiviral supernatant

The generation and concentration of virus supernatant was performed by the group of Prof. Dr. med. Rothenfusser (University Hospital, LMU Munich, Germany). Prior to transfection, 4 x 10^6 293T cells were plated onto a 10 cm dish in 10 ml pre-warmed DMEM medium, supplemented with 10% FCS, Pen/Strep and L-Glutamine. After reaching a confluence of 60-70%, cells were transfected with the respective plasmids. Therefore, a transfection solution was prepared with OptiMEM (486 µl) and TransIT-X2 solution (15 µl). After an incubation of 15 min at room temperature, 2.5 µg of the pCDH-eFFLuc-T2A-eGFP plasmid DNA and 1.25 µg each of the packaging plasmids pCMV-VSV-G and PCMV-dR8.2 were added, carefully mixed and incubated for 15 min more. Meanwhile, the medium from 293T cells was removed from the 10 cm dishes and 5 ml fresh, pre-warmed growth medium together with the transfection solution was added. After 24 h of incubation, 5 ml of fresh growth medium were added. Subsequently, the virus containing supernatant was harvested 48 h post transfection and filtrated through 0.45 µm filters. For concentration, the supernatant was centrifuged, the pellet resuspended in 500 µl growth medium and the virus containing supernatant stored at -80 °C until transduction.

3.2.2.1.2 Transduction of HUH7-R cells

For lentiviral transduction, 2 x 10^6 HUH7-R cells were plated in growth medium into a 6-well plate and grown overnight to 60-70% of confluence. Thereafter, 2 ml of virus supernatant and 3.8 µg/ml polybrene were added per well. Polybrene enhances the fusion of viral particles with the target cells. Cells were washed in PBS and the polybrene containing transduction mixture was replaced by fresh growth medium after 16 h due to cytotoxicity. The transduced cells were expanded after three passaging cycles and FACS-sorted for the eGFP-positive HUH7-R-LUC population, which was used for the *in vivo* assessment of tumor size by bioluminescence imaging *(chapter 3.2.12.3)*.

3.2.2.2 Transient gene silencing and overexpression

Transient siRNA-gene silencing experiments were performed with siRNA pools targeting the mitochondrial enzymes isocitrate dehydrogenase 2 IDH2 (siIDH2) and oxoglutarate dehydrogenase OGDH (siOGDH). A non-targeting siRNA for luciferase (siLUC) was thereby used as a negative

control (*Table 14*). For transfection, the respective siRNA was applied in an initial concentration of 50 nM per well with 0.08% transfection reagent DharmaFECT 1 *(chapter 3.1.5)*. The cells were incubated with the transfection solution for 1.5 h and either left untreated or stimulated as indicated for the experiment, with a final concentration of 25 nM siRNA and 0.04% DharmaFECT 1 per well. All experiments were carried out 72 h post transfection and the gene silencing efficiency was monitored by Western blot analysis of the OGDH and IHD2 protein abundance *(chapter 3.2.4)*. For transient transfection with the Rab-9-GFP plasmid *(Figure S8 C),* cells were seeded in ibidi®-µslides and grown overnight to 80-90% of confluence. The plasmid DNA was diluted 1:100 in DMEM and 1.75% DharmaFECT1 was used as a transfection reagent as described above. Cells were incubated with the transfection solution for 4 h, fresh growth medium was added and live cell imaging was performed after 24 h, as subsequently described *(chapter 3.2.5.3)*.

3.2.3 Proliferation assays

3.2.3.1 Crystal violet staining

For sensitivity testing of cells towards a variety of compounds, as well as lactate assay *(chapter 3.2.9.2)* and ROS assay *(chapter 3.2.11.2)* normalization, a crystal violet proliferation assay was performed. Therefore, the cells were seeded in triplicates at a density of 10,000 cells/well (40,000 cells/well for HUH7-R(+)) in a transparent, flat-bottom 96-well plate. The cells were grown for 24 h before stimulation. After incubation respectively sorafenib withdrawal for 72 h, cells were stained with 100 µM crystal violet solution for 10 min at room temperature and washed with distilled water. In order to quantify proliferation, the bound dye was solubilized by adding 200 µl dissolving buffer and the absorbance at 550 nm was measured in a SpectraFluor®PLUS plate-reading photometer.

Table 19. *Buffers and solutions for crystal violet staining.*

Crystal violet solution		**Dissolving buffer**	
Crystal violet	0.5%	Trisodium citrate	50 mM
Methanol	20%	Ethanol	50%
H_2O	add	H_2O	add

3.2.3.2 Impedance measurement

The real-time proliferation of HCC cells was assessed by impedance measurements using the xCELLigence system. The cells were seeded at a density of 2,500 cells/well in triplicates in equilibrated 16-well E-plates. Cells were grown in growth medium for 24 h before treatment or sorafenib withdrawal for 72 h. The cell index, which is proportional to the cell count per well, was assessed every hour and normalized to the start point of treatment respectively sorafenib withdrawal. The growth rate was calculated by the RTCA software as slope of the cell-index curve.

3.2.4 Western blot

3.2.4.1 Cell lysis and sample preparation

The protein levels of interest were examined by Western blot analysis. Therefore, cells were seeded in a 6-well culture dish and grown overnight to confluence. The next day, cells were washed once with ice-cold PBS, 100 µl lysis buffer was added and cells were frozen at -80 °C for at least 20 min. In order to load equal amounts of protein of all samples onto the polyacrylamide gel electrophoresis (PAGE), protein concentrations were determined by Bradford assay (Bradford, 1976). Therefore, 10 µl re-diluted protein samples were incubated with 190 µl 1:5-diluted Bradford reagent Roti® Quant for 5 min. The absorbance of each sample, which correlates with the respective protein concentration, was measured at 592 nm on a SpectraFluor®PLUS plate reading photometer and linear regression was performed using a BSA dilution series. The protein concentrations were adjusted by adding 1x sodium dodecyl sulfate (SDS) sample buffer to a total of 80 µl per sample. In order to optimize protein denaturation for obtaining an equal protein size-to-charge ratio, 20 µl 5x SDS sample buffer were added per 80 µl of adjusted sample prior to denaturation at 95 °C for 5 min. Exclusively samples for analysis of the respiratory chain (OxPhos WB Antibody Cocktail) were heated to 37 °C for 1 h, as the complex I signal decreases at temperatures above 50 °C.

Table 20. *Lysis and SDS sample buffer for Western blot sample preparation.*

Lysis buffer premixture		**Add to Lysis buffer before use**	
Tris/HCl	50 mM	Complete®EDTAfree	4 mM
NaCl	150 mM	PMSF	1 mM
Nonidet NP-40	1%	H_2O_2	600 µM
Sodium deoxycholate	0.25%	**5x SDS sample buffer**	
SDS	0.10%	Tris/HCl pH 6.8	3.125 M
activated Na_2VO_4	300 µM	Glycerol	50%
NaF	1 mM	SDS	5%
β-glycerophosphate	3 mM	DTT	2%
pyrophosphate	10 mM	Pryonin Y	0.025%
H_2O	add	H_2O	add

3.2.4.2 Polyacrylamide gel electrophoresis (PAGE)

An equal amount of protein was separated via one of both SDS electrophoretic techniques, Glycine-SDS-Page or Tricine-SDS-PAGE. Protein separation was performed on discontinuous polyacrylamide gels, consisting of a separation and a stacking gel (*Table 21*).

Table 21. *Polyacrylamide gels for PAGE.*

	Stacking gel	Separation gel		
		10%	**12%**	**15%**
Rotiophorese™ Gel 30	17%	33%	40%	50%
Tris base (pH 6.8)	125 mM	-	-	-
Tris base (pH 8.8)	-	375 mM	375 mM	375 mM
SDS	0.1%	0.1%	0.1%	0.1%
TEMED	0.2%	0.1%	0.1%	0.1%
APS	0.1%	0.05%	0.05%	0.05%
TCE	-	0.5%	0.5%	0.5%
H_2O	add	add	add	add

3.2.4.2.1 Glycine-SDS-PAGE

The Glycine-SDS-PAGE (Laemmli, 1970) uses a glycine-tris buffer system and is the most commonly applied electrophoretic technique, with optimal separation for proteins larger than 30 kDa. The concentration of acrylamide in the gel can be varied, in order to adapt the separation capacity to higher or lower protein mass ranges. In the following, 10%, 12% and 15% 1.5 mm separation gels were used (*Table 21*), which are defined by the total percentage concentration of acrylamide monomers and the cross linker Ammonium persulfate (APS), in relation to the total gel volume (Hjertén, 1962). An equal amount of protein was separated in electrophoresis buffer (*Table 22*) at a constant voltage (100 V, 21 min for stacking gel/ 200 V, 43 min for separation gel).

Table 22. *Buffers for Glycine-SDS-PAGE and Tricine-SDS-PAGE.*

	(Laemmli, 1970)	(Schagger, 2006)	
	Electophoresis buffer	**Anode buffer**	**Cathode buffer**
Tris base	4.9 mM	100 mM	100 mM
Glycine	38 mM	-	-
Tricine	-	-	100 mM
SDS	0.1%	-	0.1%
HCl	-	22.5 mM	
H_2O	add	add	add
pH	8.3	8.9	~ 8.25

3.2.4.2.2 Tricine-SDS-PAGE

The Tricine-SDS-PAGE (Schagger, 2006) is based on a tricine-tris buffer system and is currently the recommended electrophoretic system for the separation of proteins with a molecular weight below 30 kDa. In the following, a modified protocol with 12% 1.0 mm polyacrylamide gels (*Table 21*) was used. In this electrophoretic technique, the maximal protein load is limited by large amounts of neutral detergent and lipids in the sample. Therefore, the protein concentration was kept at approximately 20 µg per 10-15 µl of SDS sample buffer. A low SDS ratio has been previously reported to facilitate the electrophoretic separation of peptides from the bulk SDS (Schagger, 2006). The Tricine-SDS electrophoresis was performed with an anode/ cathode buffer system (*Table 22*) at a constant voltage (30 V, 21 min for stacking gel/ 150 V, 60 min for separation gel).

3.2.4.3 Tank blotting and protein detection

After electrophoretic protein separation, the total protein load of the trichloroethanol (TCE) supplemented polyacrylamide gels was determined for subsequent normalization. Therefore, the polyacrylamide gels were UV-activated on the ChemiDoc™ Touch Imaging System and the antibody band intensities were normalized to the respective protein load, using the Stainfree™ technology (Bio-Rad). Thereafter, the PVDF-membranes were activated in methanol for 5 min and the proteins were transferred via tank blotting (*Table 23*) at a constant voltage (100 V, 90 min, 4 °C). In order to prevent non-specific antibody binding, the membrane was blocked secondary to protein transfer for 1 h in 5% BSA in PBS. The membrane was incubated with the first, antigen binding antibody overnight at 4 °C (*Table 8*) on an orbital shaker. The next day, the membrane was washed 4x5 min in 1xTBS-T (*Table 23*) and the secondary, HRP-coupled antibody was added for 2 h at room temperature (*Table 9*). After a final 4x5 min washing step, membranes were shortly incubated with a freshly prepared ECL-solution (*Table 23*), activated with 17 µM H_2O_2 and the chemiluminescence was detected with the ChemiDoc™ Touch Imaging System. The received bands were evaluated by comparing the molecular weight of the proteins to the pre-stained protein ladder PageRuler™ and the protein expression was quantified with the Image Lab™ Software.

Table 23. *Buffers for tank blotting, washing of membranes and Western blot detection.*

Tank buffer		**1x TBS-T**		**ECL-solution**	
Tris base	48 mM	Tris/HCl	50 mM	Tris base (pH 8.5)	0.1 M
Glycine	39 mM	NaCl	150 mM	Luminol	2.5 mM
Methanol	20%	Tween 20	0.05%	Coumaric acid	1 mM
H_2O	add	pH	7.6	H_2O	

3.2.5 Microscopy

3.2.5.1 Phase contrast microscopy

The morphology of HUH7 and RIL175 cells was assessed under standardized culture conditions as described above *(chapter 3.2.1)*. Therefore, a Leica DMi1 microscope with a Leica MC120 HD camera was used. The cellular diameter D was assessed by the Vi-Cell™ XR cell counter and used for the calculation of the cellular volume V with the formula: $V = 4/3 \times \pi \times D/2$.

3.2.5.2 Immunostaining

For cell immunostaining and subsequent confocal microscopy, cells were seeded in ibidi®-µslides (HUH7-WT: 15,000 cells/well, HUH7-R(+): 30,000 cells/well, HUH7-R(-): 20,000 cells/well) and grown overnight. After 24 h, the cells were washed with Ca^{2+}/Mg^{2}-containing PBS (*Table 18*), fixed with 4% paraformaldehyde (PFA), permeabilized with 1% Triton X-100 and incubated with 1% BSA solution for 30 min in order to block unspecific antibody binding. Thereafter, cells were incubated with the respective primary antibody solution overnight (4 °C) (*Table 10*). Cells were washed with PBS and incubated with the secondary antibody (*Table 11*) together with the DNA-staining Hoechst reagent (1:100) diluted in 0.2% BSA for 1 h. After washing with PBS, fluorescent stainings were sealed with one drop of FluorSaveTM Reagent mounting medium and a cover slip. Samples were kept at 4 °C for longer storage and imaged using a Leica SP8 confocal laser scanning microscope. Subsequent image analysis was performed with the Leica LAS X software.

3.2.5.3 Live Cell imaging

Mitochondrial morphology and lysosomal mass distributions were assessed in living, unfixed cells in a climate chamber (37 °C, 5% CO_2, constant humidity) (Ibidi GmbH). Therefore, cells were seeded in ibidi®-µslides (HUH7-WT: 15,000 cells/well, HUH7-R(+): 30,000 cells/well, HUH7-R(-): 20,000 cells/well) and grown overnight. After 24 h, cells were washed with PBS and incubated with the respective staining dye for 30 min protected from light. In detail, cells were stained with 200 µl/well of the MitoTracker™ Green FM (1:9,000) or LysoTracker™ Red DND-99 (1:3,000) staining solution (*Table 12*). Images were obtained using a Leica TCS SP8 confocal laser scanning microscope and image analysis was performed with the Leica LAS X software.

3.2.5.4 Transmission electron microscopy (TEM)

Cells for TEM were detached, 0.5×10^6 cells centrifuged (200 g, 5 min, RT) and resuspended in 300 µl PBS. Thereafter, cells were transferred into 0.95 ml BEEM capsules, centrifuged (410 g, 10 min, RT) and fixed in 600 µl glutaraldehyde (2.5%) in sodium cacodylate buffer (Electron Microscopy Sciences) for at least 24 h. After fixation, glutaraldehyde was removed and samples were washed three times with 0.1 M sodium cacodylate buffer (Electron Microscopy Sciences).

Postfixation and prestaining was done for 45 to 60 min with 1% osmium tetroxide (*Table 24*). Samples were washed three times with ddH_2O and dehydrated with an ascending ethanol series (once 15 min with 30%, 50%, 70%, 90%, 96%, twice 10 min with 100%) and twice 30 min with propylene oxide. Subsequently, samples were embedded in Epon (*Table 24*). For microscopy, ultrathin sections were sliced with an Ultracut E Ultramicrotome and automatically stained with UranyLess EM Stain and 3% lead citrate using the contrasting system Leica EM AC20. For analysis, the samples were examined with a JEOL-1200 EXII transmission electron microscope.

Table 24. *Buffers and solutions for transmission electron microscopy.*

Osmium tetroxide 1%		**Epon**	
Osmium tetroxide 4%	10 ml	Glycidether 100	3.61 M
Sodium chloride 3.4%	10 ml	Methylnadicanhydride	1.83 M
Potassium dichromate 4.46%	10 ml	Dodecenylsuccinic anhydride	0.92 M
H_2O	10 ml	Tris(dimethylaminomethyl)phenol	5.53 mM
pH (adjusted with KOH)	7.2	H_2O	add

3.2.6 Quantitative real-time PCR analysis

3.2.6.1 Isolation of mRNA

For the isolation of mRNA from cell culture samples, the Qiagen RNeasy Mini Kit was used according to the manufacturer's protocol. Therefore, cells were seeded in a density of 0.6 x 10^6 cells/well in a 6-well plate and grown over night to 80-90% of confluence. Prior to mRNA-isolation, tumor tissues were homogenized in lysis buffer provided by the manufacturer, using the Cell Homogenizer Potter S. The mRNA concentration of each sample was determined with the NanoDrop® ND 1000 spectrophotomer and normalized among the samples.

3.2.6.2 Reverse transcription and RT-PCR

For the creation of cDNA templates by reverse transcription, the High-Capacity cDNA Reverse Transcription Kit was used as described by the manufacturer. The Real-Time-Polymerase chain reaction (RT-PCR) was performed with the QuantStudio™ 3 Real-Time PCR System. The SYBR Green Mix I was used for the amplification of E-Cadherin. For the RT-PCR of PGC-1α, the TaqMan® Gene Expression Master Mix together with the TaqMan® Gene Expression Assay PPARGC1A (Hs00173304_m1) were used according to the manufacturer's protocol. Changes in mRNA levels were assessed by the ΔΔCT method as previously described (Fleige et al., 2006).

3.2.7 Flow Cytometry

Table 25. *Isotonic buffers for flow cytometry.*

HBSS (Hank's Balanced Salt Solution), ***HHBS (Hank's Buffer with Hepes)****					
$CaCl_2$	1.26 mM	KH_2PO_4	0.44 mM	NaCl	137.9 mM
D-glucose	5.56 mM	$MgCl_2$ x 6 H_2O	0.49 mM	**HEPES*	*20 mM*
$NaHCO_3$	4.17 mM	$MgSO_4$ x 7 H_2O	0.41 mM	H_2O	add
KCl	5.33 mM	Na_2HPO_4	0.34 mM	pH	7.2

3.2.7.1 Calcein assay

For assessment of the multidrug resistance (MDR) transporter activity by flow cytometry, HUH7-WT, HUH7-R(+) and HUH7-R(-) cells were seeded at a density of 3 x 10^5 cells in duplicates in a 12-well plate and grown for 24 h. The Multi-Drug Resistance Assay Kit (Calcein AM) was used according to the manufacturer's instructions. Thereby, the cells of the positive control were stimulated with Cyclosporine A (25 µM) respectively Verapamil (50 µM) and incubated for 30 min in an incubator. The calcein solution provided by the manufacturer was added in a final concentration of 250 nM to the culture medium. Thereafter, the samples were incubated for 30 min protected from light. The cells were detached with trypsin/EDTA and transferred to FACS tubes for centrifugation (400 g, 5 min, 25 °C). The cell pellet was resuspended in 300 µl PBS and fluorescence was assessed on a FACSCanto II flow cytometer (Ex 488 nm, Em 530 nm).

3.2.7.2 Glucose uptake

For quantification of the cellular glucose uptake, cells were seeded as described above *(chapter 3.2.7.1)*, washed with PBS and stained with 100 µM of the fluorescent glucose analogue 2-(N-(7-Nitrobenz-2-oxa-1,3-diazol-4-yl)Amino)-2-Deoxyglucose (2-NBDG). The cells were incubated with 2-NBDG for 30 min protected from light. Thereafter, cells were detached with trypsin/EDTA, washed with PBS and transferred to FACS tubes for centrifugation (400 g, 5 min, 25 °C). The cell pellet was resuspended in 300 µl PBS and fluorescence was assessed on a FACSCanto II (Ex 488 nm, Em 530 nm). For analysis, the cell debris was excluded and the fluorescence intensity median normalized to the control using the FlowJo™ 7.6 analysis software.

3.2.7.3 Cellular superoxides

The cellular abundance of mitochondrial reactive oxygen species (ROS) was assessed for HUH7-WT, HUH7-R(+) and HUH7-R(-) cells, seeded as described above *(chapter 3.2.7.1)*. Cells were incubated with a 5 µM working solution of the MitoSOX™ Red Mitochondrial Superoxide Indicator for live-cell imaging diluted in HBSS (*Table 25*). Cells were incubated for 30 min protected

from light. Subsequently, cells were detached with trypsin/EDTA, culture medium was added and cells were pipetted in FACS tubes for centrifugation (400 g, 5 min, 4 °C). Cells were washed in HBSS (*Table 25*), centrifuged and kept on ice until flow cytometric measurement on a FACSCalibur (Ex 488 nm, Em 575 nm). The cell debris was excluded and the fluorescence intensity median normalized to the respective control using the FlowJo™ 7.6 analysis software.

3.2.7.4 Mitochondrial and lysosomal mass

Cells were seeded as previously described *(chapter 3.2.7.1)*, washed with PBS and incubated with the MitoTracker™ Green FM (1:9,000) or LysoTracker™ Red DND-99 (1:3,000) dye diluted in DMEM. Cells were incubated for 30 min protected from light and subsequently resuspended in 300 µl PBS for analysis on a FACSCanto II (Ex 490 nm, Em 516 nm for mitochondrial mass and Ex 577 nm, Em 590 nm for lysosomal mass). The cell debris was excluded and the fluorescence intensity median normalized to the respective control using the FlowJo™ 7.6 analysis software.

3.2.7.5 Intracellular Calcium

Cytosolic calcium levels were determined using the calcium indicator Cal-520 AM according to the manufacturer's protocol. Cells were seeded as previously described *(chapter 3.2.7.1)*, grown for 24 h and incubated with 10 µM of the Cal-520 AM dye. Cells were incubated (90 min, 37 °C, then 30 min, RT), detached and centrifuged (400 g, 5 min, RT). The cell pellet was washed and resuspended in HHBS (*Table 25*) to remove excess dye. The fluorescence intensity was analyzed on a FACSCanto II (Ex 488 nm, Em 530 nm). The cell debris was excluded and the fluorescence intensity median normalized to the respective control using the FlowJo™ 7.6 analysis software.

3.2.7.6 Apoptosis

For the assessment of apoptosis rates, a previously published method (Nicoletti et al., 1991) was used. Therefore, cells were seeded as previously described (*chapter 3.2.7.1),* trypsinized and washed twice by centrifugation (600 g, 10 min, 4 °C). After resuspension in ice-cold PBS, cells were permeabilized and DNA stained by adding a fluorochrome solution (FS), which contains the DNA-intercalator propidium iodide (PI) (*Table 26*). Cells were incubated in the FS buffer overnight at 4 °C and analyzed the next day by flow cytometry on a FACSCalibur instrument (Ex 493 nm, Em 632 nm). Given, that apoptosis is accompanied by DNA fragmentation, the low-fluorescence sub-G1 peak, which accounts for apoptosis, was quantified by the FlowJo™ 7.6 analysis software.

Table 26. *PI containing permealization buffer.*

FS buffer			
Propidium iodide	75 µM	Triton-X 100	0.1%
Trisodium citrate	0.1%	PBS	add

3.2.8 LC-MS/MS analysis of the cellular proteome and lipidome

3.2.8.1 Proteomics analysis

Mass spectrometry (MS) - based proteomics analysis of HUH7-WT, HUH7-R(+) and HUH7-R was performed and the MaxQuant analysis kindly provided by Dr. T. Fröhlich (Laboratory for Functional Genome Analysis, LAFUGA, Gene Centre, LMU, Munich, Germany).

3.2.8.1.1 Sample preparation

Cells were seeded in 6-well dishes and grown to confluence for 24 h. Thereafter, cells were washed five times with PBS, detached with trypsin/EDTA and centrifuged (1,000 rpm, 5 min, 4 °C). The cell pellets were resuspended in 100 µl ice-cold PBS and stored at -80 °C until further processing. Per 1 x 10^5 cells, 20 µl of 8 M urea/ 0.4 M NH_4HCO_3 was added. Cells were lysed using the Sonoplus GM3200 ultrasonic device with BR30 cup booster, applying 10,000 kJ. For further homogenization, samples were centrifuged through QIA-Shredder devices. Protein concentrations were determined by Bradford assays (Bradford, 1976) and adjusted to 0.6 mg/ml with 8 M urea/ 0.4 M NH_4HCO_3. To cleave bisulfide bonds, 25 µg of total protein was incubated with 1,4-Dithioerythritol (DTE) at a concentration of 4.5 mM for 30 min and free sulfhydryl residues were blocked with 10 mM iodoacetamide for 30 min in the dark. After dilution with water to a concentration of 1 M urea, 0.5 µg porcine trypsin was added and samples were incubated overnight at 37 °C.

3.2.8.1.2 Liquid-chromatography mass spectrometry (LC-MS/MS)

The chromatography of peptides was performed on an EASY-nLC 1,000 chromatography system coupled to an Orbitrap XL instrument. For analysis, 2.5 µg of peptides diluted in 0.1% formic acid (FA) were transferred to a trap column (PepMap100 C18, 75 µm x 2 cm, 3 µm particles) and separated at a flow rate of 200 nl/min (Column: PepMap RSLC C18, 75 µm x 50 cm, 2 µm particles). A 260 min linear gradient from 5% to 25% solvent B (0.1% formic acid, 100% ACN) and a consecutive 60 min linear gradient from 25% to 50% solvent B was used. For data acquisition, a top five data dependent collision-induced dissociation (CID) method was applied.

3.2.8.1.3 Data processing

For quantitative data analysis of the LC-MS/MS-proteomics screening and for subsequent volcano blot and gene cluster analysis, the MaxQuant and Perseus software packages were used, respectively. The MaxQuant dataset was filtered, in order to exclude incomplete information with less than 3 valid values per condition and protein. Further, missing label-free quantification (LFQ) intensities were filled with imputation values from the normal distribution. For volcano blot analysis, a two-sampled t-test (FDR 0.01, p-value <0.05) was performed and values outside the significance range were excluded by a cut-off-curve (setting: s0 = 2).

3.2.8.1.4 Gene set enrichment analysis (GSEA)

The GSEA software (The Broad Institute, Massachusetts, USA) is a computational method that determines whether an a priori defined set of genes shows statistically significant differences between two biological states. Therefore, gene sets were obtained from the Kyoto Encyclopedia of Genes and Genomes (KEGG) (C2.cp.keeg.v.5.1.symbols) and the gene ontology (GO) database (C5.bp.v.5.1.symbols, C5.cc.v.5.1. symbols, C5.mf.v.5.1.symbols). For subsequent analysis, gene set size filters were set to min=15/ max=500 genes per gene set. The primary result of the GSEA is the enrichment score (ES), which reflects the degree to which a gene set is overrepresented at the top or bottom of a ranked list of genes. The ES reflects the correlation of the gene with one or the other phenotype. The normalized enrichment score (NES) accounts for differences in gene set size, whereas the False Discovery Rate (FDR) is an analogue to the nominal p-value (NOM p-val), adjusted for gene set size and multiple hypothesis testing. For better comparison, gene sets were ranked according to their NOM p-val and gene sets with NOM p-val<0.05 were highlighted.

3.2.8.2 Lipidomics analysis

MS-based lipidomics analysis of HUH7-R(+) compared to HUH7-WT cells was performed and kindly provided by Dr. A. Koeberle together with Dr. H. Pein (Department of Pharmacy, Pharmaceutical Chemistry, Friedrich-Schiller-University Jena, Jena, Germany).

3.2.8.2.1 Analysis of fatty acids and phospholipids

Fatty acids and phospholipids were extracted and analyzed as previously reported (Koeberle et al., 2013; Pein et al., 2017). In detail, 1.5 x 10^6 HUH7-WT and HUH7-R(+) cells were harvested and resuspended in 150 µl PBS. Next, 365 µl of a 1,2-dimyristoyl-sn-glycero-3-phosphocholine (DMPC) standard (2 µl 0.2 mM DMPC in 363 µl methanol) and 187.5 µl chloroform was added to each sample and the tubes were vortexed for 30 seconds. Additionally, 187.5 µl chloroform was added and samples were vortexed a second time. Subsequently, 187.5 µl saline solution (0.9% NaCl) was added, samples vortexed and centrifuged (4000 rpm, 5 min, RT). The lower chloroform phase was transferred to a separate tube and the solvent was evaporated to obtain a dry lipid layer (20 min, 30 °C). The lipid films were then stored at -20 °C until further analysis.

Chromatography was carried out on an Acquity UPLC BEH C8 column (1.7 µm, 1×100 mm) using an Acquity Ultraperformance LC system. Lipids were detected by a QTRAP 5500 mass spectrometer equipped with an electrospray ionization source. The glycerophospholipids of the sample were identified and quantified in the negative ion mode based on the detection of both fatty acid anion fragments by multiple reaction monitoring (MRM). Sphingomyelins were analyzed after fragmentation and identified by the choline head group (m/z = 184) by MRM, and free fatty acids were detected by single ion monitoring in the negative ion mode. The absolute amounts of lipids

were normalized to the internal standard DMPC and the cell number. The cellular proportion of individual lipid species was calculated as percentage of all lipids within the subgroup (= 100%).

3.2.8.2.2 Analysis of acyl-CoAs

For the analysis of the cellular acyl-CoA composition, 4 x 10^6 HUH7-WT and HUH7-R(+) cells were harvested, centrifuged (1,000 rpm, 5 min, RT) and snap frozen. The cells pellets were stored at -80 °C until further analysis. Extraction and analysis of acyl-CoAs was performed as previously described (Glatzel et al., 2018), using [13C3]-malonyl-CoA as internal standard. In brief, acyl-CoAs were separated on an Acquity UPLC BEH C18 column (1.7 µM, 2.1×50 mm) and detected based on the neutral loss of 2'-phospho-ADP ($[M+H-507]^+$) in the positive ion mode using the UPLC-coupled tandem ESI-MS system described above. Subsequently, mass spectra were processed using the Analyst 1.6 software and results were displayed by heatmap analysis.

3.2.9 Metabolic assays

3.2.9.1 Cell viability

Assessment of IC_{50}-values and growth rescue experiments were determined with the CellTiter-Blue® (CTB) viability assay. Therefore, HUH7-WT, HUH7-R(-/72 h), RIL175 cells (10,000 cells/well) and HUH7-R(+) cells (40,000 cells/well) were seeded in triplicates into 96-well plates, stimulated 24 h after seeding and incubated for 72 h. Further, 20 µl CTB reagent was added to each well with a culture medium volume of 100 µl. After 4 h of incubation, the metabolic activity was quantified via dual fluorescence record at 560/590 nm on a SpectraFluor®PLUS plate reading photometer.

3.2.9.1.1 Intracellular ATP

For the assessment of the cellular dependency towards anaerobic glycolysis, HUH7-WT (10,000 cells/well), HUH7-R(+) (40,000 cells/well) and HUH7-R(-/72 h) (10,000 cells/well) cells were seeded in triplicates in a 96-well plate and grown for 24 h. Cells were stimulated with the antimetabolite 2-DG in a concentration ranging from 0 to 200 µM. After 72 h, the microplate was equilibrated to room temperature for 20 min and 100 µl of CellTiter-Glo® reagent were added to an equal amount of culture medium to each well. Cell lysis was induced on an orbital shaker for 2 min, following 10 min of incubation at RT, protected from light. The content of each well was transferred to a white walled Greiner CELLSTAR® 96-well plate and luminescence was recorded with an Orion II microplate luminometer. Similarly, ATP levels of HUH7-R cells upon rebound growth compared to HUH7-WT were assessed. Therefore cells were seeded in a 24-well plate in a density dependent on the time of rebound growth (R(-/0): 96,000 cells/well, R(-/24h): 80,000 cells/well, R(-/48 h): 48,000 cells/well, R(-/72 h): 24,000 cells/well, R(-/96 h): 16,000 cells/well, R(-/168 h): 12,000 cells/ well) and sorafenib was withdrawn for the indicated time. HUH7-WT cells were seeded in a density of 80,000 cells/well 24 h before assaying. Thereafter, cells were detached with

trypsin/EDTA, normalized to the cell number and incubated with an equal amount of CellTiter-Glo® reagent. The luminescence intensity was assessed on a luminometer as described above.

3.2.9.2 Lactate fermentation

The abundance of extracellular lactate was assessed with the L-Lactate Assay Kit according to the manufacturer's instruction. Thereby, HUH7-R(+) cells were seeded in triplicates in a 96-well plate in a density dependent on the time of rebound growth as previously described *(chapter 3.2.9.1.1)*. Sorafenib was withdrawn from HUH7-R cells for the indicated time. HUH7-WT cells were seeded in a density of 20,000 cells/well 24 h before assaying. For each condition, 200 µl of supernatant were collected and deproteinated by adding 200 µl cold 0.5 M metaphosphoric acid (MPA), as provided by the manufacturer. The samples were vortexed and placed on ice (5 min). Next, the samples were centrifuged (10,000 g, 5 min, 4 °C), in order to pellet the proteins, 360 µl supernatant was removed and neutralized with 36 µl of 2.5 M potassium carbonate. In a last centrifugation step (10,000 g, 5 min, 4 °C) precipitated salts were removed. The supernatant was used for assaying with the provided detection reagents, as described by the manufacturer's protocol. The fluorescence was measured on a SpectraFluor®PLUS plate reader (Ex 535 nm, Em 590 nm).

3.2.10 Functional analysis of glycolysis and oxidative phosphorylation

3.2.10.1 Glycolytic Stress Test

The contribution of glycolysis and oxidative phosphorylation to the cellular energy generation was analyzed by a glycolytic stress test. Therefore, HUH7-WT, HUH7-R(+) and HUH7-R(-) cells were seeded into a XFe96 microplate and grown for 24 h to confluence. The Seahorse Glycolysis Stress Test Kit was used in combination with the Seahorse XFe96 Analyzer, as described by the manufacturer. In detail, cells were initially incubated in assay medium without glucose or pyruvate and subsequently treated with D-glucose (10 mM), oligomycin (1 µM) and 2-DG (50 mM). The extracellular acidification rate (ECAR) and the oxygen consumption rate (OCR) were measured for 80 min and the basal ECAR levels and OCR levels were assessed at the plateau after D-glucose injection. Results were normalized to the DNA content, which was assessed by CyQuant® GR staining, according to the manufacturer's protocol. Data analysis was performed with the Wave 2.3.0 software and the Seahorse XF Glycolysis Stress Test Report Generator.

3.2.10.2 High resolution respirometry

In addition to the glycolytic stress test, the mitochondrial routine respiration and the respiratory capacity of HUH7-WT, HUH7-R(+) and HUH7-R(-) cells were determined by high resolution respirometry on the OROBOROS Oxygraph-2k. For analysis, 2 x 10^6 HUH7-WT cells, 2 x 10^6 HUH7-R(-) cells respective 4 x 10^6 HUH7-R(+) cells were centrifuged, resuspended in culture medium and added to the chamber of the oxygraph. Subsequently, cells were stimulated with 400 µM

oligomycin (Leak), 5 mM CCCP (ETS), 2 µM rotenone (complex II) and 500 µM antimycin A (ROX). The O_2-flux (red curve) and the total O_2-content in oxygraph chamber (blue curve) were assessed over time *(Figure 15 D)*. The parameters Leak, ETS, complex II and ROX were determined within the red segments at the plateau phase after stimulation and normalized to the cell number.

3.2.11 Redox-balance

3.2.11.1 NAD^+/NADH and $NADP^+$/NADPH

The NAD^+/NADH as well as the $NADP^+$/NADPH ratio and total content were measured using the commercially available NAD/NADH Glo™ and NADP/NADPH Glo™ kits. HUH7-R(+) cells were seeded at a density of 10,000 cells/well and sorafenib was withdrawn while cells were either left untreated, treated with the respective compounds or transiently gene-silenced for 72 h. Extraction and measurement of the reduction equivalents was performed according to the manufacturer's protocol. In brief, 60 µl PBS were added to each well and plates were frozen at -80 °C for at least 20 min. Cells were scraped off the plates and normalized in protein content using the Bradford assay (Bradford, 1976). Thereafter, aliquots of each sample were either left untreated (total NAD^+ and NADH / total $NADP^+$ and NADPH) or subjected to acid (NAD^+ and $NADP^+$), respective basic (NADH and NADPH) treatment. All acid- or base-treated samples were incubated for 15 min at 60 °C on a heating shaker. Next, samples were pH-neutralized with 0.25 M tris-base (NAD^+/$NADP^+$) or a 0.25 M HCl/Tris-base (NADH/NADPH) buffer. For detection, the neutralized samples were transferred into white walled Greiner CELLSTAR® 96-well plates and measured according to the manufacturer's protocol. Therefore, samples were incubated for 60 min and luminescence was assessed on a Spark® multimode microplate reader.

3.2.11.2 Reactive oxygen species (ROS)

Cells were seeded in 96-well plates as previously described, grown for 72 h and stimulated respectively transiently transfected for 72 h. ROS staining was performed with the ROS Detection Cell-Based Assay Kit (DCFDA) according to the manufacturer's protocol. The ROS scavenger N-acetyl cysteine (NAC) (20 mM) was used as a negative control and fluorescence was assessed via dual fluorescence record at 490/530 nm on a Spark® multimode microplate reader. The obtained fluorescence intensities were normalized on cell number by crystal violet staining.

3.2.12 *In vivo* experiments

All experiments were performed according to German respective Austrian legislation of animal protection and approved by the local government authorities (approval by the government of Upper Bavaria, Germany: Az 55.2-1-54-2532-22-2016/ approval by the federal ministry of science, research and economy, Austria: BMBWF-66.019-0041-V-3b-2018).

3.2.12.1 Mice

For ectopic tumor mouse xenografts, exclusively females of the albino immune-incompetent mouse strain „Fox Chase SCID" (CB17/Icr-Prkdcscid/IcrIcoCrl) were used. Immunodeficiency is required to avoid tumor cell rejection and the albino phenotype to enable *in vivo* bioluminescence tumor size measurements. All mice were purchased in an age between five to six weeks from Charles River.

3.2.12.2 Ectopic tumor model

Mice were shaved on the left lateral abdomen and 3 x 10^6 HUH7-WT or HUH7-R(+) cells were subcutaneously injected in the left flank of the mouse with 1 ml syringes and 27 G needles. From the day of tumor cell injection on, mice were treated by intraperitoneal injection with sorafenib (20 mg/kg), TGC (50 mg/kg, 100 mg/kg) or a DMSO control (100 µl solvent: 5% DMSO, 10% solutol, 85% PBS). Tumor size measurements were performed at the indicated time points, using a digital caliper. The tumor volume was calculated with the formula 1/6 x π x L x W x H (L=length, longest side of the tumor, W=width, widest side of the tumor, H=height, highest side of the tumor).

3.2.12.3 *In vivo* bioluminescence imaging

The size of HUH7-R-LUC tumors was assessed by detection of the bioluminescent signal with the IVIS® spectrum device. Imaging was performed at day 3 and day 6 post cell injection. Therefore, 0.3 g/kg D-luciferin sodium salt dissolved in 100 µl PBS were intraperitoneally injected in the mice, prior to narcotization in 3% isoflurane in oxygen. Mice were kept under narcotization with 2% isoflurane and imaged in lateral position. Images were taken every minute for 20 min, 13 min after luciferin injection. The bioluminescence signal within the defined region of interest (ROI) was calculated with the Living Image 4.4 software. For quantification, the area under the curve (AUC) of luminescence counts was determined for each mouse. All mice were sacrificed through cervical dislocation. Thereafter tumors were resected and the weight and volume were determined. Tumors were snap frozen in liquid nitrogen, stored at -80 °C and homogenized for further analysis.

3.2.13 Statistical analysis

All experiments described were conducted at least three times. The data are presented as the mean ± SEM, and statistical significance was considered at $p \leq 0.05$. Statistical analysis was performed with the GraphPad Prism software 7.0. For differences between two groups, an unpaired two-tailed Student's t-test was used, given the assumption that both groups are sampled from a normal distribution with equal variances. Group comparisons ($n \geq 3$) were performed using one-way ANOVA with Tukey's multiple comparison test (*$p<0.05$, **$p<0.01$, ***$p<0.001$, ****$p<0.0001$).

RESULTS

4 RESULTS

4.1 The sorafenib resistance HCC cell model

Although sorafenib is effective in prolonging the median OS of advanced-stage HCC, acquired resistance has become an obstacle for increasing the life expectancy of patients. To address this clinically highly relevant topic, we generated sorafenib-resistant HCC cell models by exposing HuH-7 and RIL-175 HCC cells to increasing doses of sorafenib *(Chapter 3.2.1.2)*. These sorafenib-resistant HUH7-R cells, which obtained resistance up to clinically relevant peak plasma concentrations of 10 µM (human dose: 800 mg/day; 8.5–15.7 µM) (Strumberg et al., 2007), were subsequently characterized. RIL175-R cells were used to confirm the major findings of this study.

4.1.1 Generation and characterization of the sorafenib-resistant HUH7-R cell line

The HUH7-R cells obtained a major morphological alteration to a spindle-shaped phenotype *(Figure 6 A)* and distinct chemoresistance up to a half maximal inhibitory concentration (IC_{50}) of 23 µM sorafenib *(Figure 6 B)* that was maintained after treatment termination *(Figure 6 C)*. This treatment robustness of HUH7-R cells to sorafenib compared to their parental HUH7-WT cell line was confirmed *in vivo* in an ectopic tumor mouse xenograft *(Figure 7 A-B)*, in which decreased vascularization but increased invasiveness occurred in sorafenib-resistant tumors *(Figure 7 C-D)*.

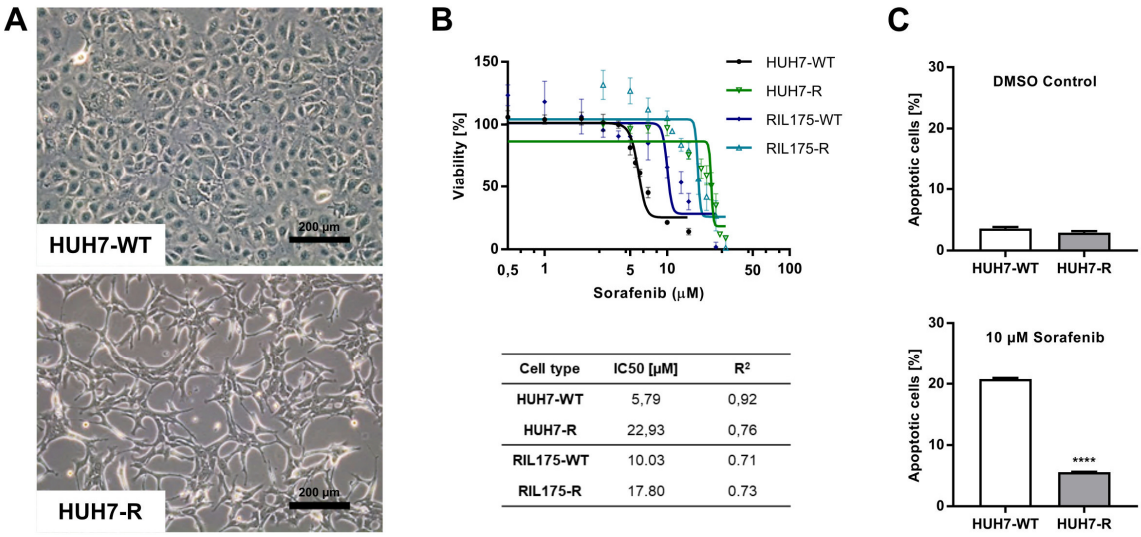

Cell type	IC50 [µM]	R^2
HUH7-WT	5,79	0,92
HUH7-R	22,93	0,76
RIL175-WT	10.03	0.71
RIL175-R	17.80	0.73

Figure 6. **The sorafenib resistance HCC cell model *in vitro*. (A)** Mesenchymal phenotype induced by sustained sorafenib exposure. Phase contrast microscopy of wild-type (HUH7-WT) and sorafenib-resistant (HUH7-R) HuH-7 cells. Scale bars indicate 200 µm. **(B)** HUH7-R and RIL175-R cells acquired resistance to sorafenib up to a clinical relevant range. Dose-response curve with corresponding IC_{50}-values and coefficient of determination R^2 are shown. **(C)** Sorafenib resistance is sustained after sorafenib withdrawal for 72 h. Flow cytometric quantification of apoptotic cells untreated (top) vs. treated with sorafenib (10 µM) for 24 h (bottom) of HUH7-R vs. HUH7-WT cells. HUH7-R cells were cultured in sorafenib (10 µM) and sorafenib was withdrawn for 72 h prior to stimulation. Values denoted as ± SEM, n=3, ****p<0.0001 (t-test).

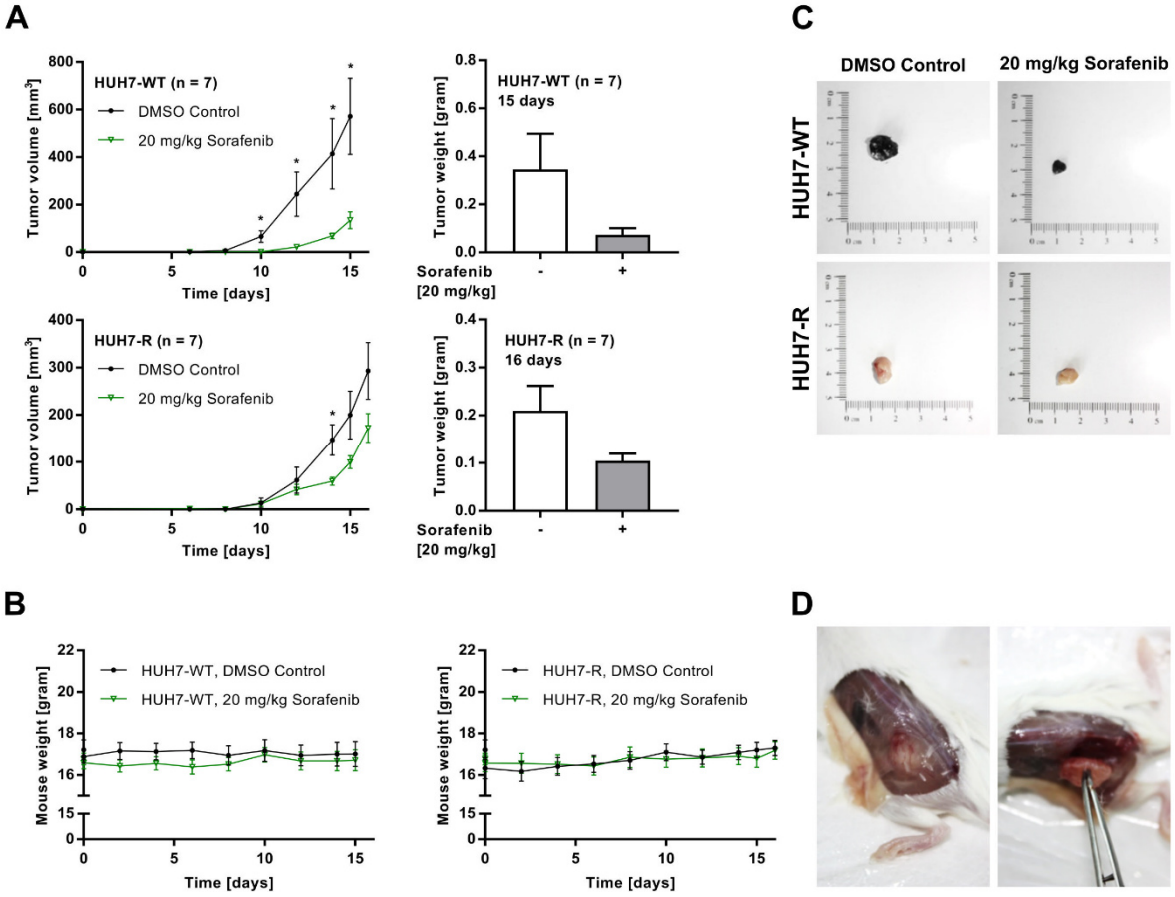

Figure 7. **The sorafenib resistance HCC cell model *in vivo*. (A)** HUH7-R cells reveal decreased sorafenib-responsiveness *in vivo*. Ectopic tumor mouse xenograft with HUH7-WT and HUH7-R cells, treated with DMSO vs. 20 mg/kg sorafenib every second day. Assessment of tumor volume (left) and tumor weight after resection (right) at the indicated time points. **(B)** Sorafenib therapy (20 mg/kg, every second day) of ectopic tumor mouse model *(Figure 7 A)* was well tolerated. The mouse weight was assessed at the indicated time points. **(C)** Sorafenib-resistant tumors show reduced vascularization compared to HUH7-WT tumors. Representative resected tumors of the 4 groups are shown. **(D)** HUH7-R cells show highly invasive tumor growth *in vivo*. Invasive growth of HUH7-R tumors in 4/7 mice of the DMSO Control group and 3/7 mice of the 20 mg/kg sorafenib treated group *(Figure 7 A)*. Values denoted as ± SEM, n=3, *p<0.05 (t-test).

4.1.2 Sorafenib-resistant HCC undergoes relapse of tumor growth upon sorafenib therapy termination

To mimic the clinical situation of advanced-stage HCC patients, in which discontinuous dosing schedules are common due to severe adverse events, sorafenib was retracted from this cell model under standardized conditions. Strikingly, after sorafenib withdrawal from the HUH7-R cells cultured in 10 µM sorafenib (HUH7-R(+) cells), a fast initial relapse of proliferation was observed within 72 h of treatment termination. In the following, these cells characterized by a rebound of proliferation are termed HUH7-R(-) cells *(Figure 8 A-B)*. Notably, under sorafenib exposure, HUH7-R(+) cells acquired broad cross-resistance to a wide variety of clinically used chemotherapeutics, but resensitized after sorafenib treatment termination *(Figure 8 C; Figure S1)*.

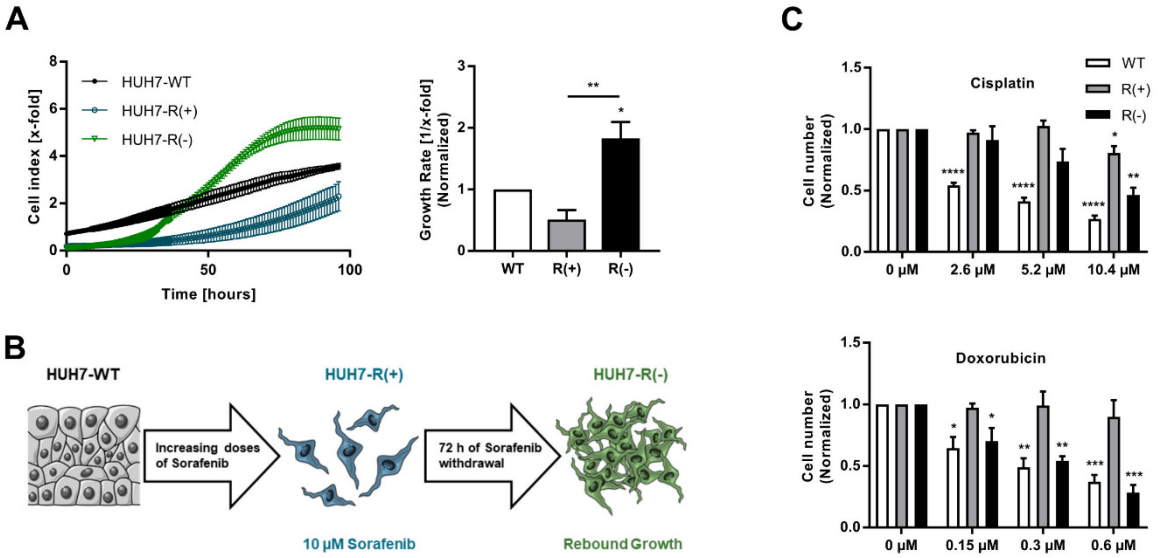

Figure 8*. Rebound growth of sorafenib-resistant HUH7-R cells with chemotherapeutic resensitization.** **(A)** Sorafenib withdrawal from HUH7-R cells, continuously cultured in 10 µM sorafenib (HUH7-R(+) cells) leads to rapid resumption of proliferation. If not mentioned otherwise, rebound growth cells are cultured without sorafenib for 96 h (HUH7-R(-) cells). Impedance measurements and the growth rate calculated from cell density (index) over 72 h are shown. **(B)** Schematic overview of the sorafenib-resistant rebound growth model. **(C)** HUH7-R(+) cells acquired reversal cross-resistance to the clinically applied chemotherapeutics cisplatin and doxorubicin. Normalized proliferation rates within 72 h of treatment are shown. Values denoted as ± SEM, n=3, *p<0.05, **p<0.01, ***p<0.001, ****p<0.0001 (ANOVA). See also ***Figure S1.

4.1.3 Reversible epithelial-to-mesenchymal transition (EMT) by PI3K/AKT pathway activation contributes to acquired sorafenib resistance

As sorafenib resistance has been shown to be independent of the multidrug resistance (MDR)-machinery *(Figure S2)*, the observed chemoresistance in HUH7-R(+) cells is suggested to be mediated by EMT. In fact, the HUH7-R(+) cells exhibit typical EMT features, such as decreased protein levels of the epithelial marker E-Cadherin, a gain of the mesenchymal marker vimentin and increased N-Cadherin surface localization in comparison to HUH7-WT *(Figure 9 A-D)*. As previously reported in this context, EMT and malignant invasiveness can be induced by evasive activation of the PI3K/AKT-signaling pathway through continuous inhibition of the sorafenib-targeted MAPK/ERK axis, as observed in sorafenib-exposed HUH7-R(+) cells *(Figure 9 E)* (Chen et al., 2011; van Malenstein et al., 2013). Both AKT phosphorylation and the mesenchymal shift in protein expression were found to be reversible after sorafenib withdrawal. Upon EMT, the invasive potential observed *in vivo* is largely dictated by the matrix metalloproteinases (MMPs) MMP-2 and MMP-9, which were both upregulated in HUH7-R(+) cells *(Figure S3)* (Son and Moon, 2010).

Summarizing, in *chapter 4.1* we established a robust sorafenib resistance HCC cell model that obtained broad chemotherapeutic cross-resistance upon sorafenib treatment and showed a rapid rebound of proliferation after therapy termination. Both phenomena possibly contribute to the overall low therapeutic benefit of sorafenib. Importantly, the resumption of tumor growth secondary to

sorafenib goes along with chemotherapeutic resensitization, implicating a potential strategy of therapeutic intervention in the second-line setting of advanced-stage sorafenib-resistant HCC.

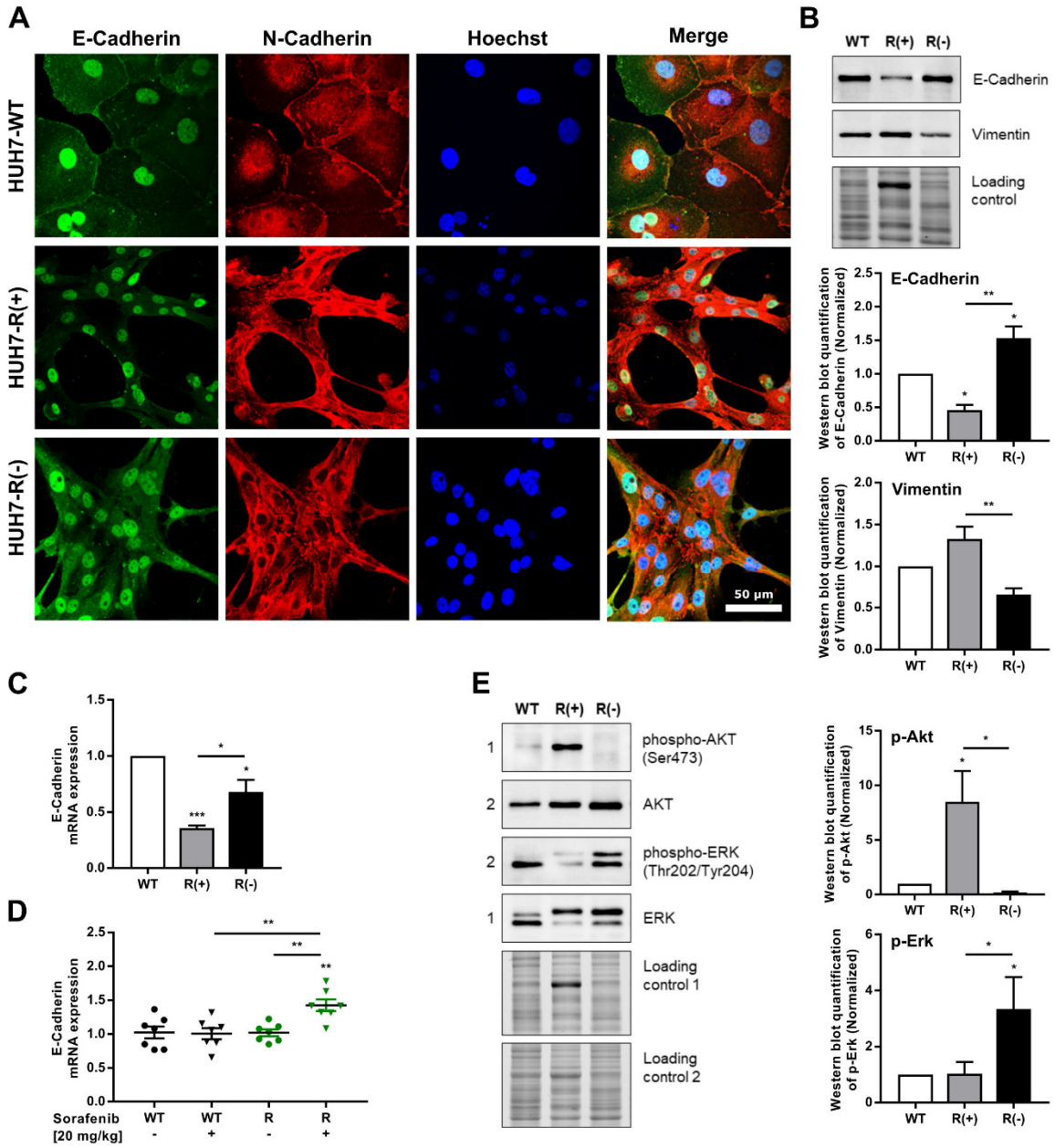

Figure 9. **Sorafenib resistance is accompanied by partial EMT and compensatory PI3K/AKT pathway activation.** **(A)** Increased surface localization of N-Cadherin under sustained sorafenib exposure. Immunostaining of the EMT markers E-Cadherin (green), N-Cadherin (red) as well as Hoechst33342 (blue). Scale bar indicates 50 µm. **(B)** Long-term sorafenib exposure induces partial EMT in HUH7-R(+) cells. Immunoblot analysis of the EMT marker E-Cadherin and vimentin, normalized to the protein load and to HUH7-WT. **(C)** E-Cadherin mRNA-expression is decreased upon sustained sorafenib exposure of HUH7-R cells *in vitro*. E-Cadherin mRNA-levels were normalized to HUH7-WT. **(D)** Sorafenib treatment modifies E-Cadherin mRNA-expression of HUH7-R cells *in vivo*. E-Cadherin mRNA levels of resected tumors (*Figure 7*) were normalized to the mean mRNA-expression of HUH7-WT. **(E)** Compensatory PI3K/Akt signaling pathway is upregulated in HUH7-R(+) cells. Immunoblot analysis was normalization to the protein load and to HUH7-WT. Values denoted as ± SEM, n=3, *p<0.05, **p<0.01, ***p<0.001 (ANOVA).

4.2 Tumor relapse is driven by metabolic and mitochondrial alterations

4.2.1 Mass spectrometry (MS)-based proteomics analysis of sorafenib resistance and rebound growth

Sorafenib treatment abrogation accompanies with an unfavorable relapse of tumor growth, but has been shown to resensitize HUH7-R cells to chemotherapeutic treatment. To obtain better insight into the underlying mechanism of sorafenib resistance and the therapy-limiting tumor relapse, we performed LC-MS/MS-based proteomics screening and identified differentially expressed proteins in sorafenib-resistant HUH7-R cells before and after treatment termination in comparison to their parental HUH7-WT cell line. As sorafenib resistance was accompanied by drastic changes of the cellular proteome, gene set enrichment analysis (GSEA) was applied to elucidate the most prominent altered protein clusters *(Figure 10; Figure S4)*. In HUH7-R(+) cells, GSEA strongly highlighted an elevated abundance of proteins related to mitochondrial structural components and glucose turnover, such as the tricarboxylic acid (TCA)-cycle, glycolysis, as well as amino and nucleotide sugar metabolism. In addition, higher lysosomal protein expression and suppressed transcriptional activity were observed when compared to HUH7-R(-) rebound growth cells.

A

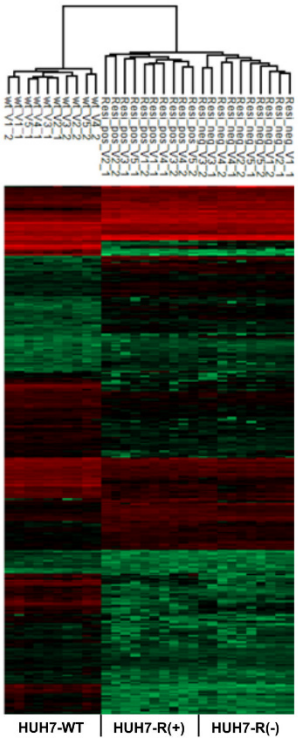

B

GENE SET –Enriched in HUH7-WT vs. HUH7-R(+)	SIZE	ES	FDR q-val	NOM p-val
RECEPTOR ACTIVITY	23	-0.6695	0.2604	0.0000
RESPONSE TO CHEMICAL STIMULUS	39	-0.5903	0.4875	0.0055
ENDOPLASMIC RETICULUM	66	-0.5006	1.0000	0.0148
ENZYME ACTIVATOR ACTIVITY	15	-0.6670	1.0000	0.0163
FATTY ACID METABOLISM	20	-0.5957	1.0000	0.0230
ALZHEIMERS DISEASE	48	-0.5046	1.0000	0.0262
MITOCHONDRION ORGANIZATION AND BIOGENESIS	18	-0.6101	1.0000	0.0284
CELLULAR LOCALIZATION	91	-0.4481	0.8513	0.0299
RESPONSE TO STRESS	64	-0.4685	1.0000	0.0314
CYTOPLASMIC PART	317	-0.3821	0.8651	0.0330

C

GENE SET –Enriched in HUH7-R(+) vs. HUH7-R(-)	SIZE	ES	FDR q-val	NOM p-val
CELL FRACTION	67	0.4082	0.6524	0.0061
MEMBRANE FRACTION	41	0.4566	0.7605	0.0076
CITRATE CYCLE TCA CYCLE	16	0.6149	0.8388	0.0101
ORGANDEVELOPMENT	44	0.3949	0.8651	0.0551
LYSOSOME	22	0.4933	0.9537	0.0574
AMINO SUGAR AND NUCLEOTIDE SUGAR METABOLISM	18	0.5049	0.9361	0.0607
MITOCHONDRION	105	0.3061	0.9706	0.0757
TRANSCRIPTION REPRESSOR ACTIVITY	15	0.5167	0.9649	0.0757
EPITHELIAL CELL SIGNALING IN HELICOBACTER PYLORI INFECTION	15	0.5279	0.7490	0.0772
GLYCOLYSIS GLUCONEOGENESIS	17	0.5040	0.8132	0.0806

Figure 10. **GSEA of the sorafenib resistance HCC cell model. (A)** HUH7-R cells reveal massive alterations in their proteome compared to their parental HUH7-WT cell line, necessitating comparison by GSEA. Gene cluster analysis of MS-proteomics screen compares HUH7-WT (wt), HUH7-R(+) (Resi_pos) and HUH7-R(-) (Resi_neg) cells. **(B)** Gene sets enriched in HUH7-WT compared to HUH7-R(+) cells and **(C)** gene sets enriched in HUH7-R(+) compared to HUH7-R(-) cells are shown. Top 10 upregulated gene sets ranked according to their nominal p-value (NOM p-val) are listed and gene sets with NOM p-val<0.05 are highlighted. ES: enrichment score; FDR: false discovery rate; NES: normalized enrichment score. See also ***Figure S4***.

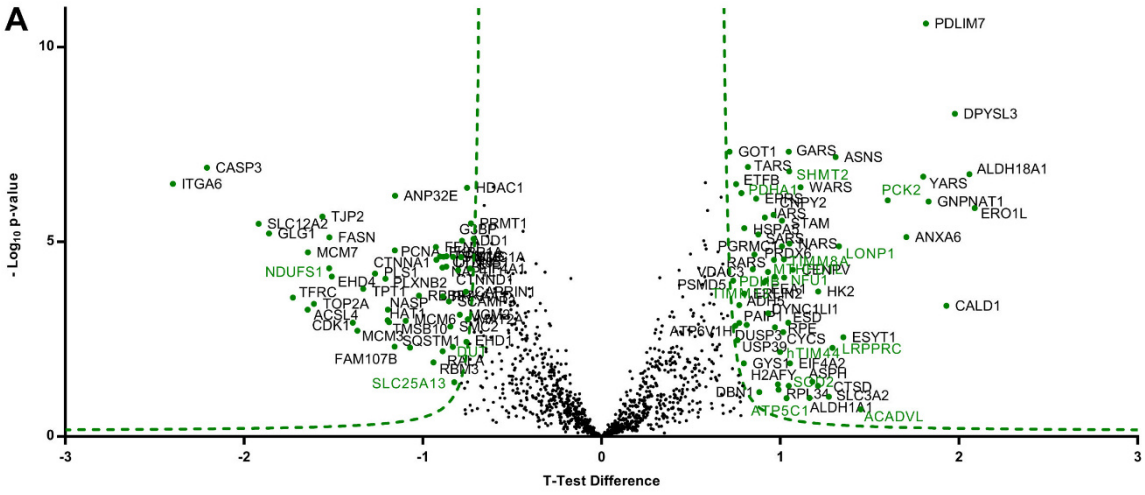

Gene names	x-fold change	T-Test Difference	-Log10 p-value	Protein names
ITGA6	-8.080	-2.398	6.488	Integrin alpha-6
MCM7	-5.309	-1.643	4.729	DNA replication licensing factor MCM7
NDUFS1	-4.783	-1.523	4.318	NADH-ubiquinone oxidoreductase 75 kDa subunit, mitochondrial
CASP3	-4.355	-2.207	6.904	Caspase-3
SLC12A2	-3.650	-1.918	5.465	Solute carrier family 12 member 2
TFRC	-3.589	-1.726	3.567	Transferrin receptor protein 1
SMC2	-3.524	-0.846	2.821	Structural maintenance of chromosomes protein 2
HAT1	-3.243	-1.196	2.986	Histone acetyltransferase type B catalytic subunit
FAM107B	-3.036	-1.157	2.305	Protein FAM107B
CDK1	-2.990	-1.391	2.922	Cyclin-dependent kinase 1
MCM6	-2.944	-1.096	2.970	DNA replication licensing factor MCM6
FEN1	-2.879	-0.926	4.868	Flap endonuclease 1
MCM3	-2.818	-1.366	2.718	DNA replication licensing factor MCM3
TMSB10	-2.816	-1.188	2.932	Thymosin beta-10
TJP2	-2.740	-1.561	5.651	Tight junction protein ZO-2
EHD4	-2.707	-1.509	4.110	EH domain-containing protein 4
ACSL4	-2.666	-1.644	3.255	Long-chain-fatty-acid--CoA ligase 4
PLXNB2	-2.609	-1.208	4.055	Plexin-B2
FASN	-2.584	-1.522	5.114	Fatty acid synthase
GLG1	-2.573	-1.860	5.215	Golgi apparatus protein 1
MCM2	-2.572	-0.792	3.129	DNA replication licensing factor MCM2
NASP	-2.506	-1.195	3.255	Nuclear autoantigenic sperm protein
PLS1	-2.445	-1.267	4.181	Plastin-1
TOP2A	-2.378	-1.608	3.406	DNA topoisomerase 2-alpha
TPT1	-2.316	-1.334	3.792	Translationally-controlled tumor protein
PRKAA1	-2.156	-0.887	3.602	5-AMP-activated protein kinase catalytic subunit alpha-1
PCNA	-2.113	-1.156	4.782	Proliferating cell nuclear antigen
ANP32B	-2.096	-1.155	6.181	Acidic leucine-rich nuclear phosphoprotein 32 family member B
PPM1G	-2.036	-0.866	4.628	Protein phosphatase 1G
SCAMP3	-2.028	-0.853	3.471	Secretory carrier-associated membrane protein 3
HDAC1	-2.015	-0.752	6.390	Histone deacetylase 1
ADD1	-1.986	-0.780	5.027	Alpha-adducin
RALA	-1.977	-0.889	2.190	Ras-related protein Ral-A
RBBP7	-1.902	-1.021	3.619	Histone-binding protein RBBP7
FKBP1A	-1.874	-0.903	4.625	Peptidyl-prolyl cis-trans isomerase FKBP1A
SQSTM1	-1.858	-1.071	2.284	Sequestosome-1
DUT	-1.842	-0.832	2.304	Deoxyuridine 5-triphosphate nucleotidohydrolase, mitochondrial
CTNNA1	-1.828	-0.923	4.540	Catenin alpha-1
CTNNB1	-1.828	-0.882	4.615	Catenin beta-1
NAP1L1	-1.810	-0.890	4.340	Nucleosome assembly protein 1-like 1
SLC25A13	-1.777	-0.823	1.396	Calcium-binding mitochondrial carrier protein Aralar2
SMC3	-1.768	-0.830	4.610	Structural maintenance of chromosomes protein 3
DDX5	-1.746	-0.869	4.362	Probable ATP-dependent RNA helicase DDX5
SMC1A	-1.696	-0.786	4.605	Structural maintenance of chromosomes protein 1A
CTNND1	-1.693	-0.802	4.267	Catenin delta-1
RBM3	-1.679	-0.941	1.901	Putative RNA-binding protein 3
CAPRIN1	-1.659	-0.759	3.718	Caprin-1
PRMT1	-1.634	-0.730	5.478	Protein arginine N-methyltransferase 1
EIF4A1	-1.631	-0.736	4.314	Eukaryotic initiation factor 4A-I
MAT2A	-1.622	-0.748	3.012	S-adenosylmethionine synthase isoform type-2
EHD1	-1.557	-0.756	2.434	EH domain-containing protein 1

Gene names	x-fold change	T-Test Difference	-Log10 p-value	Protein names
CALD1	6.580	1.930	3.359	Caldesmon
DPYSL3	4.148	1.978	8.289	Dihydropyrimidinase-related protein 3
GNPNAT1	3.849	1.831	6.035	Glucosamine 6-phosphate N-acetyltransferase
ALDH18A1	3.777	2.059	6.735	Delta-1-pyrroline-5-carboxylate synthase
ERO1L	3.769	2.088	5.867	ERO1-like protein alpha
PDLIM7	3.731	1.816	10.607	PDZ and LIM domain protein 7
CTSD	3.646	1.212	1.298	Cathepsin D
ANXA6	3.636	1.707	5.122	Annexin A6
ALDH1A1	3.481	1.164	0.988	Retinal dehydrogenase 1
YARS	3.367	1.801	6.673	Tyrosine--tRNA ligase, cytoplasmic
PCK2	2.795	1.602	6.068	Phosphoenolpyruvate carboxykinase [GTP], mitochondrial
RPL34	2.623	0.991	1.199	60S ribosomal protein L34
SOD2	2.413	1.048	1.299	Superoxide dismutase, mitochondrial
ASNS	2.411	1.310	7.175	Asparagine synthetase
NFU1	2.369	1.023	4.085	NFU1 iron-sulfur cluster scaffold homolog, mitochondrial
PGRMC1	2.357	1.011	4.884	Membrane-associated progesterone receptor component 1
ESYT1	2.350	1.354	2.550	Extended synaptotagmin-1
LONP1	2.335	1.330	4.883	Lon protease homolog, mitochondrial
CYCS	2.334	1.016	2.680	Cytochrome c
hTIM44	2.314	1.000	2.171	Mitochondrial import inner membrane translocase subunit TIM44
SLC3A2	2.276	1.273	1.022	4F2 cell-surface antigen heavy chain
HK2	2.240	1.213	3.721	Hexokinase-2
CENPV	2.220	1.071	4.280	Centromere protein V
ESD	2.196	1.045	2.923	S-formylglutathione hydrolase
EIF4A2	2.179	1.054	1.877	Eukaryotic initiation factor 4A-II
WARS	2.171	1.115	6.400	Tryptophan--tRNA ligase, cytoplasmic
PDHB	2.127	0.969	4.101	Pyruvate dehydrogenase E1 subunit beta, mitochondrial
TIMM8A	2.120	1.021	4.549	Mitochondrial import inner membrane translocase subunit Tim8 A
GARS	2.076	1.048	7.317	Glycine--tRNA ligase
H2AFY	2.044	0.987	1.338	Histone H2A
SHMT2	2.042	1.050	6.812	Serine hydroxymethyltransferase, mitochondrial
NARS	2.027	1.052	4.951	Asparagine--tRNA ligase, cytoplasmic
CNPY2	1.994	0.963	5.693	Protein canopy homolog 2
LRPPRC	1.972	1.292	2.278	Leucine-rich PPR motif-containing protein, mitochondrial
RARS	1.963	0.966	4.535	Arginine--tRNA ligase, cytoplasmic
RPE	1.950	0.971	2.805	Ribulose-phosphate 3-epimerase
DUSP3	1.925	0.813	2.865	Dual specificity protein phosphatase 3
EEA1	1.904	0.921	4.005	Early endosome antigen 1
STAM	1.904	1.011	5.546	Signal transducing adapter molecule 1
DYNC1LI1	1.887	0.934	3.163	Cytoplasmic dynein 1 light intermediate chain 1
SARS	1.877	0.877	5.191	Serine--tRNA ligase, cytoplasmic
GYS1	1.872	0.797	1.880	Glycogen [starch] synthase. muscle
ACADVL	1.865	1.451	0.702	Very long-chain specific acyl-CoA dehydrogenase, mitochondrial
MTHFD1L	1.854	0.932	4.224	Monofunctional C1-tetrahydrofolate synthase, mitochondrial
IARS	1.846	0.914	5.627	Isoleucine--tRNA ligase, cytoplasmic
EPRS	1.831	0.865	6.107	Bifunctional glutamate/proline--tRNA ligase
PRDX6	1.807	0.856	4.677	Peroxiredoxin-6
VDAC3	1.796	0.847	4.296	Voltage-dependent anion-selective channel protein 3
TARS	1.767	0.819	6.922	Threonine--tRNA ligase, cytoplasmic
HSPA5	1.765	0.799	5.352	78 kDa glucose-regulated protein
TIMM13	1.729	0.909	3.956	Mitochondrial import inner membrane translocase subunit Tim13
ADH5	1.708	0.770	3.377	Alcohol dehydrogenase class-3
ATP6V1H	1.703	0.749	2.844	V-type proton ATPase subunit H
PDHA1	1.696	0.783	6.250	Pyruvate dehydrogenase E1 subunit alpha, mitochondrial
ERLIN2	1.676	0.799	3.667	Erlin-2
ATP5C1	1.653	1.036	0.986	ATP synthase subunit gamma, mitochondrial
PAIP1	1.426	0.771	2.917	Polyadenylate-binding protein-interacting protein 1
PSMD5	1.344	0.737	4.005	26S proteasome non-ATPase regulatory subunit 5
DBN1	1.333	0.883	1.142	Drebrin
ASPH	1.309	1.180	1.409	Aspartyl/asparaginyl beta-hydroxylase

Figure 11. **Volcano blot analysis comparing the proteome of HUH7-R(+) and HUH7-R(-) cells. (A)** T-test Difference and Log_{10} p-value are shown. Proteins lower and higher than the cut-off FDR 0.05, s0=2 (dashed green line) are highlighted with green dots. **(B)** Autophagic proteins and the mitochondrial complex I (NDUFS1) are upregulated upon rebound growth. Proteins with a t-test Difference <-0.715 (higher abundance in HUH7-R(-) cells) are listed according to their x-fold change. **(C)** Mitochondrial proteins are downregulated upon rebound growth. Proteins with a t-test Difference >0.715 (higher abundance in HUH7-R(+) cells) are listed according to their x-fold change. Proteins of mitochondrial origin are highlighted in green. Values denoted as ± SEM, n=5. Experiments were performed in technical duplicates.

Interestingly, volcano blot analysis at the single-protein level revealed a central role of the mitochondrial NDUF subunit 1, complex I of the respiratory chain, in HUH7-R(-) cells, as the NDUF was found to be almost 5-fold increased among tumor relapse *(Figure 11 A-B)*. The mitochondrial ETC accounts not only for the majority of cellular ATP production, but it also supplies through its complex I activity mitochondria with the oxidized cofactor NAD^+. This intrinsic electron acceptor, in turn, fuels TCA cycle activity driving biosynthesis and proliferation (Sullivan et al., 2015; Vander Heiden et al., 2009). In addition, we found a higher abundance of proteins involved in DNA-replication, translation and autophagosome formation, such as Sequestosome-1 (SQSTM1; p62), in HUH7-R(-) compared to HUH7-R(+) cells. In contrast, mitochondrial proteins involved in protein import through the IMM, superoxide defense and the overall TCA cycle activity were upregulated in HUH7-R(+) cells *(Figure 11 C)*. Relative quantification of the protein classes in HUH7-R cells before and after sorafenib withdrawal indicated an increased requirement of oxidoreductases (13%) and hydrolases (17%) in HUH7-R(+) cells, whereas cell adhesion molecules (0%) and chaperones (2%) were found to be underrepresented in comparison to HUH7-R(-) cells *(Figure 12; Figure S5)*.

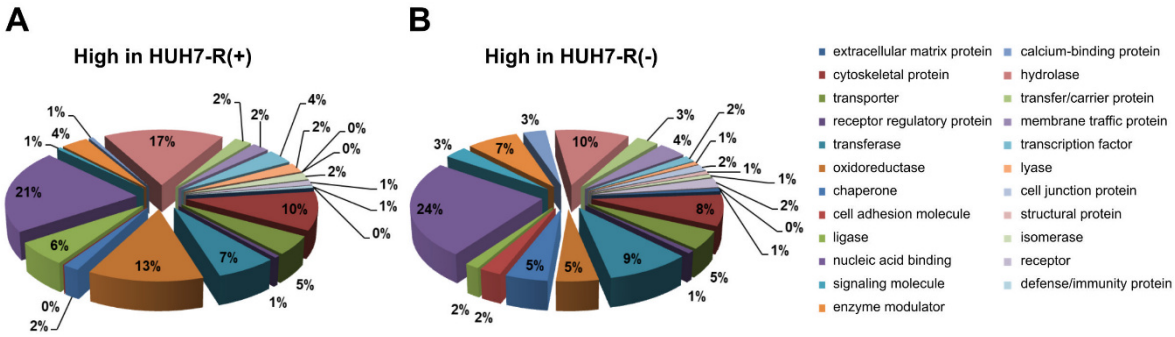

Figure 12. **Alterations of protein classes upon rebound growth. (A)** Oxidoreductases and hydrolases are upregulated in HUH7-R(+) cells. Protein classes >1.5-fold upregulated in HUH7-R(+) vs. HUH7-R(-) are shown. **(B)** Chaperones and cell adhesion proteins are upregulated in HUH7-R(-) cells. Protein classes >1.5-fold upregulated in HUH7-R(-) vs. HUH7-R(+) are shown. The analysis of protein classes of the MS-proteomics screening was performed with pantherdb.org (Gene ontology database). See also ***Figure S5***.

4.2.2 HUH7-R(-) cells undergo a metabolic switch to increased respiratory activity

In addition to the MS-proteomics screening, metabolic profiling by a glycolytic stress test showed that HUH7-R(-) cells shift towards a strongly energy-producing phenotype with a high oxygen consumption rate (OCR) *(Figure 13 A)* and a boost of ATP levels was observed upon growth resumption *(Figure 13 B)*. In contrast, sustained sorafenib exposure was accompanied by an increased rate of lactate fermentation *(Figure 13 B)*, an anaerobic high-flux elimination of extra-mitochondrial pyruvate (Curi et al., 1988), which was gradually reversed after sorafenib withdrawal. These HUH7-R(+) cells were highly dependent on anaerobic glycolysis for ATP production, which was confirmed by an increased cellular glucose uptake *(Figure 13 C)* compared to HUH7-R(-) cells.

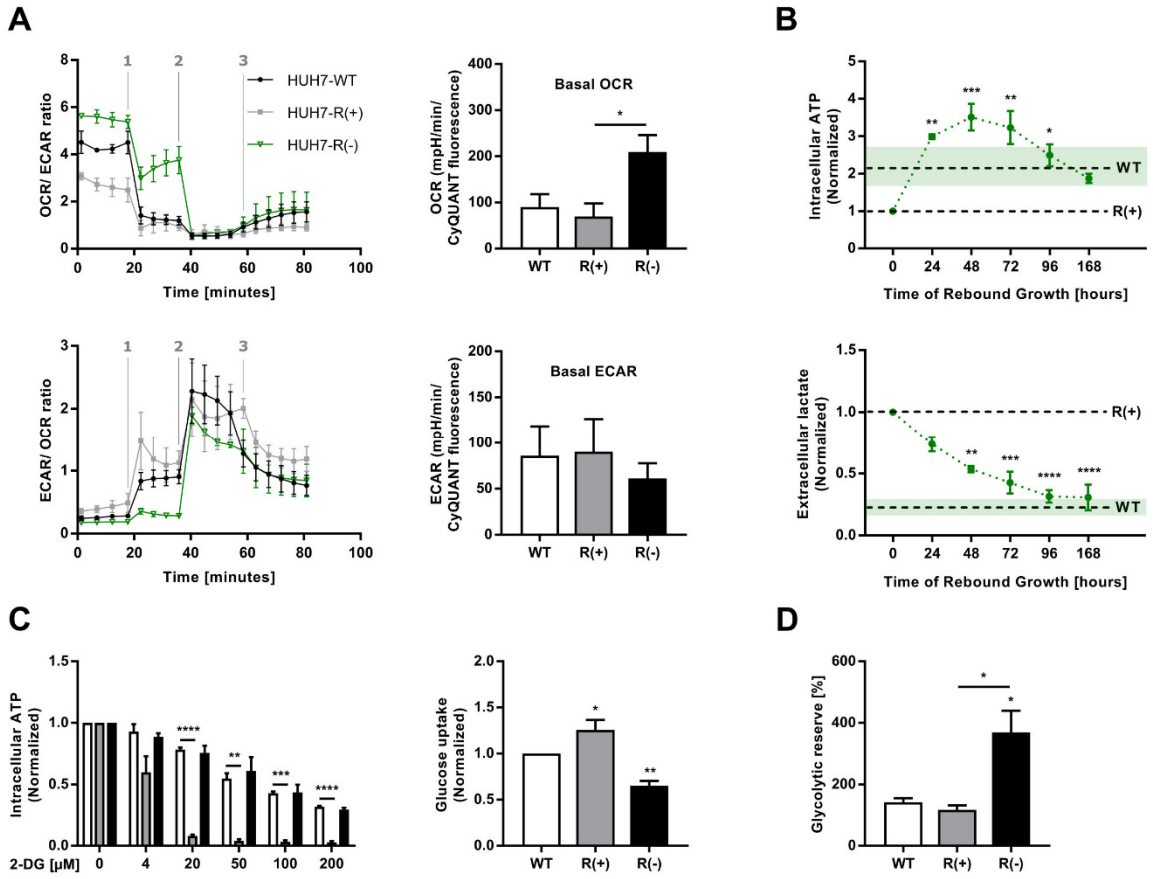

Figure 13. **Metabolic profiling of the sorafenib-resistant rebound growth model. (A)** Metabolic switch from glycolysis to respiration upon rebound growth. Oxygen consumption rate (OCR) and extracellular acidification rate (ECAR) were assessed simultaneously by a glycolytic stress test. The cells were treated with (1) D-glucose (10 mM), (2) oligomycin (1 µM) and (3) 2-deoxy-D-glucose (2-DG) (50 mM). Basal ECAR- and OCR-levels was determined at the plateau after D-glucose injection and normalized to the cell number. **(B)** Anaerobic lactate fermentation in HUH7-R(+) cells with insufficient ATP-generation. Measurements upon sorafenib withdrawal from HUH7-R(+) cells for 168 h every 24 h and normalization to HUH7-R(+). Mean (dashed line) and SEM (green area) of HUH7-WT are presented for comparison. **(C)** HUH7-R(+) cells are strongly dependent on glycolysis for energy generation. ATP levels within 72 h of glycolysis inhibition by 2-DG were assessed and normalized to the untreated control (left). Glucose uptake within 30 min was determined by flow cytometry and normalized to the cellular volume *(Figure S6)* and to HUH7-WT (right). **(D)** HUH7-R(-) cells have a strong capacity to switch from respiration to glycolysis. The glycolytic reserve depicts the percentage change of ECAR before and after oligomycin treatment in a glycolytic stress test (*Figure 13 A)*. Values shown as ± SEM, n=3, *p<0.05, **p<0.01, ***p<0.001, ****p<0.0001 (ANOVA).

Upon rebound growth, respiratory active HUH7-R(-) cells obtained a flexible metabolic phenotype and displayed the ability to switch to glycolysis after ETC inhibition *(Figure 13 D)*. In summary, on the one hand, the sorafenib-resistant HUH7-R(+) cells increase their glucose metabolism and are dependent on glycolysis for ATP production. This so-called Warburg effect (Warburg, 1956), has been previously associated with acquired chemoresistance in cancer cells (Shen et al., 2012). However, on the other hand, the aerobic pyruvate turnover by the TCA cycle of HUH7-R(+) cells appears to be insufficient and results in elevated lactate excretion. Thus, the presented data suggests that sustained sorafenib exposure impairs the mitochondrial metabolic functionality of HCC cells.

4.3 Sorafenib exposure mediates mitochondrial damage

4.3.1 Rebound growth is accompanied by dynamics in mitochondrial fission and fusion

Prominent alterations in mitochondria and their metabolic pathways, as revealed by LC-MS/MS-based proteomics analysis, warrant a detailed investigation of mitochondrial morphology and its functional dynamics upon tumor growth resumption. Mitochondria form a highly dynamic network undergoing constant fission and fusion to maintain functionality, adapt to environmental stressors and to drive metabolism (McBride et al., 2006). Fission and fusion processes are regulated by the GTPase dynamin-related protein (Drp1) and marked by mitofusin (Mfn-1) expression on the outer mitochondrial membranes (OMM) (Wong et al., 2018). A strong increase in mitochondrial mass *(Figure 14 A)* together with mitochondrial fission was observed in sorafenib-treated HUH7-R(+) cells compared to the parental HUH7-WT cell line *(Figure 14 B)*. Interestingly, both morphological alterations were reversible in HUH7-R(-) cells upon 96 h of sorafenib withdrawal.

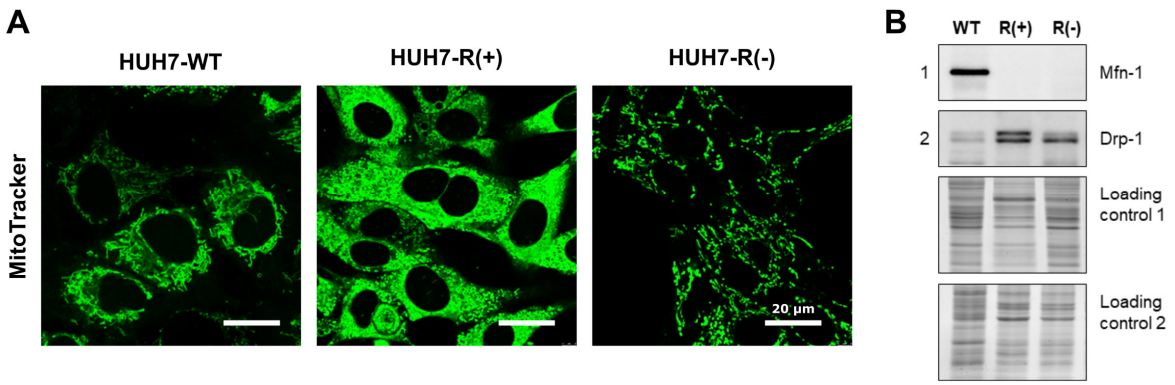

Figure 14. **Sorafenib-resistant HUH7-R(+) cells undergo mitochondrial fission. (A)** Metabolic switch is accompanied by major dynamics in fission/fusion processes and a reversible increase of mitochondrial mass upon sustained sorafenib exposure. MitoTracker staining of mitochondrial network is shown. Scale bars indicate 20 µm. **(B)** Immunoblot analysis of mitochondrial fusion- respective fission-marker Mfn-1 and Drp-1 are shown. Experiments were performed n=3 and representative images are shown.

4.3.2 Sustained sorafenib exposure impairs mitochondrial functionality

Sorafenib treatment impaired not only the mitochondrial network but may also have an impact on their functionality. First, sustained electron leakage from the ETC led to excessive production of mitochondrial superoxides (O_2^-) in HUH7-R(+) cells *(Figure 15 A)*. This elevated electron leakage might be partially due to the reduced protein expression of complex I (CI-NDUFB6) and complex V (CV-ATP5A) respiratory chain subunits in HUH7-R(+) cells *(Figure 15 B)* (Murphy, 2009). In fact, enhanced O_2^- levels were found to be directly linked to sorafenib exposure and reversed upon drug withdrawal *(Figure S7 A)*. Second, disrupted mitochondrial functionality was confirmed by low ETS capacity and routine respiration, as determined by high-resolution respirometry *(Figure 15 C-D)*.

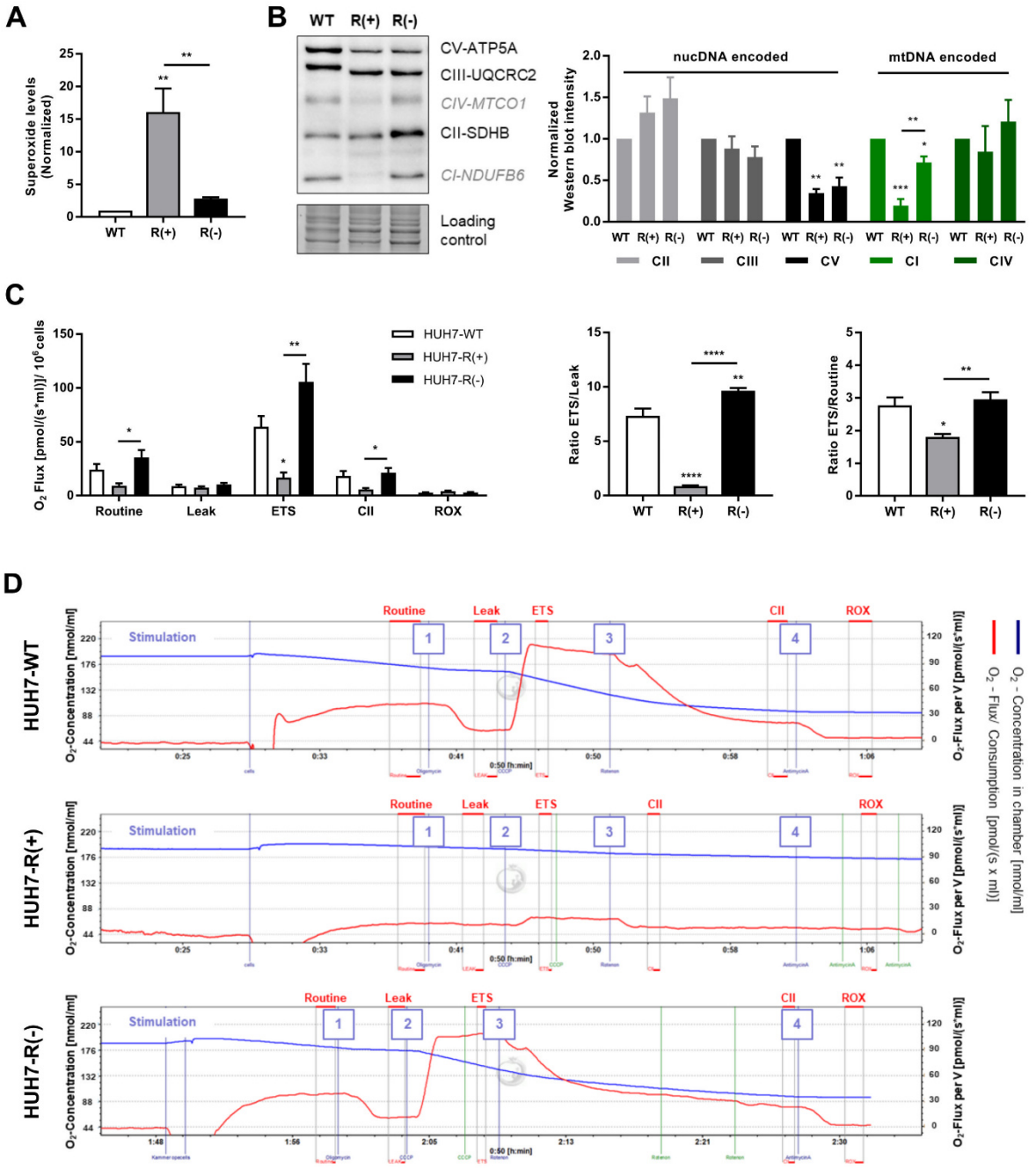

Figure 15. **Sorafenib impairs composition and functionality of the ETC. (A)** Sorafenib induces electron leakage from the ETC in HUH7-R(+) cells. Flow cytometric quantification of superoxide levels with normalization to the cellular volume *(Figure S6)* and to HUH7-WT. **(B)** Sorafenib impairs the protein expression of the nucDNA-encoded subunit CV-ATP5A and the mtDNA-encoded ETC subunit CI-NDUFB6. Immunoblot analysis of mtDNA- (CI-NDUFB6, CIV-MTCO1) and nucDNA-encoded ETC subunits (CII-SDHB, CIII-UQCRC2, CV-ATP5A). The protein expression was normalized to the protein load and to HUH7-WT. **(C)** Renewed mitochondria obtain increased ETC capacity. High-resolution O_2-flux measurements untreated (Routine) and after oligomycin (Leak), CCCP (ETS), rotenone (complex II) and antimycin A (ROX) stimulation, normalized to cell number and cellular volume *(Figure S6).* **(D)** Representative O_2-flux measurements (red curves) of 1.6 x 10^6 HUH7-WT, HUH7-R(-) and 3.2 x 10^6 HUH7-R(+) cells are shown with the stimulation time points of oligomycin (400 µM), CCCP (5 mM), rotenone (2 µM) and antimycin A (500 µM). For quantitative assessment, the parameters Routine, Leak, ETS, complex II and ROX were determined within the red segments. Values denoted as ± SEM, n=3 for A and B, n=4 for C and D, *p<0.05, **p<0.01, ***p<0.001, ****p<0.0001 (ANOVA). See also ***Figure S7 A***.

4.3.3 Endoplasmatic reticulum (ER)-stress links mitochondrial damage to mitophagy in sorafenib-resistant cells

The origin of mitochondrial damage in HUH7-R(+) cells evoked to be closely linked to prominent ER-stress, as previously reported in the context of acquired chemoresistance through persistent sorafenib exposure (Holz et al., 2013; Ma et al., 2017). Indeed, the key-mediators of ER-stress NFκB and GADD 153/CHOP were strongly activated in HUH7-R cells *(Figure 16 A)*. This implicates mitochondrial damage through excessing levels of free intracellular calcium (Ca^{2+}), which is released from the ER. In addition, ER-stress induces, on a transcriptionally level, mitochondrial degradation with subsequent mitochondrial biogenesis in order to regain respiratory functionality *(Figure 16 B)*.

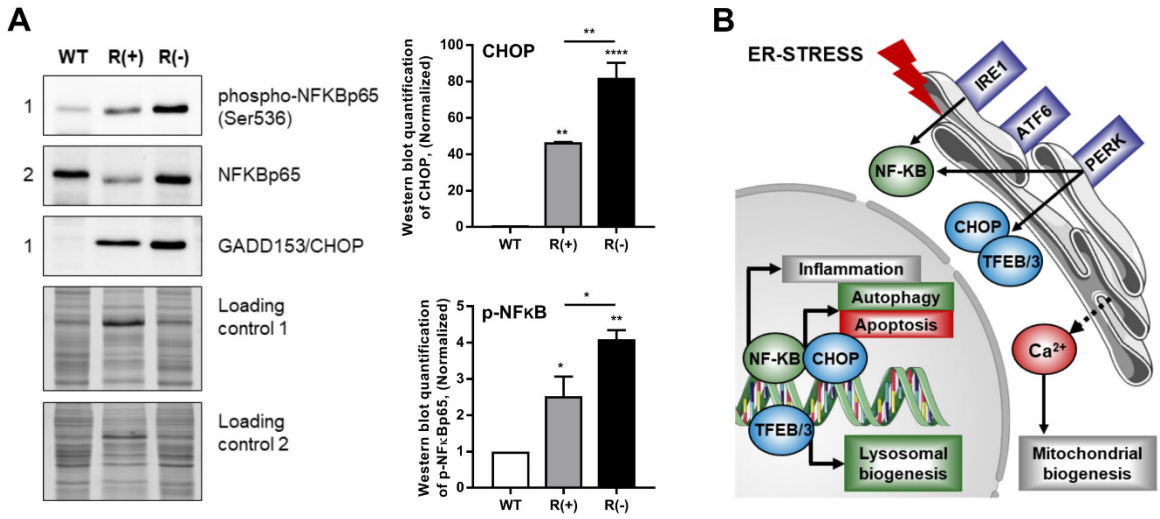

Figure 16. **ER-stress links Ca^{2+}-induced mitochondrial damage, activation of mitophagy and mitochondrial biogenesis. (A)** ER-stress pathways are strongly upregulated in HUH7-R cells. Immunoblot analysis of CHOP and NFκB activation were normalized to the respective protein load and to HUH7-WT. **(B)** ER-stress links mitochondrial degradation and mitochondrial biogenesis upon sorafenib resistance and rebound growth. Values shown as ± SEM, n=3, *p<0.05, **p<0.01, ****p<0.0001 (ANOVA).

4.3.4 Efficient autophagy of damaged mitochondria after sorafenib withdrawal

As mitochondria play a critical role in cellular homeostasis, they not only undergo dynamic reformation but also constant quality control, whereby damaged or functionally disturbed mitochondria are engulfed by autophagosomes that fuse with lysosomes for degradation (Pickles et al., 2018). Hints for the occurrence of mitophagy in HUH7-R(+) cells were obtained by the LC-MS/MS proteomics-based GSEA *(Figure 10 C)*, by elevated lysosomal mass *(Figure 17 A-B)*, and by the increased protein expression of TFEB and TFE3, which are transcriptional activators of lysosomal biogenesis *(Figure 17 C)*. Along with mitophagy, mitochondrial proteases and ubiquitin-mediated proteasomal degradation represent the main paradigms of mitochondrial quality control (Sugiura et al., 2014). In a first-line defense, mitochondrial proteases degrade unfolded and oxidized

proteins within the matrix and intermembrane space (Tatsuta and Langer, 2009). In a second-line defense, OMM proteins, such as Mfn-1 and Bcl-2 family members, tend to be ubiquitinated and degraded by retrotranslocation and delivery to the cytosolic proteasome (Tanaka et al., 2010). Indeed, proteasomal removal of the OMM proteins Bak, Bcl-2 *(Figure 17 D)* and Mfn-1 *(Figure 14 B)* was observed in HUH7-R cells, whereas protein expression of the cytosolic Bax persisted *(Figure 17 D)*.

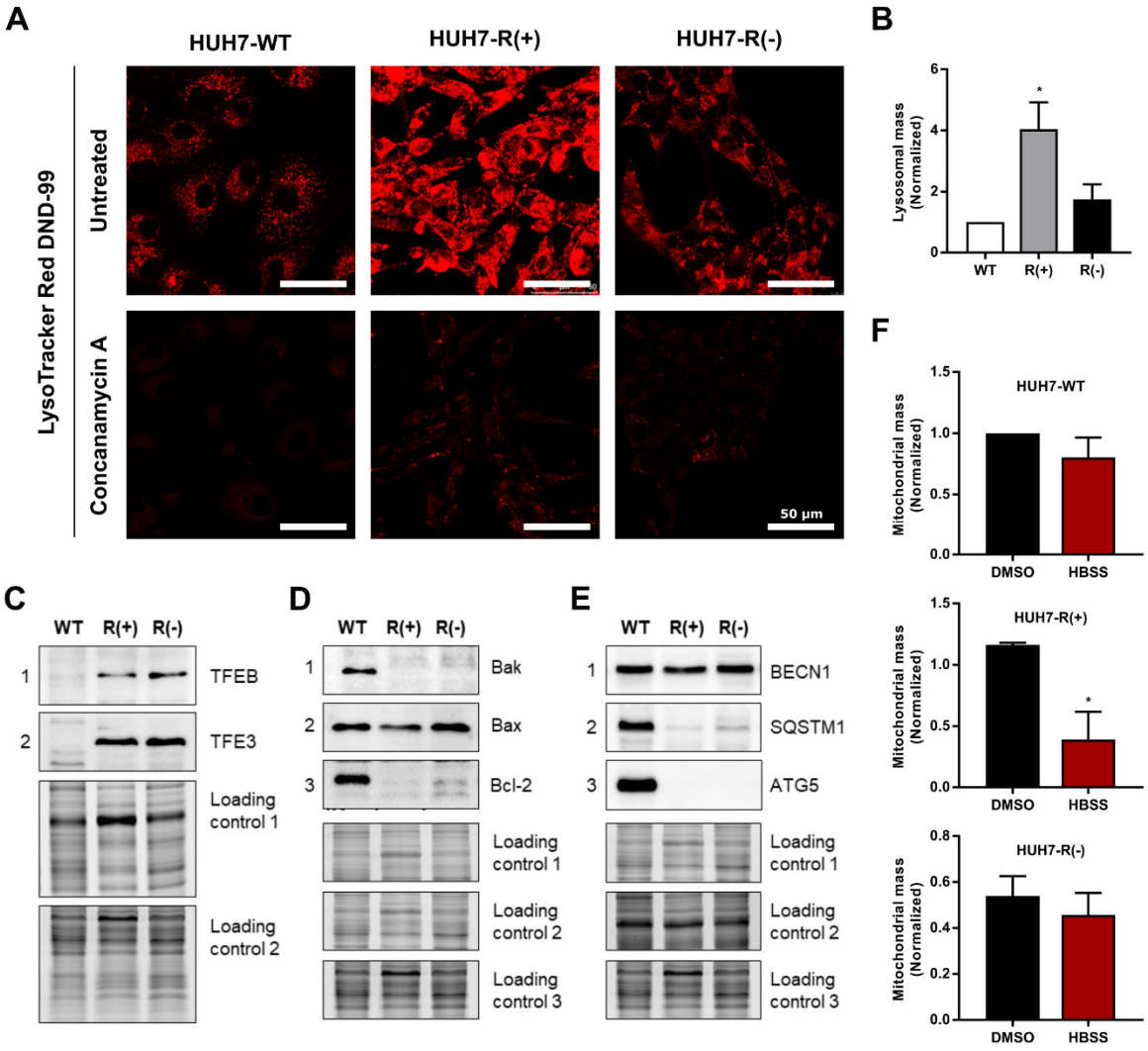

Figure 17. **Lysosomal biogenesis and mitophagy are upregulated in HUH7-R(+) cells. (A)** Induction of lysosomal biogenesis upon sorafenib resistance. For LysoTracker staining, concanamycin A (1 µM) pre-treatment for 4 h was used as negative control. Scale bars indicate 50 µm. **(B)** Flow cytometric quantification of the lysosomal mass, normalized to the cellular volume *(Figure S6)* and to HUH7-WT. **(C)** Lysosomal biogenesis is activated in HUH7-R cells. Immunoblot analysis of TFEB and TFE3 was normalized to the respective protein load. **(D)** Selective degradation of OMM proteins in HUH7-R cells. Immunoblot analysis of apoptosis regulators Bak and Bcl-2, located on the OMM as well as the cytoplasmic protein Bak was normalized to the protein load. **(E)** Strongly diminished expression of ATG5 and SQSTM-1, which contribute to autophagosome formation. Immunoblot analysis of proteins involved in autophagy was normalized to the protein load. **(F)** HUH7-R(+) cells have highest capacity of starvation-induced mitophagy. Cells were incubated with HBSS for 6 h before mitochondrial mass was assessed by flow cytometry and normalized to the untreated control of HUH7-WT cells. Values denoted as ± SEM, n=3, *p<0.05 (ANOVA).

Despite the presumably impaired autophagosome formation in HUH7-R cells *(Figure 17 E)*, mitophagy remained inducible under starvation conditions prior to sorafenib withdrawal *(Figure 17 F)*. Thus, starvation induced mitophagy is possibly mediated by direct translocation of mitochondrial cargo to the lysosomes via vesicular transport (Sugiura et al., 2014). In summary, we suggest that sorafenib-induced ER-stress not only contributes to the unfolding or oxidation of certain OMM proteins, but also leads to an overall impairment of mitochondrial function and consequent removal of those by the overlapping activity of different mitochondrial degradation pathways. Upon complete mitochondrial dysfunction, as indicated by fission or depolarization, the entire organelle is targeted to the autophagosome (Pickles et al., 2018). Autophagosome formation is thereby initiated with involvement of Beclin-1 (BECN-1), elongated by the ATG5-complex and subsequently conjugated to the adaptor of ubiquitinated proteins SQSTM-1 *(Figure 18 A)* (Kang et al., 2011). Nonetheless, due to insufficient levels of LC3II-positive, mature autophagosomes under sorafenib treatment *(Figure 18 B)*, defective mitochondria were only efficiently degraded after 96 h of growth resumption. Inhibition of autophagy by 3-MA, however, was able to prevent mitochondrial degradation and significantly rescued superoxide levels upon rebound growth *(Figure 18 C; Figure S7 A-B)*. Further, the recovery of intact mitochondrial mass in HUH7-R(-) cells indicates mitochondrial biogenesis after sorafenib withdrawal from HUH7-R(+) cells *(Figure S7 C)*.

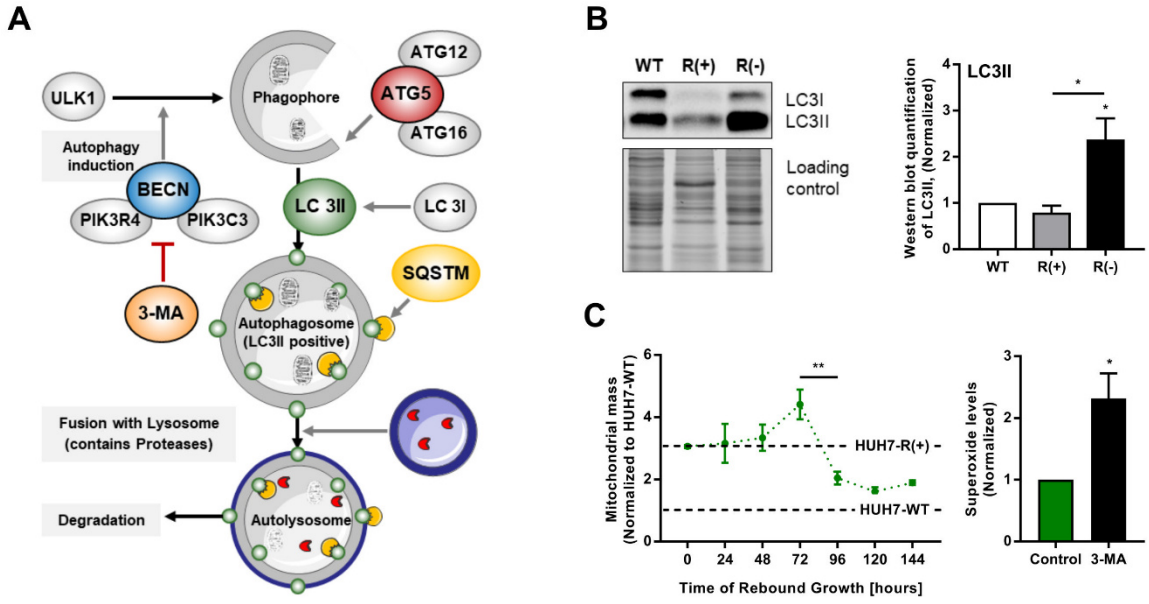

Figure 18. **Autophagic degradation of damaged mitochondria upon tumor relapse. (A)** Illustration showing the involvement of BECN1, SQSTM-1, ATG5 *(Figure 17 E)* and LC3II in autophagosome formation. **(B)** Autophagic flux is increased in HUH7-R(-) cells. Immunoblot analysis for mature autophagosomes (high LC3II protein levels) was normalized to the protein load and to HUH7-WT (ANOVA). **(C)** Damaged mitochondria are degraded within 96 h of rebound growth. Mitochondrial mass was assessed by flow cytometry upon rebound growth for 144 h every 24 h and normalized to the cellular volume *(Figure S6)* and to HUH7-WT (left) (ANOVA). Superoxide levels were measured by flow cytometry upon 72 h of sorafenib withdrawal with inhibition of autophagy by 3-MA (5 mM) and normalized to the cellular volume *(Figure S6)* and to HUH7-WT (right) (t-test). Values denoted as ± SEM, n=3, *p<0.05, **p<0.01. See also ***Figure S7 B-C***.

Even though sorafenib-resistant cells lack ATG5, elevated levels of mature autophagosomes were observed in HUH7-R(-) cells, which correlates with low levels of apoptosis *(Figure 19 A)*. However, in contrast to HUH7-R(+) cells, HUH7-R(-) cells obtained reduced colocalization of mitochondria with lysosomes, indicating diminished mitophagy *(Figure 19 B; Figure S8 A)*. Thus, we hypothesize that in addition to mitochondrial biogenesis, an ATG5-independent mechanism of autophagy contributes to increased cell survival upon growth resumption *(Figure 19 C-D; Figure S8 B)*. It was previously reported that upon ATG5-independent autophagy, the Rab9 protein may replace the function of LC3 in autophagosome formation (Nishida et al., 2009). However, no alterations in Rab9 localization were observed in HUH7-R compared to HUH7-WT cells *(Figure 19 E, Figure S8 C)*.

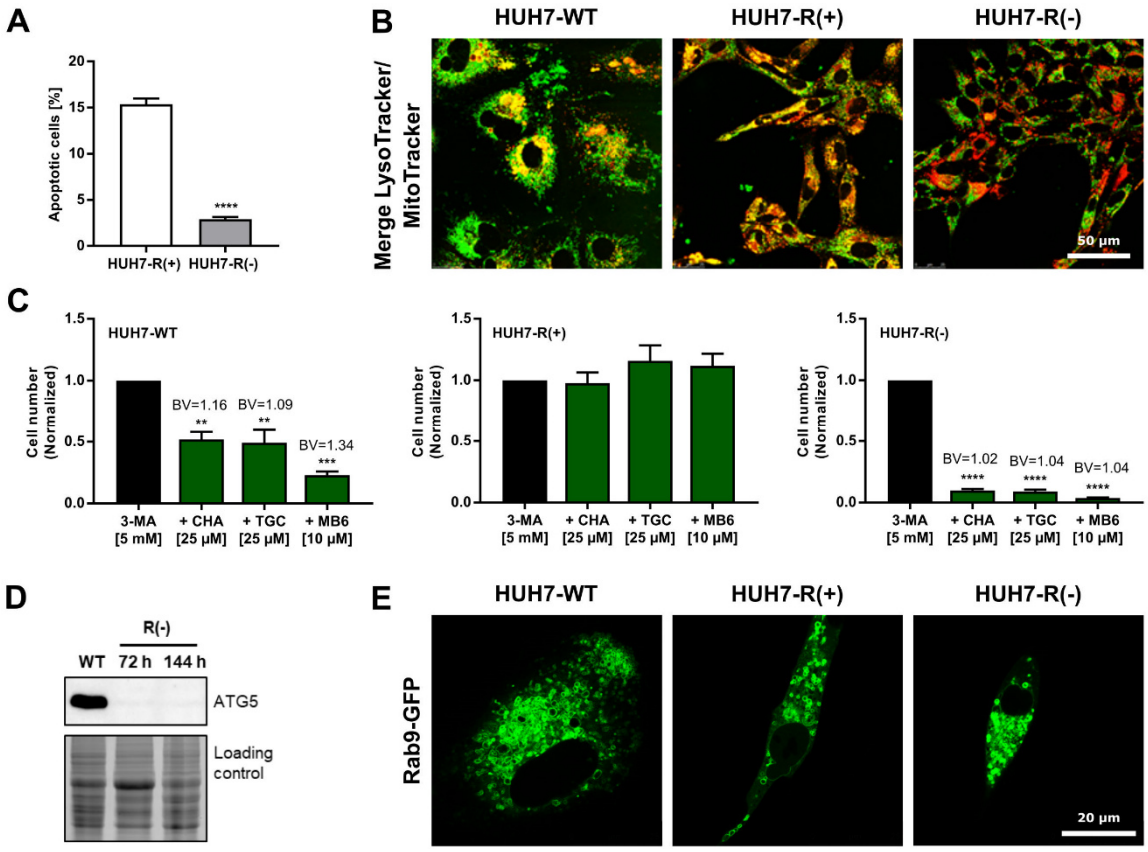

Figure 19.* Growth resumption: Proapoptotic vs. prosurvival autophagy. (A)** Increased autophagy was accompanied by decreased apoptosis. Flow cytometric quantification of apoptosis of HUH7-R(+) vs. HUH7-R(-) cells is shown (t-test). **(B)** Colocalization (yellow) of mitochondria and lysosomes indicates mitophagy in HUH7-R(+) cells. Merged images of LysoTracker (red) and MitoTracker (green) live cell imaging are shown (see also *Figure S8 A*). Scale bar indicates 50 µm. **(C)** Combined inhibition of mitochondrial biogenesis and autophagy results in additive growth inhibition. Cells were stimulated with 3-MA alone (control) or in combination with tigecycline (TGC), chloramphenicol (CHA) or MitoBlock-6 (MB6) for 72 h upon rebound growth (the use of TGC, CHA and MB6 is specified in *chapter 4.5* and *chapter 6.1.3.1*). The cell number was assessed by crystal violet staining and normalized to the 3-MA-treated control (for calculation of the Bliss value (BV) see *Figure S8 B*) (ANOVA). **(D)** ATG5 protein level of HUH7-R(-) cells was not regained after sorafenib withdrawal. Protein expression was assessed upon 72 h and 144 h of rebound growth (see also *Figure 17 E*). **(E)** Rab9 localization remained unchanged upon growth resumption. Cells were transiently transfected with Rab9-GFP expressing plasmid (*Figure S8 C)* and living cells are shown. Scale bar indicates 20 µm. Values shown as ± SEM, n=3, **p<0.01, ***p<0.001, ****p<0.0001. See also ***Figure S8.

4.4 Mitochondria are newly biosynthesized upon rebound growth

4.4.1 PGC-1α-dependent mitochondrial biogenesis in sorafenib-resistant cells

Mitochondrial quality control pathways not only eliminate damaged mitochondrial proteins, mitochondrial patches or the entire organelle by mitophagy but also renew components by adding proteins and lipids through biogenesis, collectively resulting in mitochondrial turnover (Pickles et al., 2018). Considering that a re-establishment of the respiratory functionality *(Figure 15 C-D)* and an initial increase in mitochondrial mass (*Figure 18 C)* were observed upon rebound growth, we hypothesized that mitochondrial biogenesis occurs in an early phase after sorafenib withdrawal. ER-stress was shown to increase intracellular Ca^{2+}-levels *(Figure 20 A)*, which despite damaging mitochondria, induced protein expression of the key-regulator of mitochondrial biogenesis, peroxisome proliferator activated receptor gamma coactivator-1 alpha (PGC-1α) *(Figure 20 B)*.

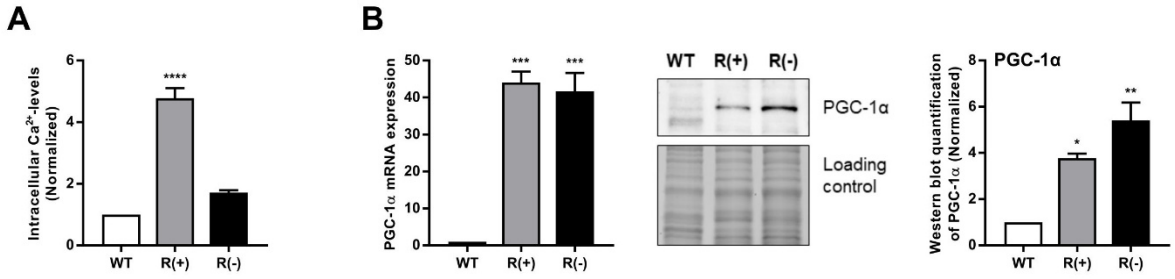

Figure 20. **Mitochondrial damage correlates with elevated PGC-1α protein expression. (A)** Free intracellular Ca^{2+} strongly increased in HUH7-R(+) cells. Flow cytometric quantification of intracellular Ca^{2+} with normalization to the cellular volume *(Figure S6)* and to HUH7-WT. **(B)** Induction of transcription and protein expression of PGC-1α in HUH7-R cells. mRNA (left) and protein expression (right) of PGC-1α were normalized to HUH7-WT. Values denoted as ± SEM, n=3, *p<0.05, **p<0.01, ****p<0.0001 (ANOVA).

PGC-1α is a transcriptional coregulator, which is posttranslationally modified by cellular metabolic sensors and thereby regulates homeostasis during bioenergetic crises by integrating mitochondrial and fatty acid biogenesis, oxidative phosphorylation and adaptive thermogenesis (LeBleu et al., 2014). In fact, PGC-1α is activated through phosphorylation by the mediator of cellular energy depletion, AMP-activated protein kinase (AMPK), and by p38 MAPK-signaling *(Figure 21 A)*. Secondary to activation, PGC-1α was found to translocate to the nucleus in HUH7-R cells for becoming transcriptionally active *(Figure 21 B-C)*. Elevated PGC-1α mRNA levels were also found in an ectopic murine xenograft *in vivo,* with significantly higher PGC-1α mRNA expression in sorafenib-resistant HUH7-R(-) tumors of mice, which were not treated with sorafenib *(Figure 21 D)*.

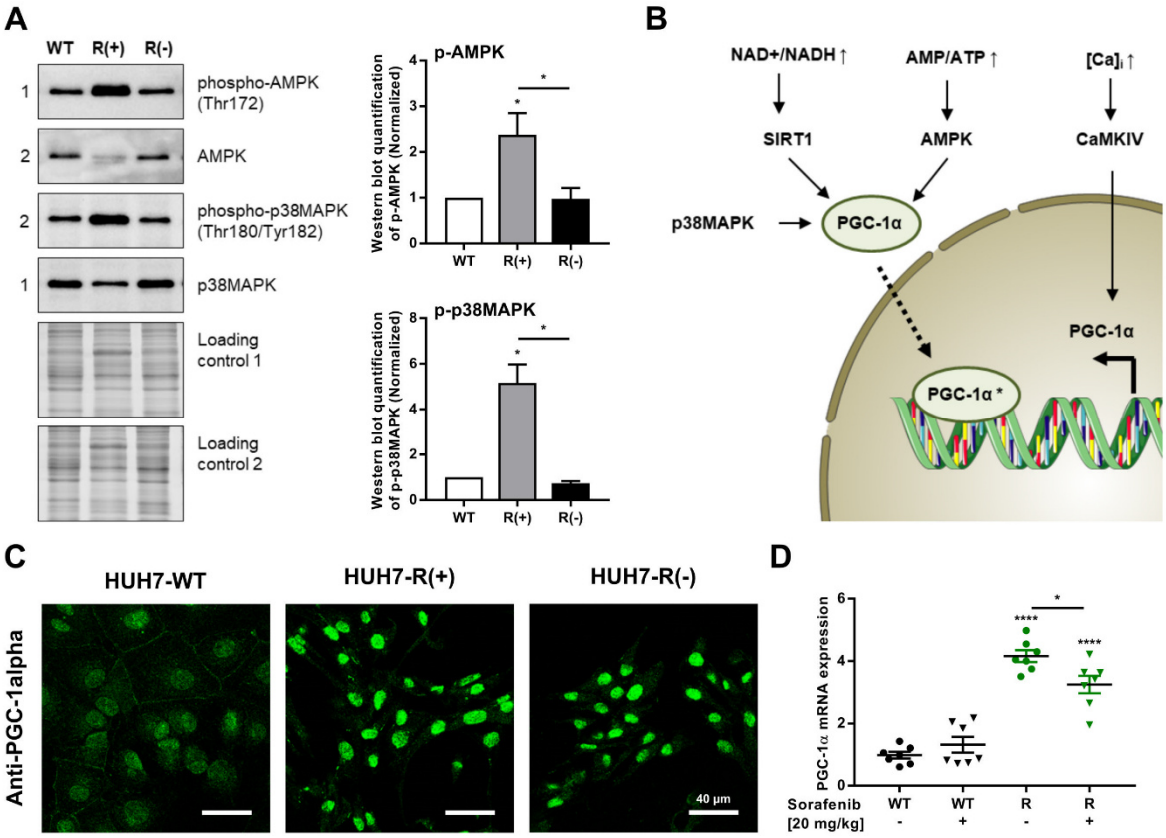

***Figure 21*. Mitochondrial biogenesis occurs in a PGC-1α-dependent manner. (A)** Phosphorylation of the metabolic sensors AMPK and p38 MAPK, required for the activation of PGC-1α and subsequent nuclear translocation. Immunoblots were normalized to the respective protein load and to HUH7-WT. **(B)** Schematic illustration of the PGC-1α activation cascade for induction of mitochondrial biogenesis in response to altered metabolic requirements and elevated cytosolic Ca^{2+}-levels. **(C)** PGC-1α is activated in sorafenib-resistant cells and translocated to the nucleus, as revealed by immunostaining. Scale bars indicate 40 µm. **(D)** In contrast to their parental HUH7-WT cell line, PGC-1α mRNA-expression of HUH7-R is modified by sorafenib treatment *in vivo*. PGC-1α mRNA-levels in resected tumors of the previously presented ectopic mouse xenograft *(Figure 7)* are normalized to the mean of HUH7-WT expression. Values denoted as ± SEM, n=3, *p<0.05, ****p<0.0001 (ANOVA).

4.4.2 Recovery of mitochondrial integrity upon rebound growth with adaptions of the HUH7-R(+) lipidome towards increased cardiolipin biosynthesis

As we demonstrated the simultaneous occurrence of mitochondrial degradation and biogenesis pathways upon rebound growth, we suggested an overall renewal of the mitochondrial integrity and morphology. Indeed, TEM of sorafenib-resistant cells revealed severe mitochondrial damage in HUH7-R(+) cells when compared to HUH7-WT cells and complete mitochondrial recovery within 72 h of growth resumption. In these newly biosynthesized mitochondria, prominent cristae suggested high respiratory activity *(Figure 22 A)*. Mitochondrial biogenesis was also supported by a LC-MS/MS-based lipidomics analysis comparing HUH7-R(+) to HUH7-WT cells. On the one hand, lipidomics analysis confirmed the strongly reduced fatty acid (FA) metabolism as previously observed by proteomics screening *(Figure 10 B)*. The reduction of FA synthesis was indicated by a drastic decline of activated Acyl-CoA-species (ACAs) to 4.6% of the total ACA-level in HUH7-WT cells, whereas the relative amount of free fatty acids (FFA) remained unchanged *(Figure 22 B; Figure S9 A)*. ACAs are intermediates and products of the mitochondrial β-oxidation and essential for FA synthesis (Schulz, 1991). Thus, when the FA synthesis is decreased, a reduced abundance of various phospholipid subspecies is the consequence *(Figure 22 C)*. However, on the other hand, levels of the phospholipid phosphatidylglycerol (PG) were significantly higher in HUH7-R(+) cells compared to HUH7-WT *(Figure 22 C)*. PG is the precursor metabolite of cardiolipin, which is exclusively integrated into the IMM. In the IMM, cardiolipin acts as an essential constituent for cristae formation and contributes to energy conversion via respiration. Thus, cardiolipin represents a hallmark lipid of mitochondrial biogenesis (Dudek, 2017). Moreover, we found that sustained sorafenib exposure led to adaptions in lipid saturation and FA chain lengths. A significant increase in long chain FAs was observed for phosphatidylcholine (PC) and phosphatidylserine (PS), which are the main components of the cellular membrane *(Figure S9 B)*. Importantly, intracellular ROS is known to attack polyunsaturated fatty acids (PUFAs), thereby initiating lipid peroxidation (Esterbauer et al., 1991). This results in the formation of aldehyde byproducts that diffuse from their site of origin and amplify the effects of oxidative stress (Browning and Horton, 2004). Interestingly, in a presumably protective mechanism, the abundance of PUFAs was reduced in HUH7-R(+) cells *(Figure S9 C)*, whereas the activity of ROS neutralizing peroxisomes was upregulated, which is indicated by a massive increase of ether-phospholipids *(Figure S9 D-E)* (da Silva et al., 2012).

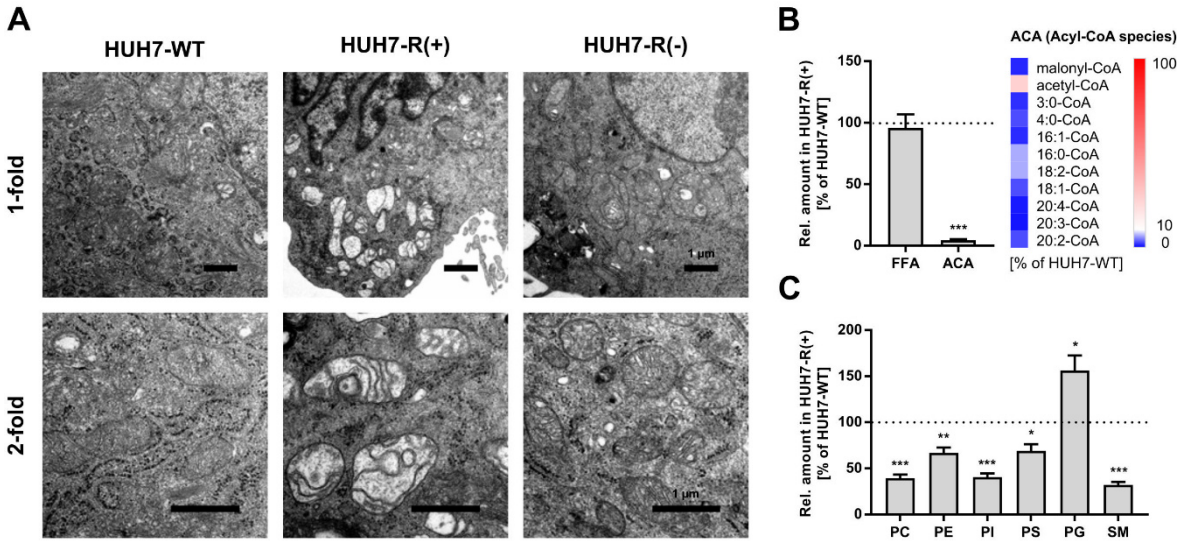

Figure 22. **Mitochondrial renewal upon rebound growth by induction of mitochondrial biosynthesis. (A)** Damage of mitochondrial integrity in HUH7-R(+) and regeneration after sorafenib withdrawal. TEM was performed for mitochondria of the HUH7 rebound cell model. Scale bars indicate 1 µm. **(B)** Breakdown of fatty acid (FA) synthesis in HUH7-R(+) cells compared to HUH7-WT. MS-based lipidomics of HUH7-WT and HUH7-R(+) cells is shown. The absolute amount of free fatty acids (FFA) and acyl-Co A species (ACA) of HUH7-R(+) cells was normalized to HUH7-WT. The heatmap of ACA subspecies is color-coded according to the relative abundance in HUH7-R(+) cells compared to HUH7-WT from blue (0%) to white (10%) to red (100%) (t-test). **(C)** The cardiolipin precursor PG was significantly increased in HUH7-R(+) cells. Lipidomics analysis of HUH7-WT and HUH7-R(+) cells with the normalized abundance of phosphatidylcholine (PC), phosphatidylethanolamine (PE), phosphatidylinositol (PI), phosphatidylserine (PS), phosphaditylglycerol (PG) and sphingomyeline (SM) to HUH7-WT is shown (ANOVA). Values denoted as ± SEM, n=3 for A, n=5 for B and C, *p<0.05, **p<0.01, ***p<0.001. See also ***Figure S9***.

Summarizing, sustained sorafenib exposure has been shown to impair mitochondrial integrity and functionality, as well as the abundance of ETC subunits required to fuel tumor growth resumption. Given that the mitochondrial renewal upon rebound growth is essentially driven by the induction of mitochondrial biogenesis, targeted inhibition of the regeneration of the mitochondrial ETS aroused as a potential target for second-line therapeutic strategies after sorafenib therapy termination.

4.5 Translation-inhibiting antibiotics impair rebound growth *in vitro*

According to the endosymbiont hypothesis, mitochondria descend from α-protobacteria that were enveloped by pre-eukaryotic cells, providing an additional energy source and thereby conferring a competitive advantage (Sagan, 1967). Notably, mitochondrial ETC subunits are partially encoded by both the nuclear (nucDNA) and the prokaryotic-derived mtDNA (Taanman, 1999). With regard to its clinical potential, we hypothesized that suppressing biogenesis of mtDNA-encoded subunits by bacterial translation inhibiting antibiotics would block the metabolic switch and consequently the growth resumption of HUH7-R cells when released from sustained sorafenib treatment.

Therefore, we tested the antiproliferative potential of inhibitors of mitochondrial biogenesis in HUH7-R cells. In addition to the S50-ribosomal subunit binding compounds chloramphenicol (CHA) and linezolid *(Figure 23 A)*, the effectiveness of translation-inhibiting antibiotics was assessed with the S30-subunit binder tigecycline (TGC) *(Figure 23 B-C)*. Further, we tested the experimental compound MitoBlock-6 (MB6), which inhibits the endogenous retroviral sequence 1 (Erv1)-activity. MB6 blocks the intermembrane space import and assembly protein 40 (Mia40)/ Erv1 redox-mediated import pathway, which translocates proteins for translation across the OMM (Dabir et al., 2013) *(Figure 23 D)*. All tested compounds revealed the strongest inhibition of proliferation in HUH7-R(-) cells, whereas HUH7-R(+) cells were refractory towards therapy as previously shown *(Figure 8 C)*.

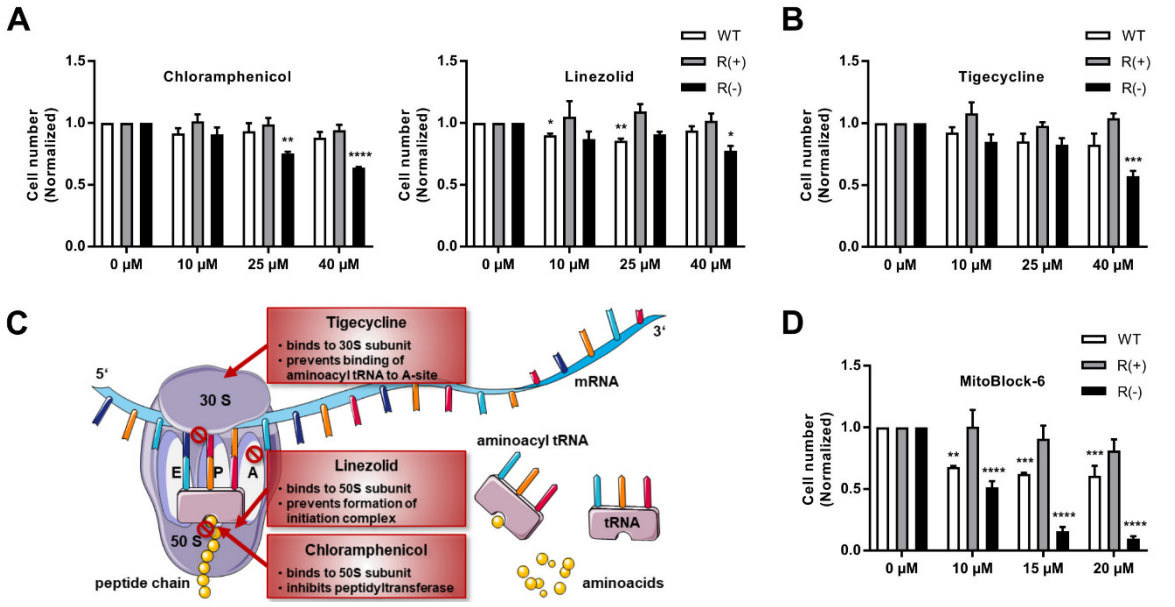

Figure 23. **Inhibitors of mitochondrial biogenesis have highest effectiveness in HUH7-R(-) cells.** Inhibition of proliferation is shown for **(A)** the ribosomal S50-subunit binding antibiotics chloramphenicol (CHA) and linezolid, **(B)** the ribosomal S50-subunit binding antibiotic tigecycline (TGC). **(C)** Illustrated mode of action of the antibiotic compounds tested in *Figure 23 A-B*. **(D)** Proliferation of HUH7-R(-) cells was also inhibited by the OMM import inhibitor MitoBlock-6 (MB6). Proliferation rates within 72 h of treatment for HUH7-WT (white), HUH7-R(+) (grey) and HUH7-R(-) (black), normalized to the respective untreated control are shown for A, B and D. Values denoted as ± SEM, n=3, *p<0.05, **p<0.01, ***p<0.001, ****p<0.0001 (ANOVA).

4.5.1 TGC prevents the biogenesis of mtDNA-encoded ETC subunits and inhibits growth resumption by reducing aerobic glycolysis

As TGC is a well-tolerated, approved by the Food and Drug Administration (FDA) and has been previously shown to possess anticancer potential, this drug was used for subsequent mechanistic studies in HUH7-R and RIL175-R cells (Skrtic et al., 2011). Indeed, TGC impaired the biogenesis of mtDNA-encoded subunits CI-NDUFB6 and CIV-MTCO1, thereby abrogating the recurrence of tumor growth dose-dependently *(Figure 24 A-B)*. At a TGC concentration (25 µM) that significantly impaired cell proliferation but did not induce apoptosis, concomitant reduction in NAD^+-recovery and increased lactate fermentation were observed, whereas cellular ATP-levels remained unaffected *(Figure 24 C)*. Therefore, rebound growth appears to be limited by the reduction of aerobic glycolysis through a diminished NAD^+/NADH ratio rather than by the cell's energetic state.

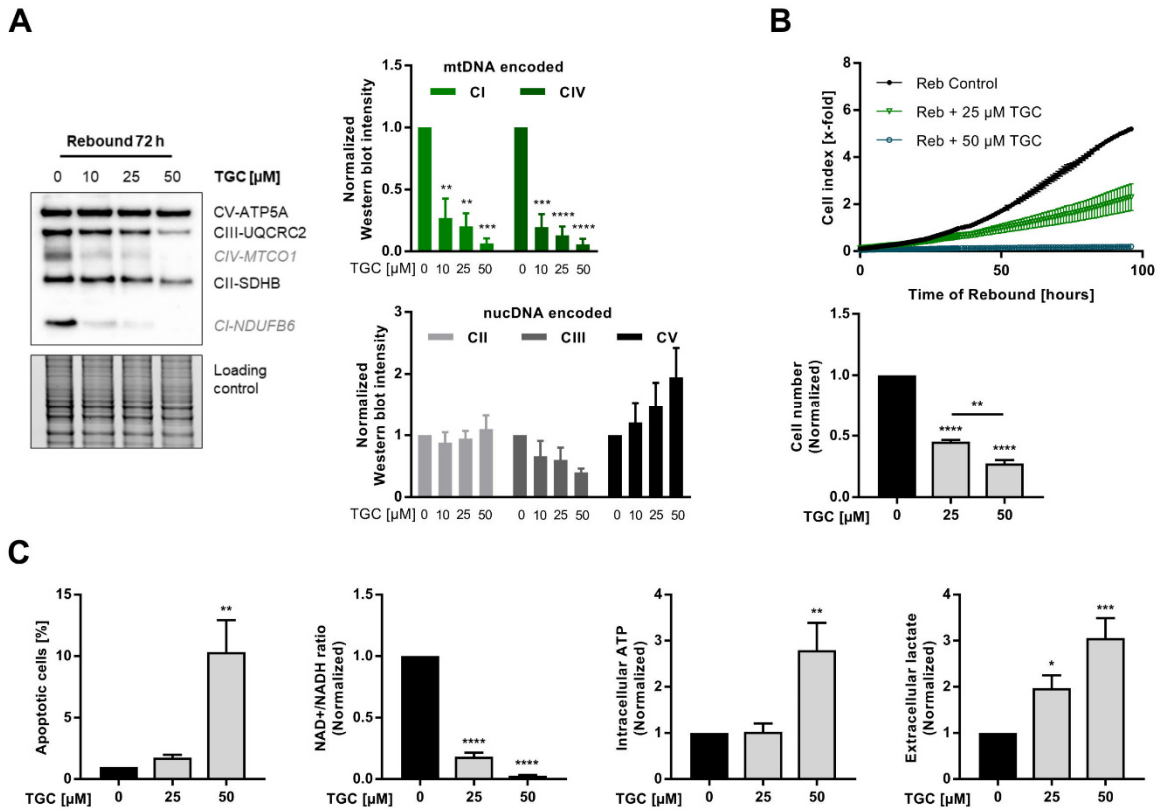

Figure 24. **TGC impairs tumor growth resumption by inhibition of TCA cycle activity. (A)** TGC inhibits the biogenesis of mtDNA-encoded ETC subunits. Immunoblot analysis of HUH7-R cells treated with TGC upon 72 h of sorafenib withdrawal was normalized to the respective protein load and to the untreated control. **(B)** TGC prevents rebound growth of HUH7-R cells second-line to sorafenib. Proliferation rate, assessed by impedance measurement is shown as cell counts (cell index) over time (top). Proliferation inhibition by TGC upon 72 h of treatment and equal treatment conditions as in *Figure 24 C* was determined by crystal violet staining and normalized to the untreated control. **(C)** Inhibition of growth resumption by TGC is caused by an insufficient TCA cycle activity. Assessment of apoptosis (percentage of whole cell count), NAD^+/NADH ratio, intracellular ATP and extracellular lactate levels, normalized to untreated HUH7-R cells is shown. Values denoted as ± SEM, n=3, *p<0.05, **p<0.01, ***p<0.001, ****p<0.0001 (ANOVA).

Both effects, the abrogation of tumor relapse and the increase in anaerobic glycolysis were confirmed by the antibiotic CHA and the mitochondrial import inhibitor MB6 in HUH7-R cells upon rebound growth. However, the mechanism of action, especially for MB6, might deviate from that of TGC *(Figure 25 A-B)*. These findings highlight the role of the TCA cycle activity in mitochondria for providing intermediates as substrates for *de novo* synthesis of lipids and nonessential amino acids required for rebound proliferation after sorafenib withdrawal (DeBerardinis et al., 2008).

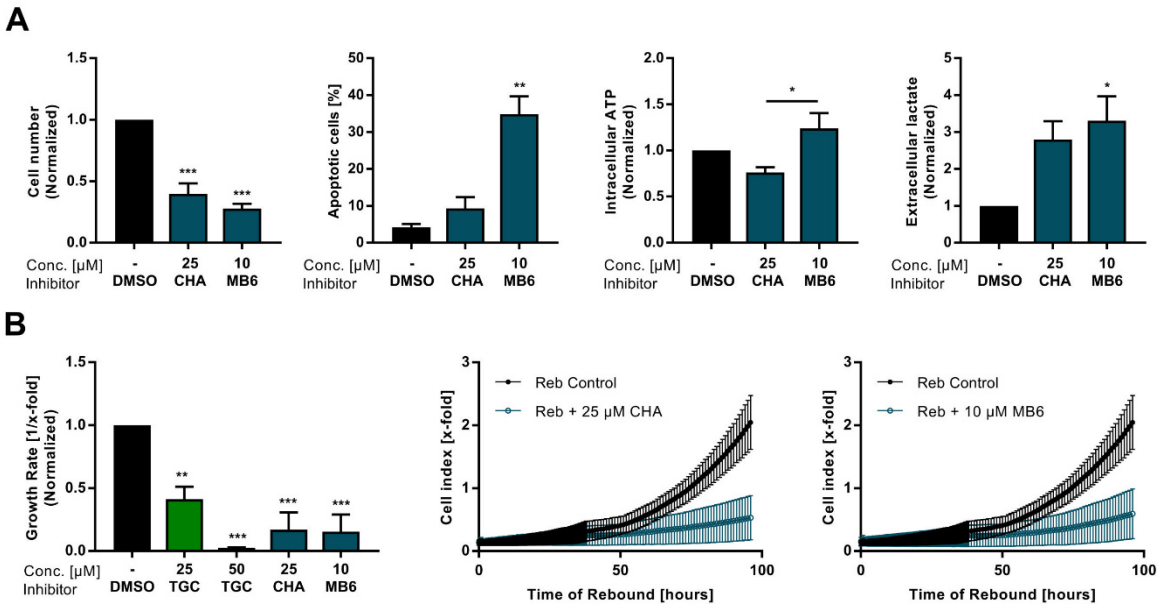

Figure 25. **Rebound growth inhibiting effect of TGC confirmed by CHA and MB6. (A)** CHA and MB6 prevent growth resumption of HUH7-R cells second-line to sorafenib and promote anaerobic glycolysis. Proliferation inhibition, intracellular ATP, extracellular lactate (normalized to untreated control) and apoptosis (percentage of whole cell count) of HUH7-R cells was assessed after treatment with CHA or MB6 upon 72 h of rebound growth. **(B)** Experiments with TGC were performed in a concentration range with comparable efficiency to CHA and MB6. Growth rates of HUH7-R cells treated with TGC, CHA or MB6 upon rebound growth were calculated from the cell counts over 72 h. Growth rates of impedance measurements were normalized to the untreated control. For proliferation curves over time of TGC treatment see *Figure **24** B*. Values shown as ± SEM, n=3, *p<0.05, **p<0.01, ***p<0.001 (ANOVA).

4.5.2 TGC impairs rebound growth by establishing auxotrophy for electron acceptors

To scrutinize the limiting precursors required for the growth resumption of HUH7-R cells, we performed rescue experiments with various TCA cycle intermediates and precursor metabolites of related anabolic pathways. Surprisingly, among the metabolites tested, only pyruvate (PYR), α-ketoglutarate (AKG) and oxaloacetate (OAA) sufficiently restored rebound proliferation by reversing NAD^+-depletion, whereas no rebound growth rescue was observed with Acetyl-CoA (ACoA), malate (MAL), citrate (CIT), cysteine (CYS) and aspartate (ASP) *(Figure 26)*. We hypothesized a structural causality of successful growth rescue, as the alpha-ketoacids PYR, AKG and OAA are substrates of NAD^+-regenerating dehydrogenases *(Figure 27 A)*.

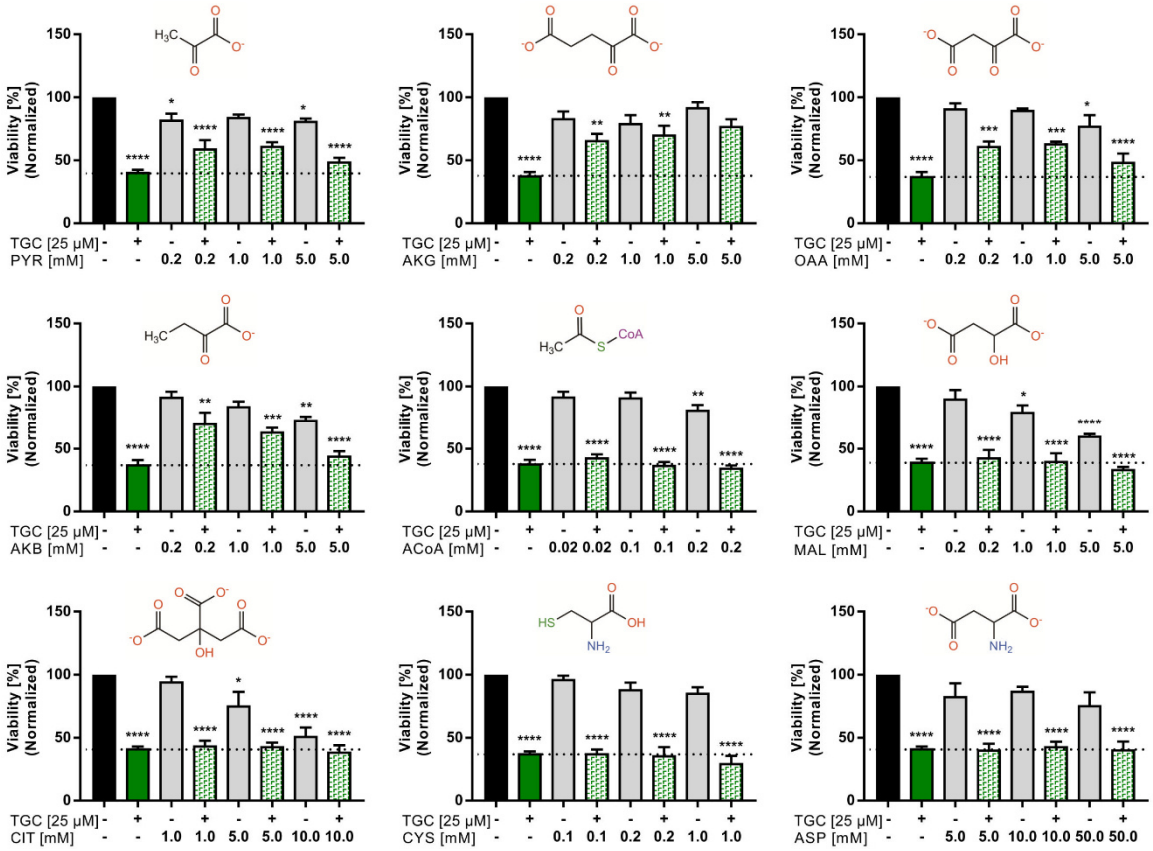

Figure 26. **TGC prevents rebound growth by limiting NAD$^+$-recovery.** Rebound growth rescue upon TGC treatment was only obtained for alpha-ketoacids. HUH7-R cells upon 72 h of rebound growth were left untreated, treated with TGC, treated with PYR, AKG, OAA, α ketobutyrate (AKB), ACH, MAL, CIT, CYS, ASP or a combination of TGC and the respective metabolite. The viability was normalized to the respective untreated control. Values shown as ± SEM, n=3, *p<0.05, **p<0.01, ***p<0.001, ****p<0.0001 (ANOVA).

To uncouple the role of TCA cycle intermediates as NAD$^+$-regenerating electron acceptors from their role as carbon sources for cellular biogenesis, we supplemented TGC-treated HUH7-R cells after sorafenib withdrawal with the four-carbon metabolite α-ketobutyrate (AKB), which is not part of the TCA cycle. As shown previously, AKB acts as a substrate of dehydrogenases and oxidizes NADH to NAD$^+$, while supplying cells neither carbon nor ATP (King and Attardi, 1989; Sullivan et al., 2015). Indeed, AKB successfully restored rebound proliferation of HUH7-R cells to a similar extent as the electron accepting TCA cycle intermediates PYR, AKG and OAA *(Figure 27 B-C)*. Altogether, this data suggest that inhibited biogenesis of mtDNA-encoded respiratory chain subunits upon TGC treatment leads to an impaired NAD$^+$-recovery by the NDUF, further diminishing aerobic glycolysis in HUH7-R cells upon sorafenib withdrawal. Although a partial recovery of NAD$^+$ by cytosolic lactate fermentation is possible, cells suffer reductive stress. Thus, mitochondrial NAD$^+$ depletion renders the exogenous electron acceptor supply a limiting requirement for restoring growth resumption, which cannot be met by TCA cycle intermediates that only donate carbon.

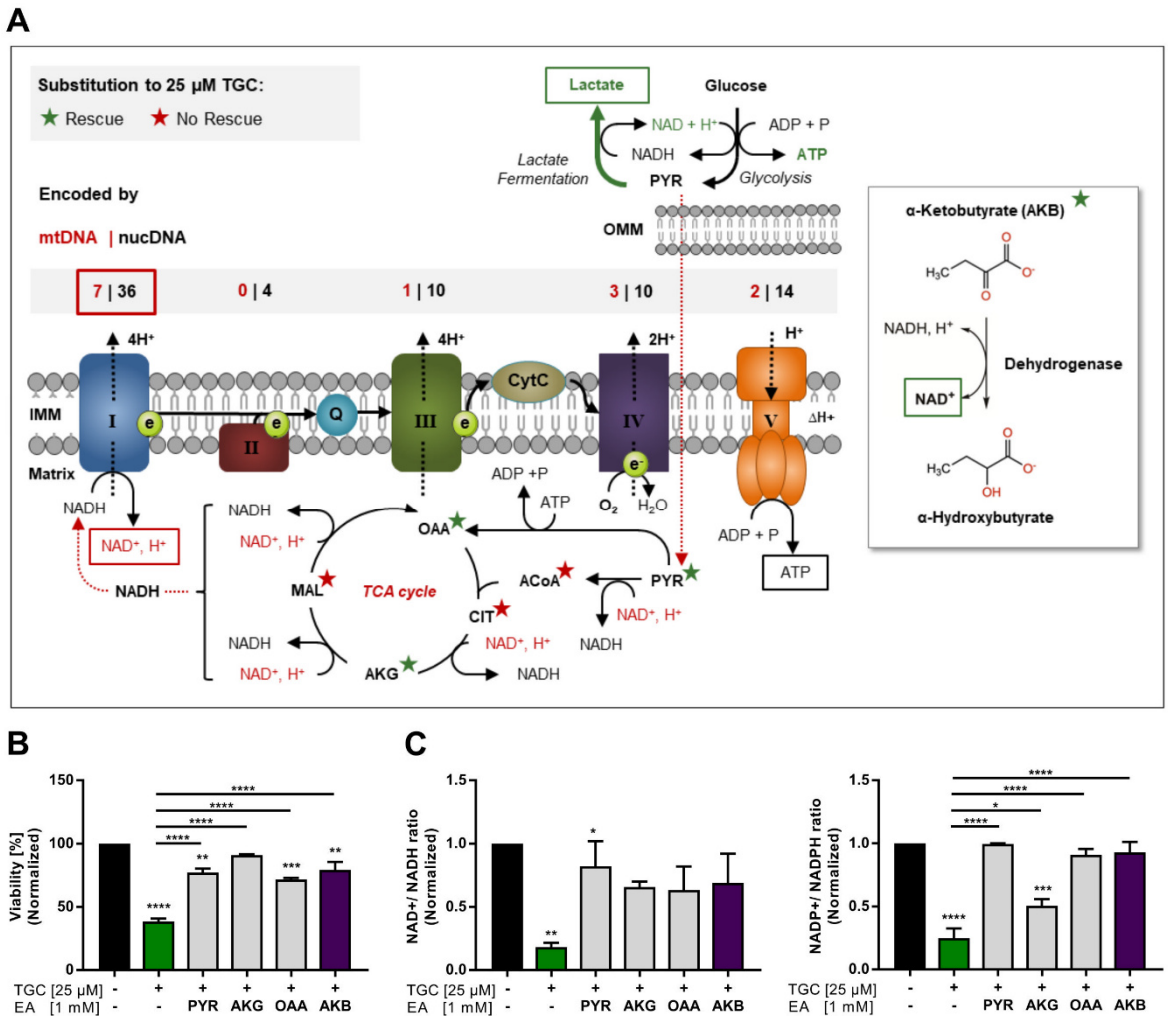

Figure 27. **AKB rescues rebound growth proliferation by restoring NAD$^+$-levels. (A)** Illustration of the impact of TGC on NAD$^+$-turnover and TCA cycle activity. The ETC is constantly powered by NADH-turnover of the TCA cycle. A decreased biogenesis of mtDNA-encoded complex I subunits by TGC impairs NADH-oxidation, leading to decreased TCA cycle activity and extracellular lactate fermentation. Substitution with extracellular electron acceptors (EAs) restores intracellular NAD$^+$-levels and rescues rebound growth, as EAs are substrates of intracellular dehydrogenases. **(B)** Exogenous substitution with NAD$^+$-regenerating EAs rescues rebound growth. Determination of viability of HUH7-R cells untreated, treated with TGC only or TGC in combination with PYR, AKG, OAA or AKB by subtraction of the metabolite specific toxicity when applied as single-treatment (*Figure 26)*. The viability was normalized to the untreated control. **(C)** The cellular reductive stress upon TGC treatment is displayed by the NAD$^+$/NADH ratio (left) and the NADP$^+$/NADPH ratio (right). Both ratios were assessed in HUH7-R cells after sorafenib withdrawal and normalized to the untreated control. Values shown as ± SEM, n=3, **p<0.01, ***p<0.001, ****p<0.0001 (ANOVA).

In order to substantiate the rebound growth inhibiting effect of TGC second-line to sorafenib, which was so far restricted to the HUH7-R cell model, key-experiments were additionally performed with sorafenib-resistant RIL175-R cells. RIL175-R cells obtained resistance to 10 µM sorafenib in the growth medium *(Figure 6)* and revealed a resumption of proliferation upon sorafenib withdrawal comparable to HUH7-R cells *(Figure S10)*. Importantly, the effect of TGC and the rebound growth rescue by AKB were confirmed by this alternative HCC rebound growth cell model *(Figure 28)*.

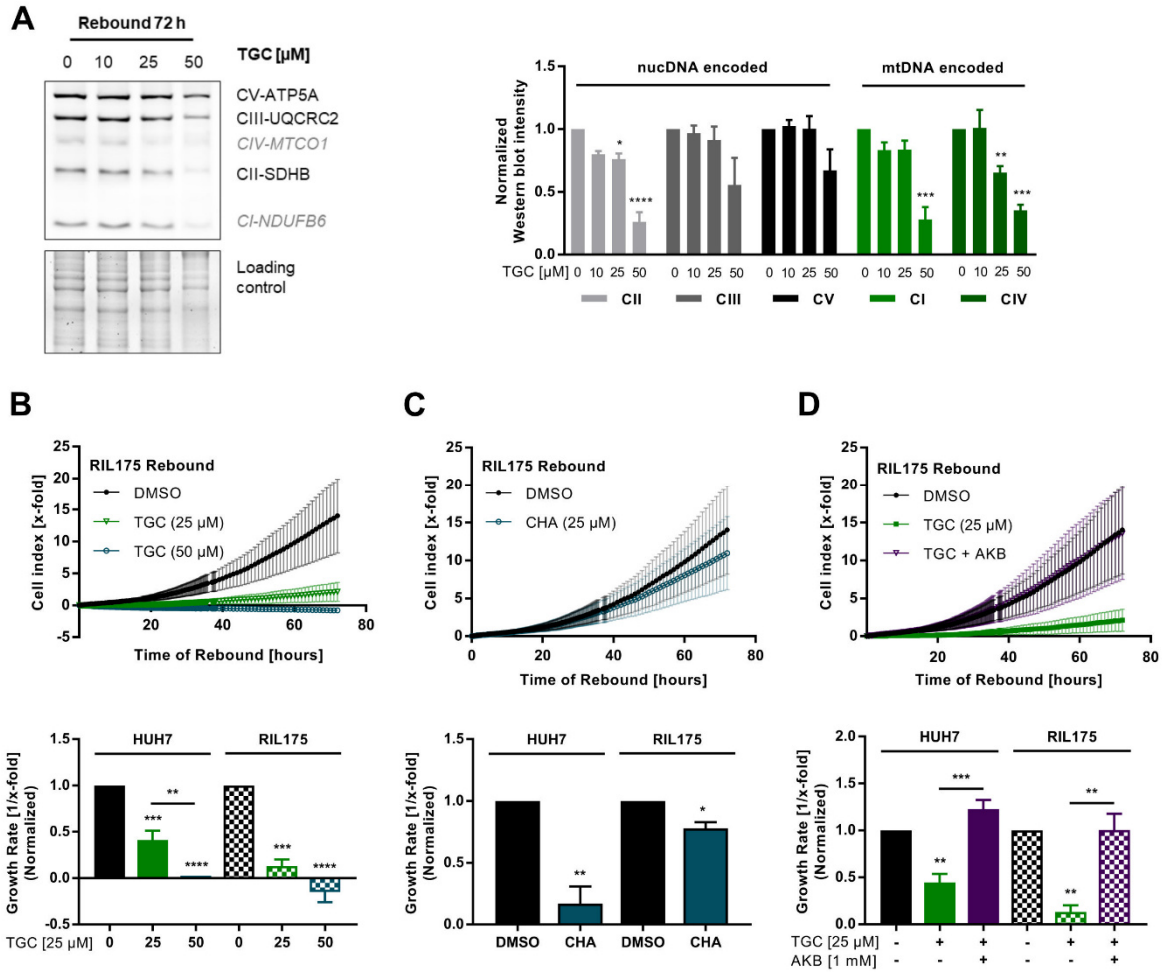

Figure 28. **RIL175 cells confirm the inhibition of rebound growth by TGC through electron acceptor depletion. (A)** TGC inhibits the biogenesis of mtDNA-encoded ETC subunits in RIL175-R cells. Immunoblot analysis of RIL175-R cells treated with TGC upon 72 h of sorafenib withdrawal was normalized to the respective protein load and to the untreated control. **(B)** TGC highly efficiently prevents rebound growth of RIL175-R cells second-line to sorafenib. For proliferation curves over time of TGC treatment see *Figure **24** B*. **(C)** HUH7-R cells are more susceptible to the inhibition of rebound growth by CHA then RIL175-R cells. For proliferation curves over time of CHA (25 µM) treatment see *Figure 25 B*. **(D)** AKB rescues rebound growth upon TGC treatment in RIL175-R cells. For proliferation curves over time of TGC and AKB treatment see *Figure S10.* For (B), (C) and (D) proliferation rates, which were assessed by impedance measurement are shown as cell counts (cell index) over time (top). Growth rates of HUH7-R and RIL175-R treated upon rebound growth were calculated from the cell counts over 72 h and normalized to the untreated control (bottom). Values shown as ± SEM, n=3, *p<0.05, **p<0.01, ***p<0.001, ****p<0.0001 (ANOVA). See also ***Figure S10***.

Summarizing, we could demonstrate that translation-inhibiting antibiotics, such as TGC, efficiently prevent growth resumption of HUH7-R and RIL175-R cells after sorafenib withdrawal *in vitro*. Importantly, approved antibiotic compounds are generally characterized by favorable safety profiles with low incidence of adverse side-effects and good experience on dosing schedules. Thus, inhibiting the biogenesis of mitochondrial respiratory chain subunits by the antibiotic TGC may constitute a promising second-line therapeutic approach for advanced-stage HCC patients after sorafenib failure.

4.6 TGC promotes sustained mitochondrial damage

Next, we aimed to investigate in detail how the diminished NAD^+/NADH recovery under TGC treatment affects oxidative processes and prevents HUH7-R cells from undergoing rebound growth. It is known that despite the presence of glucose, glutamine is one of the most consumed nutrients to fuel oxidative TCA cycle activity. Thus, glutamine essentially contributes to cellular energy generation and biosynthesis, thereby driving tumor growth (Fan et al., 2013; Zielke et al., 1984).

4.6.1 TGC abrogates tumor relapse-fueling oxidative glutamine metabolism

To analyze the contributions of glucose and glutamine to tumor relapse after sorafenib withdrawal, we transiently silenced oxoglutarate dehydrogenase (OGDH) downstream of glutamine-derived AKG in the oxidative pathway, respectively isocitrate dehydrogenases (IDH2) downstream of glucose, but upstream of glutamine oxidation, with an efficiency of 81.2% and 90.5% *(Figure 29)*.

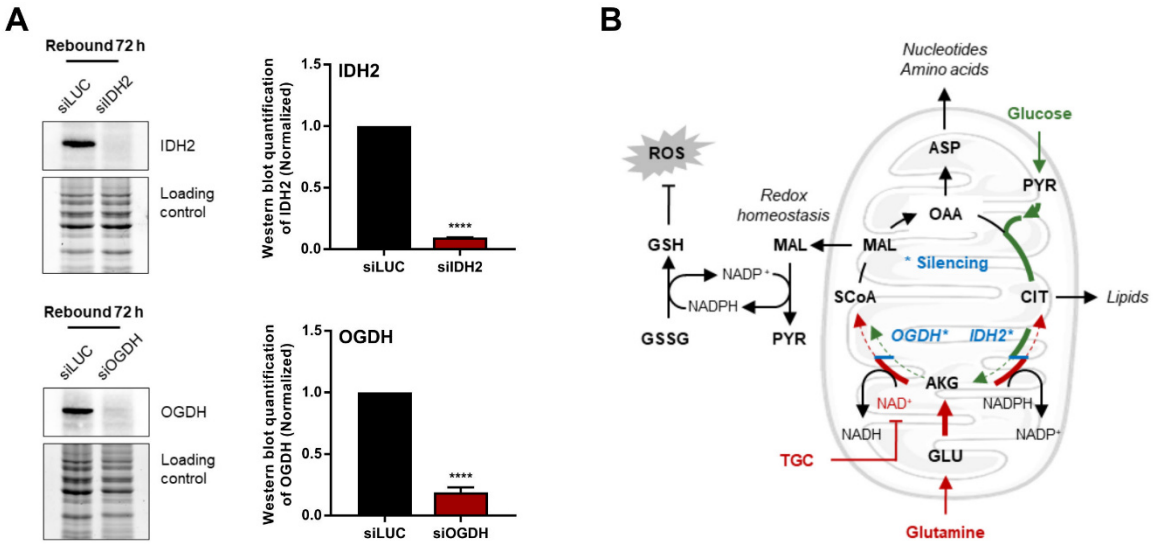

Figure 29. **The role of glutamine oxidation in tumor relapse and the maintenance of cellular superoxide defense. (A)** Transient gene silencing of the TCA cycle enzymes isocitrate dehydrogenases (IDH2) and oxoglutarate dehydrogenase (OGDH) upon rebound growth of HUH7-R cells. Immunoblot analysis of IDH2 upstream and OGDH downstream of oxidative glutamine metabolism of the TCA cycle were normalized to the respective protein load and to the siLUC-transfected control. **(B)** Schematic illustration of the impact of IDH2- and OGDH silencing on the glucose and glutamine metabolism as well as the redox-mediated ROS production. Values denoted as ± SEM, n=3, ****p<0.0001 (t-test).

Interestingly, suppression of OGDH expression impaired rebound growth and diminished the NAD^+/NADH ratio upon sorafenib withdrawal comparable to 25 µM TGC. In contrast, both rebound growth and the NAD^+ ratio remained unaffected by IDH2 silencing *(Figure 30 A-B)*. In addition, OGDH protein levels, which were not directly regulated by TGC treatment *(Figure 30 C),* were significantly increased in HUH7-R(-) cells, whereas IDH2-abundance was reduced upon sorafenib

withdrawal *(Figure 30 D)*. Thus, both the dependency of proliferation on OGDH activity and the increased OGDH protein abundance support an essential role of glutamine oxidation as a driving force for rebound growth. In turn, the ETS is substantially powered by NADH, which is provided by the glutamine-fueled oxidative TCA cycle (Fan et al., 2013). Therefore, NDUF activity is not only impaired by TGC but also by impairment of the TCA cycle through transient OGDH silencing.

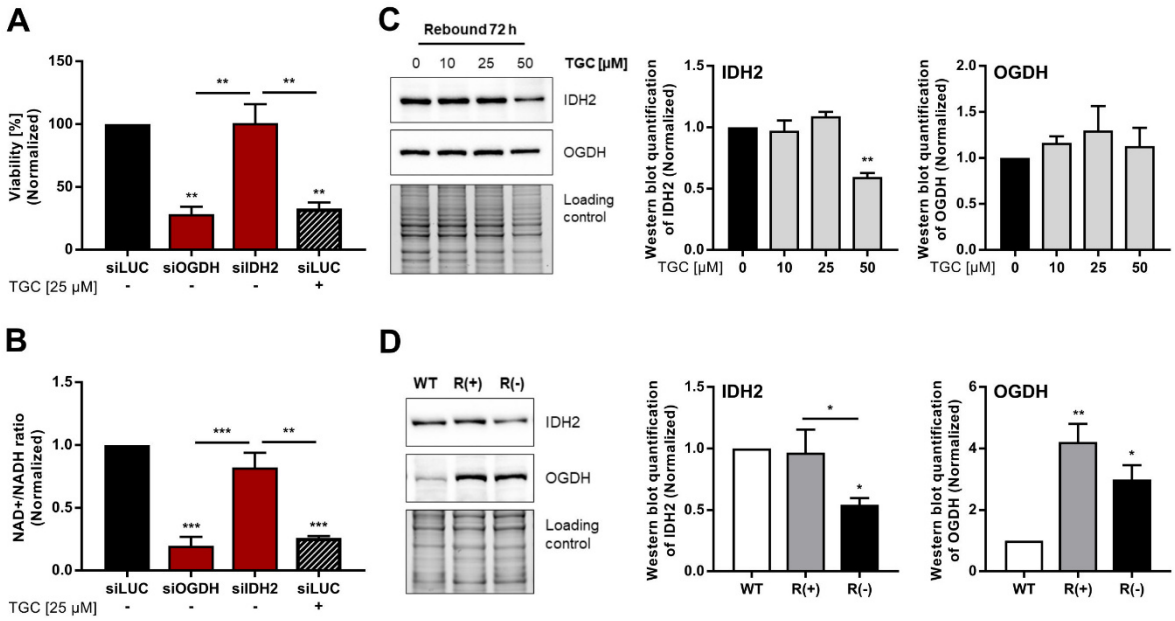

Figure 30. **OGDH silencing impairs viability and NAD$^+$ recovery upon rebound growth comparable to 25 µM TGC. (A)** Inhibited glutamine oxidation by OGDH silencing prevents tumor relapse whereas IDH2 silencing *per se* has no effect on viability. Viability of HUH7-R cells was determined upon 72 h of rebound growth. Cells were transfected with siLUC, siOGDH, siIDH2 and left either untreated or treated with TGC. **(B)** OGDH silencing reduces NAD$^+$ recovery by the NDUF. The NAD$^+$/NADH ratio was assessed upon 72 h of rebound growth in HUH7-R cells, transfected with siLUC, siOGDH or siIDH2 and left either untreated or treated with TGC. Both viability *(Figure 32 A)* and the NAD$^+$/NADH ratio were normalized to the siLUC-transfected, untreated control. **(C)** TGC has no effect on IDH2 and OGDH protein levels. Immunoblot analysis of IDH2 and OGDH upon tumor relapse, untreated vs. treated with TGC is shown. **(D)** Increased protein expression of OGDH in HUH7-R cells. Immunoblot analysis of IDH2 and OGDH of the sorafenib-resistant HUH7 cell model is shown. Values shown as ± SEM, n=3, *p<0.05, **p<0.01, ***p<0.001 (ANOVA).

4.6.2 Oxidative glutamine metabolism provides intermediates for aspartate biosynthesis

Herein, we demonstrated that abrogation of the oxidative TCA cycle critically impairs the NAD$^+$ turnover by the NDUF, which is required for rebound proliferation of HCC cells. In a bidirectional manner, the NDUF oxidizes NADH to NAD$^+$, thus, providing electron acceptors required to drive oxidative TCA cycle activity in order to generate biosynthetic intermediates for lipids, amino acids, and nucleotides. Among these precursor metabolites, especially aspartate was reported to be limiting for proliferation upon ETC deficiency or complex I inhibition (Birsoy et al., 2015; DeBerardinis et al., 2007; Sullivan et al., 2015). Although we confirmed that TGC hinders aspartate production, we

found that aspartate levels were not equally rescued by exogenous electron acceptors, and that no rebound growth rescue occurred by aspartate supplementation *(Figure 31; Figure 26)*. Thus, aspartate alone was not limiting for growth resumption of HUH7-R cells after sorafenib retraction.

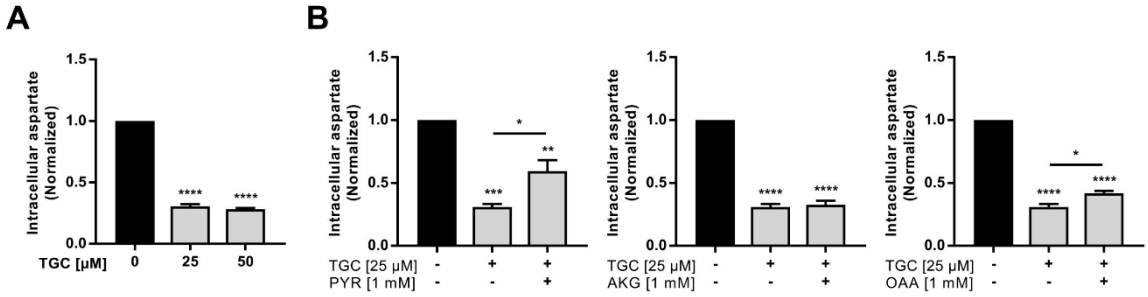

Figure 31. **Aspartate levels are not restored upon rebound growth rescue. (A)** TGC treatment decreases the aspartate abundance. The intracellular aspartate level of HUH7-R cells was assessed upon TGC treatment with subsequent normalization to the untreated control. **(B)** AKG rescues growth resumption *(Figure 27 B)* independent of aspartate levels. Intracellular aspartate was assessed for HUH7-R cells untreated, treated with TGC or a combination of TGC with PYR, AKG or OAA. Aspartate levels were normalized to the untreated control. Values shown as ± SEM, n=3, *p<0.05, **p<0.01, ***p<0.001, ****p<0.0001 (ANOVA).

4.6.3 Translation-inhibiting antibiotics disturb glutamine-dependent redox-balance and promote sustained mitochondrial damage

Although aspartate does not directly limit rebound growth of HUH7-R cells, TCA cycle-derived aspartate or malate is exported to the cytosol, where it is converted to pyruvate to replenish NADPH. We found that the measured $NADP^+$/NADPH ratio remains constant upon OGDH and IDH2 silencing. However, no prediction on the mitochondrial and cytosolic distribution could be made. A diminished cytosolic $NADP^+$/NADPH ratio may be partially covered by a high mitochondrial NADPH abundance. High mitochondrial NADPH levels, in turn, may reflect a low NDUF activity due to the enzymatic hydride transfer from NADH to $NADP^+$ *(Figure 32 A-B; Figure 27 C)* (Altman et al., 2016). While the generation of NADH is dependent on NDUF activity, NADPH is an electron donor for biosynthetic processes that can transfer its reducing potential to glutathione (GSSG) for ROS elimination (Murphy, 2009). In fact, ROS levels were elevated by both OGDH silencing as well as TGC treatment and rescued by the ROS scavenger N-acetyl cysteine (NAC) *(Figure 32 C-D)*. Moreover, impaired maintenance of redox homeostasis by inhibiting the biogenesis of the ETS was confirmed by CHA and MB6 treatment upon growth resumption *(Figure 32 E)*. Thus, defective elimination of ROS by TGC treatment or abrogation of glutamine oxidation via OGDH silencing alters the integrity of mitochondrial cristae *(Figure 32 F)*. This might not only prevent rebound proliferation of tumor cells but may also contribute to a long-term treatment benefit.

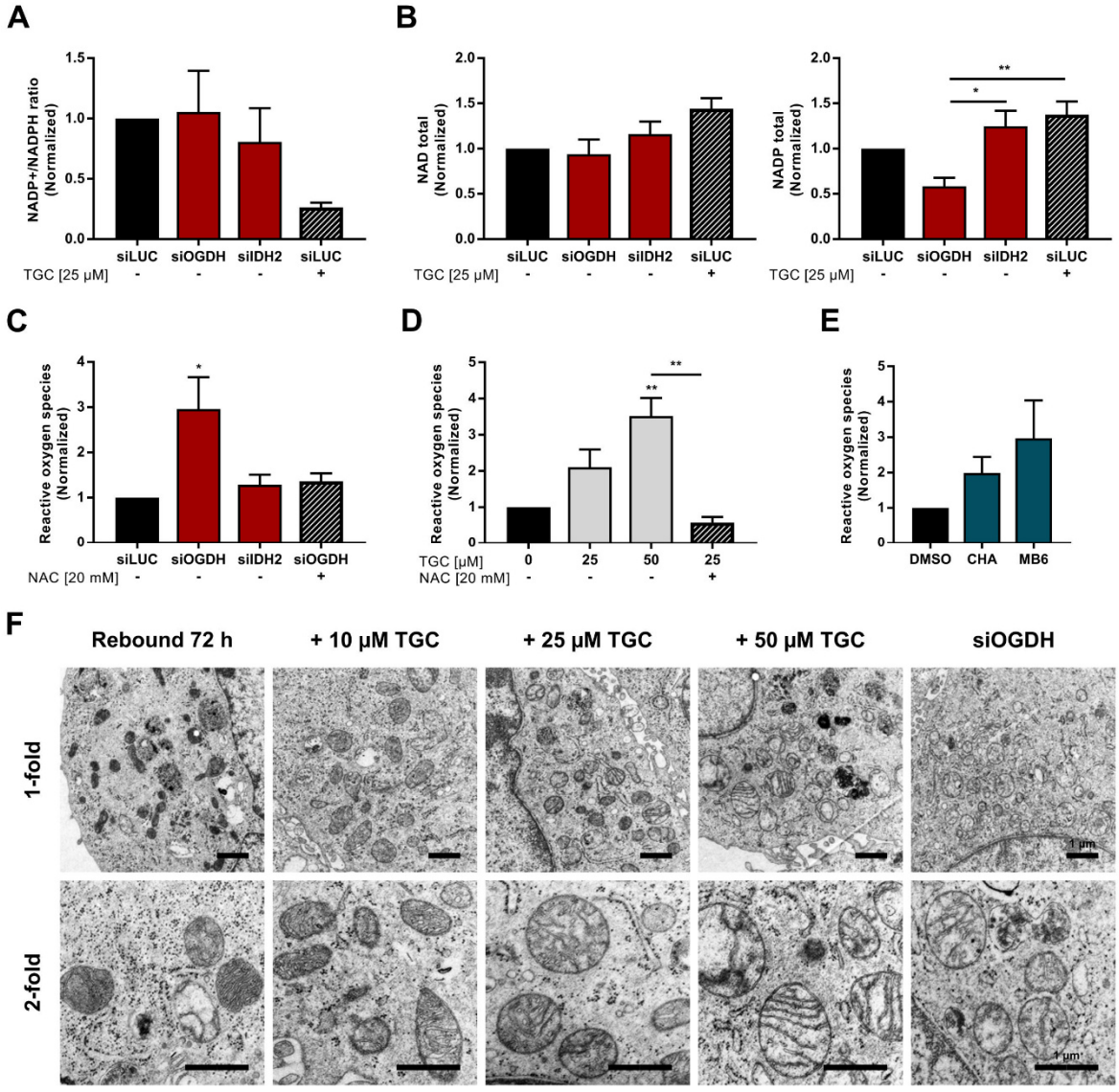

Figure 32. **ROS-induced mitochondrial damage by OGDH silencing and antibiotic treatment upon rebound growth. (A)** The $NADP^+$/NADPH ratio remains constant upon OGDH-silencing. HUH7-R cells upon 72 h of rebound growth were transfected with siLUC (Control), siOGDH or siIDH2 respectively treated with TGC. The $NADP^+$/NADPH ratio was normalized to the siLUC transfected, untreated control. **(B)** Biogenesis of NADP is sensitive to TCA cycle inhibition. Total NAD and NADP levels of *Figure 30 B* and *Figure 32 A* were assessed and normalized to the siLUC transfected, untreated control. **(C)** Abrogation of glutamine oxidation increases ROS production. ROS levels were assessed for HUH7-R cells transfected with siLUC (Control), siOGDH or siIDH2 respectively treated with TGC. The ROS scavenger N-acetyl cysteine (NAC) was used as a negative control and ROS levels were normalized to the untreated, siLUC transfected control. **(D)** Increased ROS production confirmed by TGC treatment, and by **(E)** treatment of HUH7-R cells with CHA and MB6 for 72 h upon rebound growth is shown. NAC was used as a negative control (for *Figure 32 D)* and ROS levels were normalized to the DMSO-treated control. **(F)** TGC treatment and OGDH silencing increases ROS-mediated mitochondrial damage upon rebound growth. TEM images of HUH7-R cells untreated, treated with TGC or transiently transfected with siOGDH upon 72 h of rebound growth are shown. Scale bars indicate 1 µm. Values denoted as ± SEM, n=3, *p<0.05, **p<0.01 (ANOVA).

4.7 TGC impairs resumption of tumor growth as second-line therapy to sorafenib *in vivo*

4.7.1 TGC prevents tumor relapse and NDUF biosynthesis in short-term therapy *in vivo*

The translation-inhibiting antibiotic TGC was previously shown to prevent rebound growth after sorafenib retraction *in vitro* by limiting the electron acceptor turnover, required for proliferation-fueling glutamine oxidation. To assess TGC as a second-line therapy *in vivo*, we established an ectopic tumor mouse xenograft with stably luciferase-expressing HUH7-R-LUC cells, cultured in sorafenib prior to injection. We could confirm that TGC treatment also significantly prevented tumor relapse upon sorafenib withdrawal *in vivo,* with a tumor size as well as growth rate comparable to that of persistently sorafenib treated mice. Both sorafenib and TGC therapy were well-tolerated *(Figure 33)*. The excised tumors were visually smaller in the TGC treated group, with a mean weight of 58.4 mg/tumor compared to 246.7 mg/tumor of the untreated group *(Figure 34 A-B)*.

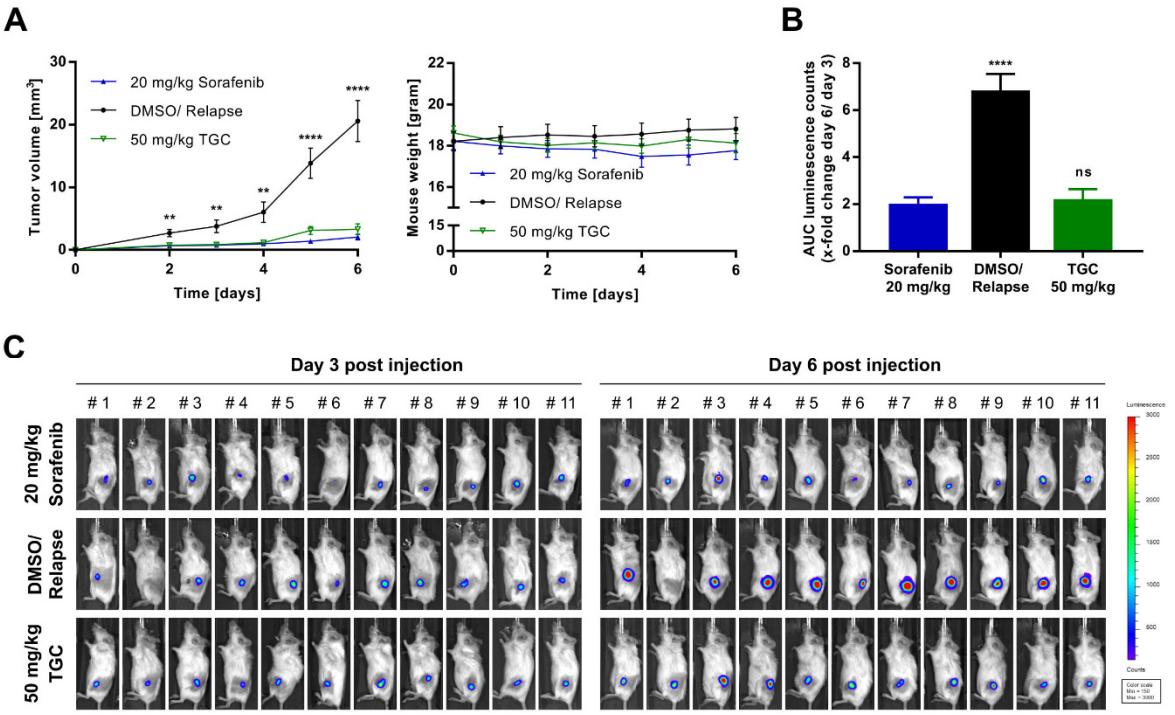

Figure 33. **TGC prevents rebound growth second-line to sorafenib *in vivo*. (A)** TGC prevents tumor relapse in an ectopic tumor mouse model of HUH7-R(+)-LUC cells. Cells were cultured in sorafenib prior to injection. Mice were treated with 20 mg/kg sorafenib (Control), DMSO (Relapse) or 50 mg/kg TGC daily for 6 days. DMSO #2 was excluded from statistical analysis as no tumor was detected until day 6 post cell injection. Tumor volume and mouse weight were assessed by digital Caliper measurements at the indicated time points. **(B)** Growth rate determined as x-fold change of *in vivo* bioluminescence imaging performed at day 3 and day 6 after HUH7-R(+)-LUC cell injection. The area under the curve (AUC) of luminescence counts was assessed for 20 min after 13 min of 0.3 g/kg luciferin injection for each mouse. **(C)** Images of *in vivo* bioluminescence imaging were taken 20 min after 0.3 g/kg luciferin injection (binning 4, min=150 counts; max=3000 counts). Values denoted as ± SEM, n=11 (n=10 for DMSO Control), **p<0.01, ****p<0.0001 (ANOVA).

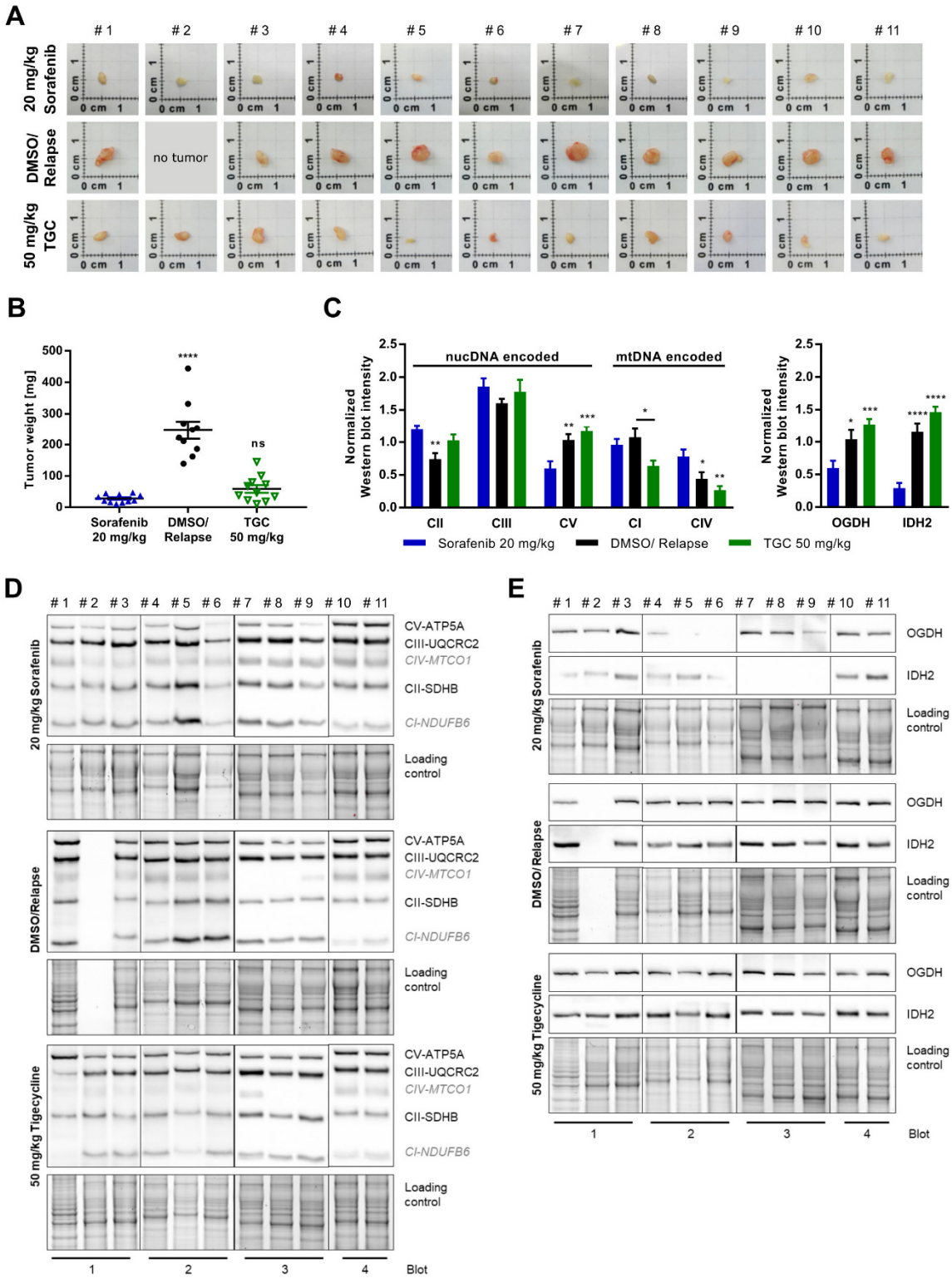

Figure 34. **TGC diminished CI-NDUFB6 expression of respected tumors *in vivo*. (A)** Size of resected tumors at day 6 post cell injection of ectopic tumor mouse model *(Figure 33)*. **(B)** Weight of resected tumors *(Figure 33)*. **(C)** Significantly reduced protein expression of mtDNA-encoded CI-NDUFB6 subunit upon TGC treatment *in vivo*. Quantitative immunoblot analysis of ETC subunits respectively TCA cycle enzymes IDH2 and OGDH from resected tumors *(Figure 34 A)*. **(D)** Immunoblot analysis of resected tumors for the protein abundance of the ETC subunits, respectively **(E)** protein levels of the enzymes IDH2 and OGDH. The immunoblots were normalized to the protein load and to the mean band intensity per blot. Values denoted as ± SEM, n=11 (n=10 for DMSO Control), *p<0.05, **p<0.01, ***p<0.001, ****p<0.0001 (ANOVA).

The impact of TGC on the biogenesis of mtDNA-encoded subunits *in vivo* was supported by a significantly reduced CI-NDUFB6 protein expression in resected tumors, whereas protein levels of nucDNA-encoded subunits remained unaffected *(Figure 34 C)*. Sorafenib withdrawal increased the abundance of nucDNA-encoded CV-ATP5A subunit, as demonstrated *in vitro*, but had no effect on CI-NDUFB6 expression *in vivo (Figure 34 D)*. In contrast to previous *in vitro* studies, tumor relapse accompanied with elevated levels of the TCA cycle enzymes OGDH and IDH2 *(Figure 34 E)*.

4.7.2 TGC shows effectiveness in long-term treatment second-line to sorafenib *in vivo*

A comparable ectopic tumor mouse xenograft implemented over 14 days, showed a strong initial effect of TGC treatment *(Figure 35 A-B; Figure S11 A)*, though no alterations were observed in expression patterns of the ETC subunits, OGDH or IDH2, at the time of tumor excision *(Figure 35 C-D; Figure S11 B-C)*. We suggest that protein expression of these proteins underlies regulatory dynamics over the time of therapy with the strongest effectiveness of TGC in an early phase after sorafenib withdrawal. Altogether, these *in vivo* results are consistent with the *in vitro* findings presented above, indicating the biogenesis of mtDNA-encoded ETC subunits as a selective and potent target for therapeutic intervention in a second-line setting of sorafenib-resistant HCC.

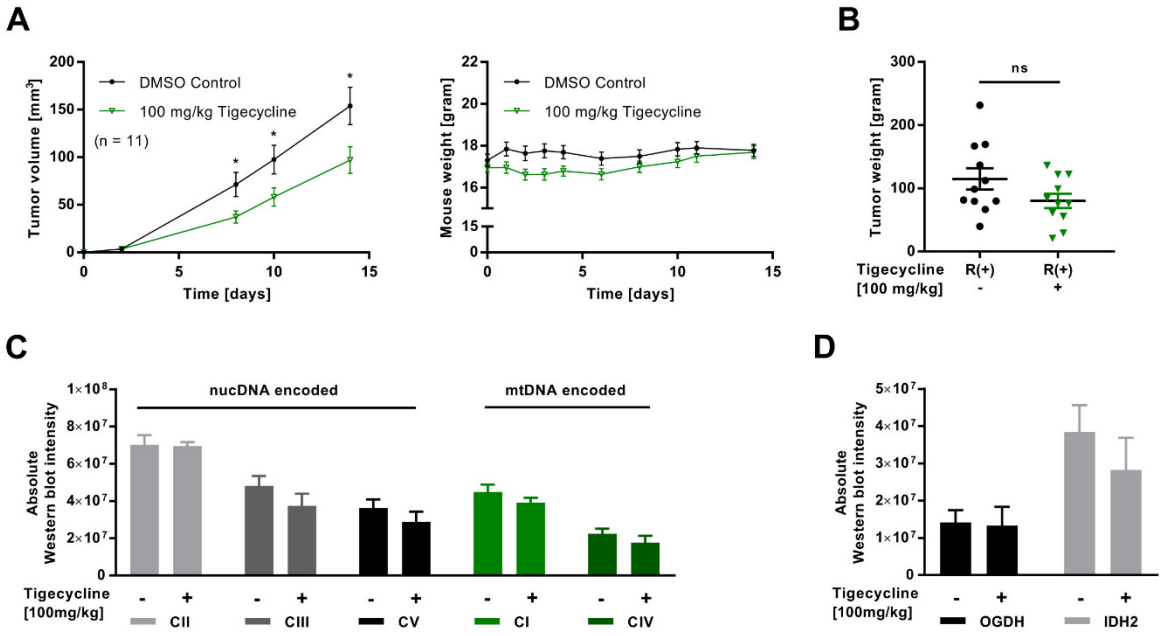

Figure 35. **TGC shows strongest inhibition of tumor relapse in initial phase. (A)** TGC prevents tumor relapse under long-term treatment in ectopic tumor mouse xenograft of HUH7-R(+) cells. Mice were treated with a DMSO or 100 mg/kg TGC every second day for 14 days. Tumor volume and mouse weight were assessed at the indicated time points. **(B)** Tumor weight after resection is decreased in tendency. For images of the resected tumors at day 14 see *Figure S11 A.* **(C)** TGC has no effect on biogenesis of ETC subunits under long-term treatment. Immunoblot quantification *(Figure S11 B)* is shown for mtDNA- (CI-NDUFB6, CIV-MTCO1) and nucDNA-encoded subunits (CII-SDHB, CIII-UQCRC2, CV-ATP5A). **(D)** TGC has no effect on IDH2 and OGDH protein levels under long-term treatment. Immunoblot quantification of *Figure S11 C* is shown. Values denoted as ± SEM, n=11, *p<0.05 (t-test). See also ***Figure S11***.

5 SUMMARY

In the following, the key findings of this study are summarized in brief:

1. We established a robust **sorafenib resistance HCC model**, revealing partial EMT and broad chemotherapeutic cross-resistance upon sorafenib exposure. Importantly, sorafenib withdrawal resensitized cells but was accompanied by an unfavorable relapse of tumor growth.
2. MS-based proteomics and metabolic profiling of this cell model indicated that tumor growth resumption is **driven by metabolic and mitochondrial alterations** towards high ETS activity.
3. By means of TEM and high resolution respirometry we found that **sorafenib therapy mediates mitochondrial impairment.** These damaged mitochondria are efficiently degraded upon rebound growth. Thus, mitophagy contributes to regeneration of the mitochondrial functionality.
4. In addition to autophagic pathways, **mitochondria are newly biosynthesized upon rebound growth** due to starvation-induced activation of PGC-1α. Mitochondrial biogenesis was confirmed by increased biosynthesis of cardiolipin, which is a hallmark lipid of the IMM.
5. The **translation inhibiting antibiotic compound TGC** impairs biogenesis of mtDNA-encoded ETC subunits, limiting the electron acceptor turnover by the NDUF and establishing auxotrophy for NAD^+. TGC thereby prevents the therapy-limiting tumor relapse *in vitro*.
6. The electron acceptor turnover is required for the proliferation-fueling glutamine oxidation. TGC impairs the cellular redox balance and promotes **sustained mitochondrial damage.**
7. By demonstrating that **TGC significantly impairs tumor relapse *in vivo***, we present a promising therapeutic approach for advanced-stage HCC second-line to sorafenib therapy.

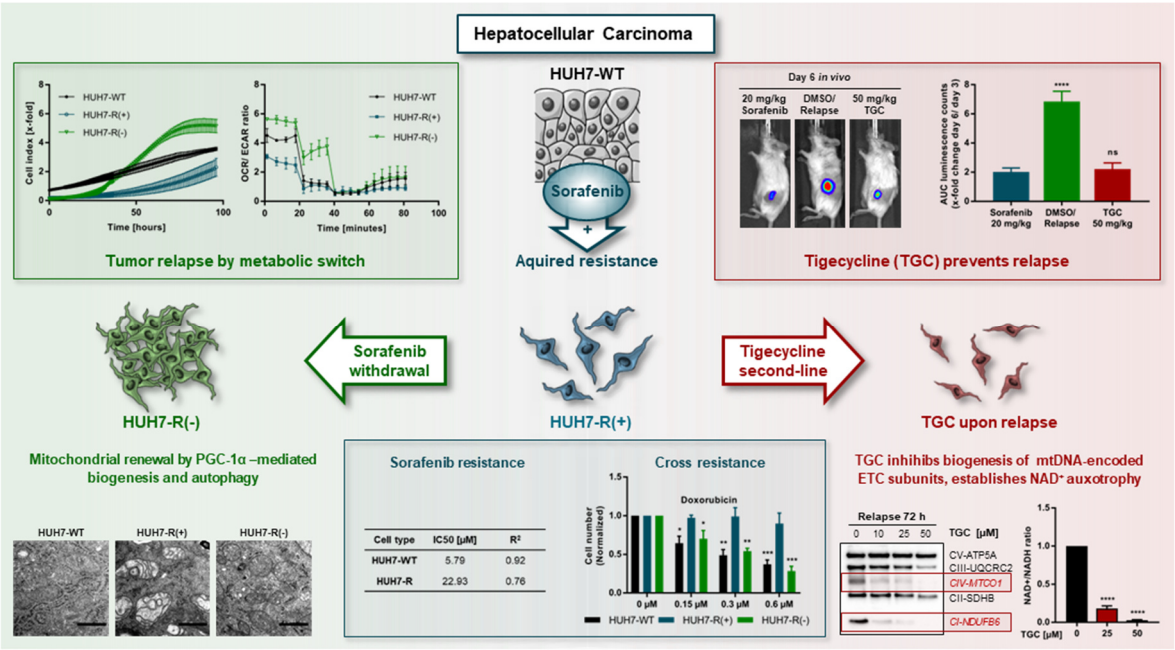

Figure 36. **Overview of the key results obtained in this study.**

DISCUSSION

6 DISCUSSION

Since the 1970s, the epidemic of HCC has spread beyond Eastern Asia, with almost a doubling of cases reported in the United States and Canada within the following two decades (El-Serag et al., 2003). To date, sorafenib is still a standard of care first-line therapy for advanced-stage HCC. Nonetheless, with only 2% of patients showing a partial response, sorafenib resistance and consequent tumor relapse represent a serious challenge for prolonging the OS. In this study, we aimed to unravel unknown mechanistic features of sorafenib resistance with a special focus on tumor growth resumption after sorafenib withdrawal. Both sorafenib resistance and rebound growth contribute to the low therapeutic benefit of this drug as well as to the frequent failure of first-line and second-line therapeutic approaches in clinical trials (Kudo, 2017). Thus, clarifying the molecular basis of acquired sorafenib resistance and tumor relapse could help to find innovative therapeutic options for advanced-stage HCC patients. In the following, the contributions of evasive pathway signaling and autophagy to acquired resistance are discussed. Further, the role of metabolic reprogramming and mitochondrial biogenesis in rapid tumor relapse is highlighted and the rationale using translation-inhibiting antibiotics as second line therapy after sorafenib failure is reviewed.

6.1 The mechanistic interplay conferring sorafenib resistance

In this study, we developed a human HCC cell line with acquired resistance to sorafenib in a range equivalent to the serum concentration of patients on a recommended sorafenib intake of 400 mg, twice daily (Al-Rajabi et al., 2015). We showed that these sorafenib-resistant HUH7-R(+) cells were highly refractory to all tested chemotherapeutics when cultured in sorafenib but that they regained sensitivity when therapy was withdrawn. We suggest that acquired sorafenib resistance constitutes an interplay of diverse survival mechanisms, promoted by sustained MAPK pathway inhibition, ER-stress and lysosomal drug sequestration, which will be outlined in the following.

6.1.1 Evasive PI3K/AKT signaling promotes EMT and glycolysis but prevents autophagy

6.1.1.1 Invasive tumor growth triggered by PI3K/AKT-mediated EMT

Preclinical and clinical observations indicate that limited sorafenib responsiveness may be caused by acquired therapy evasion in which EMT plays a decisive role (van Malenstein et al., 2013). EMT is triggered by compensatory PI3K/Akt-pathway activation upon sustained inhibition of the MAPK/ERK axis and was therefore reversible after sorafenib withdrawal (van Malenstein et al., 2013). Nonetheless, HUH7-R(+) cells undergo only partial EMT with low but maintained E-Cadherin expression *(Figure 9)*, suggesting that EMT does not solely mediate sorafenib resistance. However, cancer cell invasion, tumor malignancy and the OS of patients may be guided by the acquisition of EMT features (Marcucci and Rumio, 2018; Thiery, 2002). Thereby, matrix

metalloproteinases (MMPs) are involved in the spreading of metastasis via enzymatic degradation of extracellular matrix components (Son and Moon, 2010). The invasive potential is mainly dictated by MMP-2 and MMP-9, which were upregulated in HUH7-R(+) cells *(Figure S3)*. In order to adapt to the microenvironment upon secondary tumor formation, metastasizing tumors are capable of reversing mesenchymal cells to epithelial derivatives via mesenchymal-to-epithelial transition (MET) (Kalluri and Weinberg, 2009). We found that upon sorafenib withdrawal HUH7-R(-) cells regained and even increased their epithelial phenotype *(Figure 9 A-B)*, while resensitizing towards chemotherapy *(Figure 8 C; Figure S1)*. However, in contrast to previous findings, HUH7-R(-) cells did not reverse their mesenchymal plasticity neither regain MMP-2 protein levels (van Malenstein et al., 2013). In summary, we hypothesize that EMT contributes to chemotherapeutic resistance of HUH7-R(+) cells and conveys an elevated invasive potential via MMPs.

6.1.1.2 Sorafenib alters tumor microenvironment and promotes ER-stress

ER-stress is the consequence of cellular adaptive mechanisms towards intrinsic and extrinsic stressors, such as oncogene activation, nutrient deprivation or chemotherapy (Avril et al., 2017). Thereby, the tumor microenvironment contributes to the limited cellular oxygen supply through inadequate vascularization, which was observed upon sorafenib therapy *in vivo (Figure 7 C)*. The cancer cell adaptions to such milieu of hypoxia, pH variation and nutrient depletion include the unfolded protein response (UPR) and selection of drug-resistant cells, which circumvent the amplification of microenvironmental stress by anticancer agents (Mann and Hendershot, 2006). Thus, we hypothesize that HUH7-R cells induce secretion of MMPs and the EMT-associated transcription factors NFκB and interleukin-6 in the course of ER-stress, to sustain their metabolic demands and to adapt to a challenging environment. In turn, these transcription factors promote an EMT-like phenotype and may therefore increase the invasive potential of HUH7-R cells (Sheshadri et al., 2014). To date, the clinical evidence of ER-stress-mediated drug resistance is limited to breast cancer (Avril et al., 2017). Herein, we reveal a possible involvement in acquired sorafenib resistance of HCC by integrating EMT, autophagy and reprogramming of the glucose metabolism.

6.1.2 Lysosomal sorafenib sequestration

Besides promoting EMT and anaerobic glycolysis, evasive PI3K/AKT pathway signaling activates mTOR, which exerts an inhibitory effect on autophagy induction (Zhai and Sun, 2013). Indeed, HUH7-R(+) cells were found to possess low levels of mature autophagosomes (low LC3II lipidation) *(Figure 18 B)*, which contributes to an insufficient mitochondrial degradation by macroautophagy and results in an accumulation of dysfunctional mitochondrial structures *(Figure 15 C; Figure S7 C)*. In addition, sustained sorafenib exposure was found to drive lysosomal biogenesis. However, the accumulation of lysosomal mass in HUH7-R(+) cells implicates impaired autophagosomal degradation *(Figure 17 A-C)*. Consequently, due to this perturbed autophagic flux, lysosomes that

are not fused with autophagosomes may be involved in drug sequestration and inactivation, thereby conferring sorafenib resistance (Abdel-Aziz et al., 2017). Previous studies indicated that P-glycoprotein (P-gp)-positive cytoplasmic vacuoles of lysosomal origin sequester the multikinase inhibitor sunitinib in HCC (Colombo et al., 2014). This process of drug entrapment describes the enrichment of hydrophobic weak base chemotherapeutics, such as doxorubicin and vincristine, in the lysosomal compartment. These drugs accumulate due to the highly acidic luminal pH of the lysosomes and are consequently prevented from reaching their therapeutic targets (Duvvuri et al., 2005). To date, the lysosomal lumen alkalizers chloroquine and its derivate hydroxychloroquine are the only clinically available autophagy-inhibiting drugs. Both were shown to neutralize the lysosomal pH, block the fusion of autophagosomes with lysosomes and enhance tumor cell sensitivity of HCC to various chemotherapeutic agents *in vitro* and *in vivo* (Sheng et al., 2018; Shimizu et al., 2012). Thus, preventing lysosomal acidification independently of P-gp *(Figure S2)* evoked as a promising target for resensitizing HUH7-R cells towards sorafenib therapy and will therefore be subject of further investigations (Mueller et al., unpublished data).

6.1.3 The choice between autophagy and apoptosis

Importantly, autophagy is not solely controlled by the PI3K/AKT-axis as a panoply of other growth factors act upstream of mTORC1 and activate the ribosomal S6 kinase (RSK), protein kinase B (PKB), AKT and ERK. They all ultimately feed into the tuberous sclerosis complexes 1 and 2 (TSC1 and TSC2), which are critical integrators of growth factors, nutrients and stress signals (He and Klionsky, 2009; Paquette et al., 2018). In the presence of nutrients or growth factors mTORC1 is activated and abolishes autophagy through phosphorylation and inhibition of TFEB and TFE3. In addition, mTORC1 inhibits the UNC-51-like kinases 1 (ULK1) complex, which acts with BECN-1 and LC3 in the induction of autophagosome formation. In contrast, AMPK prevents mTORC1 activation and promotes autophagy when the ATP/AMP ratio is low or upon activation of the DNA damage-induced p53 signaling (Paquette et al., 2018; Prieto-Domínguez et al., 2016). Thus, in response to the same selection of stress mediators, cells can preferentially undergo apoptosis or autophagy, a choice that is dictated by the intensity of the respective stimulus *(Figure 37)*.

Those stimulants of apoptosis and autophagy comprise ROS, the elevation of cytosolic Ca^{2+} and BH3-only proteins, such as BIM and BID (Maiuri et al., 2007). As shown previously, the PI3K/AKT signaling to mTORC1 is induced in HUH7-R(+) cells *(Figure 9 E)*, but mTORC1 activation might be counter-regulated by phosphorylation of the AMPK *(Figure 20 C)* due to energy depletion *(Figure 13 B)* and excessive mitochondrial ROS production *(Figure 15 A)*. In addition, sustained sorafenib exposure was found to promote lysosomal biogenesis by elevating TFEB/TFE3 protein levels *(Figure 17 C)* and the ER-stress-mediated Ca^{2+} release to the cytoplasm *(Figure 16 B; Figure 20 A)*. Further, the abundance of the antiapoptotic Bcl-2 protein was reduced, possibly due to increased proteasomal degradation *(Figure 17 D)*. Thus, sorafenib strongly intervenes with the

regulation of both apoptosis and autophagy in HUH7-R cells. Notably, Bcl-2 has drawn attention in regulating prosurvival autophagy by interacting with BECN-1 through a BH3-domain (Abdel-Aziz et al., 2017). However, competitive disruption of this inhibitory interaction by the BH3-only proteins BID and BIM, which activate the proapoptotic mediators Bax and Bak, can also stimulate autophagy (Maiuri et al., 2007). This switch from apoptosis to autophagy might play a decisive role in the growth resumption secondary to sorafenib withdrawal, as HUH7-R(-) cells reveal a decrease of cytosolic Ca^{2+} and mitochondrial ROS (*Figure 15 A; Figure 20 A*), resulting in reduced apoptosis but elevated levels of mature autophagosomes *(Figure 19 A; Figure 18 B)*. Given that sorafenib retraction from HUH7-R cells promotes a switch from apoptosis to autophagy, a combinational treatment of antibiotics with autophagy inhibitors might be beneficial to increase the effect of TGC.

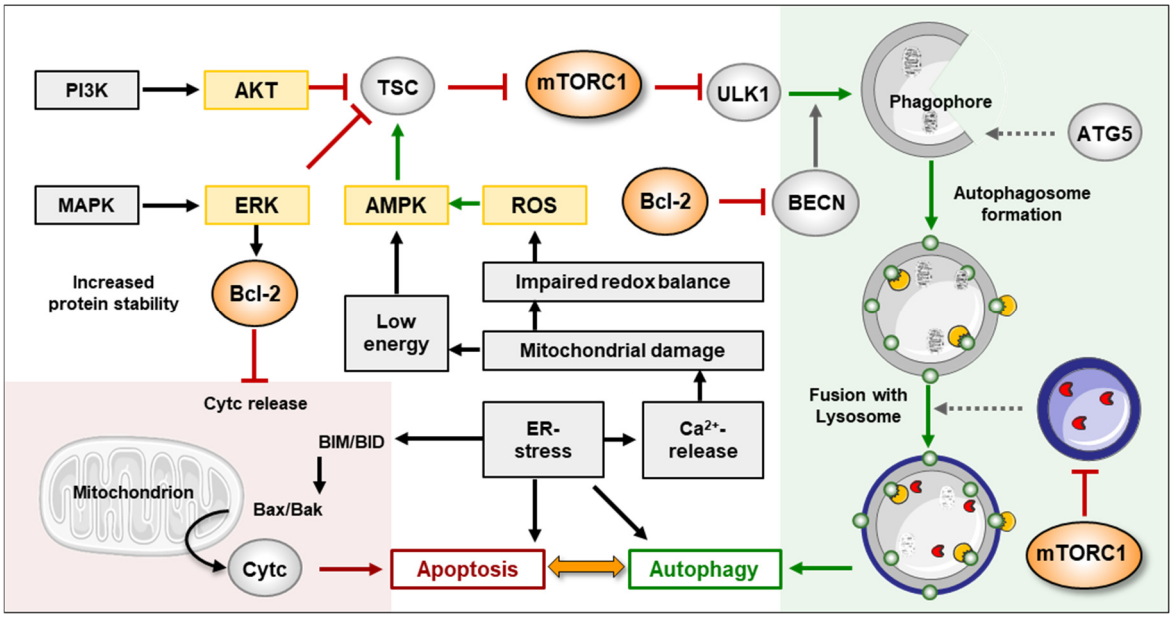

Figure 37. **The crosstalk of autophagy and apoptosis.** In response to the same panoply of stressors cells can either undergo apoptosis or autophagy. Thereby, mTORC1 and Bcl-2 play a key role in the regulation of both processes, which are dependent on PI3K or MAPK pathway signaling and the cellular energy status.

6.1.3.1 Combinational therapy of antibiotics with autophagy inhibitors

Short-term sorafenib treatment has been previously shown to induce autophagy in various HCC cell lines, which is attained by increased LC3II lipidation and expression of the autophagy mediators Beclin-1, ATG5, ATG7 or LC3 (Shi et al., 2011; Shimizu et al., 2012). Thus, silencing of key autophagy genes or the combinational use of autophagy inhibitors could enhance the cytotoxic effect of sorafenib on HCC cells (Sheng et al., 2018). In fact, HUH7-R(+) cells obtained an increased colocalization of mitochondria with lysosomes, indicating autophagic sequestration of damaged mitochondria and subsequent fusion with lysosomes for degradation *(Figure 19 B; Figure S8 A)*.

However, 3-MA was not capable of sensitizing HUH7-R(+) towards sorafenib treatment, suggesting that autophagosome formation was not induced in these cells and that conventional autophagy is not the key-mechanism of acquired sorafenib resistance *(Figure S7 C)*. Nonetheless, LC3II lipidation and autophagic removal of damaged mitochondria were strongly induced upon growth resumption *(Figure 18 B-C)*. Thus, we hypothesized that the inhibition of autophagy might constitute a possible adjuvant therapy to translation-inhibiting antibiotics, as both mitophagy and mitochondrial biogenesis contribute to the tumor relapse after sorafenib therapy termination. In fact, the combinational use of TGC with 3-MA obtained additive growth inhibition in HUH7-R(-) cells *(Figure 19 C; Figure S8 B)*. However, autophagy inhibitors are solely recommended for acute application, as long-term use of those agents is limited due to intolerance and toxicity (Weinberg and Chandel, 2015). In summary, autophagy inhibitors additively enhance the effect of antibiotics as second-line therapy to sorafenib, but possess inferior relevance for clinical translation.

6.1.3.2 Autophagy protein 5 (ATG5)-independent autophagy

Autophagy is a tightly regulated process contributing to mitochondrial quality control with critical involvement of the ATG proteins. Among those, ATG5 was long thought to be indispensable for autophagy induction and vesicle formation (Sugiura et al., 2014). In addition to its role in autophagy, ATG5 can be cleaved by calpain cysteine proteases, thereby losing its proautophagic property and becoming a proapoptotic molecule (Maiuri et al., 2007). Surprisingly, although ATG5 silencing was shown to sensitize Mhcc97-L and PLc/PRF/5 HCC cells towards sorafenib therapy (Shi et al., 2011), HUH7-R cells lack ATG5 protein expression *(Figure 17 E)*, which was not recovered upon sorafenib withdrawal *(Figure 19 D).* We hypothesized that degradation of the ATG5 protein might be the result of increased ER-stress in HUH7-R cells, which leads to elevated cytosolic Ca^{2+} levels that activate the ATG5-cleaving cysteine protease calpain and induce the UPR in these cells *(Figure 16; Figure 20 A)*. The UPR aims at limiting the accumulation of misfolded proteins in the ER by transiently attenuating protein translation, by enhancing the ER folding capacity through enhanced transcription of local chaperones and by promoting protein clearance from the ER via increasing its degradation capacity (Avril et al., 2017). As damaged mitochondria were efficiently degraded upon rebound growth, HUH7-R cells were suggested to undergo ATG5-independent autophagy, which allows the degradation of organelles and formation of autophagosomes in the absence of ATG5 and ATG7 (Nishida et al., 2009). It has been previously reported that upon ATG5-independent autophagy, the Rab9 protein may replace the function of LC3 in autophagosome formation (Nishida et al., 2009). In conventional, ATG5-dependent autophagy, Rab9 mediates protein traffic between late endosomes and the *trans*-Golgi network (Lombardi et al., 1993). Nonetheless, no alterations in Rab9 localization were observed in HUH7-R compared to HUH7-WT cells *(Figure 19 E; Figure S8 C)*. Thus, the mechanism of ATG5- and Rab9 independent autophagy of HUH7-R cells remains elusive and requires further investigations.

6.2 Metabolic reprogramming – a new hallmark of cancer malignancy?

The acquisition of resistance and growth resumption following sorafenib therapy termination have been previously described (Ebos et al., 2009; van Malenstein et al., 2013), though the underlying metabolic mechanism has not been investigated thus far. In this study, we provided evidence that upon sustained sorafenib exposure, severe mitochondrial damage and ETC dysfunction render HUH7-R(+) cells dependent on glucose metabolism for ATP homeostasis and NAD^+ recycling. In contrast, tumor rebound growth upon sorafenib withdrawal was accompanied by increased ETC activity and glutamine turnover to drive precursor metabolite biosynthesis by the oxidative TCA cycle. Herein, we emphasize renewal of the ETC and metabolic reprogramming as a driving force behind tumor relapse and as a potential target for therapeutic intervention second-line to sorafenib.

6.2.1 Mitochondria as gatekeepers for sorafenib responsiveness

Mitochondria are integral organelles required for cellular stress sensing and for conveying bioenergetic adaptation to environmental alterations. Recently, multiple studies have highlighted that mitochondria are not only indispensable for energy production and survival of the eukaryotic cell, but also play a role in malignant transformation (Vyas et al., 2016). Moreover, they are crucial regulators of the intrinsic (mitochondrial) pathway of apoptosis (Fulda et al., 2010).

6.2.1.1 Bak-deficiency of HUH7-R cells might convey resistance to intrinsic apoptosis

Proteins of the Bcl-2 family control apoptosis at the mitochondria through regulation of OMM permeabilization by the pore-forming proteins Bax and Bak. These proteins promote the release of cytochrome c and smac/DIABLO to the cytosol, leading to caspase activation and rapid cell death. Thus, OMM permeabilization is tightly regulated by the Bax/Bak activating BH_3-only proteins BID or BIM, which are induced upon the ER-stress-mediated UPR (Glab et al., 2017). In addition, a changing ratio of Bcl-2 activators and repressors may result in cell death or in the appearance of drug resistance, as reported for sorafenib and regorafenib in the therapy of HCC (Tutusaus et al., 2018). Interestingly, both Bak and Bcl-2 protein levels were diminished in HUH7-R cells, whereas Bax-levels persisted *(Figure 17 D).* Evidence is given that activation preferences exist upon which BID preferentially activates Bak, while BIM preferentially activates Bax. Thus, cells lacking Bak, such as HUH7-R cells, are expected to be resistant towards agents that require BID activation for the induction of mitochondrial apoptosis. Those include DNA damaging chemotherapeutics and other agents that activate cell surface death receptors by the ligands FasL, TNF and TRAIL (Sarosiek et al., 2013). However, the MS-proteomics screening revealed that protein levels of the apoptosis executioner caspase-3 (CASP3), which is activated by both intrinsic and extrinsic pathways, were strongly increased in HUH7-R cells (22-fold higher in HUH7-R(-) vs. HUH7-WT; 4-fold higher in HUH7-R(-) vs. HUH7-R(+)) *(Figure 11 A-B)*. This might be a regulatory consequence of the reduced

activation of intrinsic and extrinsic apoptosis due to Bak-deficiency. We hypothesized that HUH7-R(+) cells possibly undergo an alternative route of programmed cell death, termed ferroptosis, which is regulated by iron or ROS and induced by sorafenib treatment and ER-stress (Galluzzi et al., 2018). Ferroptosis is morphologically characterized by mitochondrial abnormalities, involving the reduction of crista, increased mitochondrial membrane density and OMM rupture (Xie et al., 2016). In addition, ferroptosis leads to the accumulation of lipid peroxidation products and lethal iron metabolism-derived ROS, which are characteristics found in high abundance in HUH7-R(+) cells *(Figure 15 A; Figure S4 B, D; Figure S9 D)*.

6.2.1.2 The metabolic component in acquired drug resistance

As mentioned above, the mitochondrial regulation of programmed cell death may involve a large metabolic component and also the overall therapeutic response may be influenced by the cellular metabolism and mitochondrial reprogramming upon chemotherapeutic treatment (Porporato et al., 2017). Notably, evasive activation of the PI3K/Akt pathway by sorafenib physiologically promotes glucose uptake and turnover, promoting rapid but inefficient anabolism and lactate fermentation (Elstrom et al., 2004; Pfeiffer et al., 2001). Cancer cells partially adapt their metabolic demands under these conditions of nutrient deprivation, microenvironmental stress by the UPR, through activation of the hexosamine biosynthetic pathway. Thereby, glucose is converted to substrates for the O- and N-glycosylation of proteins, which improve protein folding, stability and cell adhesion (Avril et al., 2017; Shental-Bechor and Levy, 2008). Indeed, the MS-proteomics screening revealed enhanced amino sugar metabolism in HUH7-R(+) cells possibly caused by sorafenib-induced ER-stress or nutrient depletion *(Figure 10 C)*. In addition, previous metabolomics studies reported a higher demand for glucose in sorafenib-resistant leukemia cells (You et al., 2019) and an increased glucose flux into the PPP of sorafenib-resistant HCC cells. The study further reports elevated glutamine-derived lipid biosynthetic pathways in these resistant HCC cells with a high tolerance to oxidative stress due to an elevated glutamine turnover (Kim et al., 2017). This observed phenotype therefore combines metabolic key-characteristics of sorafenib-resistant HUH7-R and RIL175-R cells upon sorafenib treatment respectively drug withdrawal conditions. Notably, the impact of the metabolism on resistance *in vitro*, may be amplified in patients by the antiangiogenic effects of sorafenib therapy, which reduces microvessel density and promotes intratumoral hypoxia and HIF-mediated cellular responses. Hypoxia favors the selection of resistant cells that are adapted to the oxygen-deficient microenvironment by their enhanced glucose turnover (Avril et al., 2017; Méndez-Blanco et al., 2018; Zhai and Sun, 2013). Moreover, nutrient deprivation, growth factor withdrawal, hypoxia, ER-stress or ROS accumulation not only promote metabolic adaptions but have the ability to induce or modify autophagy via the nutrient sensor AMPK, which may also contribute to acquired drug resistance (He and Klionsky, 2009; Prieto-Domínguez et al., 2016).

6.2.2 The oncogenic potential of metabolic reprogramming

As reviewed above *(chapter 2.3.2)* tumor suppressors and oncogenes have been reported to regulate the Warburg effect, which acts in cancer cells concurrently to respiration (Koppenol et al., 2011). Interestingly, mutations in metabolic enzymes appear to have *vice versa* oncogenic potential and specifically citric acid cycle enzymes, such as IDH1 and IDH2, are causally linked to familial and spontaneous cancers (Dang et al., 2009; Koppenol et al., 2011). Thereby, an IDH1 gain-of-function mutation catalyzes the NADPH-dependent reduction of AKG to the oncometabolite 2-hydroxy-glutarate, which accumulates and contributes to the malignant progression of gliomas (Dang et al., 2009). Further, a variety of studies proofed that isoforms of metabolic enzymes, which are preferentially expressed in cancer cells, are involved in metabolic reprogramming upon tumorigenesis by enhancing the glycolytic flux due to deviating enzymatic kinetics (Cassago et al., 2012; Christofk et al., 2008). Thus, it is suggested that metabolites themselves can be oncogenic by altering cell signaling and blocking cellular differentiation (Ward and Thompson, 2012).

6.2.2.1 Metabolic rewiring and tumor growth resumption

Conceptual progress in the last decade has added the emerging neoplastic traits “reprogramming of energy metabolism” and “evading immune destruction” to the six commonly known hallmarks of cancer (Hanahan and Weinberg, 2011). Thereby, oncogenic activation may increase the mitochondrial metabolism to generate ATP and TCA cycle intermediates. These are redirected into anabolic pathways in order to accumulate cellular building blocks required for rapid tumor growth (Weinberg and Chandel, 2015). Given that TGC enhanced CV-ATP5A expression *(Figure 24 A)* and intracellular ATP levels at high concentrations *(Figure 24 C)*, we conclude that mitochondrial ATP generation may not be crucial for rebound growth of HUH-R and RIL175-R cells. Among the TCA cycle metabolites provided by the mitochondrial metabolism, citrate is exported to the cytosol and supports lipid synthesis via ACoA, whereas nucleotide synthesis is driven by OAA (Weinberg and Chandel, 2015). It has been previously shown that following TKI withdrawal, tumor cells undergo a metabolic shift to *de novo* lipogenesis, which is associated with rapid tumor regrowth and accelerated metastatic dissemination (Sounni et al., 2014). This growth resumption involved upregulation of the fatty acid synthase (FASN), herein confirmed by volcano plot analysis through a 2.6-fold increase of this enzyme in HUH-R(-) cells in comparison to HUH-R(+) cells *(Figure 11 A-B)*. To sufficiently supply tumors with TCA cycle intermediates, cells utilize glutamine, which is stepwise oxidized to AKG and OAA, subsequently (DeBerardinis et al., 2007). Therefore, glutamine is replenished by autophagy, a cellular process that supplies cancer cells with additional energy by degrading protein aggregates or damaged organelles, to sustain the mitochondrial metabolism and fast proliferation (Altman et al., 2016). It is assumed that, on the one hand, mTOR and EMT, which are active in HUH7-R(+) cells and, on the other hand, AMPK and autophagy negatively regulate each other (Marcucci and Rumio, 2018). Thus, sorafenib treatment impairs the initiation of autophagy, but

withdrawal conditions might reverse this phenotype, promoting glutamine supply and rapid growth recurrence (He and Klionsky, 2009; Zhai and Sun, 2013). In addition to the contribution of glutamine to the biogenesis of macromolecular building blocks, this amino acid is required to recycle reducing equivalents by the TCA cycle to drive ETC activity and to maintain ROS homeostasis (DeBerardinis et al., 2007; Sun, 2010). In fact, upon rebound growth, HUH7-R cells essentially rely on both ETC activity and glutamine oxidation *(Figure 24; Figure 30 A).* In summary, this study provided evidence that mitochondrial alterations are the key-drivers of tumor relapse following sorafenib treatment abrogation. Thus, we presented the inhibition of ETC renewal, which impairs glutamine oxidation, and consequently the supply of TCA cycle-derived anabolic metabolites as efficacious second-line therapy for HCC patients.

6.2.2.2 Mitochondria confer metabolic requirements for aggressive tumor growth

Complementing the role in energy generation, biosynthesis, signal transduction and the initiation of programmed cell death, it has been established that mitochondria are crucially involved in the regulation of stem cell identity and differentiation. In contrast to their differentiated counterparts, stem cells rely on glycolysis for ATP production and undergo a shift toward OXPHOS upon dedifferentiation (Margineantu and Hockenbery, 2016). In addition, dedifferentiation is accompanied by mitochondrial structural remodeling from fragmented organelles with poorly developed cristae, towards mature elongated mitochondria forming tubular networks (Skoda et al., 2019). This tendency of mitochondria to undergo fission by upregulation of Drp-1 and reduction of Mfn-1 has been associated with a high invasive potential, drug resistance, tumor recurrence and an overall poor prognosis in many human cancers (Anderson et al., 2018; Skoda et al., 2019). As these characteristics strongly resemble the mitochondrial morphology of HUH-R(+) cells and the dedifferentiating phenotype upon sorafenib withdrawal, we hypothesize that sustained treatment may induce stem cell-like properties in these cells *(Figure 13 A; Figure 14; Figure 22 A)*. Of note, despite imbalances in mitochondrial dynamics, defective mitophagy and elevated respiration have also been linked to ROS overproduction and consequent metastatic dissemination (Porporato et al., 2017). Moreover, phosphorylation of the AMPK upon energy depletion, which was observed in HUH7-R(+) cells, promotes mitochondrial biogenesis via the transcriptional coactivator PGC-1α, thereby enhancing respiration and oxygen consumption *(Figure 20 C-E)*. PGC-1α expression strongly correlates with the malignant potential of cancer cells and the formation of distant metastases, whereas silencing of PGC-1α suspends their invasive potential and attenuated metastasis without affecting proliferation, primary tumor growth or EMT (LeBleu et al., 2014). In summary, the aggressive growth of HUH7-R cells *in vivo* may be an interplay of PI3K/AKT induced EMT, hypoxia and the invasive potential conferred by mitochondrial fission, ROS overproduction and the metabolic activation of PGC-1α upon sorafenib exposure *(Figure 7 D)*.

6.3 Antibiotics for anticancer therapy

In this study, we efficiently prevented the growth resumption secondary to sorafenib by the bacterial translation-inhibiting antibiotic TGC, which suppresses the biogenesis of mtDNA-encoded ETC subunits. To date, the use of antibiotics has not been investigated in HCC or as a second-line therapy for any other type of cancer. Thus, we presented an innovative treatment approach for advanced-stage HCC, which holds tremendous promise for clinical translation. In the following, the mechanistic background of TGC as a second-line therapy for sorafenib-resistant HCC is reviewed and the potential of a possible evaluation of new designation in this setting is discussed.

6.3.1 Translation-inhibiting antibiotics impair glutamine oxidation

The endosymbiotic theory hypothesizes, that mitochondria descended from α-protobacteria that were engulfed by eukaryotic cells, proving an additional energy source and thereby conferring a competitive advantage (Sagan, 1967). Thus, the respiratory chain is a relic of evolution and the ETC subunits are encoded by both eukaryotic (nuclear) and prokaryotic (mitochondrial) DNA. Translation-inhibiting antibiotics are known to suppress the biogenesis of mtDNA-encoded ETC subunits, which account in total for 13 essential subunits of the respiratory chain complexes I (7 subunits), III (1 subunit), IV (3 subunits), and V (2 subunits) (Scarpulla, 2006; Taanman, 1999). Given this broad involvement, we sought to determine which product of the mitochondrial metabolism was rate-limiting for growth resumption of HUH7-R cells after sorafenib withdrawal.

6.3.1.1 The effect of TGC on aspartate biosynthesis

In addition to producing ATP, the ETC oxidizes NADH to NAD^+, which is required for driving aerobic TCA cycle activity to generate biosynthetic intermediates for lipids, amino acids, and nucleotides (Birsoy et al., 2015; DeBerardinis et al., 2007). The substitution experiments presented herein clearly demonstrated that TGC treatment established auxotrophy for exogenous electron acceptors that restore the proliferation-limiting glutamine oxidation by regenerating the oxidized cofactor NAD^+ *(Figure 27 B-C)*. Among the TCA-cycle derived precursor metabolites, aspartate has been previously reported to be limiting for proliferation in ETC-deficient cells (Birsoy et al., 2015; DeBerardinis et al., 2007; Sullivan et al., 2015). This amino acid plays an essential role in nucleotide biosynthesis and can be generated directly from glutamate via transamination and from AKG via both glutamine-dependent reductive carboxylation and oxidative pathways. Thus, aspartate production is limited by the electron acceptor NAD^+ and the overall glutamate respectively AKG abundance (Fendt et al., 2013; Mullen et al., 2014). Indeed, TGC limited the carbon requirement of the TCA cycle for sufficient maintenance of aspartate synthesis *(Figure 31 A)*. Nonetheless, aspartate substitution *per se* did not rescue the effect of TGC *(Figure 26)* and aspartate levels are mostly restored by pyruvate, which can form aspartate independently of NAD^+ via carboxylation to OAA

and subsequent transamination *(Figure 31 B; Figure 3)* (Altman et al., 2016; Sullivan et al., 2015). Thus, aspartate depletion is not rebound growth limiting and might therefore occur independently of inhibited glutamine oxidation. It has been previously shown that the glutamine consumption may exceed the nitrogen demand of cancer cells, because glutamine also supports the use of glucose-derived carbon for biogenesis (DeBerardinis et al., 2007). Thus, we hypothesize that HUH7-R(-) cells preferentially drive metabolism by glutamine oxidation. However, these cells also engage glucose derived OAA in biosynthetic pathways and aspartate depletion might be obtained by impaired aerobic glycolysis independently of the NDUF activity.

6.3.1.2 TGC disturbs redox balance upon growth resumption

Although the amino acid aspartate does not directly confer the growth inhibiting effect of TGC, it essentially contributes to redox homeostasis via the malate-aspartate shuttle, which exchange transfers reducing equivalents across the mitochondrial membrane without translocating carbon or nitrogen. Further, aspartate replenishes mitochondrial and cytosolic OAA for precursor metabolite biosynthesis *(Figure 3)* (DeBerardinis et al., 2007; Greenhouse and Lehninger, 1977). Cytosolic OAA is then metabolized via malate to pyruvate and NADPH, which provides the reducing power to maintain reduced glutathione pools for the antioxidant defense (Cairns et al., 2011). Thus, depleting cancer cells of aspartate and disrupting their malate-aspartate shuttle, damages mitochondria, results in the accumulation of ROS and consequently increases the genomic instability (Cheng et al., 2018). In general, glutamine metabolism provides an essential nitrogen source for nucleotide synthesis or the maintenance of nonessential amino acid pools. Among those, the amino acids glutamate, cysteine and glycine, which are required for synthesis of the ROS-neutralizing tri-peptide glutathione, are all critically dependent on glutamine input (Altman et al., 2016). In addition, abrogation of glutamine oxidation diminishes pools of malate and NADPH, both of which contribute to ROS elimination (DeBerardinis et al., 2008). The mitochondrial $NADP^+$/NADPH ratio thereby reflects NDUF impairment via enzymatic hydride transfer from NADH to $NADP^+$ *(Figure 27 C)*, which is possibly compensated by evasive NADPH-consuming reductive carboxylation in OGDH-silenced HUH7-R cells (Mullen et al., 2014). In contrast, cytosolic NADPH levels essentially rely on TCA cycle-dependent malate turnover *(Figure 29 B)* (DeBerardinis et al., 2008). In summary, we could show that TGC treatment leads to electron acceptor depletion, which limits glutamine oxidation, required to promote tumor relapse and to generate directly ROS-controlling products. Notably, elevated ROS levels are able to promote metabolic reprogramming, tumor growth and malignant progression, which might contribute to the rebound growth phenotype in HUH7-R and RIL175-R cells (Panieri and Santoro, 2016). Therefore, we conclude that disabling antioxidant defense mechanisms by TGC may constitute an efficient second-line approach to prevent tumor growth resumption after sorafenib retraction.

6.3.2 Up-to-date research and clinical experience

As mitochondria descent from bacteria, a multitude of FDA-approved antibiotic classes target in addition to the bacterial also the mitochondrial biogenesis and therefore confer mild side-effects. However, antibiotics are well-tolerated in most patients and may be harnessed as therapeutic tools to address biogenesis and metabolic reprograming of mitochondria, which promotes malignant tumor progression. To date, there is scant knowledge on the therapeutic benefit of antibiotics in cancer, as most studies focus on administration for cancer-associated infections. Cancer patients are prone to acquire infections due to intensive myelosuppressive chemotherapy and surgical site infections that indicate the use of broad-spectrum antibiotics (Razzouk et al., 2006). Thereby, growing clinical evidence demonstrated that besides eradicating chemotherapy-related infections, antibiotics may have anticancer potential *per se*. In initial endeavors, TGC was shown to selectively induce cell death in a panel of leukemia cell lines (Skrtic et al., 2011), to target sub-forms of lung- and breast cancer (Jia et al., 2016; Jones et al., 2016) and to eradicate cancer stem cells, which were resistant to the TKI imatinib (Kuntz et al., 2017). Moreover, recent work demonstrated that the inhibition of mitochondrial translation by TGC, effectively targets renal cell carcinoma and sensitizes cells to chemotherapy (Wang et al., 2017). So far, studies with TGC have been performed on 15 solid or hematologic tumor types, resulting in reduced ETC activity while inducing intrinsic apoptosis, autophagy and oxidative damage *(Table 27)* (Dong et al., 2019).

Table 27. *TGC used for the treatment of different solid tumors.*

Cancer Type	Biological phenotypes	Target/ Signaling pathways
Breast cancer*	ATP↓, OXPHOS↓	Mitochondrial translation↓
Cervical SCC	intrinsic apoptosis↑	Wnt/β-catenin↓
Gastric cancer	autophagy↑	AMPK-mTOR↑
Glioma/ Neuroblastoma	cell cycle arrest↑	AKT-FOXO3a↓
HCC/ NSCLC	ATP↓, OXPHOS↓, ROS↑	Mitochondrial translation↓
Melanoma	cell cycle arrest, invasion↓	Cytoplasmic p21↓
Multiple myeloma	cell cycle arrest↑, autophagy↑	AMPK-mTOR↑
Oral SCC	cell cycle arrest↑	CDK4-CCNE2↓
Ovarian cancer	OXPHOS↓, ROS↑, cell cycle arrest↑, intrinsic apoptosis↑	Mitochondrial translation↓
Renal cell carcinoma	intrinsic apoptosis↑	Mitochondrial translation↓, PI3K/AKT-mTOR↓
Retinoblastoma	intrinsic apoptosis↑, angiogenesis↓, ATP↓	-

*retinoblastoma susceptibility gene (RB-1)-deficient triple-negative breast cancer; NSCLC, non-small cell lung cancer; SCC, squamous cell carcinoma (Dong et al., 2019).

Until now, anticancer potential has been confirmed for the four mitochondria-targeting antibiotic classes, erythromycins, tetracyclines, glycylcyclines and chloramphenicol (Dong et al., 2019; Lamb et al., 2015). Further, combination therapies of TGC with the chemotherapeutics daunorubicin or cytarabine were found to exhibit an additive respectively synergistic cytotoxic effect on acute myeloid leukemia cells (Jaras and Ebert, 2011) and to enhance cisplatin efficiency in HCC (Tan et al., 2017). A first phase I dose-escalation study with TGC was performed in acute myeloid leukemia patients (Reed et al., 2016) and a clinical pilot study supported therapeutic success of the tetracycline doxycycline in targeting cancer stem cells of early breast cancer patients (Scatena et al., 2018). The possible usage of antibiotics in cancer therapy drew increasing scientific attention within the last years; however, mechanistic insights on their mode of action remain sparse.

6.3.3 The rationale behind antibiotics as chemotherapeutic agents

To date, a panoply of antibiotic classes are already clinically harnessed as chemotherapeutic agents, including the anthracyclines doxorubicin and daunorubicin (Hortobagyi, 1997), dactinomycins (Langholz et al., 2011), mitomycins (Volpe et al., 2010), bleomycins (Blum et al., 1973) and macrolides (Lagler et al., 2019). In addition, recent reports implicate that the modulation of the microbiome with antibiotics may affect the success of cancer immunotherapies (Dong et al., 2019; Luke and Pal, 2018). This study, however, focuses on the effect of antibiotics on mitochondria, which has been previously suggested to modulate energy production and apoptosis of cancer cells (Lamb et al., 2015). TGC is a low-cost FDA-approved antimicrobial agent, which belongs to the class of glycylcyclines and is used to treat complicated skin- and intraabdominal infections with a low incidence of side-effects (Bradford et al., 2005). TGC targets the S30 small ribosomal subunit, blocks the binding of aminoacyl-tRNAs to the A-site of the ribosome and exhibits broad spectrum anti-bacterial activity against gram-positive and gram-negative bacteria (Thaden et al., 2017; Xu et al., 2016). In contrast, CHA selectively binds to the S50 subunit and inhibits the activity of the peptidyl-transferase, thereby preventing peptide bond formation and protein chain elongation *(Figure 23 C)*. Importantly, both antibiotics prevent the translation of essential mitochondrial ETC subunits (Lamb et al., 2015). So far, a problem of targeting the mitochondrial metabolism in patients was that immune effector cells, in particular $CD8^+$ cytotoxic T-lymphocytes, display remarkable metabolic similarities to malignant cells (Porporato et al., 2017). However, TGC specifically targets the mitochondrial ribosome (Skrtic et al., 2011; Wang et al., 2017) and impairs translation of the NAD^+-recycling NDUF, which evoked to be a sensitive target for controlling tumor cell proliferation (King and Attardi, 1989; Wheaton et al., 2014). Moreover, TGC impairs the antioxidant defense of cancer cells and, thus, in adjuvant use, sensitizes tumors to chemotherapy (Panieri and Santoro, 2016). TGC may have additional direct targets that contribute to its biological phenotypes upon anticancer treatment that, however, remain still unknown.

6.3.4 Clinical relevance of this study

6.3.4.1 Is the era of sorafenib ending?

Sorafenib has evolved as the only systemic treatment for unresectable HCC, until 2018, when data from the phase III REFLECT trial revealed non-inferiority of the multikinase inhibitor lenvatinib in terms of OS *(Table 28)* (Kudo et al., 2018a). Further, lenvatinib increased the TTP from 3.7 to 7.4 months (hazard-ratio (HR): 0.61; P<0.0001) and the PFS *(Table 28)*. The overall safety profile was similar with both drugs, but patients treated with lenvatinib had a higher rate of hypertension (42% versus 30%) and a lower rate of hand-foot syndrome (27% versus 52%) than patients treated with sorafenib (Kudo et al., 2018a). Overall, the incidence of grade ≥3 treatment-emergent adverse events (57% versus 49%) was higher in the lenvatinib arm compared to sorafenib (Reig et al., 2018).
Encouraging efficacy was also reported by a phase I/II trial of the immune checkpoint inhibitor nivolumab (CheckMate-459) in the first-line setting of unresectable HCC *(Table 1)*, and most recently, synergism has been postulated for VEGFR-2 inhibitors and immunotherapy (El-Khoueiry et al., 2017; Personeni et al., 2019). Even though, a phase III trial with nivolumab failed to achieve statistical significance in terms of OS, improvement was observed, and further immunotherapy-based trials have been launched challenging first-line sorafenib *(Table 1)* (Liu et al., 2019). To date, the ongoing phase III trial, IMbrave150, compares a combination of atezolizumab (anti-PD-L1) and bevacizumab (anti-VEGF) to sorafenib in patients with advanced or metastatic HCC, who have not received prior systemic therapy. In fact, a preliminary outcome reported significantly prolonged OS and PFS with a comparable prevalence of grade 3-5 adverse events *(Table 28)* (Cheng et al., 2019).

Table 28. *Study endpoints of the REFLECT and the IMbrave150 phase III clinical trials.*

Study endpoints	**REFLECT trial**		**IMbrave150 trial (ongoing)**	
Treatment	**lenvatinib**	**sorafenib**	**atezolizumab + bevacizumab**	**sorafenib**
	12 mg/day ≥60 kg or 8 mg/day <60 kg; 1x daily	400 mg; 2x daily	atezo.1.2 g and bev. 15 mg/kg; 21-day cycles	400 mg; 2x daily
Group size	n = 478	n = 476	n = 336	n = 165
Median OS (95% CI)*	13.6 (12.1-14.9)	12.3 (10.4-13.9)	NE	13.2 (10.4-NE)
HR (95% CI) of OS	0.92 (0.79-1.06)		0.58 (0.42-0.79)	
P-value OS	not significant		0.0006	
Median PFS (95% CI)*	7.3 (5.6-7.5)	3.6 (3.6-3.9)	6.8 (5.7-8.3)	4.3 (4.0-5.6)
HR (95% CI) of PFS	0.65 (0.56-0.77)		0.59 (0.47-0.76)	
P-value PFS	<0.0001		<0.0001	

*atezo., atezolizumab; bev., bevaciumab; CI, confidence interval; HR, hazard ratio; NE, non-estimable; PFS, progression-free survival; median OS and PFS are shown in months (Cheng et al., 2019; Kudo et al., 2018a).

In summary, lenvatinib evoked as first-line treatment alternative to sorafenib in unresectable HCC and also immunotherapy has the potential to be practice changing. However, an optimal treatment strategy that includes lenvatinib has still to be defined and the impact of different regional etiologies and ethnicities on treatment success remains elusive. The REFLECT trial enrolled 33% of patients from western countries and 67% from the Asia-Pacific region. As already shown for sorafenib in the SHARP (Llovet et al., 2008) and AP-trial (Cheng et al., 2009), therapeutic success may yield locally discrepant outcomes. Thus, major efforts are ongoing in order to identify molecular biomarkers that may guide the choice of a preferable first-line treatment strategy (Capozzi et al., 2019).

Notably, as for sorafenib, most HCC patients also develop resistance to lenvatinib and, so far, there is no information on the mechanistic background. We hypothesize that the mechanisms of sorafenib resistance presented herein might be applicable for various multikinase inhibitors and, therefore, provide the basis for ongoing studies on lenvatinib resistance (Ardelt, M. A., unpublished data).

Most recently, also novel second-line treatment options were developed for advanced-stage HCC, which, however, have been proven effective only in sorafenib-experienced patients. Although the spectrum of kinase inhibition generated by lenvatinib and sorafenib is overlapping, lenvatinib more potently inhibits VEGFR than sorafenib and additionally targets fibroblast growth factor receptors (FGFRs) (Yamamoto et al., 2014). Thus, post-study survivals and the efficacy of second-line therapies might differ when applied after first-line lenvatinib, which supports a favorable role of sorafenib until clinical evidence on the optimal drug sequencing after lenvatinib is provided.

6.3.4.2 Second-line therapeutic options for sorafenib-experienced patients

In 2017, the TKI regorafenib was granted approval as the first second-line therapy to sorafenib in advanced-stage HCC. The mechanism of action of both drugs is similar due to their structural similarity, but not identical. In comparison to sorafenib, regorafenib shows more potent activity against VEGFR, c-Kit, and partially blocks TIE2, which is not a target of sorafenib (Wilhelm et al., 2011). Notably, the RESORCE trial only included patients who tolerated at least 400 mg/day of sorafenib (Bruix et al., 2017; Reig et al., 2018). However, it has been previously reported that the OS of patients who discontinued sorafenib because of adverse events is better than that of patients who discontinued sorafenib because of tumor progression *(Figure 38)* (Iavarone et al., 2015). Thus, regorafenib is not only limited to a subset of patients, but its efficiency may be overestimated by recruiting a biased study cohort with particularly poor OS. We suggest that this poor survival after treatment discontinuation indicates rapid tumor regrowth upon sorafenib retraction, making these patients potential candidates for a second-line therapy with translation-inhibiting antibiotics.

Unfortunately, most of subsequent phase III trials failed to demonstrate improvement in OS or were successful only for a predefined subset of patients, such as REACH-2 *(Table 1; chapter 2.1.2.2.2)*. In 2018, the phase III trial CELESTIAL was announced positive as the small molecule TKI cabozantinib significantly improved OS of both patients with progressive disease and sorafenib-

intolerant patients. However, regarding safety, 62% of patients in the cabozantinib arm required dose reduction and 16% of patients discontinued therapy due to treatment-related hand-foot syndrome (17%), hypertension (16%), fatigue (10%) or diarrhea (10%) (Abou-Alfa et al., 2018a).

Almost simultaneously, the immune checkpoint inhibitors nivolumab and pembrolizumab were conditionally approved by the FDA as second-line therapies for sorafenib-experienced HCC (El-Khoueiry et al., 2017; Zhu et al., 2018a). Both drugs achieved durable responses, long-term survival, and favorable safety profiles in phase I/II trials (Capozzi et al., 2019). Although a phase III trial of second-line pembrolizumab (KEYNOTE-240) failed to reach significance, PFS was prolonged and mortality reduced by 22% *(Figure 38)* (Liu et al., 2019). Based on these promising results and positive preliminary endpoints of a CHECKMATE-040 cohort with 49 patients, the FDA further approved the combination of nivolumab and ipilimumab for HCC in march 2020 (FDA, 2020).

Besides numerous recent approvals, immunotherapy for HCC is still in its infancy and yet faces limitations. Resistance is complex and involves mutations affecting immunogenicity of cancers (Wnt/CTNNB1 mutation in ~37% of patients), defective cytokine signaling, and upregulation of evasive immune checkpoint pathways (Xu et al., 2019). In addition, reports of hyperprogressors upon immunotherapy of advanced-stage malignancies have emerged (Champiat et al., 2017). Thus, the identification of biomarkers remains an area of active research to predict nonresponders and hyperprogressors, in order to provide personalized therapeutic strategies in the future.

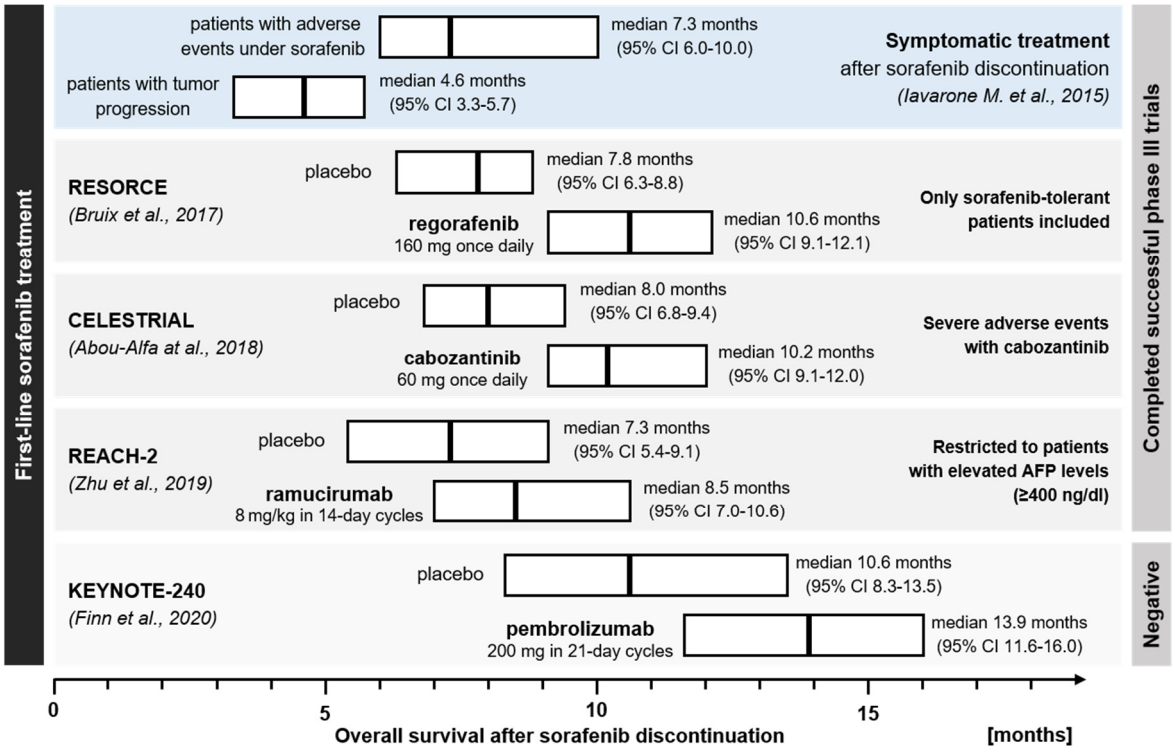

***Figure 38*. Overall survival of patient cohorts that were enrolled in clinical phase III trials of approved second-line treatment options after sorafenib discontinuation.** The median overall survival (in months) with corresponding 95% confidence intervals (95% CI) for each experimental and placebo arm are illustrated.

6.4 Conclusion

Acquired sorafenib resistance occurs frequently during therapy of HCC and is accompanied by a rapid recurrence of tumor growth after sorafenib treatment termination. In this study we aimed to characterize the underlying mechanism of sorafenib resistance and the unfavorable resumption of cancer cell proliferation to provide the basis for a potential second-line therapeutic approach.

We provided evidence that sorafenib-resistant HCC exhibits mitochondrial dysfunction and chemotherapeutic cross-resistance, but resensitized upon sorafenib withdrawal. This suggests that a second-line therapy following sorafenib retraction may be beneficial in comparison to an adjuvant treatment. Importantly, we found that a drastic renewal of mitochondrial structures and a metabolic switch toward high respiratory chain activity resulted in a relapse of tumor growth upon sorafenib withdrawal. Inhibition of the biogenesis of mtDNA-encoded ETC subunits using the antibiotic TGC impaired mitochondrial translation, the cellular antioxidant defense and limited the electron acceptor turnover required for proliferation-fueling glutamine oxidation. Thereby, TGC efficiently prevented the therapy-limiting tumor growth resumption *in vitro* and *in vivo*.

So far, numerous alternative molecular-targeted agents have been developed and tested in clinical trials; however, all have failed to prolong OS compared to sorafenib in a systemic first-line setting. An improved OS was obtained with both regorafenib and ramucirumab second-line to sorafenib, but its applications are restricted to sorafenib-tolerant patients for regorafenib and patients with elevated AFP levels for ramucirumab, respectively. As second-line cabozantinib is associated with severe adverse-events, a second-line therapy to sorafenib with a reliable safety profile for sorafenib-intolerant HCC patients still remains an urgent need. Thus, the results presented herein offer a novel promising second-line therapeutic approach for both sorafenib-resistant and sorafenib-intolerant advanced-stage HCC patients. Approved bacterial translation-inhibiting antibiotics are characterized by favorable safety profiles with low incidence of adverse side-effects and good experience on dosing schedules, therefore holding tremendous promise for clinical translation. In contrast to other available second-line options, tigecycline counteracts the metabolic origin of tumor relapse and may, thus, be a promising therapeutic option for sorafenib-experienced patients with progressive disease. In summary, we encourage a clinical evaluation of TGC for a new designation in advanced-stage HCC, to prevent tumor relapse and prolong the life expectancy after sorafenib failure.

SUPPLEMENTARY

7 SUPPLEMENTARY

7.1 EMT-mediated reversible cross-resistance of HUH7-R cells

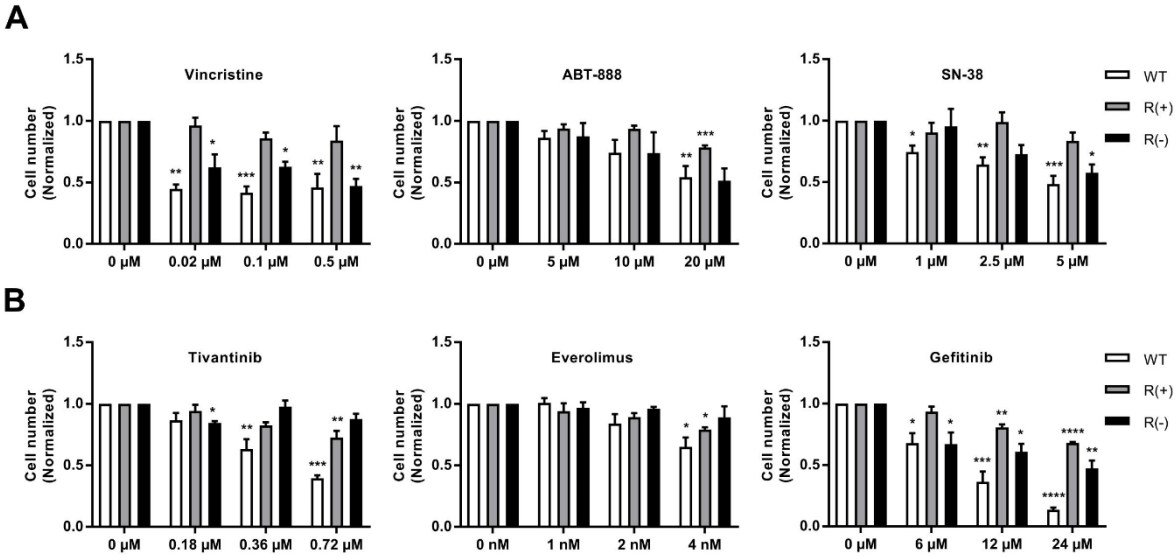

Figure S1. **Broad chemoresistance and resensitization after sorafenib withdrawal. (A)** Cross-resistance of HUH7-R(+) cells upon sorafenib-exposure was also obtained for: chemotherapeutics as the microtubule-binding alkaloid vincristine, the PARP-inhibitor ABT-888, the topoisomerase I inhibitor SN-38, **(B)** the mTOR-inhibitor everolimus as well as the MET-, respective EGF-receptor inhibitors tivantinib and gefitinib. Proliferation rates within 72 h of treatment were normalized to the untreated control. Values denoted as ± SEM, n=3, *p<0.05, **p<0.01, ***p<0.001, ****p<0.0001 (ANOVA). Figure is related to **Figure 8**.

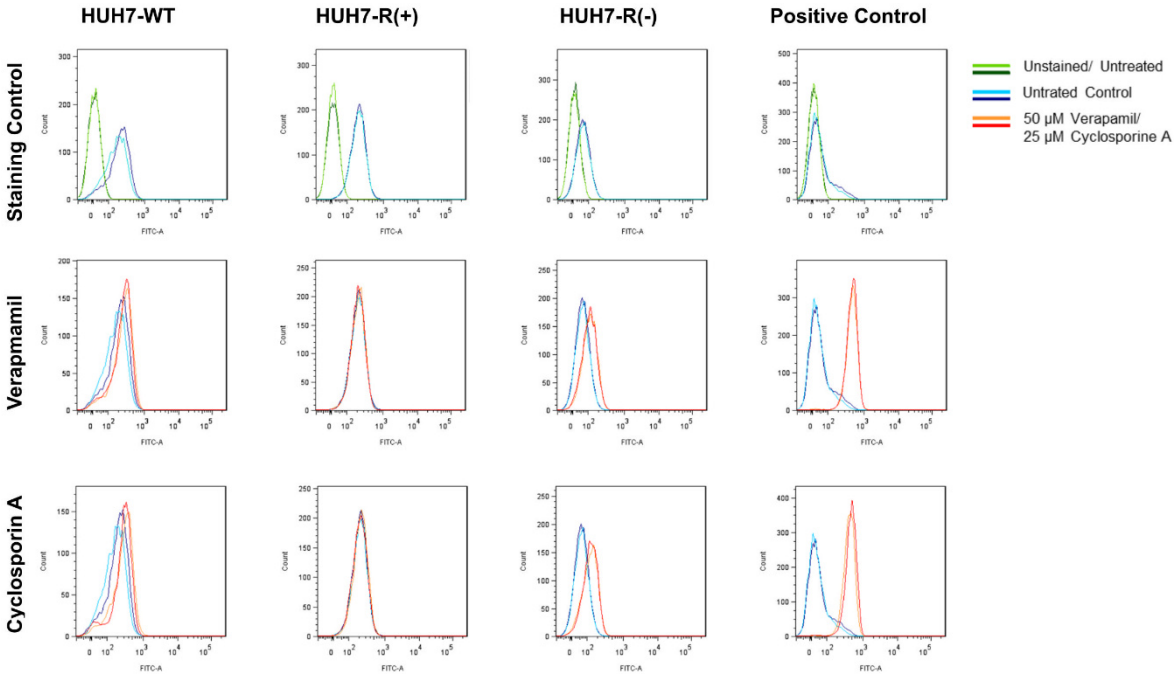

Figure S2. **The MDR-proteins P-gp and MRP are not involved in the broad resistance spectrum of HUH7-R(+) cells upon sorafenib exposure.** Calcein retention was assessed by flow cytometry and MDR-positive vincristine-resistant CEM/VCR-R cells (Haber et al., 1989) were used as a positive control. Verapamil and cyclosporine A block MDR-transporters causing a shift in intracellular calcium retention.

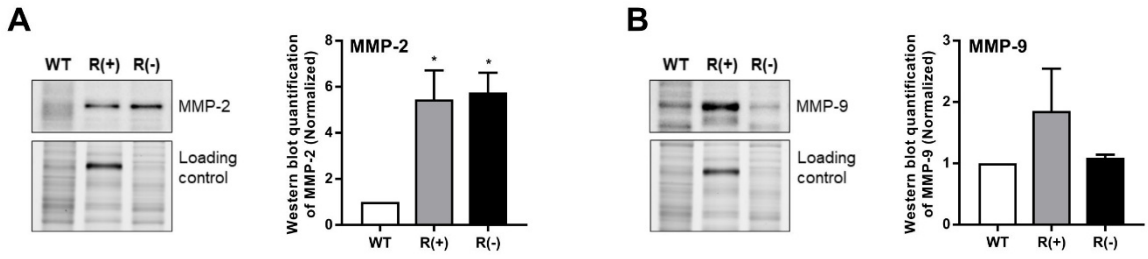

Figure S3. **Matrix metalloproteinase (MMP)-2 and MMP-9 might be involved in conferring invasive potential to HUH7-R cells *in vivo (Figure 7)*. (A)** Immunoblot analysis of MMP-2 and **(B)** MMP-9, normalized to the protein load and to HUH7-WT. Values shown as ± SEM, n=3, *p<0.05 (ANOVA).

7.2 MS-proteomics screening and GSEA

A

Gene sets enriched in HUH7-R(-) vs. HUH7-R(+)	SIZE	ES	FDR q-val	NOM p-val
PROTEIN DIMERIZATION ACTIVITY	33	0,5518	0,2574	0,0000
REGULATION OF CELL CYCLE	19	0,6428	0,1378	0,0000
PROTEIN COMPLEX	184	0,3292	0,3541	0,0020
CELL CYCLE (Gene ontology)	44	0,4851	0,3119	0,0021
PROTEIN HETERODIMERIZATION ACTIVITY	22	0,6044	0,1185	0,0042
CHROMOSOMAL PART	20	0,5714	0,2523	0,0079
PURINE NUCLEOTIDE BINDING	29	0,5014	0,2304	0,0081
CELL CYCLE(KEGG)	23	0,5476	0,2519	0,0084
OOCYTE MEIOSIS	23	0,5465	0,2176	0,0097
MITOTIC CELL CYCLE	24	0,5246	0,2124	0,0104

B

Gene sets enriched in HUH7-R(+) vs. HUH7-WT	SIZE	ES	FDR q-val	NOM p-val
EPITHELIAL CELL SIGNALING IN HELICOBACTER PYLORI INFECTION	15	0,7161	0,0290	0,0000
REGULATION OF CELL PROLIFERATION	27	0,5524	0,0714	0,0000
TRANSITION METAL ION BINDING	15	0,5511	0,2123	0,0364
STRUCTURAL CONSTITUENT OF CYTOSKELETON	17	0,4778	0,5426	0,0632
REGULATION OF CELLULAR COMPONENT ORGANIZATION AND BIOGENESIS	28	0,3360	1,0000	0,1892
IMMUNE SYSTEM PROCESS	17	0,4076	1,0000	0,1979
CITRATE CYCLE TCA CYCLE	16	0,3813	1,0000	0,2126
AMINOACYL TRNA BIOSYNTHESIS	18	0,3647	1,0000	0,2264
STRUCTURAL MOLECULE ACTIVITY	91	0,2556	1,0000	0,2286
ORGAN DEVELOPMENT	44	0,2881	1,0000	0,2462

C

Gene sets enriched in HUH7-WT vs. HUH7-R(-)	SIZE	ES	FDR q-val	NOM p-val
RECEPTOR ACTIVITY	23	-0,6424	0,7689	0,0023
ARGININEAND PROLINE METABOLISM	22	-0,6076	1,0000	0,0197
RESPONSE TO CHEMICAL STIMULUS	39	-0,5500	1,0000	0,0141
ALZHEIMERS DISEASE	48	-0,5216	1,0000	0,0128
ENZYME ACTIVATOR ACTIVITY	15	-0,6181	1,0000	0,0479
RESPONSE TO STRESS	64	-0,4846	1,0000	0,0146
OXIDATIVE PHOSPHORYLATION	42	-0,5183	1,0000	0,0290
PARKINSONS DISEASE	40	-0,5152	1,0000	0,0319
ACTIVE TRANSMEMBRANE TRANSPORTER ACTIVITY	17	-0,5836	1,0000	0,0604
MITOCHONDRIAL MEMBRANE PART	21	-0,5538	1,0000	0,0735

D

Gene sets enriched in HUH7-R(-) vs. HUH7-WT	SIZE	ES	FDR q-val	NOM p-val
RIBOSOME	70	0,3001	0,3393	0,0000
STRUCTURAL MOLECULE ACTIVITY	91	0,2800	0,3657	0,0000
TRANSLATION INITIATION FACTOR ACTIVITY	17	0,4820	0,2031	0,0118
EPITHELIAL CELL SIGNALING IN HELICOBACTER PYLORI INFECTION	15	0,6044	0,0877	0,0165
REGULATION OF CELL PROLIFERATION	27	0,4489	0,2391	0,0256
ADHERENS JUNCTION	27	0,4008	0,2620	0,0385
TRANSITION METAL ION BINDING	15	0,4504	0,4260	0,0914
IMMUNE SYSTEM PROCESS	17	0,4238	0,3879	0,1149
STRUCTURAL CONSTITUENT OF CYTOSKELETON	17	0,4150	0,3858	0,1311
WNT SIGNALING PATHWAY	21	0,3714	0,4059	0,1400

Figure S4. **GSEA of the sorafenib-resistant rebound growth model. (A)** Gene sets enriched in HUH7-R(-) cells compared to HUH7-R(+), **(B)** Gene sets enriched in HUH7-R(+) cells compared to HUH7-WT, **(C)** Gene sets enriched in HUH7-WT cells compared to HUH7-R(-) and **(D)** Gene sets enriched in HUH7-R(-) cells compared to HUH7-WT. The top 10 upregulated gene sets, ranked according to their nominal p-value (NOM p-val) are shown. Gene sets with NOM p-val<0.01 are highlighted. ES: enrichment score, NES: normalized enrichment score, FDR: false discovery rate. Figure is related to **Figure 10**.

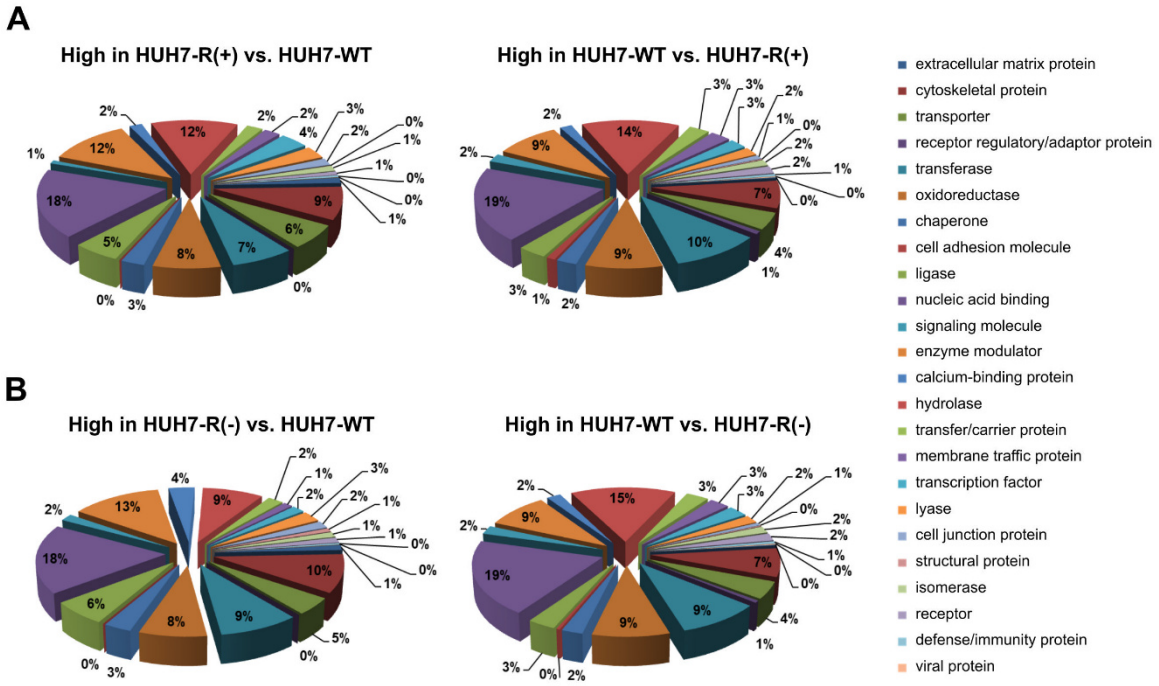

Figure S5. **Composition of protein classes largely maintained upon sorafenib resistance. (A)** Similar distribution of protein classes obtained in HUH7-R(+) cells compared to HUH7-WT. Protein classes that are >1.5-fold altered are shown. **(B)** Decreased abundance of hydrolases is associated with the sorafenib resistance phenotype. Protein classes that are >1.5-fold altered in HUH7-R(-) cells vs. HUH7-WT are shown. Analysis was performed with pantherdb.org (Gene ontology database). Figure is related to **Figure 12**.

7.3 Normalization of the cellular volume of HUH7-R cells

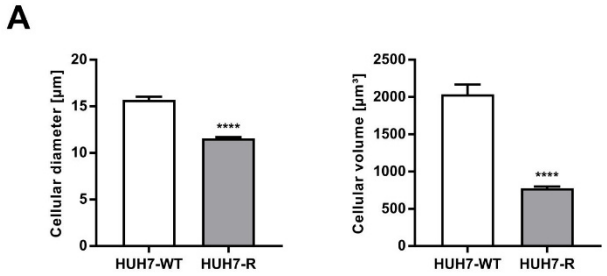

B

Cell type	Diameter [µm]	Volume [µm³]
HUH7-WT	15.71 ± 0.34	2036.58 ± 130.60
HUH7-R	11.57 ± 0.14	776.41 ± 23.00
Normalization factor of cellular volume		2,62

Figure S6. **Determination of normalization factor for cellular volume. (A)** HUH7-R cells have a significantly decreased cellular volume compared to HUH7-WT cells. The cellular diameter of HUH7-WT and HUH7-R cells (left) was assessed via image analysis by the ViCell cell counter and used for calculation of the cellular volume (right). **(B)** The ratio of cellular volume of HUH7-WT and HUH7-R cells results in a correction factor used for normalization of cellular fluorescent intensities obtained by flow cytometry, cellular ATP levels and cellular oxygen consumption. Values shown as ± SEM, n=4, ****p<0.0001 (t-test).

7.4 Autophagy upon rebound growth

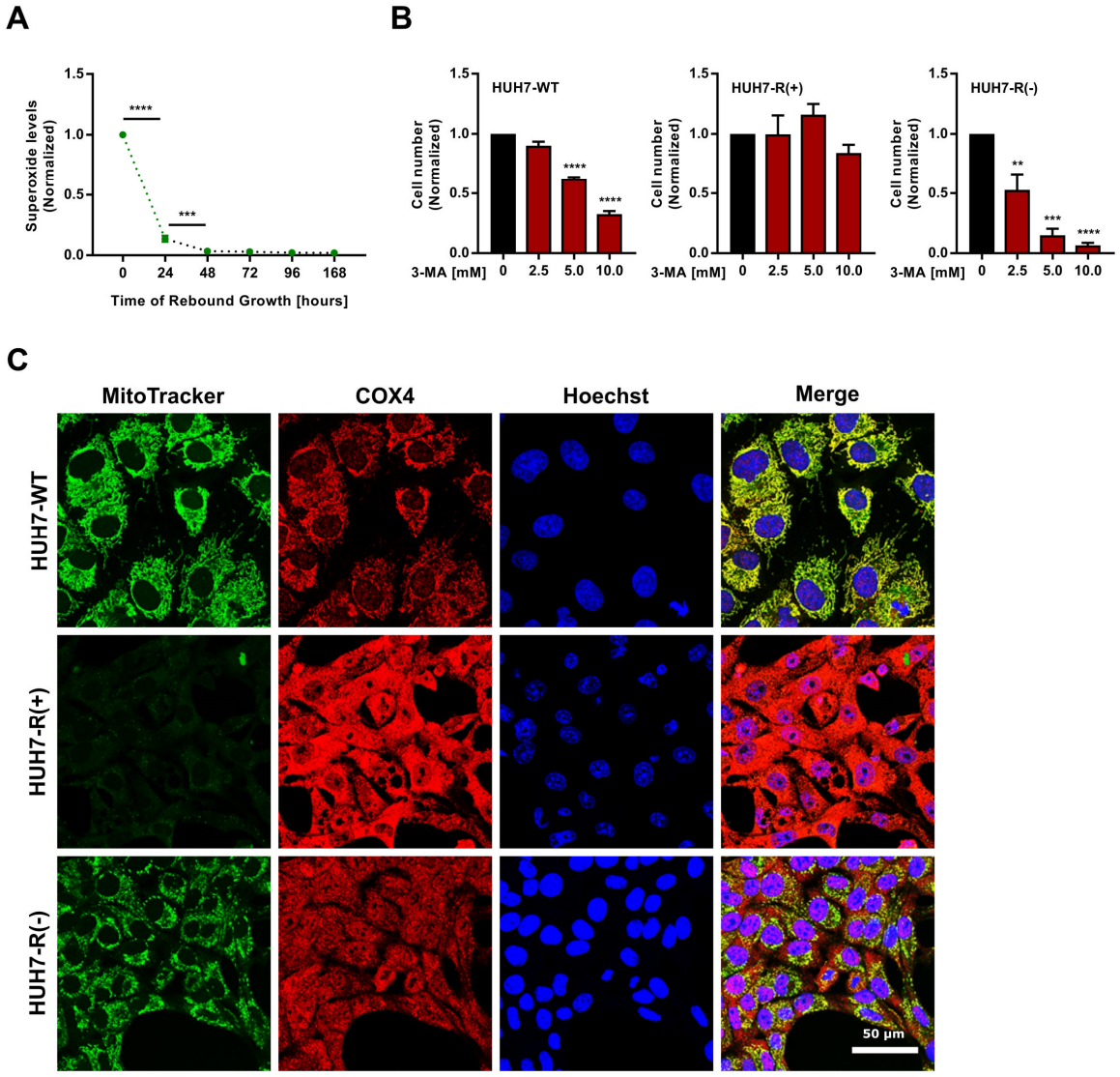

Figure S7. **Damaged mitochondria are degraded upon rebound growth. (A)** Sorafenib causes excessive superoxide production in HUH7-R(+) cells. Superoxide levels were assessed by flow cytometry upon rebound growth at the indicated time points and normalized to the superoxide abundance of HUH7-R(+) cells. **(B)** HUH7-R(-) cells show highest susceptibility towards autophagy inhibition by 3-MA. Proliferation rates within 72 h of treatment were assessed for HUH7-WT, HUH7-R(+) and HUH7-R(-) cells and normalized to the untreated control. **(C)** Localization of MitoTracker dye indicates mitochondrial biogenesis in HUH7-R(-) cells. Membrane potential-dependent staining (MitoTracker, green) and immunostaining (COX4, red) of the mitochondrial network after fixation are shown. Cell nuclei were stained with Hoechst33342 (blue). Scale bar indicates 50 µm. Values denoted as ± SEM, n=3, **p<0.01, ***p<0.001, ****p<0.0001 (ANOVA). Figure is related to **Figure 18**.

7.5 ATG5-independent autophagy in HUH7-R cells

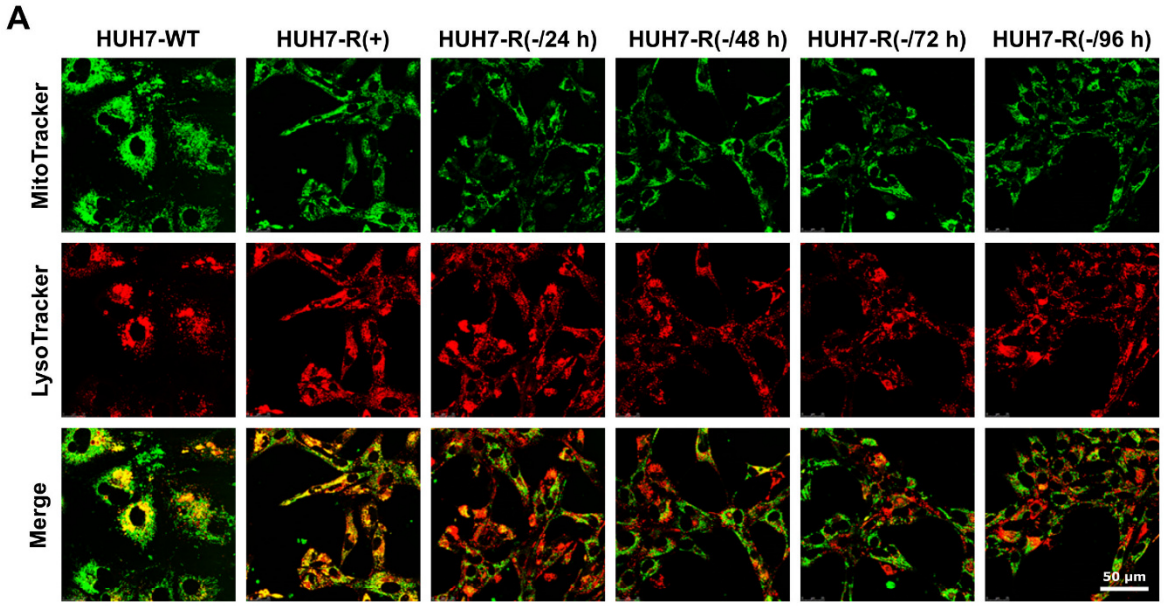

B

The Bliss Value (BV) was evaluated by comparing the effects of drug A (E_A) and drug B (E_B) with the effect of the combination of both drugs (E_{AB}) according to the following formula:

$$BV = \frac{E_{AB}}{(E_A + E_B) - (E_A \times E_B)}$$

Result	BV
synergism	>1.05
antagonism	<0.95
additivity	0.95-1.05

Cell line	Compound	E_A	E_B (3-MA)	E_{AB}
HUH7-WT	CHA 25 µM	0,066		0,482
	TGC 25 µM	0,147	0,376	0,510
	MB6 10 µM	0,321		0,771
HUH7-R(-)	CHA 25 µM	0,246		0,902
	TGC 25 µM	0,173	0,850	0,911
	MB6 10 µM	0,487		0,963

C

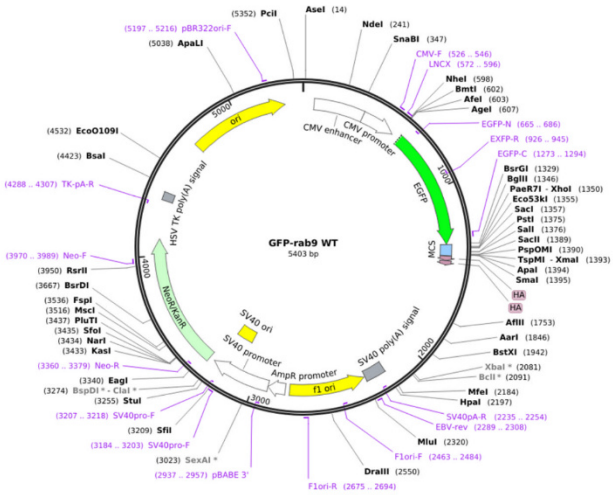

Figure S8. **Mitophagy of HUH7-R cells might be independent of autophagosome fusion to lysosomes.** **(A)** No colocalization of mitochondria and lysosomes upon rebound growth. Colocalization (yellow) of MitoTracker (green) and LysoTracker (red) live cell staining indicates mitophagy and was assessed in HUH7-WT, HUH7-R(+) cells and over the course of rebound growth. Scale bar indicates 50 µm. **(B)** Synergism of 3-MA and inhibitors of mitochondrial biogenesis was calculated using the Bliss Independence model (Berenbaum, 1989). **(C)** Map of the Rab9-GFP plasmid. Figure is related to **Figure 19.**

7.6 LC-MS/MS-based lipidomics analysis

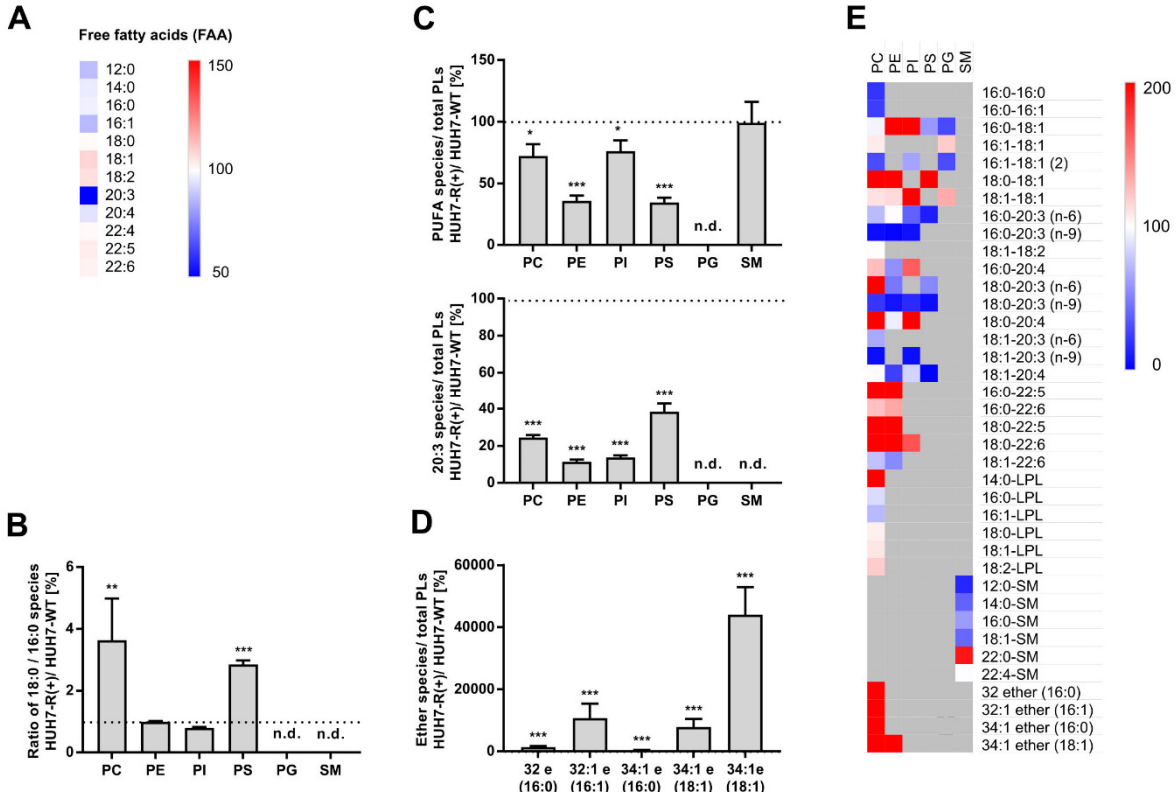

Figure S9. **Adaption of the lipidome to the excessive ROS exposure in HUH7-R(+) cells. (A)** The 20:3 FAA subspecies was reduced in HUH7-R(+) cells. The abundance of FAA subspecies in HUH7-R(+) cells compared to HUH7-WT is shown. The heatmap (relative abundance in HUH-R(+) cells) is color-coded from blue (50%) to white (100%) to red (200%). **(B)** Increase of long-chain FAs as compensation for reduction of 20:3 FFAs. The 18:0/16:0 ratio of FAs was normalized to the total level of phospholipids (PLs), comparing HUH7-R(+) cells to HUH7-WT cells. **(C)** Reduction of the 20:3 PL subspecies causes overall reduction of polyunsaturated fatty acids (PUFAs). PUFAs and 20:3 PL subspecies were normalized to the total abundance of PLs, comparing HUH7-R(+) cells to HUH7-WT cells. **(D)** High abundance of ether-phospholipids in HUH7-R(+) cells. Ether-PL subspecies were normalized to the total abundance of PLs, comparing HUH7-R(+) cells to HUH7-WT cells. **(E)** Overview of the saturation of all measured PLs in HUH7-R(+) cells in comparison to HUH7-WT is shown. The heatmap is color-coded from blue (0%) to white (100%) to red (200%).Values denoted as ± SEM, n=3, *p<0.05, **p<0.01, ***p<0.001 (ANOVA). Figure is related to **Figure 22**.

7.7 The rebound growth model with sorafenib-resistant RIL175-R cells

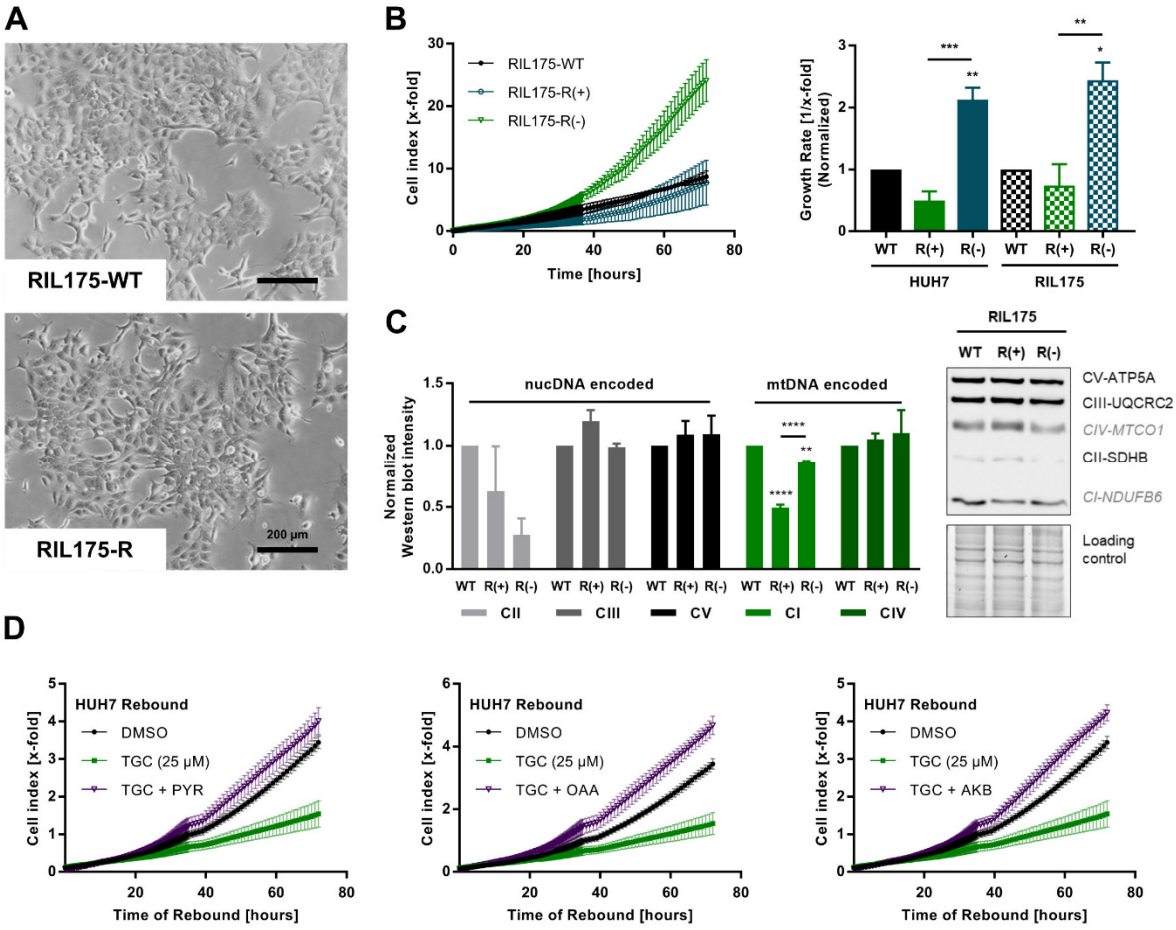

Figure S10. **The sorafenib-resistant HCC rebound growth model with RIL175 cells. (A)** RIL175 cells do not alter their morphology upon acquired sorafenib resistance. Phase-contrast microscopy of wild-type (RIL175-WT) and sorafenib-resistant (RIL175-R) RIL-175 cells. Scale bars indicate 200 µm. **(B)** Sorafenib withdrawal from RIL175-R cells continuously cultured in 10 µM sorafenib (RIL175-R(+)) leads to significantly increased resumption of proliferation. Cells upon rebound growth were cultured, as already described for HUH7-R cells, without sorafenib for 72 h before seeding (RIL175 R(-)). Proliferation rates, which were assessed by impedance measurement are shown as cell counts (cell index) over time (left). Growth rates of HUH7-R and RIL175-R treated upon rebound growth were calculated from the cell counts over 72 h (right). For proliferation curves over time of HUH7 cells see *Figure 8 A*. **(C)** Protein expression of NDUF is impaired in RIL175-R(+) cells and relapses upon sorafenib withdrawal. Immunoblot quantification of mtDNA- (CI-NDUFB6, CIV-MTCO1) and nucDNA-encoded ETC-subunits (CII-SDHB, CIII-UQCRC2, CV-ATP5A) was normalized to RIL175-WT (ANOVA). **(D)** Rebound growth rescue for the electron acceptors PYR, OAA and AKB confirmed in HUH7-R cells by impedance measurements. The calculated growth rates over 72 h for AKB are shown in *Figure 28 D* (bottom). Values are shown as ± SEM, n=3, *p<0.05, **p<0.01, ***p<0.001, ****p<0.0001 (ANOVA). Figure is related to **Figure 6** and **Figure 28**.

7.8 *In vivo* long-term treatment with TGC second-line to sorafenib

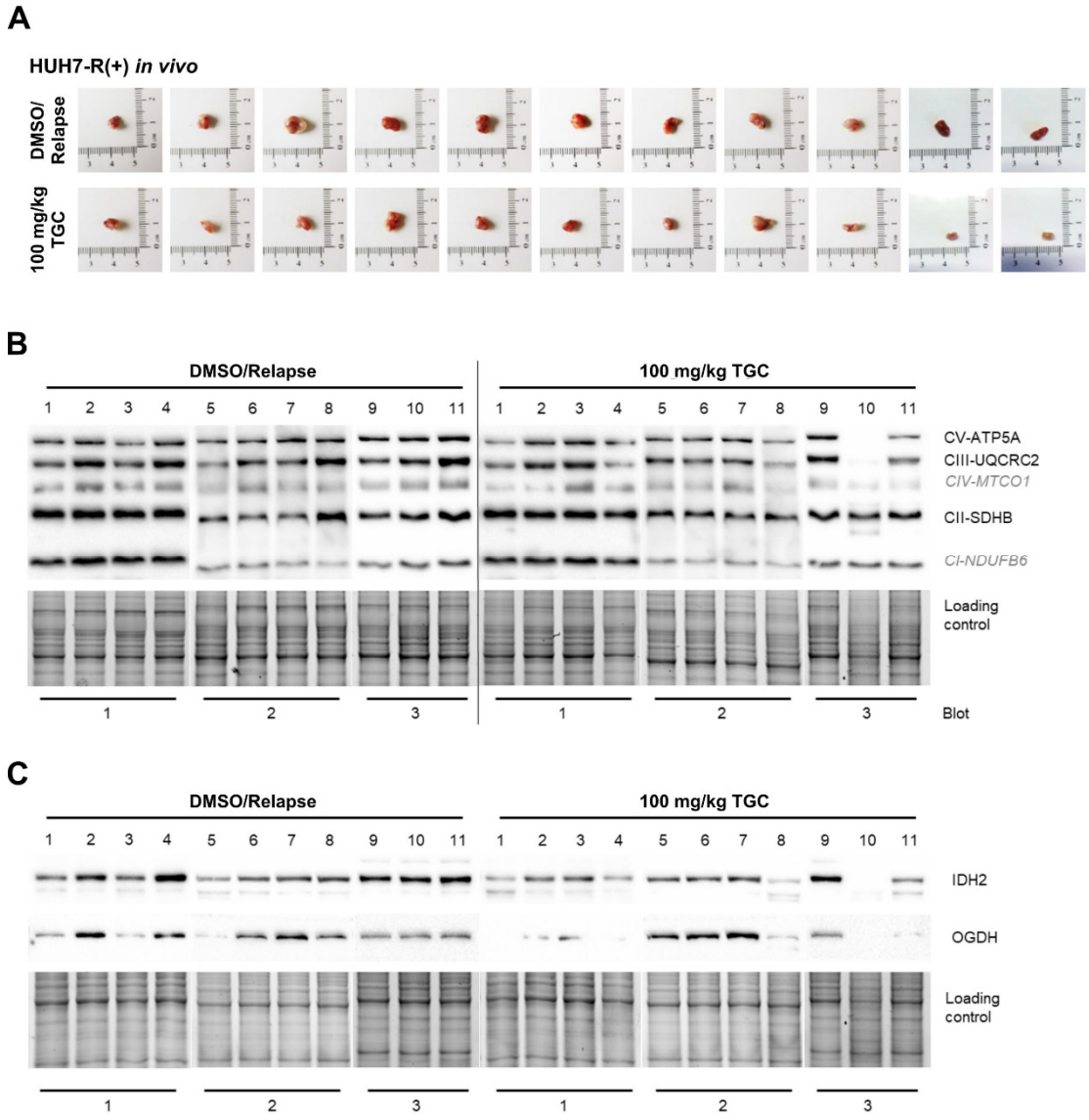

Figure S11. **TGC has no impact on the protein expression of ETC subunits, IDH2 or OGDH upon long-term treatment (14 days). (A)** The size of resected tumors *(Figure 35 B)* was decreased in tendency in the TGC treated group. **(B)** Immunoblot analysis of resected tumors for the ETC subunits and **(C)** the TCA cycle enzymes IDH2 and OGDH is shown. For quantification *(Figure 35 C-D),* immunoblots were normalized to the protein load and to the mean band intensity of the respective blot. Figure is related to **Figure *35***.

REFERENCES

8 CITATIONS

Abdel-Aziz, A. K., Abdel-Naim, A. B., Shouman, S., Minucci, S., and Elgendy, M. (2017). From Resistance to Sensitivity: Insights and Implications of Biphasic Modulation of Autophagy by Sunitinib. Front Pharmacol *8*, 718.

Abou-Alfa, G. K., Johnson, P., Knox, J. J., Capanu, M., Davidenko, I., Lacava, J., Leung, T., Gansukh, B., and Saltz, L. B. (2010). Doxorubicin plus sorafenib vs doxorubicin alone in patients with advanced hepatocellular carcinoma: a randomized trial. Jama *304*, 2154-2160.

Abou-Alfa, G. K., Meyer, T., Cheng, A.-L., El-Khoueiry, A. B., Rimassa, L., Ryoo, B.-Y., Cicin, I., Merle, P., Park, J.-W., Blanc, J.-F.*, et al.* (2018a). Cabozantinib (C) versus placebo (P) in patients (pts) with advanced hepatocellular carcinoma (HCC) who have received prior sorafenib: Results from the randomized phase III CELESTIAL trial. Journal of Clinical Oncology *36*, 207-207.

Abou-Alfa, G. K., Qin, S., Ryoo, B. Y., Lu, S. N., Yen, C. J., Feng, Y. H., Lim, H. Y., Izzo, F., Colombo, M., Sarker, D.*, et al.* (2018b). Phase III randomized study of second line ADI-PEG 20 plus best supportive care versus placebo plus best supportive care in patients with advanced hepatocellular carcinoma. Annals of oncology : official journal of the European Society for Medical Oncology *29*, 1402-1408.

Ahn, C. S., and Metallo, C. M. (2015). Mitochondria as biosynthetic factories for cancer proliferation. Cancer Metab *3*, 1-1.

Al-Rajabi, R., Patel, S., Ketchum, N. S., Jaime, N. A., Lu, T.-W., Pollock, B. H., and Mahalingam, D. (2015). Comparative dosing and efficacy of sorafenib in hepatocellular cancer patients with varying liver dysfunction. Journal of gastrointestinal oncology *6*, 259-267.

Altekruse, S. F., McGlynn, K. A., and Reichman, M. E. (2009). Hepatocellular carcinoma incidence, mortality, and survival trends in the United States from 1975 to 2005. Journal of clinical oncology : official journal of the American Society of Clinical Oncology *27*, 1485-1491.

Altman, B. J., Stine, Z. E., and Dang, C. V. (2016). From Krebs to clinic: glutamine metabolism to cancer therapy. Nature reviews Cancer *16*, 619-634.

Anderson, G. R., Wardell, S. E., Cakir, M., Yip, C., Ahn, Y.-r., Ali, M., Yllanes, A. P., Chao, C. A., McDonnell, D. P., and Wood, K. C. (2018). Dysregulation of mitochondrial dynamics proteins are a targetable feature of human tumors. Nature Communications *9*, 1677.

Ashkenazi, A., Fairbrother, W. J., Leverson, J. D., and Souers, A. J. (2017). From basic apoptosis discoveries to advanced selective BCL-2 family inhibitors. Nature reviews Drug discovery *16*, 273-284.

Avril, T., Vauléon, E., and Chevet, E. (2017). Endoplasmic reticulum stress signaling and chemotherapy resistance in solid cancers. Oncogenesis *6*, e373.

Baecker, A., Liu, X., La Vecchia, C., and Zhang, Z.-F. (2018). Worldwide incidence of hepatocellular carcinoma cases attributable to major risk factors. Eur J Cancer Prev *27*, 205-212.

Bagri, A., Berry, L., Gunter, B., Singh, M., Kasman, I., Damico, L. A., Xiang, H., Schmidt, M., Fuh, G., Hollister, B.*, et al.* (2010). Effects of Anti-VEGF Treatment Duration on Tumor Growth, Tumor Regrowth, and Treatment Efficacy. Clinical Cancer Research *16*, 3887.

Barban, S., and Schulze, H. O. (1961). The effects of 2-deoxyglucose on the growth and metabolism of cultured human cells. The Journal of biological chemistry *236*, 1887-1890.

Batlle, E., Sancho, E., Francí, C., Domínguez, D., Monfar, M., Baulida, J., and García de Herreros, A. (2000). The transcription factor Snail is a repressor of E-cadherin gene expression in epithelial tumour cells. Nature Cell Biology *2*, 84-89.

Benz, R., and McLaughlin, S. (1983). The molecular mechanism of action of the proton ionophore FCCP (carbonylcyanide p-trifluoromethoxyphenylhydrazone). Biophys J *41*, 381-398.

Berenbaum, M. C. (1989). What is synergy? Pharmacological reviews *41*, 93-141.

Birsoy, K., Wang, T., Chen, W., Freinkman, E., Abu-Remaileh, M., and Sabatini, D. M. (2015). An essential role of the mitochondrial electron transport chain in cell proliferation is to enable aspartate synthesis. Cell *162*, 540-551.

Bismuth, H., and Majno, P. E. (2000). Hepatobiliary surgery. Journal of hepatology *32*, 208-224.

Blum, R. H., Carter, S. K., and Agre, K. (1973). A clinical review of bleomycin--a new antineoplastic agent. Cancer *31*, 903-914.

Bosch, F. X., Ribes, J., Diaz, M., and Cleries, R. (2004). Primary liver cancer: worldwide incidence and trends. Gastroenterology *127*, S5-s16.

Boudou-Rouquette, P., Ropert, S., Mir, O., Coriat, R., Billemont, B., Tod, M., Cabanes, L., Franck, N., Blanchet, B., and Goldwasser, F. (2012). Variability of sorafenib toxicity and exposure over time: a pharmacokinetic/pharmacodynamic analysis. Oncologist *17*, 1204-1212.

Bradford, M. M. (1976). A rapid and sensitive method for the quantitation of microgram quantities of protein utilizing the principle of protein-dye binding. Analytical biochemistry *72*, 248-254.

Bradford, P. A., Weaver-Sands, D. T., and Petersen, P. J. (2005). In vitro activity of tigecycline against isolates from patients enrolled in phase 3 clinical trials of treatment for complicated skin and skin-structure infections and complicated intra-abdominal infections. Clinical infectious diseases : an official publication of the Infectious Diseases Society of America *41 Suppl 5*, S315-332.

Browning, J. D., and Horton, J. D. (2004). Molecular mediators of hepatic steatosis and liver injury. The Journal of Clinical Investigation *114*, 147-152.

Bruix, J., and Llovet, J. M. (2002). Prognostic prediction and treatment strategy in hepatocellular carcinoma. Hepatology (Baltimore, Md) *35*, 519-524.

Bruix, J., Qin, S., Merle, P., Granito, A., Huang, Y.-H., Bodoky, G., Pracht, M., Yokosuka, O., Rosmorduc, O., Breder, V.*, et al.* (2017). Regorafenib for patients with hepatocellular carcinoma who progressed on sorafenib treatment (RESORCE): a randomised, double-blind, placebo-controlled, phase 3 trial. The Lancet *389*, 56-66.

Bruix, J., Reig, M., and Sherman, M. (2016). Evidence-Based Diagnosis, Staging, and Treatment of Patients With Hepatocellular Carcinoma. Gastroenterology *150*, 835-853.

Bruix, J. a. S., M. (2011). Management of hepatocellular carcinoma: An update Hepatology (Baltimore, Md) *53*, 1020–1022.

Bugianesi, E. (2007). Non-alcoholic steatohepatitis and cancer. Clinics in liver disease *11*, 191-207, x-xi.

Cainap, C., Qin, S., Huang, W.-T., Chung, I. J., Pan, H., Cheng, Y., Kudo, M., Kang, Y.-K., Chen, P.-J., Toh, H.-C.*, et al.* (2015). Linifanib Versus Sorafenib in Patients With Advanced Hepatocellular Carcinoma: Results of a Randomized Phase III Trial. Journal of Clinical Oncology *33*, 172-179.

Cairns, R. A., Harris, I. S., and Mak, T. W. (2011). Regulation of cancer cell metabolism. Nature reviews Cancer *11*, 85-95.

Capozzi, M., De Divitiis, C., Ottaiano, A., von Arx, C., Scala, S., Tatangelo, F., Delrio, P., and Tafuto, S. (2019). Lenvatinib, a molecule with versatile application: from preclinical evidence to future development in anti-cancer treatment. Cancer Manag Res *11*, 3847-3860.

Cassago, A., Ferreira, A. P., Ferreira, I. M., Fornezari, C., Gomes, E. R., Greene, K. S., Pereira, H. M., Garratt, R. C., Dias, S. M., and Ambrosio, A. L. (2012). Mitochondrial localization and structure-based phosphate activation mechanism of Glutaminase C with implications for cancer metabolism. Proceedings of the National Academy of Sciences of the United States of America *109*, 1092-1097.

Cervello, M., Bachvarov, D., Lampiasi, N., Cusimano, A., Azzolina, A., McCubrey, J. A., and Montalto, G. (2012). Molecular mechanisms of sorafenib action in liver cancer cells. Cell cycle (Georgetown, Tex) *11*, 2843-2855.

Champiat, S., Dercle, L., Ammari, S., Massard, C., Hollebecque, A., Postel-Vinay, S., Chaput, N., Eggermont, A., Marabelle, A., Soria, J. C., and Ferte, C. (2017). Hyperprogressive Disease Is a New Pattern of Progression in Cancer Patients Treated by Anti-PD-1/PD-L1. Clinical cancer research : an official journal of the American Association for Cancer Research *23*, 1920-1928.

Chang, Y. S., Adnane, J., Trail, P. A., Levy, J., Henderson, A., Xue, D., Bortolon, E., Ichetovkin, M., Chen, C., McNabola, A.*, et al.* (2007). Sorafenib (BAY 43-9006) inhibits tumor growth and vascularization and induces tumor apoptosis and hypoxia in RCC xenograft models. Cancer chemotherapy and pharmacology *59*, 561-574.

Chen, K. F., Chen, H. L., Tai, W. T., Feng, W. C., Hsu, C. H., Chen, P. J., and Cheng, A. L. (2011). Activation of phosphatidylinositol 3-kinase/Akt signaling pathway mediates acquired resistance to sorafenib in hepatocellular carcinoma cells. The Journal of pharmacology and experimental therapeutics *337*, 155-161.

Chen, L., Zhang, Z., Hoshino, A., Zheng, H. D., Morley, M., Arany, Z., and Rabinowitz, J. D. (2019). NADPH production by the oxidative pentose-phosphate pathway supports folate metabolism. Nature Metabolism *1*, 404-415.

Chen, L. B. (1988). Mitochondrial membrane potential in living cells. Annual review of cell biology *4*, 155-181.

Cheng, A.-L., Kang, Y.-K., Chen, Z., Tsao, C.-J., Qin, S., Kim, J. S., Luo, R., Feng, J., Ye, S., Yang, T.-S.*, et al.* (2009). Efficacy and safety of sorafenib in patients in the Asia-Pacific region with advanced hepatocellular carcinoma: a phase III randomised, double-blind, placebo-controlled trial. The Lancet Oncology *10*, 25-34.

Cheng, A.-L., Kang, Y.-K., Lin, D.-Y., Park, J.-W., Kudo, M., Qin, S., Chung, H.-C., Song, X., Xu, J., Poggi, G.*, et al.* (2013). Sunitinib Versus Sorafenib in Advanced Hepatocellular Cancer: Results of a Randomized Phase III Trial. Journal of Clinical Oncology *31*, 4067-4075.

Cheng, A. L., Qin, S., Ikeda, M., Galle, P., Ducreux, M., Zhu, A., Kim, T. Y., Kudo, M., Breder, V., Merle, P.*, et al.* (2019). LBA3 - IMbrave150: Efficacy and safety results from a ph III study evaluating atezolizumab (atezo) + bevacizumab (bev) vs sorafenib (Sor) as first treatment (tx) for patients (pts) with unresectable hepatocellular carcinoma (HCC). Annals of Oncology *30*, ix186-ix187.

Cheng, C.-T., Qi, Y., Wang, Y.-C., Chi, K. K., Chung, Y., Ouyang, C., Chen, Y.-R., Oh, M. E., Sheng, X., Tang, Y., *et al.* (2018). Arginine starvation kills tumor cells through aspartate exhaustion and mitochondrial dysfunction. Communications Biology *1*, 178.

Chow, P. K. H., Gandhi, M., Tan, S. B., Khin, M. W., Khasbazar, A., Ong, J., Choo, S. P., Cheow, P. C., Chotipanich, C., Lim, K., *et al.* (2018). SIRveNIB: Selective Internal Radiation Therapy Versus Sorafenib in Asia-Pacific Patients With Hepatocellular Carcinoma. Journal of clinical oncology : official journal of the American Society of Clinical Oncology *36*, 1913-1921.

Christofk, H. R., Vander Heiden, M. G., Harris, M. H., Ramanathan, A., Gerszten, R. E., Wei, R., Fleming, M. D., Schreiber, S. L., and Cantley, L. C. (2008). The M2 splice isoform of pyruvate kinase is important for cancer metabolism and tumour growth. Nature *452*, 230-233.

Colombo, F., Trombetta, E., Cetrangolo, P., Maggioni, M., Razini, P., De Santis, F., Torrente, Y., Prati, D., Torresani, E., and Porretti, L. (2014). Giant Lysosomes as a Chemotherapy Resistance Mechanism in Hepatocellular Carcinoma Cells. PLOS ONE *9*, e114787.

Curi, R., Newsholme, P., and Newsholme, E. A. (1988). Metabolism of pyruvate by isolated rat mesenteric lymphocytes, lymphocyte mitochondria and isolated mouse macrophages. Biochem J *250*, 383-388.

da Silva, T. F., Sousa, V. F., Malheiro, A. R., and Brites, P. (2012). The importance of ether-phospholipids: A view from the perspective of mouse models. Biochimica et Biophysica Acta (BBA) - Molecular Basis of Disease *1822*, 1501-1508.

Dabir, D. V., Hasson, S. A., Setoguchi, K., Johnson, M. E., Wongkongkathep, P., Douglas, C. J., Zimmerman, J., Damoiseaux, R., Teitell, M. A., and Koehler, C. M. (2013). A small molecule inhibitor of redox-regulated protein translocation into mitochondria. Developmental cell *25*, 81-92.

Daher, S., Massarwa, M., Benson, A. A., and Khoury, T. (2018). Current and Future Treatment of Hepatocellular Carcinoma: An Updated Comprehensive Review. J Clin Transl Hepatol *6*, 69-78.

Dang, L., White, D. W., Gross, S., Bennett, B. D., Bittinger, M. A., Driggers, E. M., Fantin, V. R., Jang, H. G., Jin, S., Keenan, M. C., *et al.* (2009). Cancer-associated IDH1 mutations produce 2-hydroxyglutarate. Nature *462*, 739-744.

DeBerardinis, R. J., Lum, J. J., Hatzivassiliou, G., and Thompson, C. B. (2008). The biology of cancer: metabolic reprogramming fuels cell growth and proliferation. Cell Metab *7*, 11-20.

DeBerardinis, R. J., Mancuso, A., Daikhin, E., Nissim, I., Yudkoff, M., Wehrli, S., and Thompson, C. B. (2007). Beyond aerobic glycolysis: transformed cells can engage in glutamine metabolism that exceeds the requirement for protein and nucleotide synthesis. Proceedings of the National Academy of Sciences of the United States of America *104*, 19345-19350.

Degli Esposti, M. (1998). Inhibitors of NADH–ubiquinone reductase: an overview. Biochimica et Biophysica Acta (BBA) - Bioenergetics *1364*, 222-235.

di Tomaso, E., Snuderl, M., Kamoun, W. S., Duda, D. G., Auluck, P. K., Fazlollahi, L., Andronesi, O. C., Frosch, M. P., Wen, P. Y., Plotkin, S. R., *et al.* (2011). Glioblastoma Recurrence after Cediranib Therapy in Patients: Lack of "Rebound" Revascularization as Mode of Escape. Cancer research *71*, 19.

Dong, Z., Abbas, M. N., Kausar, S., Yang, J., Li, L., Tan, L., and Cui, H. (2019). Biological Functions and Molecular Mechanisms of Antibiotic Tigecycline in the Treatment of Cancers. Int J Mol Sci *20*, 3577.

Drose, S., and Brandt, U. (2012). Molecular mechanisms of superoxide production by the mitochondrial respiratory chain. Advances in experimental medicine and biology *748*, 145-169.

Dudek, J. (2017). Role of Cardiolipin in Mitochondrial Signaling Pathways. Frontiers in cell and developmental biology *5*, 90.

Duvvuri, M., Konkar, S., Funk, R. S., Krise, J. M., and Krise, J. P. (2005). A chemical strategy to manipulate the intracellular localization of drugs in resistant cancer cells. Biochemistry *44*, 15743-15749.

Ebos, J. M., Lee, C. R., Cruz-Munoz, W., Bjarnason, G. A., Christensen, J. G., and Kerbel, R. S. (2009). Accelerated metastasis after short-term treatment with a potent inhibitor of tumor angiogenesis. Cancer Cell *15*, 232-239.

Ebos, J. M. L., and Pili, R. (2012). Mind the Gap: Potential for Rebounds during Antiangiogenic Treatment Breaks. Clinical Cancer Research *18*, 3719.

El-Khoueiry, A. B., Sangro, B., Yau, T., Crocenzi, T. S., Kudo, M., Hsu, C., Kim, T.-Y., Choo, S.-P., Trojan, J., Welling, T. H., 3rd, *et al.* (2017). Nivolumab in patients with advanced hepatocellular carcinoma (CheckMate 040): an open-label, non-comparative, phase 1/2 dose escalation and expansion trial. The Lancet *389*, 2492-2502.

El-Serag, H. B. (2012). Epidemiology of viral hepatitis and hepatocellular carcinoma. Gastroenterology *142*, 1264-1273.e1261.

El-Serag, H. B., Davila, J. A., Petersen, N. J., and McGlynn, K. A. (2003). The continuing increase in the incidence of hepatocellular carcinoma in the United States: an update. Annals of internal medicine *139*, 817-823.

Elstrom, R. L., Bauer, D. E., Buzzai, M., Karnauskas, R., Harris, M. H., Plas, D. R., Zhuang, H., Cinalli, R. M., Alavi, A., Rudin, C. M., and Thompson, C. B. (2004). Akt stimulates aerobic glycolysis in cancer cells. Cancer research *64*, 3892-3899.

Esterbauer, H., Schaur, R. J., and Zollner, H. (1991). Chemistry and biochemistry of 4-hydroxynonenal, malonaldehyde and related aldehydes. Free Radical Biology and Medicine *11*, 81-128.

Fan, J., Kamphorst, J. J., Mathew, R., Chung, M. K., White, E., Shlomi, T., and Rabinowitz, J. D. (2013). Glutamine-driven oxidative phosphorylation is a major ATP source in transformed mammalian cells in both normoxia and hypoxia. Molecular Systems Biology *9*, 712-n/a.

Fendt, S. M., Bell, E. L., Keibler, M. A., Davidson, S. M., Wirth, G. J., Fiske, B., Mayers, J. R., Schwab, M., Bellinger, G., Csibi, A.*, et al.* (2013). Metformin decreases glucose oxidation and increases the dependency of prostate cancer cells on reductive glutamine metabolism. Cancer research *73*, 4429-4438.

Finkelmeier, F., Waidmann, O., and Trojan, J. (2018). Nivolumab for the treatment of hepatocellular carcinoma. Expert review of anticancer therapy *18*, 1169-1175.

Finn, R. S., Ryoo, B. Y., Merle, P., Kudo, M., Bouattour, M., Lim, H. Y., Breder, V., Edeline, J., Chao, Y., Ogasawara, S.*, et al.* (2020). Pembrolizumab As Second-Line Therapy in Patients With Advanced Hepatocellular Carcinoma in KEYNOTE-240: A Randomized, Double-Blind, Phase III Trial. Journal of clinical oncology : official journal of the American Society of Clinical Oncology *38*, 193-202.

Fleige, S., Walf, V., Huch, S., Prgomet, C., Sehm, J., and Pfaffl, M. W. (2006). Comparison of relative mRNA quantification models and the impact of RNA integrity in quantitative real-time RT-PCR. Biotechnology Letters *28*, 1601-1613.

Forner, A., Reig, M. E., de Lope, C. R., and Bruix, J. (2010). Current strategy for staging and treatment: the BCLC update and future prospects. Seminars in liver disease *30*, 61-74.

Fulda, S., Galluzzi, L., and Kroemer, G. (2010). Targeting mitochondria for cancer therapy. Nature Reviews Drug Discovery *9*, 447.

Galluzzi, L., Vitale, I., Aaronson, S. A., Abrams, J. M., Adam, D., Agostinis, P., Alnemri, E. S., Altucci, L., Amelio, I., Andrews, D. W.*, et al.* (2018). Molecular mechanisms of cell death: recommendations of the Nomenclature Committee on Cell Death 2018. Cell Death & Differentiation *25*, 486-541.

Ghouri, Y. A., Mian, I., and Rowe, J. H. (2017). Review of hepatocellular carcinoma: Epidemiology, etiology, and carcinogenesis. Journal of carcinogenesis *16*, 1.

Glab, J. A., Doerflinger, M., and Puthalakath, H. (2017). BH3-only proteins: the thorny end of the ER stress response. Cell Death Dis *8*, e2889-e2889.

Glatzel, D. K., Koeberle, A., Pein, H., Loser, K., Stark, A., Keksel, N., Werz, O., Muller, R., Bischoff, I., and Furst, R. (2018). Acetyl-CoA carboxylase 1 regulates endothelial cell migration by shifting the phospholipid composition. Journal of lipid research *59*, 298-311.

Greenhouse, W. V., and Lehninger, A. L. (1977). Magnitude of malate-aspartate reduced nicotinamide adenine dinucleotide shuttle activity in intact respiring tumor cells. Cancer research *37*, 4173-4181.

Haber, M., Norris, M. D., Kavallaris, M., Bell, D. R., Davey, R. A., White, L., and Stewart, B. W. (1989). Atypical multidrug resistance in a therapy-induced drug-resistant human leukemia cell line (LALW-2): resistance to Vinca alkaloids independent of P-glycoprotein. Cancer research *49*, 5281-5287.

Hanahan, D., and Weinberg, R. A. (2011). Hallmarks of cancer: the next generation. Cell *144*, 646-674.

He, C., and Klionsky, D. J. (2009). Regulation mechanisms and signaling pathways of autophagy. Annual review of genetics *43*, 67-93.

Hjertén, S. (1962). Chromatographic separation according to size of macromolecules and cell particles on columns of agarose suspensions. Archives of Biochemistry and Biophysics *99*, 466-475.

Holz, M. S., Janning, A., Renne, C., Gattenlohner, S., Spieker, T., and Brauninger, A. (2013). Induction of endoplasmic reticulum stress by sorafenib and activation of NF-kappaB by lestaurtinib as a novel resistance mechanism in Hodgkin lymphoma cell lines. Molecular cancer therapeutics *12*, 173-183.

Hortobagyi, G. N. (1997). Anthracyclines in the treatment of cancer. An overview. Drugs *54 Suppl 4*, 1-7.

Hsieh, Y.-Y., Yang, S.-T., Li, W.-H., Hu, C.-J., and Wang, L.-S. (2015). Primary Leptomeningeal Melanoma Mimicking Meningitis: A Case Report and Literature Review. Journal of Clinical Oncology *33*, e57-e61.

Hurwitz , H., Fehrenbacher , L., Novotny , W., Cartwright , T., Hainsworth , J., Heim , W., Berlin , J., Baron , A., Griffing , S., Holmgren , E.*, et al.* (2004). Bevacizumab plus Irinotecan, Fluorouracil, and Leucovorin for Metastatic Colorectal Cancer. New England Journal of Medicine *350*, 2335-2342.

Iavarone, M., Cabibbo, G., Biolato, M., Della Corte, C., Maida, M., Barbara, M., Basso, M., Vavassori, S., Craxi, A., Grieco, A.*, et al.* (2015). Predictors of survival in patients with advanced hepatocellular carcinoma who permanently discontinued sorafenib. Hepatology (Baltimore, Md) *62*, 784-791.

Jain, R. K. (2001). Normalizing tumor vasculature with anti-angiogenic therapy: a new paradigm for combination therapy. Nature medicine *7*, 987-989.

Jaras, M., and Ebert, B. L. (2011). Power cut: inhibiting mitochondrial translation to target leukemia. Cancer Cell *20*, 555-556.

Jia, X., Gu, Z., Chen, W., and Jiao, J. (2016). Tigecycline targets nonsmall cell lung cancer through inhibition of mitochondrial function. Fundamental & clinical pharmacology *30*, 297-306.

Johnson, P. J., Qin, S., Park, J.-W., Poon, R. T. P., Raoul, J.-L., Philip, P. A., Hsu, C.-H., Hu, T.-H., Heo, J., Xu, J.*, et al.* (2013). Brivanib Versus Sorafenib As First-Line Therapy in Patients With Unresectable, Advanced Hepatocellular Carcinoma: Results From the Randomized Phase III BRISK-FL Study. Journal of Clinical Oncology *31*, 3517-3524.

Jones, R. A., Robinson, T. J., Liu, J. C., Shrestha, M., Voisin, V., Ju, Y., Chung, P. E., Pellecchia, G., Fell, V. L., Bae, S.*, et al.* (2016). RB1 deficiency in triple-negative breast cancer induces mitochondrial protein translation. J Clin Invest *126*, 3739-3757.

Kalbacova, M., Vrbacky, M., Drahota, Z., and Melkova, Z. (2003). Comparison of the effect of mitochondrial inhibitors on mitochondrial membrane potential in two different cell lines using flow cytometry and spectrofluorometry. Cytometry Part A : the journal of the International Society for Analytical Cytology *52*, 110-116.

Kalluri, R., and Weinberg, R. A. (2009). The basics of epithelial-mesenchymal transition. The Journal of clinical investigation *119*, 1420-1428.

Kang, R., Zeh, H. J., Lotze, M. T., and Tang, D. (2011). The Beclin 1 network regulates autophagy and apoptosis. Cell Death Differ *18*, 571-580.

Kapanadze, T., Gamrekelashvili, J., Ma, C., Chan, C., Zhao, F., Hewitt, S., Zender, L., Kapoor, V., Felsher, D. W., Manns, M. P.*, et al.* (2013). Regulation of accumulation and function of myeloid derived suppressor cells in different murine models of hepatocellular carcinoma. Journal of hepatology *59*, 1007-1013.

Kim, M. J., Choi, Y. K., Park, S. Y., Jang, S. Y., Lee, J. Y., Ham, H. J., Kim, B. G., Jeon, H. J., Kim, J. H., Kim, J. G.*, et al.* (2017). PPARdelta Reprograms Glutamine Metabolism in Sorafenib-Resistant HCC. Molecular cancer research : MCR *15*, 1230-1242.

King, M., and Attardi, G. (1989). Human cells lacking mtDNA: repopulation with exogenous mitochondria by complementation. Science (New York, NY) *246*, 500-503.

Koeberle, A., Shindou, H., Koeberle, S. C., Laufer, S. A., Shimizu, T., and Werz, O. (2013). Arachidonoyl-phosphatidylcholine oscillates during the cell cycle and counteracts proliferation by suppressing Akt membrane binding. Proceedings of the National Academy of Sciences *110*, 2546-2551.

Koppenol, W. H., Bounds, P. L., and Dang, C. V. (2011). Otto Warburg's contributions to current concepts of cancer metabolism. Nature reviews Cancer *11*, 325-337.

Kuczynski, E. A., Lee, C. R., Man, S., Chen, E., and Kerbel, R. S. (2015). Effects of Sorafenib Dose on Acquired Reversible Resistance and Toxicity in Hepatocellular Carcinoma. Cancer research *75*, 2510-2519.

Kudo, M. (2017). Lenvatinib in Advanced Hepatocellular Carcinoma. Liver Cancer *6*, 253-263.

Kudo, M., Finn, R. S., Qin, S., Han, K. H., Ikeda, K., Piscaglia, F., Baron, A., Park, J. W., Han, G., Jassem, J.*, et al.* (2018a). Lenvatinib versus sorafenib in first-line treatment of patients with unresectable hepatocellular carcinoma: a randomised phase 3 non-inferiority trial. Lancet (London, England) *391*, 1163-1173.

Kudo, M., Ueshima, K., Yokosuka, O., Ogasawara, S., Obi, S., Izumi, N., Aikata, H., Nagano, H., Hatano, E., Sasaki, Y.*, et al.* (2018b). Sorafenib plus low-dose cisplatin and fluorouracil hepatic arterial infusion chemotherapy versus sorafenib alone in patients with advanced hepatocellular carcinoma (SILIUS): a randomised, open label, phase 3 trial. The lancet Gastroenterology & hepatology *3*, 424-432.

Kuntz, E. M., Baquero, P., Michie, A. M., Dunn, K., Tardito, S., Holyoake, T. L., Helgason, G. V., and Gottlieb, E. (2017). Targeting mitochondrial oxidative phosphorylation eradicates therapy-resistant chronic myeloid leukemia stem cells. Nature medicine *23*, 1234-1240.

Laemmli, U. K. (1970). Cleavage of Structural Proteins during the Assembly of the Head of Bacteriophage T4. Nature *227*, 680.

Lagler, H., Kiesewetter, B., Dolak, W., Obermueller, M., Simonitsch-Klupp, I., Lukas, J., Neuper, O., Lamm, W. W., Mayerhoefer, M. E., and Raderer, M. (2019). Treatment of mucosa associated lymphoid tissue lymphoma with a long-term once-weekly regimen of oral azithromycin: Results from the phase II MALT-A trial. Hematological oncology *37*, 22-26.

Lamb, R., Ozsvari, B., Lisanti, C. L., Tanowitz, H. B., Howell, A., Martinez-Outschoorn, U. E., Sotgia, F., and Lisanti, M. P. (2015). Antibiotics that target mitochondria effectively eradicate cancer stem cells, across multiple tumor types: treating cancer like an infectious disease. Oncotarget *6*, 4569-4584.

Langholz, B., Skolnik, J. M., Barrett, J. S., Renbarger, J., Seibel, N. L., Zajicek, A., and Arndt, C. A. (2011). Dactinomycin and vincristine toxicity in the treatment of childhood cancer: a retrospective study from the Children's Oncology Group. Pediatric blood & cancer *57*, 252-257.

Larosa, V., and Remacle, C. (2018). Insights into the respiratory chain and oxidative stress. Biosci Rep *38*, BSR20171492.

LeBleu, V. S., O'Connell, J. T., Gonzalez Herrera, K. N., Wikman, H., Pantel, K., Haigis, M. C., de Carvalho, F. M., Damascena, A., Domingos Chinen, L. T., Rocha, R. M.*, et al.* (2014). PGC-1alpha mediates mitochondrial biogenesis and oxidative phosphorylation in cancer cells to promote metastasis. Nat Cell Biol *16*, 992-1003, 1001-1015.

Lencioni, R., Kudo, M., Ye, S. L., Bronowicki, J. P., Chen, X. P., Dagher, L., Furuse, J., Geschwind, J. F., de Guevara, L. L., Papandreou, C.*, et al.* (2014). GIDEON (Global Investigation of therapeutic DEcisions in hepatocellular carcinoma and Of its treatment with sorafeNib): second interim analysis. International journal of clinical practice *68*, 609-617.

Levashova, Z., Backer, M., Hamby, C. V., Pizzonia, J., Backer, J. M., and Blankenberg, F. G. (2010). Molecular Imaging of Changes in the Prevalence of Vascular Endothelial Growth Factor Receptor in Sunitinib-Treated Murine Mammary Tumors. Journal of Nuclear Medicine *51*, 959-966.

Liu, L. P., Ho, R. L., Chen, G. G., and Lai, P. B. (2012). Sorafenib inhibits hypoxia-inducible factor-1alpha synthesis: implications for antiangiogenic activity in hepatocellular carcinoma. Clinical cancer research : an official journal of the American Association for Cancer Research *18*, 5662-5671.

Liu, Z., Lin, Y., Zhang, J., Zhang, Y., Li, Y., Liu, Z., Li, Q., Luo, M., Liang, R., and Ye, J. (2019). Molecular targeted and immune checkpoint therapy for advanced hepatocellular carcinoma. J Exp Clin Cancer Res *38*, 447-447.

Llovet, J. M., Bru, C., and Bruix, J. (1999). Prognosis of hepatocellular carcinoma: the BCLC staging classification. Seminars in liver disease *19*, 329-338.

Llovet, J. M., Decaens, T., Raoul, J.-L., Boucher, E., Kudo, M., Chang, C., Kang, Y.-K., Assenat, E., Lim, H.-Y., Boige, V.*, et al.* (2013). Brivanib in Patients With Advanced Hepatocellular Carcinoma Who Were Intolerant to Sorafenib or for Whom Sorafenib Failed: Results From the Randomized Phase III BRISK-PS Study. Journal of Clinical Oncology *31*, 3509-3516.

Llovet, J. M., Ricci, S., Mazzaferro, V., Hilgard, P., Gane, E., Blanc, J.-F., de Oliveira, A. C., Santoro, A., Raoul, J.-L., Forner, A.*, et al.* (2008). Sorafenib in Advanced Hepatocellular Carcinoma. New England Journal of Medicine *359*, 378-390.

Lombardi, D., Soldati, T., Riederer, M. A., Goda, Y., Zerial, M., and Pfeffer, S. R. (1993). Rab9 functions in transport between late endosomes and the trans Golgi network. The EMBO journal *12*, 677-682.

Luke, J. J., and Pal, S. K. (2018). Further evidence to support judicious use of antibiotics in patients with cancer. Annals of oncology : official journal of the European Society for Medical Oncology *29*, 1349-1351.

Ma, M. K. F., Lau, E. Y. T., Leung, D. H. W., Lo, J., Ho, N. P. Y., Cheng, L. K. W., Ma, S., Lin, C. H., Copland, J. A., Ding, J.*, et al.* (2017). Stearoyl-CoA desaturase regulates sorafenib resistance via modulation of ER stress-induced differentiation. Journal of hepatology *67*, 979-990.

Maiuri, M. C., Zalckvar, E., Kimchi, A., and Kroemer, G. (2007). Self-eating and self-killing: crosstalk between autophagy and apoptosis. Nature reviews Molecular cell biology *8*, 741-752.

Mancuso, M. R., Davis, R., Norberg, S. M., x, Brien, S., Sennino, B., Nakahara, T., Yao, V. J., Inai, T., Brooks, P.*, et al.* (2006). Rapid vascular regrowth in tumors after reversal of VEGF inhibition. The Journal of Clinical Investigation *116*, 2610-2621.

Mann, M. J., and Hendershot, L. M. (2006). UPR activation alters chemosensitivity of tumor cells. Cancer Biol Ther *5*, 736-740.

Marcucci, F., and Rumio, C. (2018). How Tumor Cells Choose Between Epithelial-Mesenchymal Transition and Autophagy to Resist Stress-Therapeutic Implications. Front Pharmacol *9*, 714-714.

Marelli, L., Stigliano, R., Triantos, C., Senzolo, M., Cholongitas, E., Davies, N., Tibballs, J., Meyer, T., Patch, D. W., and Burroughs, A. K. (2007). Transarterial therapy for hepatocellular carcinoma: which technique is more effective? A systematic review of cohort and randomized studies. Cardiovascular and interventional radiology *30*, 6-25.

Margineantu, D. H., and Hockenbery, D. M. (2016). Mitochondrial functions in stem cells. Current Opinion in Genetics & Development *38*, 110-117.

Marrero, J. A., Kudo, M., Venook, A. P., Ye, S. L., Bronowicki, J. P., Chen, X. P., Dagher, L., Furuse, J., Geschwind, J. H., de Guevara, L. L.*, et al.* (2016). Observational registry of sorafenib use in clinical practice across Child-Pugh subgroups: The GIDEON study. Journal of hepatology *65*, 1140-1147.

McBride, H. M., Neuspiel, M., and Wasiak, S. (2006). Mitochondria: More Than Just a Powerhouse. Current Biology *16*, R551-R560.

Méndez-Blanco, C., Fondevila, F., García-Palomo, A., González-Gallego, J., and Mauriz, J. L. (2018). Sorafenib resistance in hepatocarcinoma: role of hypoxia-inducible factors. Experimental & Molecular Medicine *50*, 134.

Mitchell, P. (1961). Coupling of Phosphorylation to Electron and Hydrogen Transfer by a Chemi-Osmotic type of Mechanism. Nature *191*, 144-148.

Mullen, A. R., Hu, Z., Shi, X., Jiang, L., Boroughs, L. K., Kovacs, Z., Boriack, R., Rakheja, D., Sullivan, L. B., Linehan, W. M.*, et al.* (2014). Oxidation of alpha-ketoglutarate is required for reductive carboxylation in cancer cells with mitochondrial defects. Cell reports *7*, 1679-1690.

Mullen, A. R., Wheaton, W. W., Jin, E. S., Chen, P. H., Sullivan, L. B., Cheng, T., Yang, Y., Linehan, W. M., Chandel, N. S., and DeBerardinis, R. J. (2011). Reductive carboxylation supports growth in tumour cells with defective mitochondria. Nature *481*, 385-388.

Murphy, M. P. (2009). How mitochondria produce reactive oxygen species. The Biochemical journal *417*, 1-13.

Nagengast, W. B., Lub-de Hooge, M. N., Oosting, S. F., den Dunnen, W. F., Warnders, F. J., Brouwers, A. H., de Jong, J. R., Price, P. M., Hollema, H., Hospers, G. A.*, et al.* (2011). VEGF-PET imaging is a noninvasive biomarker showing differential changes in the tumor during sunitinib treatment. Cancer research *71*, 143-153.

Nagle, D. G., and Zhou, Y.-D. (2010). 2.20 - Natural Products as Probes of Selected Targets in Tumor Cell Biology and Hypoxic Signaling. In Comprehensive Natural Products II, H.-W. Liu, and L. Mander, eds. (Oxford: Elsevier), pp. 651-683.

Nicoletti, I., Migliorati, G., Pagliacci, M. C., Grignani, F., and Riccardi, C. (1991). A rapid and simple method for measuring thymocyte apoptosis by propidium iodide staining and flow cytometry. Journal of immunological methods *139*, 271-279.

Nishida, Y., Arakawa, S., Fujitani, K., Yamaguchi, H., Mizuta, T., Kanaseki, T., Komatsu, M., Otsu, K., Tsujimoto, Y., and Shimizu, S. (2009). Discovery of Atg5/Atg7-independent alternative macroautophagy. Nature *461*, 654-658.

Njei, B., Rotman, Y., Ditah, I., and Lim, J. K. (2015). Emerging trends in hepatocellular carcinoma incidence and mortality. Hepatology (Baltimore, Md) *61*, 191-199.

Panieri, E., and Santoro, M. M. (2016). ROS homeostasis and metabolism: a dangerous liason in cancer cells. Cell Death &Amp; Disease *7*, e2253.

Paquette, M., El-Houjeiri, L., and Pause, A. (2018). mTOR Pathways in Cancer and Autophagy. Cancers (Basel) *10*, 18.

Parikh, S., and Hyman, D. (2007). Hepatocellular cancer: a guide for the internist. The American journal of medicine *120*, 194-202.

Parkin, D. M., Bray, F., Ferlay, J., and Pisani, P. (2005). Global cancer statistics, 2002. CA: a cancer journal for clinicians *55*, 74-108.

Pein, H., Koeberle, S. C., Voelkel, M., Schneider, F., Rossi, A., Thurmer, M., Loeser, K., Sautebin, L., Morrison, H., Werz, O., and Koeberle, A. (2017). Vitamin A regulates Akt signaling through the phospholipid fatty acid composition. FASEB journal : official publication of the Federation of American Societies for Experimental Biology *31*, 4566-4577.

Personeni, N., Pressiani, T., and Rimassa, L. (2019). Lenvatinib for the treatment of unresectable hepatocellular carcinoma: evidence to date. J Hepatocell Carcinoma *6*, 31-39.

Pfeiffer, T., Schuster, S., and Bonhoeffer, S. (2001). Cooperation and competition in the evolution of ATP-producing pathways. Science (New York, NY) *292*, 504-507.

Pickles, S., Vigie, P., and Youle, R. J. (2018). Mitophagy and Quality Control Mechanisms in Mitochondrial Maintenance. Current biology : CB *28*, R170-r185.

Porporato, P. E., Filigheddu, N., Pedro, J. M. B.-S., Kroemer, G., and Galluzzi, L. (2017). Mitochondrial metabolism and cancer. Cell Research *28*, 265.

Prieto-Domínguez, N., Ordóñez, R., Fernández, A., García-Palomo, A., Muntané, J., González-Gallego, J., and Mauriz, J. L. (2016). Modulation of Autophagy by Sorafenib: Effects on Treatment Response. Front Pharmacol *7*, 151-151.

Rabinovich, B. A., Ye, Y., Etto, T., Chen, J. Q., Levitsky, H. I., Overwijk, W. W., Cooper, L. J. N., Gelovani, J., and Hwu, P. (2008). Visualizing fewer than 10 mouse T cells with an enhanced firefly luciferase in immunocompetent mouse models of cancer. Proceedings of the National Academy of Sciences *105*, 14342-14346.

Raoul, J.-L., Kudo, M., Finn, R. S., Edeline, J., Reig, M., and Galle, P. R. (2018). Systemic therapy for intermediate and advanced hepatocellular carcinoma: Sorafenib and beyond. Cancer Treatment Reviews *68*, 16-24.

Razzouk, B. I., Hord, J. D., Hockenberry, M., Hinds, P. S., Feusner, J., Williams, D., and Rackoff, W. R. (2006). Double-blind, placebo-controlled study of quality of life, hematologic end points, and safety of weekly epoetin alfa in children with cancer receiving myelosuppressive chemotherapy. Journal of clinical oncology : official journal of the American Society of Clinical Oncology *24*, 3583-3589.

Reed, G. A., Schiller, G. J., Kambhampati, S., Tallman, M. S., Douer, D., Minden, M. D., Yee, K. W., Gupta, V., Brandwein, J., Jitkova, Y.*, et al.* (2016). A Phase 1 study of intravenous infusions of tigecycline in patients with acute myeloid leukemia. Cancer Med *5*, 3031-3040.

Reig, M., da Fonseca, L. G., and Faivre, S. (2018). New trials and results in systemic treatment of HCC. Journal of hepatology *69*, 525-533.

Rimassa, L., Assenat, E., Peck-Radosavljevic, M., Pracht, M., Zagonel, V., Mathurin, P., Rota Caremoli, E., Porta, C., Daniele, B., Bolondi, L.*, et al.* (2018). Tivantinib for second-line treatment of MET-high, advanced hepatocellular carcinoma (METIV-HCC): a final analysis of a phase 3, randomised, placebo-controlled study. The Lancet Oncology *19*, 682-693.

Sagan, L. (1967). On the origin of mitosing cells. Journal of theoretical biology *14*, 255-274.

Sarosiek, K. A., Ni Chonghaile, T., and Letai, A. (2013). Mitochondria: gatekeepers of response to chemotherapy. Trends in Cell Biology *23*, 612-619.

Sborov, D. W., Haverkos, B. M., and Harris, P. J. (2015). Investigational cancer drugs targeting cell metabolism in clinical development. Expert Opin Investig Drugs *24*, 79-94.

Scarpulla, R. C. (2006). Nuclear control of respiratory gene expression in mammalian cells. Journal of cellular biochemistry *97*, 673-683.

Scatena, C., Roncella, M., Di Paolo, A., Aretini, P., Menicagli, M., Fanelli, G., Marini, C., Mazzanti, C. M., Ghilli, M., Sotgia, F.*, et al.* (2018). Doxycycline, an Inhibitor of Mitochondrial Biogenesis, Effectively Reduces Cancer Stem Cells (CSCs) in Early Breast Cancer Patients: A Clinical Pilot Study. Frontiers in oncology *8*, 452.

Schagger, H. (2006). Tricine-SDS-PAGE. Nature protocols *1*, 16-22.

Schlachterman, A., Craft Jr, W. W., Hilgenfeldt, E., Mitra, A., and Cabrera, R. (2015). Current and future treatments for hepatocellular carcinoma. World Journal of Gastroenterology : WJG *21*, 8478-8491.

Schulz, H. (1991). Beta oxidation of fatty acids. Biochimica et Biophysica Acta (BBA) - Lipids and Lipid Metabolism *1081*, 109-120.

Shen, Y. C., Ou, D. L., Hsu, C., Lin, K. L., Chang, C. Y., Lin, C. Y., Liu, S. H., and Cheng, A. L. (2012). Activating oxidative phosphorylation by a pyruvate dehydrogenase kinase inhibitor overcomes sorafenib resistance of hepatocellular carcinoma. British Journal Of Cancer *108*, 72.

Sheng, J., Qin, H., Zhang, K., Li, B., and Zhang, X. (2018). Targeting autophagy in chemotherapy-resistant of hepatocellular carcinoma. American journal of cancer research *8*, 354-365.

Shental-Bechor, D., and Levy, Y. (2008). Effect of glycosylation on protein folding: a close look at thermodynamic stabilization. Proceedings of the National Academy of Sciences of the United States of America *105*, 8256-8261.

Sheshadri, N., Catanzaro, J. M., Bott, A. J., Sun, Y., Ullman, E., Chen, E. I., Pan, J. A., Wu, S., Crawford, H. C., Zhang, J., and Zong, W. X. (2014). SCCA1/SERPINB3 promotes oncogenesis and epithelial-mesenchymal transition via the unfolded protein response and IL6 signaling. Cancer research *74*, 6318-6329.

Shi, Y. H., Ding, Z. B., Zhou, J., Hui, B., Shi, G. M., Ke, A. W., Wang, X. Y., Dai, Z., Peng, Y. F., Gu, C. Y.*, et al.* (2011). Targeting autophagy enhances sorafenib lethality for hepatocellular carcinoma via ER stress-related apoptosis. Autophagy *7*, 1159-1172.

Shimizu, S., Takehara, T., Hikita, H., Kodama, T., Tsunematsu, H., Miyagi, T., Hosui, A., Ishida, H., Tatsumi, T., Kanto, T.*, et al.* (2012). Inhibition of autophagy potentiates the antitumor effect of the multikinase inhibitor sorafenib in hepatocellular carcinoma. International journal of cancer *131*, 548-557.

Skoda, J., Borankova, K., Jansson, P. J., Huang, M. L. H., Veselska, R., and Richardson, D. R. (2019). Pharmacological targeting of mitochondria in cancer stem cells: An ancient organelle at the crossroad of novel anti-cancer therapies. Pharmacological Research *139*, 298-313.

Skrtic, M., Sriskanthadevan, S., Jhas, B., Gebbia, M., Wang, X., Wang, Z., Hurren, R., Jitkova, Y., Gronda, M., Maclean, N.*, et al.* (2011). Inhibition of mitochondrial translation as a therapeutic strategy for human acute myeloid leukemia. Cancer Cell *20*, 674-688.

Son, H., and Moon, A. (2010). Epithelial-mesenchymal Transition and Cell Invasion. Toxicol Res *26*, 245-252.

Sounni, Nor E., Cimino, J., Blacher, S., Primac, I., Truong, A., Mazzucchelli, G., Paye, A., Calligaris, D., Debois, D., De Tullio, P.*, et al.* (2014). Blocking Lipid Synthesis Overcomes Tumor Regrowth and Metastasis after Antiangiogenic Therapy Withdrawal. Cell Metabolism *20*, 280-294.

Strumberg, D., Clark, J. W., Awada, A., Moore, M. J., Richly, H., Hendlisz, A., Hirte, H. W., Eder, J. P., Lenz, H.-J., and Schwartz, B. (2007). Safety, Pharmacokinetics, and Preliminary Antitumor Activity of Sorafenib: A Review of Four Phase I Trials in Patients with Advanced Refractory Solid Tumors. The Oncologist *12*, 426-437.

Sugiura, A., McLelland, G. L., Fon, E. A., and McBride, H. M. (2014). A new pathway for mitochondrial quality control: mitochondrial-derived vesicles. The EMBO journal *33*, 2142-2156.

Sullivan, Lucas B., Gui, Dan Y., Hosios, Aaron M., Bush, Lauren N., Freinkman, E., and Vander Heiden, Matthew G. (2015). Supporting Aspartate Biosynthesis Is an Essential Function of Respiration in Proliferating Cells. Cell *162*, 552-563.

Sun, S.-Y. (2010). N-acetylcysteine, reactive oxygen species and beyond. Cancer Biol Ther *9*, 109-110.

Taanman, J. W. (1999). The mitochondrial genome: structure, transcription, translation and replication. Biochimica et biophysica acta *1410*, 103-123.

Tan, J., Song, M., Zhou, M., and Hu, Y. (2017). Antibiotic tigecycline enhances cisplatin activity against human hepatocellular carcinoma through inducing mitochondrial dysfunction and oxidative damage. Biochemical and biophysical research communications *483*, 17-23.

Tanaka, A., Cleland, M. M., Xu, S., Narendra, D. P., Suen, D. F., Karbowski, M., and Youle, R. J. (2010). Proteasome and p97 mediate mitophagy and degradation of mitofusins induced by Parkin. The Journal of cell biology *191*, 1367-1380.

Tatsuta, T., and Langer, T. (2009). AAA proteases in mitochondria: diverse functions of membrane-bound proteolytic machines. Research in microbiology *160*, 711-717.

Thaden, J. T., Pogue, J. M., and Kaye, K. S. (2017). Role of newer and re-emerging older agents in the treatment of infections caused by carbapenem-resistant Enterobacteriaceae. Virulence *8*, 403-416.

Thiery, J. P. (2002). Epithelial–mesenchymal transitions in tumour progression. Nature Reviews Cancer *2*, 442-454.

Turrens, J. F. (2003). Mitochondrial formation of reactive oxygen species. J Physiol *552*, 335-344.

Tutusaus, A., Stefanovic, M., Cucarull, B., Mari, M., Boix, L., Reig, M., Bruix, J., and Morales, A. (2018). Sorafenib/Regorafenib resistance and BH3-mimetics efficacy in hepatocellular carcinoma treatment is determined by mitochondrial changes in the BCL-2 profile. Journal of hepatology *68*, S686-S687.

van Malenstein, H., Dekervel, J., Verslype, C., Van Cutsem, E., Windmolders, P., Nevens, F., and van Pelt, J. (2013). Long-term exposure to sorafenib of liver cancer cells induces resistance with epithelial-to-mesenchymal transition, increased invasion and risk of rebound growth. Cancer letters *329*, 74-83.

Vander Heiden, M. G., Cantley, L. C., and Thompson, C. B. (2009). Understanding the Warburg effect: the metabolic requirements of cell proliferation. Science (New York, NY) *324*, 1029-1033.

Vilgrain, V., Pereira, H., Assenat, E., Guiu, B., Ilonca, A. D., Pageaux, G. P., Sibert, A., Bouattour, M., Lebtahi, R., Allaham, W.*, et al.* (2017). Efficacy and safety of selective internal radiotherapy with yttrium-90 resin microspheres compared with sorafenib in locally advanced and inoperable hepatocellular carcinoma (SARAH): an open-label randomised controlled phase 3 trial. The Lancet Oncology *18*, 1624-1636.

Volpe, A., Racioppi, M., D'Agostino, D., Cappa, E., Filianoti, A., and Bassi, P. F. (2010). Mitomycin C for the treatment of bladder cancer. Minerva urologica e nefrologica = The Italian journal of urology and nephrology *62*, 133-144.

Vyas, S., Zaganjor, E., and Haigis, M. C. (2016). Mitochondria and Cancer. Cell *166*, 555-566.

Wang, B., Ao, J., Yu, D., Rao, T., Ruan, Y., and Yao, X. (2017). Inhibition of mitochondrial translation effectively sensitizes renal cell carcinoma to chemotherapy. Biochemical and biophysical research communications *490*, 767-773.

Warburg, O. (1956). On the origin of cancer cells. Science (New York, NY) *123*, 309-314.

Ward, P. S., and Thompson, C. B. (2012). Metabolic reprogramming: a cancer hallmark even warburg did not anticipate. Cancer Cell *21*, 297-308.

Weinberg, S. E., and Chandel, N. S. (2015). Targeting mitochondria metabolism for cancer therapy. Nat Chem Biol *11*, 9-15.

Wellen, K. E., Hatzivassiliou, G., Sachdeva, U. M., Bui, T. V., Cross, J. R., and Thompson, C. B. (2009). ATP-citrate lyase links cellular metabolism to histone acetylation. Science (New York, NY) *324*, 1076-1080.

Wellen, K. E., and Thompson, C. B. (2010). Cellular metabolic stress: considering how cells respond to nutrient excess. Mol Cell *40*, 323-332.

Wheaton, W. W., Weinberg, S. E., Hamanaka, R. B., Soberanes, S., Sullivan, L. B., Anso, E., Glasauer, A., Dufour, E., Mutlu, G. M., Budigner, G. S., and Chandel, N. S. (2014). Metformin inhibits mitochondrial complex I of cancer cells to reduce tumorigenesis. eLife *3*, e02242.

WHO (2012). (World Health Organization, I.A.f.R.o.C.); Estimated Cancer Incidence, Mortality and Prevalence Worldwide in 2012. http://wwwglobocaniarcfr/Pages/fact_sheets_populationaspx.

Wilhelm, S., Carter, C., Lynch, M., Lowinger, T., Dumas, J., Smith, R. A., Schwartz, B., Simantov, R., and Kelley, S. (2006). Discovery and development of sorafenib: a multikinase inhibitor for treating cancer. Nature Reviews Drug Discovery *5*, 835-844.

Wilhelm, S. M., Carter, C., Tang, L., Wilkie, D., McNabola, A., Rong, H., Chen, C., Zhang, X., Vincent, P., McHugh, M.*, et al.* (2004). BAY 43-9006 exhibits broad spectrum oral antitumor activity and targets the RAF/MEK/ERK pathway and receptor tyrosine kinases involved in tumor progression and angiogenesis. Cancer research *64*, 7099-7109.

Wilhelm, S. M., Dumas, J., Adnane, L., Lynch, M., Carter, C. A., Schutz, G., Thierauch, K. H., and Zopf, D. (2011). Regorafenib (BAY 73-4506): a new oral multikinase inhibitor of angiogenic, stromal and oncogenic receptor tyrosine kinases with potent preclinical antitumor activity. International journal of cancer *129*, 245-255.

Wong, Y. C., Ysselstein, D., and Krainc, D. (2018). Mitochondria-lysosome contacts regulate mitochondrial fission via RAB7 GTP hydrolysis. Nature *554*, 382-386.

Xie, Y., Hou, W., Song, X., Yu, Y., Huang, J., Sun, X., Kang, R., and Tang, D. (2016). Ferroptosis: process and function. Cell Death Differ *23*, 369.

Xu, W., Liu, K., Chen, M., Sun, J.-Y., McCaughan, G. W., Lu, X.-J., and Ji, J. (2019). Immunotherapy for hepatocellular carcinoma: recent advances and future perspectives. Therapeutic Advances in Medical Oncology *11*, 1758835919862692.

Xu, Z., Yan, Y., Li, Z., Qian, L., and Gong, Z. (2016). The Antibiotic Drug Tigecycline: A Focus on its Promising Anticancer Properties. Front Pharmacol *7*, 473-473.

Yamamoto, Y., Matsui, J., Matsushima, T., Obaishi, H., Miyazaki, K., Nakamura, K., Tohyama, O., Semba, T., Yamaguchi, A., Hoshi, S. S*., et al.* (2014). Lenvatinib, an angiogenesis inhibitor targeting VEGFR/FGFR, shows broad antitumor activity in human tumor xenograft models associated with microvessel density and pericyte coverage. Vascular cell *6*, 18.

You, X., Jiang, W., Lu, W., Zhang, H., Yu, T., Tian, J., Wen, S., Garcia-Manero, G., Huang, P., and Hu, Y. (2019). Metabolic reprogramming and redox adaptation in sorafenib-resistant leukemia cells: detected by untargeted metabolomics and stable isotope tracing analysis. Cancer Communications *39*, 17.

Zhai, B., and Sun, X. Y. (2013). Mechanisms of resistance to sorafenib and the corresponding strategies in hepatocellular carcinoma. World journal of hepatology *5*, 345-352.

Zhu, A. X., Finn, R. S., Edeline, J., Cattan, S., Ogasawara, S., Palmer, D., Verslype, C., Zagonel, V., Fartoux, L., Vogel, A*., et al.* (2018a). Pembrolizumab in patients with advanced hepatocellular carcinoma previously treated with sorafenib (KEYNOTE-224): a non-randomised, open-label phase 2 trial. The Lancet Oncology *19*, 940-952.

Zhu, A. X., Kang, Y.-K., Yen, C.-J., Finn, R. S., Galle, P. R., Llovet, J. M., Assenat, E., Brandi, G., Lim, H. Y., Pracht, M*., et al.* (2018b). REACH-2: A randomized, double-blind, placebo-controlled phase 3 study of ramucirumab versus placebo as second-line treatment in patients with advanced hepatocellular carcinoma (HCC) and elevated baseline alpha-fetoprotein (AFP) following first-line sorafenib. Journal of Clinical Oncology *36*, 4003-4003.

Zhu, A. X., Kudo, M., Assenat, E., Cattan, S., Kang, Y.-K., Lim, H. Y., Poon, R. T. P., Blanc, J.-F., Vogel, A., Chen, C.-L*., et al.* (2014). Effect of Everolimus on Survival in Advanced Hepatocellular Carcinoma After Failure of Sorafenib: The EVOLVE-1 Randomized Clinical TrialEverolimus for Advanced Hepatocellular CarcinomaEverolimus for Advanced Hepatocellular Carcinoma. Jama *312*, 57-67.

Zhu, A. X., Park, J. O., Ryoo, B.-Y., Yen, C.-J., Poon, R., Pastorelli, D., Blanc, J.-F., Chung, H. C., Baron, A. D., Pfiffer, T. E. F*., et al.* (2015a). Ramucirumab versus placebo as second-line treatment in patients with advanced hepatocellular carcinoma following first-line therapy with sorafenib (REACH): a randomised, double-blind, multicentre, phase 3 trial. The Lancet Oncology *16*, 859-870.

Zhu, A. X., Rosmorduc, O., Evans, T. R. J., Ross, P. J., Santoro, A., Carrilho, F. J., Bruix, J., Qin, S., Thuluvath, P. J., Llovet, J. M*., et al.* (2015b). SEARCH: A Phase III, Randomized, Double-Blind, Placebo-Controlled Trial of Sorafenib Plus Erlotinib in Patients With Advanced Hepatocellular Carcinoma. Journal of Clinical Oncology *33*, 559-566.

Zhu, Y.-J., Zheng, B., Wang, H.-Y., and Chen, L. (2017). New knowledge of the mechanisms of sorafenib resistance in liver cancer. Acta Pharmacol Sin *38*, 614-622.

Zielke, H. R., Zielke, C. L., and Ozand, P. T. (1984). Glutamine: a major energy source for cultured mammalian cells. Federation proceedings *43*, 121-125.

APPENDIX

9 APPENDIX

9.1 Abbreviations

Table 29. *List of abbreviations*

Abbreviation	Full name
2-DG	2-deoxy-D-glucose
3-MA	3-methyladenine
^{90}Y	yttrium-90
ACA	acyl-CoA-species
ACoA	acetyl-coenzyme A
AKB	α-ketobutyrate
AKG	α-ketoglutarate
AMPK	5′ adenosine monophosphate-activated protein kinase
AP	Asia-pacific
APS	ammonium persulfate
ASP	aspartate
ATG5/7	autophagy protein 5/7
ATP	adenosine-5'-triphosphate
AUC	area under the curve
BCLC	Barcelona Clinic Liver Cancer
Bcl-X	B-cell lymphoma X
BECN-1	beclin-1
BSA	bovine serum albumin
BV	Bliss value
CCCP	carbonyl cyanide 3-chlorophenylhydrazone
CHA	chloramphenicol
CI	confidence interval
CLT; LDLT	cadaveric liver transplantation; living donor liver transplantation
CoQ (Q)	coenzyme Q (or ubiquinone)
CST	Cell Signaling Technologies
CTB	CellTiterBlue®
CYP3A4	cytochrome P450 3A4
CYS	cysteine
DMEM	Dulbecco's Modified Eagle Medium
DMSO	dimethyl sulfoxide
DNA; mt/nucDNA	deoxyribonucleic acid; mitochondrial/ nuclear DNA

Drp-1	dynamin-related protein-1
DTT	dithiothreitol
ECAR	extracellular acidification rate
ECL	enhanced chemiluminescence
EDTA	ethylenediaminetetraacetic acid
EMT	epithelial-to-mesenchymal transition
ER	endoplasmatic reticulum
ERK	extracellular signaling-regulated kinase
ES	enrichment score
ETC/ ETS	electron transport system/ electron transport chain
FA; FFA	fatty acid; free fatty acid
FACS	fluorescence activated cell sorter
FAD; $FADH_2$	oxidized flavin adenine dinucleotide; reduced flavin adenine dinucleotide
FCS	fetal calf serum
FDR	false discovery rate
FGF(R)	fibroblast growth factor (receptor)
Flt-3	FMS-like tyrosine kinase-3
FOCM	folate one-carbon metabolism
FS	fluorochrome solution
GIDEON	global investigation of therapeutic decisions in HCC and of its treatment with
GLU	glutamate
GSEA	Gene Set Enrichment Analysis
GSSH; GSH	reduced glutathione; oxidized glutathione
HAIC	hepatic arterial infusion chemotherapy
HBV; HCV	hepatitis B virus; hepatitis C virus
HCC	hepatocellular carcinoma
HEPES	4- (2-hydroxyethyl)-1-piperazineethanesulfonic acid
HFSR	hand–foot skin reaction
HIF-1α	hypoxia-inducible factor-1α
HRP	horseradish peroxidase
HUH7-R	sorafenib-resistant HUH7 cell line
HUH7-R(-)	HUH7-R cell line cultured without sorafenib for 96 h
HUH7-R(-/X h)	HUH7-R cell line cultured without sorafenib for X h
HUH7-R(+)	HUH7-R cell line persistently cultured in 10 µM sorafenib
HUH7-R-LUC	stable luciferase transfected HUH7-R cell line
HUH7-WT	wild type HuH-7 cell line
IC_{50}	half maximal inhibitory concentration

IDH1; IDH2	isocitate dehydrogenase 1; isocitate dehydrogenase 2
IMM	inner mitochondrial membrane
JCRB	Japanese Collection of Research Bioresources
KEGG	Kyoto Encyclopedia of Genes and Genomes
MAL	malate
MAPK	mitogen-activated protein kinase
MB6	MitoBlock-6
Mcl-1	myeloid cell leukemia 1
MDR	multidrug resistance
MET	mesenchymal-to-epithelial transition
Mfn-1	mitofusin-1
MMP	matrix metalloproteinase
MS	mass spectrometry
mTOR(C)	mammalian target of rapamycin (complex)
NAC	N-acetyl cysteine
NAD(P)$^+$/ NAD(P)H	oxidized/ reduced nicotinamide adenine dinucleotide (phosphate)
NDUF	NADH-ubiquinone oxidoreductase
NNT	nicotinamide nucleotide transhydrogenase
NOM p-val	nominal p-value
OAA	oxaloacetate
OCR	oxygen consumption rate
OGDH	oxoglutarate dehydrogenase
OMM	outer mitochondrial membrane
OS	overall survival
OXPHOS	oxidative phosphorylation
PBS	phosphate buffered saline
PC; PE; PG; PI; PS	phosphatidyl-choline; -ethanolamine; -glycerol; -inositol; -serine
PCA; PDH	pyruvate carboxylase; pyruvate dehydrogenase
PDGF(R)	platelet-derived growth factor (receptor)
PEI	percutaneous ethanol injection
PFA	paraformaldehyde
PFS	progression-free survival
PGC-1α	peroxisome proliferator activated receptor gamma coactivator-1 alpha
P-gp	P-glycoprotein
PI	propidium iodide
PI3K	phosphatidylinositol-4.5-bisphosphate 3-kinase
PMSF	phenylmethylsulfonyl fluoride

PPP	pentose phosphate pathway
PST	performance status test
PUFAs	polyunsaturated fatty acids
PYR	pyruvate
qPCR	quantitative polymerase chain reaction
R^2	coefficient of determination
REFLECT	clinical phase III trial: lenvatinib vs. sorafenib *(Table 1; Table 28)*
RESOURCE	clinical phase III trial: regorafenib vs. placebo *(Table 1)*
RF(A)	radiofrequency (ablation)
RNA	ribonucleic acid
ROS	reactive oxygen species
rpm	revolutions per minute
RT	room temperature
SDS(-PAGE)	sodium dodecyl sulfate (polyacrylamide gel electrophoresis)
SEM	standard error of the mean value
SHARP	sorafenib Hepatocellular Carcinoma Assessment Randomized Protocol
SIRT	selective internal radiation therapy
SM	sphingomyeline
SQSTM-1	sequestosome-1 (or: p62)
T/E	trypsin/EDTA
TACE	transarterial chemoembolization
TBS-T	tris-buffered saline with tween20
TCA	tricarboxylic acid cycle
TEM	transmission electron microscopy
TEMED	N', N', N', N' tetramethylethylene diamine
TGC	tigecycline
TGFβ	transforming growth factor β
THF	tetrahydrofolate
TKI	tyrosine kinase inhibitor
Tris	trishydroxymethylaminomethane
TSC1/2	tuberous sclerosis complex 1/ 2
TTP	time to progression
ULK1	UNC-51-like kinases 1
UPR	unfolded protein response
VEGF(R)	vascular endothelial growth factor (receptor)
WHO	World health organization

*abbreviations of clinical trials that are not used repeatedly are not listed (see *Table 1*).

9.2 Index of figures and tables

9.2.1 Index of main figures

9.2.2 Index of supplementary figures

9.2.3 Index of tables

9.3 List of publications and conference contributions

9.3.1 Articles

Martina Meßner & Melanie M. Mandl, Mathias W. Hackl, Maximilian A. Ardelt, Julian E. Frädrich, Jens Waschke, Irmela Jeremias, Anja Fux, Matthias Stahl, Angelika M. Vollmar, Stephan A. Sieber, & Johanna Pachmayr. *Small molecule inhibitors of the mitochondrial ClpXP protease possess cytostatic potential and re-sensitize chemo-resistant cancers.* (submitted)

Maria Thuermer, Helmut Pein, Elif Gelmez, Natalie Wielsch, Konstantin Löser, René Winkler, Yohei Morita, Anika Döding, **Martina Meßner**, Simona Pace, Johanna Pachmayr, Konstantin Neukirch, André Gollowitzer, Cristina González-Estévez, Lenhard Rudolph, Ulrike Schulze-Späte, Christian Kosan, Aleš Svatoš & Andreas Koeberle. *PI(18:1/18:1) is a SCD-1-derived lipokine that limits stress signaling*. (submitted)

Martina Meßner, Sabine Schmitt, Maximilian A. Ardelt, Thomas Fröhlich, Martin Müller, Helmut Pein, Petra Huber-Cantonati, Carina Ortler, Lars M. Koenig, Lena Zobel, Andreas Koeberle, Georg J. Arnold, Simon Rothenfußer, Alexandra K. Kiemer, Alexander L. Gerbes, Hans Zischka, Angelika M. Vollmar, Johanna Pachmayr. *Metabolic implication of tigecycline as an efficacious second-line treatment for sorafenib-resistant hepatocellular carcinoma*. (in revision)

Maximilian A. Ardelt, Thomas Fröhlich, Emanuele Martini, Martin Müller, Veronika Kanitz, Carina Atzberger, Petra Cantonati, **Martina Meßner**, Laura Posselt, Thorsten Lehr, Jan-Georg Wojtyniak, Melanie Ulrich, Georg J. Arnold, Lars M. König, Dario Parazzoli, Stefan Zahler, Simon Rothenfußer, Doris Mayr, Alexander L. Gerbes, Giorgio Scita, Angelika M. Vollmar, Johanna Pachmayr (2019). *Inhibition of Cyclin-Dependent Kinase 5: A Strategy to Improve Sorafenib Response in Hepatocellular Carcinoma Therapy.* Hepatology (Baltimore, Md) 69, 376-393.

Thomas F. Gronauer, Melanie M. Mandl, Markus Lakemeyer, Mathias W. Hackl, **Martina Meßner**, Vadim S. Korotkov, Johanna Pachmayr, Stephan A. Sieber (2018). *Design and synthesis of tailored human caseinolytic protease P inhibitors*. Chemical communications (Cambridge, England) 54, 9833-9836.

Birgit Linkus, Diana Wiesner, **Martina Meßner**, Alexander Karabatsiakis, Annika Scheffold, K. Lenhard Rudolph, Dietmar R. Thal, Jochen H. Weishaupt, Albert C. Ludolph, Karin M. Danzer (2016). *Telomere shortening leads to earlier age of onset in ALS mice*. Aging 8, 382-393.

9.3.2 Presentations

Martina Meßner, Hans Zischka, Sabine Schmitt, Maximilian A. Ardelt, Petra Huber-Cantonati, Thomas Fröhlich, Georg J. Arnold, Carina Atzberger, Martin Müller, Helmut Pein, Andreas Koeberle, Lena Zobel, Lars M. Koenig, Angelika M. Vollmar, Johanna Pachmayr; *Diamonds in the rough – With low application antibiotics against tumor relapse of sorafenib-resistant hepatocellular carcinoma,* 26th Scientific Congress of the Austrian Pharmaceutical Society (ÖPhG), Graz, Austria, April 25-27, 2019 (oral presentation).

Martina Meßner, Hans Zischka, Sabine Schmitt, Maximilian A. Ardelt, Petra Huber-Cantonati, Thomas Fröhlich, Georg J. Arnold, Carina Atzberger, Martin Müller, Helmut Pein, Andreas Koeberle, Lena Zobel, Lars M. Koenig, Angelika M. Vollmar, Johanna Pachmayr; *Tigecycline blocks the glutamine-fuelled tumor relapse of sorafenib-resistant hepatocellular carcinoma patients,* International PhD students/Postdocs meeting 2019 of the German Pharmaceutical Society (DPhG) at Merck, Darmstadt, Germany, March 27-29, 2019 (poster presentation and oral presentation).

Martina Meßner, Hans Zischka, Sabine Schmitt, Maximilian A. Ardelt, Thomas Fröhlich, Georg J. Arnold, Carina Atzberger, Martin Müller, Helmut Pein, Andreas Koeberle, Angelika M. Vollmar, Johanna Pachmayr; *Switching lanes - Metabolic implication of tigecycline as an efficacious second-line treatment for patients with sorafenib-resistant hepatocellular carcinoma,* Annual Meeting of the German Pharmaceutical Society (DPhG), Hamburg, Germany, October 2-5, 2018 (poster presentation and oral presentation; awarded with "Lesmüller-Posterpreis").

Martina Meßner, Maximilian A. Ardelt, Thomas Fröhlich, Georg J. Arnold, Angelika M. Vollmar, Johanna Pachmayr; *Stumbling blocks for sorafenib in the treatment of advanced-stage hepatocellular carcinoma,* International Liver Cancer Association (ILCA) 12th Annual Conference, London, United Kingdom, September 14-16, 2018 (E-poster presentation).

Martina Meßner, Maximilian A. Ardelt, Thomas Fröhlich, Georg J. Arnold, Angelika M. Vollmar, Johanna Pachmayr; *Epithelial-to-mesenchymal transition and evasive PI3K/Akt-pathway activation contribute to sorafenib resistance of hepatocellular carcinoma,* Science Get Together 2018, Paracelsus Medical University (PMU), Salzburg, Austria, June 29, 2018 (poster presentation).

Martina Meßner, Maximilian A. Ardelt, Katrin Meyer, Thomas Fröhlich, Angelika M. Vollmar, Johanna Liebl; *Characterization of sorafenib resistance and rebound growth in hepatocellular carcinoma cells,* Annual Meeting of the German Pharmaceutical Society (DPhG), Munich, Germany, October 4-7, 2016 (poster presentation).

9.4 Acknowledgements

Mein herzlichster Dank gilt Frau Prof. Dr. Johanna Pachmayr und Frau Prof. Dr. Angelika Vollmar für die Möglichkeit, meine Dissertation am Lehrstuhl für Pharmazeutische Biologie an der Ludwig-Maximilians-Universität (LMU) München und später am Institut für Pharmazie der Paracelsus Medizinischen Privatuniversität (PMU) in Salzburg anzufertigen.

Liebe Hanna, ich danke dir für die Zusammenarbeit der letzten Jahre, die Betreuung der Masterarbeit bis hin zur Promotion und für die Möglichkeit in Salzburg beim Aufbau des neuen Lehrstuhls mitzuwirken. Du standest mir nicht nur bei meinen Projekten mit Rat und Tat zur Seite, sondern hattest auch stets ein offenes Ohr für Belange jeder Art. Ich danke dir für die Freiheit bei der Projektgestaltung, sowie für die unzähligen Telefonate und motivierenden Worte.

Frau Vollmar, ich danke Ihnen für den wissenschaftlichen und persönlichen Austausch in unseren monatlichen Achievement-Meetings, die meine Doktorarbeit zu Beginn stark bereichert und vorangetrieben haben. Vielen Dank für Ihr Vertrauen in meine Arbeit, ihre ansteckende wissenschaftliche Neugier und dass Sie mich auch nach dem Umzug nach Salzburg weiterhin tatkräftig unterstützt haben. Ich habe die Zeit in Ihrem Arbeitskreis sehr genossen!

Der Prüfungskommission bestehend aus Frau Prof. Dr. Johanna Pachmayr, Frau Prof. Dr. Angelika M. Vollmar, Herrn Prof. Dr. Hans Zischka, Herrn Dr. Elvir Becirovic, Herrn Prof. Dr. Stylianos Michalakis und Herrn Prof. Dr. Stefan Zahler möchte ich für die Bereitschaft zur Bewertung meiner Arbeit und dem damit verbundenen Zeitaufwand herzlich danken.

Vielen Dank auch an meine zahlreichen Kooperationspartner, die in den vergangenen Jahren maßgeblich zu dem Fortschritt meiner Projekte beigetragen haben: Prof. Dr. Georg Arnold und Dr. Thomas Fröhlich (LAFUGA, Gene Centre, LMU München), Prof. Dr. Simon Rothenfußer und Dr. Lars König (Klinische Pharmakologie, Universitätsklinikum LMU München), Dr. Andreas Koeberle und Dr. Helmut Pein (Pharmazeutische/Medizinische Chemie, Friedrich-Schiller-Universität Jena), Prof. Dr. Alexandra Kiemer (Pharmazeutische Biologie, Universität des Saarlandes), Prof. Dr. Andreas Sieber und Dr. Mathias Hackl (Institut für Chemie, Technische Universität München), sowie Prof. Dr. Alexander Gerbes (Leberzentrum, Universitätsklinikum LMU München).

Ein ganz besonderes Dankeschön geht dabei an Prof. Dr. Hans Zischka und Dr. Sabine Schmitt (Institut für Toxikologie und Umwelthygiene, Technische Universität München). Ich danke euch für die produktive Zusammenarbeit, die kreativen Ideen bei der Projektgestaltung, all der Zeit und Hilfe bei der technischen Umsetzung, sowie für die fortwährende Unterstützung beim Publizieren. Ich war immer gern zu Gast bei euch im Labor und ich habe viel von euch gelernt!

Lieber Max, danke dir für die engagierte Betreuung meiner Masterarbeit, für alles was du mir in den letzten Jahren beigebracht hast und die gute Zusammenarbeit bei gemeinsamen Projekten während der Promotion. Du warst mir in den letzten Jahren ein wichtiger Ansprechpartner und ich bin sehr froh, dass du mit nach Salzburg gekommen bist!

Meiner Masterstudentin Lena Zobel und meinem Bachelorstudenten Julian Frädrich danke ich für die motivierte Projektteilnahme und die herausragende Laborarbeit, die sie im Rahmen meiner Dissertation geleistet haben.

Ein großer Dank gilt dem gesamten Arbeitskreis Vollmar für die gute Zusammenarbeit und für die schönen Erinnerungen in- und außerhalb des Labors. Carina und Kerstin, ich danke euch für die Hilfe bei den Mausversuchen. Meinen „Bench-Nachbarn“ aus B4.074, Flo und Themis, danke ich für die erfrischende allmorgendlichen Kaffeerunde und euch, Martin und Daniel, für die gute Freundschaft!

Ein herzliches Dankeschön geht auch an meine Kollegen von der PMU, Petra, Lukas und Stephi, für die Zusammenarbeit im Labor, die gemeinsame Zeit in unzähligen Praktika, sowie die emotionale Unterstützung im letzten Jahr der Doktorarbeit. Ich danke euch für die familiäre Atmosphäre, die ihr in das neue Institut gebracht habt und für die über das Labor hinausreichende Freundschaft.

Ganz besonders möchte ich mich bei meiner Familie bedanken. Danke, dass ihr mir das alles ermöglicht habt und für all die Unterstützung wann immer ich sie gebraucht habe!